

# Superconducting Josephson circuits for quantum hybrid systems with mechanical oscillators

**Dissertation**

der Mathematisch-Naturwissenschaftlichen Fakultät  
der Eberhard Karls Universität Tübingen  
zur Erlangung des Grades eines  
Doktors der Naturwissenschaften  
(Dr. rer. nat.)

vorgelegt von  
Kevin-Daniel Uhl  
aus Pfullendorf

Tübingen  
2024

Gedruckt mit Genehmigung der Mathematisch-Naturwissenschaftlichen  
Fakultät der Eberhard Karls Universität Tübingen.

Tag der mündl. Qualifikation:	28.06.2024
Dekan:	Prof. Dr. Thilo Stehle
1. Berichterstatter:	Prof. Dr. Reinhold Kleiner
2. Berichterstatter:	Assoc. Prof. Dr. Thilo Bauch

# Abstract

Josephson microwave circuits play a crucial role in advancing superconducting technologies such as quantum computation and quantum sensing. Current circuits predominantly utilize aluminum (Al) thin films or Al-AlO<sub>x</sub>-Al trilayer tunnel junctions. However, there is increasing interest in microwave circuits made from alternative materials, that provide higher magnetic field tolerance and higher operation temperatures compared to Al. Frequency-tunable cavities with weakly nonlinear Josephson junctions made of niobium (Nb) or with the high-temperature cuprate superconductor YBa<sub>2</sub>Cu<sub>3</sub>O<sub>7</sub> (YBCO) would overcome these limitations. However, obtaining microwave superconducting quantum interference device (SQUID) cavities with large-tunability made of these materials has proven to be challenging.

To address this issue, a neon focused-ion-beam (Ne-FIB) is used to create monolithic Nb three-dimensional (3D) nanoconstriction-type Josephson junctions (cJJs), where the thickness of the cJJ compared to the superconducting leads is reduced. In a first series of experiments, which involves a combination of direct-current and microwave measurement techniques, the current-phase-relation (CPR) was determined. A forward-skewed sinusoidal CPR was observed. In a second experiment it was demonstrated, that high-quality SQUID microwave circuits can be fabricated using these novel 3D Ne-FIB cJJs. In the case of YBCO, near-ideal tunnel junctions are obtained through helium focused-ion-beam irradiation. The resulting microwave SQUID cavities from both materials demonstrate frequency tunabilities, flux responsivities, and Kerr nonlinearities that are comparable to those of aluminum devices. However, they offer a broader operation parameter range in terms of temperature and magnetic field. These results suggest that these resonators are promising candidates for hybrid quantum systems involving magnons, spin ensembles, or mechanical oscillators, especially for flux-mediated optomechanics.

In particular, flux-mediated optomechanics offers a platform for increasing the performance in acceleration and force sensing, as well as for exploring quantum physics in previously unexplored regimes with high

masses and long coherence times. To approach this goal, a superconducting lead-tin sphere with a diameter of  $100\ \mu\text{m}$  was levitated within a static magnetic trap formed by an anti-Helmholtz configuration. The sphere's center-of-mass motion of the sphere is magnetically monitored using a DC-SQUID and exhibits quality factors up to  $2.6 \cdot 10^7$ .

The results presented hold promise for applications in quantum sensing, hybrid quantum systems and parametric amplifiers.

# Kurzfassung

Mikrowellenschaltungen mit Josephson Kontakten spielen eine entscheidende Rolle bei der Weiterentwicklung von Supraleitertechnologien wie der Quanteninformationsverarbeitung und der Quantensensorik. Die meisten Schaltkreise verwenden dünne Aluminium (Al)-Filme und Al-AlO<sub>x</sub>-Al Trilagen-Josephson Kontakte. Jedoch besteht ein wachsendes Interesse an Mikrowellenschaltungen aus anderen supraleitenden Materialien, die eine höhere Magnetfeldtoleranz und höherer Betriebstemperatur im Vergleich zu Al aufweisen. Mikrowellenresonatoren mit schwach nichtlinearen Josephson-Kontakten aus Niob (Nb) oder dem Hochtemperatur-Kuprat-Supraleiter YBa<sub>2</sub>Cu<sub>3</sub>O<sub>7</sub> (YBCO) könnten diese Einschränkungen überwinden. Die Herstellung von Mikrowellenresonatoren mit supraleitenden Quanteninterferometern (SQUIDs, vom englischen: Superconducting Quantum Interference Devices) aus diesen Materialien hat sich jedoch als herausfordernd erwiesen.

Um dieses Problem anzugehen, wird im Rahmen dieser Arbeit ein fokussierter Neon-Ionenstrahl (Ne-FIB, vom englischen: neon Focused-Ion-Beam) zur Herstellung von monolithischen dreidimensionalen (3D) Nb-Nanoeinschnürungen (cJJs, vom englischen: Constriction Josephson Junctions) verwendet, bei denen die Dicke zwischen den supraleitenden Zuleitungen verringert ist. In einer ersten Versuchsreihe, die eine Kombination aus Gleichstrom- und Mikrowellenmesstechniken beinhaltet, wurde die Strom-Phasen-Beziehung (CPR, vom englischen Current-Phase-Relation) bestimmt. Dabei wurde eine vorwärts geneigte sinusförmige CPR beobachtet. Darüber hinaus wurde demonstriert, dass hochwertige SQUID-Mikrowellenschaltungen mit diesen neuartigen 3D Ne-FIB cJJs hergestellt werden können. Im Fall von YBCO werden nahezu ideale SIS-Tunnelkontakte durch Bestrahlung mit einem fokussierten Helium-Ionenstrahl erhalten. Die resultierenden Mikrowellen-SQUID-Resonatoren aus beiden Materialien zeigen Frequenz-Durchstimmbarkeiten, Fluss-Responsivitäten und Kerr-Nichtlinearitäten, die mit denen von Aluminiumresonatoren vergleichbar sind. Jedoch bieten die neuartigen Resonatoren einen größeren Betriebsbereich in Bezug auf Temperatur und

Magnetfeld. Diese Ergebnisse legen nahe, dass die Resonatoren vielversprechende Kandidaten für Quaten-Hybridsysteme mit Magnonen, Spin-Ensembles oder mechanischen Oszillatoren (flussvermittelte Optomechanik) sind.

Insbesondere die flussvermittelte Optomechanik bietet eine vielversprechende Plattform für hochempfindliche Detektion von Beschleunigung- und Kraftmessung sowie für die Erforschung der Quantenphysik in bisher unerforschten Bereichen mit großen Massen und langen Kohärenzzeiten. Hierfür wurde im Rahmen dieser Arbeit eine schwebende supraleitende Blei-Zinn-Kugel mit einem Durchmesser von  $100\ \mu\text{m}$  in einer statischen Magnetfalle aufgrund des Meißner-Ochsenfeld-Effekts gefangen gehalten. Dieser Ansatz bietet die Realisierung von nanometer und sogar mikrometer großen Quantensysteme mit minimaler Dekohärenz. Die Schwerpunktsbewegung der Kugel wurde mit einem DC-SQUID magnetisch ausgelesen und weist Gütefaktoren von bis zu  $2.6 \cdot 10^7$  auf.

Die hier vorgestellten Resultate sind vielversprechend für Anwendungen in der Quantensensorik, in hybriden Quantensystemen und parametrischen Verstärkern.

# List of publications

This is a cumulative thesis based on the work published in the four papers listed below. Publication 1 to 3 describe the properties of flux-tunable microwave cavities using niobium and  $\text{YBa}_2\text{Cu}_3\text{O}_7$  as circuit material. Publication 4 presents a measurement setup to obtain information on position and oscillatory behavior of a levitated superconducting object. All publications are attached at the end of the thesis.

## Appended publications

- Publication 1** K. Uhl, D. Hackenbeck, D. Koelle, R. Kleiner, D. Bothner  
*Extracting the current-phase-relation of a monolithic three-dimensional nano-constriction using a DC-current-tunable superconducting microwave cavity*  
under review in Physical Review Applied (2024), arXiv: 2402.10276
- Publication 2** K. Uhl, D. Hackenbeck, J. Peter, R. Kleiner, D. Koelle, D. Bothner  
*Niobium quantum interference microwave circuits with monolithic three-dimensional nanobridge junctions*  
Physical Review Applied **21**, 024051 (2024)
- Publication 3** K. Uhl, D. Hackenbeck, C. Fuger, R. Kleiner, D. Koelle, D. Bothner  
*A flux-tunable  $\text{YBa}_2\text{Cu}_3\text{O}_7$  quantum interference microwave circuit*  
Applied Physics Letters **122**, 182603 (2023)

**Publication 4** J. Hofer, R. Gross, G. Higgins, H. Huebl, O. F. Kieler, R. Kleiner, D. Koelle, P. Schmidt, J. A. Slater, M. Trupke, **K. Uhl**, T. Weimann, W. Wiczorek, M. Aspelmeyer  
*High-Q magnetic levitation and control of superconducting microspheres at millikelvin temperatures*  
Physical Review Letters **131**, 043603 (2023)

### Publications not included in this thesis

**Publication 5** P. Schmidt, R. Claessen, G. Higgins, J. Hofer, J. Hansen, P. Asenbaum, **K. Uhl**, R. Kleiner, R. Gross, H. Huebl, M. Trubke, M. Aspelmeyer  
*Remote sensing of a levitated superconductor with a flux-tunable microwave cavity*  
accepted in Physical Review Applied (2023),  
arXiv: 2401.08854

# Contents

<b>1</b>	<b>Introduction</b>	<b>1</b>
<b>2</b>	<b>Summary of publications and contributions</b>	<b>9</b>
2.1	<b>Publication 1:</b> Extracting the current-phase-relation of a monolithic three-dimensional nano-constriction using a DC-current-tunable superconducting microwave cavity . . . . .	9
2.2	<b>Publication 2:</b> Niobium quantum interference microwave circuits with monolithic three-dimensional nanobridge Junctions . . . . .	16
2.3	<b>Publication 3:</b> A flux-tunable $\text{YBa}_2\text{Cu}_3\text{O}_7$ quantum interference microwave circuit . . . . .	23
2.4	<b>Publication 4:</b> High- $Q$ magnetic levitation and control of superconducting microspheres at millikelvin temperatures .	28
<b>3</b>	<b>Conclusion and outlook</b>	<b>33</b>
<b>4</b>	<b>Acknowledgements</b>	<b>37</b>
	<b>Appended publications</b>	<b>55</b>



# 1 Introduction

During the last two decades the research on micro- and nano-mechanical devices had a dramatic impact in the fields of both sensing and macroscopic quantum physics. Impressive examples include nano-mechanical mass sensors with single-atom resolution of several  $10^{-27}$  kg [1] and force sensing experiments with less than zepto-Newton sensitivity [2, 3]. At the same time, an independent research effort has resulted in first demonstrations of quantum states of motion of mechanical oscillators including cooling to the quantum ground state of motion and single-phonon control [4–6]. The study in quantum-engineering of mechanical detectors may influence physics in the fields of ultrasensitive force sensing, testing fundamental physical questions and performing hybrid quantum information processing. One of the main goals is gravitational-wave detection to answer the unknown mystery in dark matter, to study the intersection of gravity with quantum physics and to explain the mass distribution of the universe [7]. Dealing with this topic leads to extremely sensitive experiments. There, one of the fundamental limitations are quantum fluctuations of the radiation-pressure force, which imply the exchange between momentum of an object and the electromagnetic field, thereby impacting the precision of displacement measurements. This issue has gained particular significance in ultrasensitive interferometers designed for gravitational-wave detectors such as LIGO, VIRGO, and KAGRA.

With this interest, a lot of significant progressing work on the exploration and understanding of the optomechanical interaction has been done in the last decades [8]. Here, high-quality cavities are used as photon boxes to confine the light field to a small mode volume. The most prominent and simplest example of such systems, known as the Fabry-Perot cavity [9], is formed by two mirrors placed parallel to each other. Optical light is confined between those two mirrors to form an oscillating light field with a specific frequency. If one of the mirrors acts as mechanical resonator, its displacement will modulate the cavity length and therefore the resonance frequency of the electromagnetic mode of the cavity. This concept allows one to couple systems such as membranes [10], microspheres [11] or

## 1 Introduction

atoms [12] to demonstrate radiation-pressure self-oscillations [13, 14] and cavity cooling [15].

A complementary and powerful platform for optomechanics are superconducting circuits in the microwave regime [16]. Most of these systems are based on devices focusing on a capacitive coupling between the superconducting cavity mode and mechanical motion. This was first theoretically announced by Braginsky in 1967 [17] and experimentally realized by Cuthbertson in 1996 using an inductor-capacitor ( $LC$ ) microwave cavity with a movable plate capacitor [18]. The goal was to observe damping and anti-damping of the mechanical motion [19]. The interaction between the capacitive plate membrane and its mechanical motion induces a shift in the resonance frequency of the microwave cavity, cf. Fig. 1.1(a). This coupling is key for radiation-pressure cooling and parametric amplification techniques [20]. In order to maximize the coupling, the gap between the two capacitor plates has to be reduced to a minimum. So far the most optimized devices have gaps of less than 50 nm with a zero-point motion of a few femto-meters [21–23]. Nevertheless, this technological optimization reaches its limitations in nanofabricated engineering and therefore poses restrictions on the optomechanical coupling.

Especially for mechanical quantum ground state preparation and cooling of motion, the coupling strength  $g = \sqrt{n_c}g_0$  between mechanical motion and optical cavity is crucial. It is given by the cavity photon number  $n_c$  and single-photon coupling strength  $g_0$ . The progress made in optomechanical systems depended on an improvement of the parameter  $g$  through a substantial increase in  $n_c$ . This has enabled the community to experimentally achieve not only the strong coupling regime with  $g > \kappa$  [24, 25], where  $g$  surpasses the cavity decay rate  $\kappa$ , but also the ultra-strong coupling regime, where  $g$  becomes comparable to both the cavity and mechanical frequencies [26]. Despite these notable achievements, this approach comes with various drawbacks. For instance, it results in heating of the mechanical mode well beyond the temperature mode in the optical domain [27], induces position-localization decoherence [28] and lastly results in an increase of the cavity noise floor in the microwave operational range [29]. These sources of noise significantly limit the attainable cooling limit and hinder the feasibility of preparing the mechanical quantum ground state.

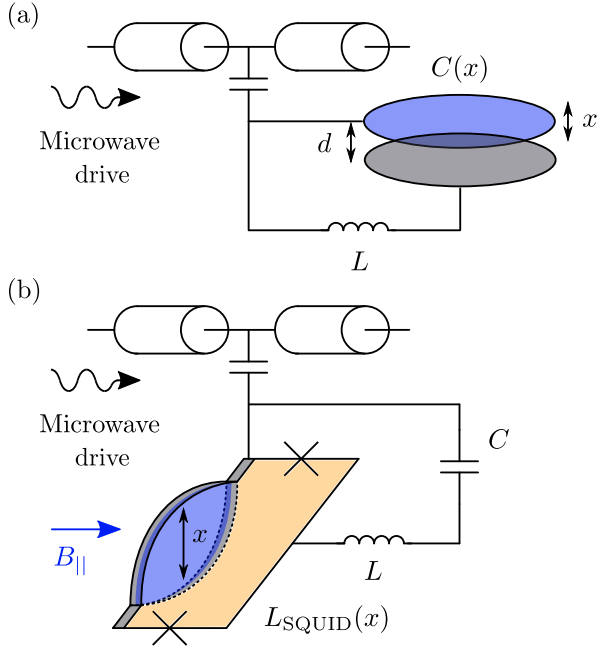


**Figure 1.1: Schematic drawing of capacitive and inductive coupling in microwave optomechanics.** In (a), a scheme of optomechanical coupling via mechanical capacitance is presented. The top plate (blue) of a parallel plate capacitor is suspended to form a mechanical resonator. The gap  $d$  between the two plates varies due to the motion  $x$  of the top plate. Therefore, the circuit capacitance  $C(x)$  and hence the resonance frequency of the  $LC$  circuit modulates. In (b), a flux-mediated optomechanical coupling is illustrated. The mechanical oscillator (gray beam) is part of the SQUID loop. The displacement  $x$  (blue area) of the mechanical resonator changes the total flux threading the SQUID (orange) in the presence of an in-plane magnetic field  $B_{\parallel}$ . Since the SQUID serves as a flux-tunable nonlinear element  $L_{\text{SQUID}}(x)$ , its inductance is modulated by the oscillating mechanical beam. Therefore the resonance frequency of the  $LC$  circuit modulates. Both microwave cavities in (a) and (b) are capacitively side-coupled to a transmission line.

## 1 Introduction

To overcome these constraints, one strategy is to enhance the single-photon coupling strength  $g_0$  to get rid of an increase in the cavity photon number. Ultimately, achieving the single-photon strong coupling regime, where  $g_0$  surpasses both the cavity decay rate and the mechanical frequency, would represent a significant advancement in preparing quantum states for mechanical modes [8, 30, 31].

In summary, the minimization of the distance of movable plate capacitors reaches its limitations in fabrication. This approach achieved a single-photon coupling  $g_0 \approx 2\pi \cdot 300 \text{ Hz}$  so far. This value is two orders of magnitude to low for reaching the single-photon strong coupling regime comparing with common  $\kappa \gtrsim 2\pi \cdot 10 \text{ kHz}$  [32–34]. However, an alternative approach to capacitance modulation involves considering the circuit inductance, which is modulated instead of the capacitance. A possible way is to engineer a flux mediated optomechanical system, which relies on a flux-tunable non-linear element, known as a Superconducting Quantum Interference Device (SQUID) [35, 36]. SQUIDs are one of the most sensitive magnetic field sensors that can detect changes in magnetic flux density in the range of  $10^{-15} \text{ T}$  [37]. The SQUID acts as a sensitive flux tunable inductor, whose inductance depends on the applied magnetic flux. A SQUID consists of a superconducting loop with a certain inductance, which is interrupted by either one or more Josephson junctions. Changing the magnetic flux through the SQUID loop enables a modulation of the resonance frequency of the SQUID cavity. This concept allows coupling of mechanical motions, which changes the magnetic flux density through the SQUID and therefore the SQUID cavity resonance frequency. Inspired from this idea, several approaches have been realized. One example is an optomechanical system featuring a cantilever with a magnetic tip that magnetically modulates the resonance frequency [36]. Another approach involves integrating the mechanical beam into the SQUID loop [38–40].

There is also a strong interest in levitating superconducting or magnetic oscillators [41, 42]. So far, these systems have relied on optical methods for readout and/or levitation [43–46]. However, utilizing photons for cooling and manipulation introduces significant limitations in terms of photon scattering and absorption, leading to position-localization decoherence and raising the object’s bulk temperature [28]. An alternative approach involves

a levitating mechanical resonator experimental setup that does not rely on photons but instead utilizes magnetostatic fields. Here, the mechanical oscillator is predicted to be well isolated from the environment, yielding large mechanical quality factors, long coherence times and enables levitation of large masses. A successful implementation of a magnetostatic levitating superconducting object would offer the potential for unprecedentedly long coherence times and sensing. In this context, a magnetic field gradient is required to generate a magnetic trap for levitating the superconducting sphere due to the Meissner effect. The superconducting shielding currents produces a flux that passes through the SQUID and depends on the center-of-mass position of the sphere. The initial steps to achieve this result are detailed in **publication 4**. Those first steps will enable applications with high performance in force sensing and for testing fundamental physical questions.

On the contrary to optimizing mechanical motion, strong flux-mediated coupling is required. Integrating the mechanical beam into the SQUID loop provides a viable way to strengthen this interaction and potentially enabling the system to enter the single-photon strong coupling regime, cf. Fig. 1.1(b). To establish a flux-mediated optomechanical connection between the mechanical beam and the LC circuit, an in-plane magnetic field  $B_{\parallel}$  is applied to induce a flux into the SQUID loop resulting from the displacement of the mechanical resonator. The zero-point motion with amplitude  $x_{\text{zpf}}$  of the beam leads to a variation in the magnetic flux passing through the SQUID and thereby induces changes in the SQUID cavity resonance frequency  $\omega_0$ . That offers the opportunity to scale the single-photon coupling strength  $g_0 \sim (\partial\omega_0/\partial\Phi)B_{\parallel}lx_{\text{zpf}}$ , where  $l$  is the length of the beam,  $\partial\omega_0/\partial\Phi$  the flux sensitivity of the SQUID cavity and  $\Phi$  the total flux in the SQUID, by applying high magnetic fields. Nevertheless, such circuits are often made out of aluminium thin films, which is a superconducting material with a critical magnetic field of only  $\sim 10 - 100$  mT [47, 48]. One potential approach to satisfy the mentioned requirements is to implement microwave circuits made out of materials like niobium [49], niobium alloys [50, 51], or even a high-temperature superconductor such as  $\text{YBa}_2\text{Cu}_3\text{O}_7$  (YBCO) [52], including high-field compatible Josephson elements such as nano-constrictions. In previous

## 1 Introduction

endeavors, it has been challenging to achieve constriction-junction SQUIDs made from these materials with substantially large flux tunability, except for YBCO [53, 54]. For YBCO, grooved constriction-junction SQUIDs have been fabricated using argon milling [55, 56]. However, their microwave SQUID cavity behavior has not been extensively studied so far and would be interesting.

Despite the potential advantages of utilizing flux-mediated optomechanical systems to enhance the single-photon coupling strength, SQUID cavities have an inherent property that is often viewed as a disadvantage - the Kerr non-linearity. This non-linearity affects the maximum number of drive photons the cavity can accommodate before transitioning into a non-linear behavior. In contrast to a linear microwave cavity coupled to a mechanical element, the flux-mediated optomechanical system's maximum drive-enhanced coupling strength is constrained by the cavity non-linearity. Considering that a significant multi-photon coupling strength is essential for various applications such as quantum ground state cooling or quantum-state transfer, the development of a system that boosts  $g_0$  without imposing a low threshold on the number of photons would be highly valuable in the field of optomechanics.

Moreover, there is also significant interest in SQUID cavities with compatibility in temperature, magnetic field and low non-linearity for hybrid-systems involving spin ensembles [57, 58], and magnons [59–61], dispersive magnetometry [62] and Josephson parametric amplifiers [63–65]. Spin ensembles, such as nitrogen-vacancy (NV) centers in diamond [66] and magnonic systems, such as yttrium iron garnet (YIG) crystals require high magnetic fields for control [67, 68]. One advantage of these systems is their experimentally accessible microwave and optical transitions that allows for an optically induced polarization in the ground state. This broad addressability makes them highly attractive for use in hybrid systems, qubit quantum states and quantum communication applications. Integrating magnonic systems with optomechanical elements would further enhance their versatility, facilitating quantum state transfer among different physical systems and enabling the study of exotic magnetic excitations and quantum sensing [69–71]. Dispersive SQUID techniques and Josephson parametric amplifiers have been studied in a variety of different microwave

circuit configurations [72–75]. Typically these devices are made out of aluminum. Extending their operation window in temperature range and high magnetic field compatibility would enable novel experiments and would push the boundaries of complex hybrid systems, such as macroscopic magnetization of spin ensembles [76] or magnomechanics.

Therefore, one of the main efforts of this thesis was to design microwave circuits for flux-mediated optomechanical systems made of niobium and YBCO. **Publication 1** and **2** deal with the realization of niobium SQUID cavities based on neon focused-ion-beam (Ne-FIB) patterned monolithic 3D nanobridge junctions. Constrictions in general are far less understood than conventional Josephson tunnel junctions, despite their critical significance in circuit designs. They combine a small junction area with high critical current densities but without adding large capacitances or lossy materials. The main characteristics of Josephson elements are their critical current and potentially nontrivial current-phase-relation (CPR). Especially the CPR, which describes the relation between the phase difference across the constriction and the current flowing through it, is hard to predict and has a huge impact on the cavity flux sensitivity [77–79]. In general, the constriction junctions are formed by a thin, narrow superconducting bridge, which is contacted by large superconducting electrodes. These are 2D nanobridges, in which the bridge and electrodes have the same thickness. However, these 2D junctions have CPRs which are only weakly nonlinear and in some cases are almost linear [79]. This can lead to a reduction of the flux sensitivity. A solution to these issues is to make a variable-thickness (3D) constriction junction, in which the bridge is much thinner in all direction than the electrodes. For better understanding of a 3D nanobridge junction and their properties, **publication 1** presents a full investigation on this topic. There, the microwave circuit allows simultaneous DC current-voltage access to a single constriction and microwave characterization of the DC-current-biased cavity using microwave reflectometry. This provides a useful method to comprehensively characterize nonlinear elements integrated in microwave circuits and could be of interest for hybrid quantum systems, parametric amplifiers and current sensors.

**Publication 2** presents the implementation of Nb microwave SQUID resonators featuring both 2D and 3D constrictions, along with the resulting

## 1 Introduction

variations in frequency tunability, flux responsivities, and Kerr nonlinearities. The devices are on par with comparable aluminum nanobridge devices, but with the opportunity of a much larger operation parameter regime - temperature and magnetic field. Additionally, the results demonstrate that focused neon-ion-beam milling is a promising approach for constructing 3D constriction junctions with adjustable junction parameters. Furthermore, the microwave circuits show significant potential for implementing them into applications of hybrid systems as e.g. spin ensembles and magnons [60] or in flux-mediated optomechanical coupling.

To increase the possible parameter range for device operation, **publication 3** presents the realization of a microwave SQUID cavity out of the material YBCO, a material with a high critical temperature and a much higher critical magnetic field tolerance, that goes up to several Tesla [80]. The SQUID is based on Josephson junctions directly written with a helium focused-ion-beam (He-FIB) using a He ion microscope (HIM). The publication demonstrates that YBCO-HIM-SQUID microwave resonators are promising candidates for quantum sensing and microwave technology applications.

**Publication 4** shows a promising platform for testing quantum physics with mechanical motions of high masses. In this approach a levitated superconducting sphere is trapped in a static magnetic anti-Helmholz configuration. This prevents scattering and absorption of photons, compared to optical systems, to lower the damping and heating rates [81]. The center-of-mass motion of the sphere is magnetically read out using a DC-SQUID for first characterization steps.

To conclude, this thesis investigated an alternative approach of flux-tunable resonators with different materials and Josephson junction fabrications. They show highly promising properties for optomechanical systems. Additionally one possibility of mechanical system for such coupling is presented.

## 2 Summary of publications and contributions

### 2.1 Publication 1: Extracting the current-phase-relation of a monolithic three-dimensional nano-constriction using a DC-current-tunable superconducting microwave cavity

In this publication, the properties of a niobium (Nb) monolithic three-dimensional (3D) nanobridge, which is embedded in a microwave circuit with direct current (DC) access, and the circuit itself are experimentally investigated.

Josephson junctions (JJs) are widely used in microwave quantum applications, such as Josephson parametric amplifiers [65, 82], tunable microwave cavities for quantum hybrid systems [79, 83] as well as for DC applications, such as for susceptometry [84] and Josephson voltage standards [85]. So far, most microwave devices have been constructed using superconductor-insulator-superconductor (SIS) trilayer Josephson junctions made of Al-AlO<sub>x</sub>-Al. However, there is an increasing interest in implementing aluminum constriction-type Josephson junctions (cJJs) due to their compatibility with high magnetic fields. Nevertheless, aluminum (Al) itself has limited magnetic field compatibility of  $\sim 10 - 100$  mT [48]. A successful implementation of cJJs using Nb enables experiments at significantly higher magnetic fields and temperatures. Nevertheless, achieving accurate control over the current-phase-relation (CPR) of these constrictions proves challenging, as it is highly sensitive to material properties, constriction dimensions, temperature and fabrication methods [86, 87]. In many cases, the CPR deviates significantly from the ideal sinusoidal shape. Designing devices and technologies based on these non-sinusoidal Josephson elements requires a deep understanding of the critical current and the CPR.

In this publication, a superconducting microwave transmission line cavity with an integrated Nb 3D nano-constriction is fabricated by patterning the cJJ with a neon focused-ion-beam using a neon-ion-microscope (NIM).

## 2 Summary of publications and contributions

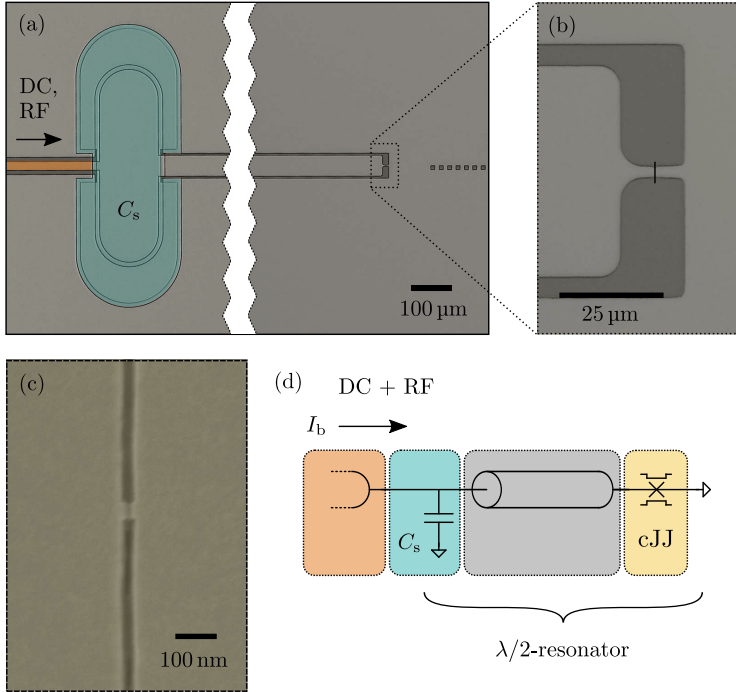


**Figure 2.1: A superconducting microwave cavity with DC access and integrated niobium nano-constriction.** (a) Optical micrograph of the  $\lambda/2$ -transmission line cavity. At the input port, the cavity is shunt-coupled by a large parallel-plate shunt capacitance (Nb-SiN<sub>x</sub>-Nb)  $C_s$  (blue) to a feedline (orange) for simultaneous microwave driving and readout as well as DC access to the constriction. At the far end, close to the connection to ground, a monolithic 3D niobium nano-cJJ is patterned into the center conductor of the coplanar waveguide resonator. Bright parts are 90 nm-thick niobium, dark parts are silicon substrate. (b) Zoom to the end part of the resonator; (c) Electron microscopy image of the cJJ. (d) Circuit equivalent of the transmission line cavity with the cJJ at the end. Figure adapted from appended publication 1.

## 2.1 **Publication 1:** *Extracting the current-phase-relation of a monolithic three-dimensional nano-constriction using a DC-current-tunable superconducting microwave cavity*

The design of the cavity allows simultaneous DC current-voltage access additionally to a microwave characterization, cf. Fig. 2.1. At its input port, the cavity is shunted to a coplanar waveguide feedline via a capacitance to ground. This coupling scheme leaves the center conductor of the waveguide uninterrupted and a bias current  $I_b$  can pass along the waveguide centre. At the far end of the transmission line cavity, the centre conductor has a narrow part, into which the constriction is cut and where it is connected to the ground forming a  $\lambda/2$ -resonator. For the constriction, a narrow  $\sim 25$  nm wide slot from both sides is cut into the narrow part with the NIM, leaving only a  $\sim 40$  nm wide constriction. Simultaneously, the thickness between the superconducting leads (film thickness  $\sim 90$  nm) is reduced to a remaining thickness of  $\sim 40$  nm.

In contrast to comparable experiments where the junction fabrication is performed simultaneously with the cavity [88, 89], this approach offers the advantage of characterizing the same cavity both with and without the constriction Josephson junction. This leads to a precise and comprehensive characterisation of the monolithically patterned 3D nano-constriction properties. In combination with microwave reflectometry and DC biasing of the device, it is possible to extract the CPR in two different experimental ways. This allows one to cross check the theory and to highlight the accuracy of the analysis.

One approach is to reconstruct the CPR by accurately determining the constriction inductance  $L_c$ . Extracting  $L_c$  relies heavily on the resonance frequency tunability of the cavity. Therefore, it is essential to use a sufficiently low microwave probe power to keep the cavity within the linear response regime. This allows the extraction of the resonance frequency  $\omega_0(I_b)$  for varying bias current  $I_b$ . The resonance frequency shifts to lower values by increasing  $I_b$  until a switching current  $I_{sw} = 39 \mu\text{A}$  is reached, cf. Fig. 2.2(a). At this point, the zero-voltage state switches to a finite-voltage state and the resonance vanishes abruptly. The total frequency range, covered with the bias current tuning, is  $\sim 13.5$  MHz at 3.9 K. This behavior is to be expected due to the nature of the superconducting nonlinear inductance  $L_c$ , which typically increases with increasing quasiparticle density and a decrease in Cooper pair density, cf. Fig. 2.2(b). The

## 2 Summary of publications and contributions

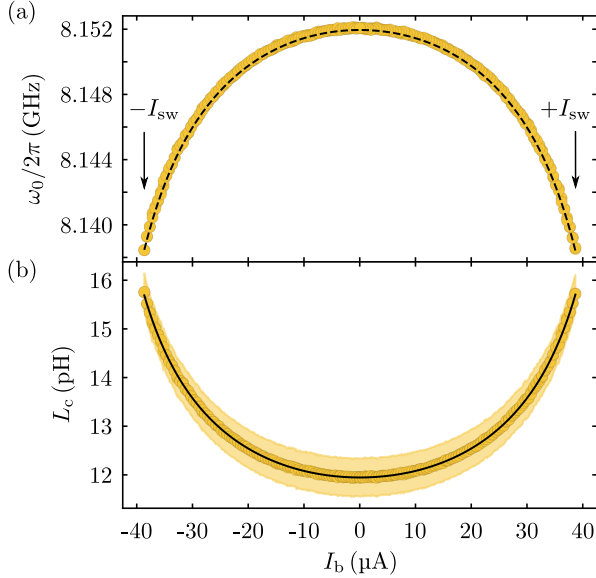


**Figure 2.2: Microwave cavity tunability with DC access.** Panel (a) presents the cavity tunability. As the bias current  $I_b$  increases, the resonance frequency  $\omega_0(I_b)$  shifts to lower values until  $I_{sw} \sim 39 \mu\text{A}$  is reached. In (b) the frequency shift is related to a change of the nonlinear constriction inductance  $L_c(I_b)$ . Symbols are data, dashed line is calculated from theory expressions and fit values, solid line is a fit using linear-plus-Josephson inductance model and the color-shaded area around the data points in (b) corresponds to estimated errors. Figure adapted from appended publication 1.

constriction inductance increases from around 12 pH at zero bias current to around 15.8 pH.

Once the cJJ inductance  $L_c$  is known for each bias current, the phase  $\delta$  of the constriction can be reconstructed by integration using

$$\delta = 2\pi/\Phi_0 \int_0^{I_b} L_c dI'_b,$$

**2.1 Publication 1:** *Extracting the current-phase-relation of a monolithic three-dimensional nano-constriction using a DC-current-tunable superconducting microwave cavity*

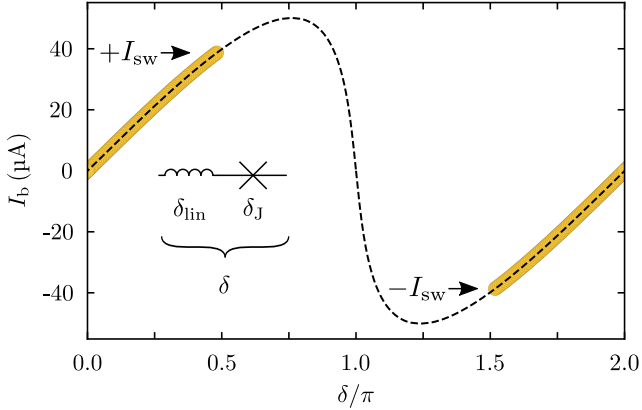


**Figure 2.3: Reconstructed CPR of the nano-constriction from junction inductance.** Integration from the cJJ inductance for each bias current point as yellow circles. Data points for  $I_b < 0$  have been manually shifted by  $+2\pi$  in phase. Describing  $L_c$  as a linear-plus-Josephson inductance, the CPR can be modeled with a total phase  $\delta = \delta_{\text{lin}} + \delta_J$ , where  $\delta_{\text{lin}}$  represents the phase across the linear part and  $\delta_J$  ideal Josephson part. The modelled result is shown as black dashed line. Figure adapted from appended publication 1.

where  $\Phi_0$  is the flux quantum, cf. Fig. 2.3. When integrated, the 3D cJJ shows a predominantly linear dependence for  $\delta \leq \pi/4$  and starts to bend towards smaller slopes as  $I_b$  increases until  $I_b = I_{\text{sw}}$ . Such a forward-skewed CPR has been found in the literature for constriction junctions and in particular made out of other materials [54, 78, 90]. This behavior can be approximated using a theoretical description of the cJJ inductance. In this model a combination of a linear inductance  $L_{\text{lin}}$  and an ideal Josephson element  $L_J$  is used to describe  $L_c$ . Previous studies have demonstrated that the linear-plus-Josephson inductance model matches with high accuracy [87, 90]. However, the experimentally observed CPR does not reach the point where the slope approaches zero, which is typically the case when  $I_b$  is approximately equal to the critical current  $I_0$  of the junction.

## 2 Summary of publications and contributions

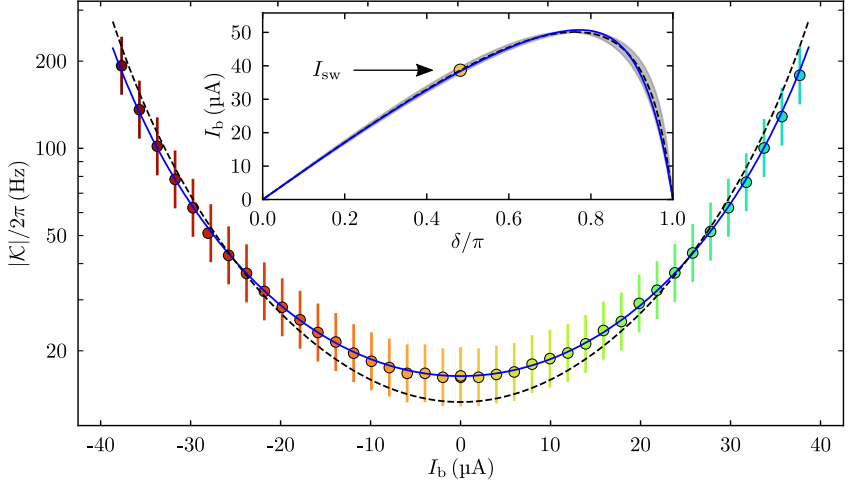


**Figure 2.4: Higher order derivatives of the CPR shape impacting the Kerr anharmonicity.** Kerr constant  $\mathcal{K}$  for multiple bias currents show an increase in magnitude with increasing  $I_b$ . For comparison of the impact of the CPR, two different theoretical lines based on nonlinear current-conservation calculations are plotted. The black dashed line is generated using the second and third derivatives of the experimentally determined CPR employing the linear-plus-sinusoidal model. The blue solid line is based on an artificially crafted CPR that closely resembles the one derived from the linear-plus-sinusoidal-inductance model for  $I_b < I_0$ . Both CPRs are directly compared in the inset. The yellow circle marks the experimentally observed switching current, and the uncertainty in the linear-plus-sinusoidal CPR is represented by the gray shaded area. Figure adapted from appended publication 1.

The other approach to obtain information about the CPR and to cross check the previous analysis, is to gain access to the derivatives of the CPR by characterizing the Kerr nonlinearity  $\mathcal{K}$ . The theoretical relation between the CPR and  $\mathcal{K}$  is given by

$$\mathcal{K} = \frac{e^2}{2\hbar C_{\text{tot}}} p_c^3 \left[ \frac{g_4}{g_2} - \frac{3g_3^2}{g_2^2} (1 - p_c) - \frac{5}{3} \frac{g_3^2}{g_2^2} p_c \right],$$

**2.1 Publication 1:** *Extracting the current-phase-relation of a monolithic three-dimensional nano-constriction using a DC-current-tunable superconducting microwave cavity*

where the coefficients  $g_n = \left. \frac{\partial^{n-1} I}{\partial \delta^{n-1}} \right|_{\delta_0}$  encode the derivatives of the CPR

and  $p_c = \frac{L_c(I_b)}{L_r + L_c(I_b)}$  is the constriction inductance participation ratio to the cavity inductance  $L_r$ . This enables a second detailed analysis of the CPR.

Utilizing the CPR obtained from the linear-plus-sinusoidal model, the theoretical Kerr constant can be easily calculated. The resulting value demonstrates acceptable agreement with the data, cf. Fig. 2.4. However, discrepancies emerge at the lowest and highest bias currents. To illustrate the significant impact of variations in the CPR on the Kerr constant, an artificial CPR based on an odd polynomial function has been constructed to describe  $\mathcal{K}$ . The result shows, that very small changes of the absolute values of the CPR can lead to larger differences in the higher order derivatives of the CPR.

### Contributions

This work was done in cooperation with D. Hackenbeck, D. Kölle, R. Kleiner and D. Bothner. For the publication, I had the leading role in device design, device fabrication, numerical simulations and experimentation. Additionally, I shared the leading role in data analysis and manuscript composition.

## 2.2 Publication 2: Niobium quantum interference microwave circuits with monolithic three-dimensional nanobridge Junctions

Publication 2 describes the realization and performance of three different niobium SQUID microwave cavities with constriction Josephson junctions (cJJs). The circuits differ in the constriction geometries, where a 2D (thickness of leads and constriction is equal) circuit is compared with different 3D (thickness of constriction is thinner than leads) cJJs.

SQUIDs in microwave applications have led to groundbreaking experimental and technological developments. They provide a Kerr nonlinearity and a tunability of the resonance frequency by external magnetic field which are magnificent for qubits, dispersive SQUID magnetometry or photon-pressure systems [91–93]. So far, aluminum is used as state of the art material with a critical magnetic field of  $B_c \sim 10 - 100$  mT and a critical temperature  $T_c = 1.2$  K [48]. The approach to realize microwave circuits out of a superconductor with higher  $B_c$  and  $T_c$  such as niobium with high-field compatible Josephson elements such as nano-constrictions turned out to be highly difficult [53]. In most endeavors thus far, it has been challenging to develop constriction-junction SQUIDs made of these material with significant tunability. This difficulty persists in both direct current (DC) operation mode and in the microwave domain [53, 94–96].

Here, the realization of three niobium SQUID microwave cavities based on cJJs patterned by neon focused-ion-beam (Ne-FIB) is reported. The microwave circuits consist of two interdigitated capacitors and a linear inductor line combined in parallel, cf. Fig. 2.5. They are capacitively sidecoupled to a coplanar waveguide transmission line. At the connection point between the two capacitors and the inductor line of each circuit is a square-shaped loop with hole size  $6 \times 6 \mu\text{m}^2$ . This loop configuration forms the SQUID after nano-patterning the constrictions. For all cJJs, two narrow 20 nm wide slots are cut from both sides into the Nb strip using the Ne-FIB. This forms an only 40 nm wide connection between the superconducting lead in each loop arm of the SQUID. Leaving the constriction thickness equal to the leads connected to them, corresponds

## 2.2 **Publication 2:** Niobium quantum interference microwave circuits with monolithic three-dimensional nanobridge Junctions

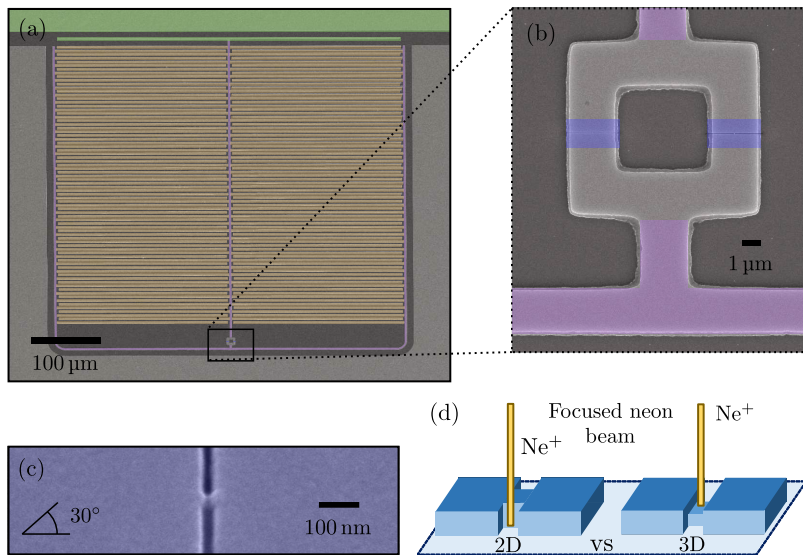


**Figure 2.5: A niobium-based quantum interference microwave circuit with monolithic 3D nanobridge junctions.** (a) False-colour optical micrograph of a typical device. The two interdigitated capacitors are orange, circuit main inductance is purple, the capacity sidecoupled to a coplanar waveguide transmission is green, the SQUID loop is uncoloured and (a)-(c) the nanobridges are blue. (c) False-colour scanning electron microscopy (SEM) image of the loop after constriction cutting, (d) zoom of a 3D constriction after cutting, taken with a SEM tilt angle of 30°. In (a)-(c) niobium is bright/coloured, silicon substrate dark grey. Panel (d) schematically illustrates the nano-constriction fabrication. For the 2D constrictions, two narrow slits are patterned into each of the SQUID arms by a focused neon ion beam; for the 3D constrictions, the nanobridges are additionally thinned down from the top by the neon beam. Adapted © 2024 American Physical Society..

to the type of constriction, which has been referred to 2D constriction. Constrictions that are thinner than the superconducting leads are 3D versions. Here the circuit film thickness can be kept larger compared to the constrictions. Consequently, the 3D constriction exhibits a low critical

## 2 Summary of publications and contributions

current and can have a less skewed current-phase-relation and lower flux noise [78, 90]. Additionally, the kinetic inductance of the circuit can be kept small.

Following the evaluation of the design and fabrication process, the performance of three SQUID cavities is presented in terms of frequency tunability, flux responsivity, and screening parameters. One resonator has 2D constrictions with a junction thickness of 90 nm, while two other resonators have 3D constrictions with thicknesses of 30 nm (3D<sub>1</sub>) and 20 nm (3D<sub>2</sub>) respectively. The film thickness of the cavity itself is consistent across all circuits at 90 nm. To see the cavity characteristics, an external magnetic field is applied perpendicular to the Nb thin film plane that introduces magnetic flux  $\Phi_{\text{ext}}$  into the SQUIDs, cf. Fig. 2.6. As a result, the resonance dip and therefore the resonance frequency shifts to lower frequencies as the magnetic flux increases. Additionally, an oscillating behaviour of the resonance frequency  $\omega_0(\Phi_{\text{ext}})$  with a periodicity of  $\Phi_0 \approx 2.068 \cdot 10^{-15} \text{ Tm}^2$  due to the fluxoid quantization in the SQUID loop was observed. Comparing the three different circuits, it turns out, that the flux-tuning range gets larger and the screening parameter lower with decreasing constriction thickness. For the 2D cJJs, a tuning range of the order of  $\sim 10$  MHz was achieved. On top of that, the individual flux archs show strong overlaps with a total observable width of  $\sim 2\Phi_0$ . The 3D<sub>2</sub> circuit instead has an tuning range on the order of  $\sim 65$  MHz and a flux hysteresis not visible in the data. For the 3D<sub>1</sub> device the tuning range is somewhere in between. Quantitatively modeling the flux-tunable resonance frequency involves

$$\omega_0(\Phi_{\text{ext}}) = \frac{\omega_b}{\sqrt{1 + \frac{1}{2L} L_c \left(\frac{\Phi}{\Phi_0}\right)}},$$

where  $L$  is the cavity inductance,  $L_c$  the constriction inductance and  $\omega_b$  the cavity resonance frequency without cJJs. The relation between the total flux in the SQUID  $\Phi$  and  $\Phi_{\text{ext}}$  normalized to the flux quantum  $\Phi_0$  is given by

$$\frac{\Phi}{\Phi_0} = \frac{\Phi_{\text{ext}}}{\Phi_0} - \frac{\beta_L}{2} \sin\left(\pi \frac{\Phi}{\Phi_0}\right),$$

2.2 **Publication 2:** Niobium quantum interference microwave circuits with monolithic three-dimensional nanobridge Junctions

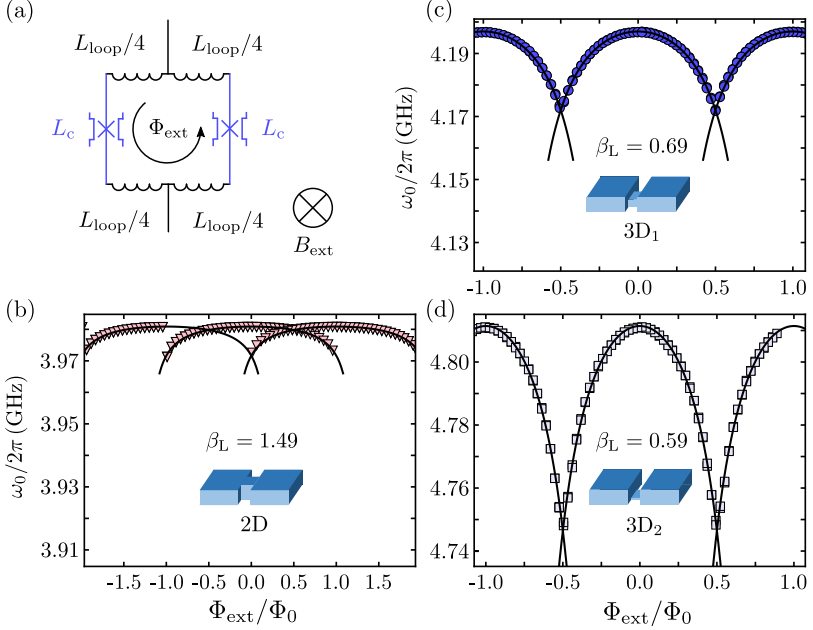


**Figure 2.6: Flux-tuning the resonance frequency of niobium quantum interference circuits with 2D and 3D constriction junctions.** (a) Circuit equivalent of the SQUID with a linear loop inductance  $L_{loop}/2$  in each arm and a constriction inductance  $L_c$ . (b)-(d) show the resonance frequency  $\omega_0$  vs external flux  $\Phi_{ext}$ . With increasing  $\Phi_{ext}$ , the resonance is shifting towards lower frequencies, indicating an increase of the constriction inductance by flux, which is shown as a function of flux in panel for the three different circuits with three different constrictions for sample temperature  $T_s = 2.5$  K. (b): 2D constriction, thickness  $\sim 90$  nm. (c): 3D constriction  $3D_1$ , thickness  $\sim 30$  nm. (d): 3D constriction  $3D_2$ , thickness  $\sim 20$  nm. With decreasing thickness of the constriction, the tuning range gets larger and screening parameter  $\beta_L$  and flux hysteresis (overlap of adjacent flux archs) decrease. Symbols are data and lines are fits from which  $\beta_L$  is extracted. Adapted © 2024 American Physical Society..

## 2 Summary of publications and contributions

where

$$\beta_L = \frac{2I_0 L_{\text{SQ}}}{\Phi_0}$$

is the effective screening parameter,  $I_0$  is the critical current of the cJJ and  $L_{\text{SQ}}$  is the total SQUID inductance. Besides obtaining a small screening parameter  $\beta_L = 0.59$  despite the large effective SQUID area  $\sim 8.5 \times 8.5 \mu\text{m}^2$ , circuit 3D<sub>2</sub> also achieves a maximum flux responsivity  $\partial\omega_0/\partial\Phi_{\text{ext}} \approx 2\pi \cdot 400 \text{ MHz}/\Phi_0$  comparable to similar aluminum constriction devices [97, 98].

An additionally interesting question in operating the Nb microwave circuits is how the properties depend on the sample temperature  $T_s$ . The observation shows, that the resonance frequency at zero-flux shifts to larger values and the tuning range of the resonance frequency grows with increasing temperature. This indicates an increase in the cJJ inductance and a decrease in the screening parameter. For the 2D device, the values for  $\beta_L$  vary between 0.6 and 1.6 and for the 3D samples between 0.4 and 0.8 for temperatures  $T_s = 2.4 - 2.8 \text{ K}$ , which are close to the critical temperature of the constrictions  $T_{\text{cc}} = 3.3 - 4.0 \text{ K}$ . This reduced transition temperature compared to the critical temperature of the niobium film, which is  $8.6 \text{ K}$ , has also been observed for electron-beam-patterned niobium nanobridges with comparable critical currents [99].

To complete the circuit characterization of the three different microwave SQUID cavities, the behaviour of the Kerr constant  $\mathcal{K}$ , also called Kerr nonlinearity, needs to be investigated. The Kerr constant is equivalent to the circuit resonance frequency shift per intracavity photon. To quantify  $\mathcal{K}$ , the cavities are measured using a two-tone scheme. Therefore a fixed-frequency pump tone, slightly blue-detuned from the undriven cavity resonance, is applied. The transmission response is recorded with a small probe tone for various pump powers in order to get the pump-shifted resonance frequency for determining the Kerr nonlinearity. For all circuits,  $\mathcal{K}$  increases with increasing flux and the absolute values differ by several orders of magnitude between the three devices. Despite this variation, the nonlinearity remains relatively low compared to other similar aluminum devices [97, 98], which is promising for applications such as photon-pressure and dispersive SQUID magnetometry, cf. Fig. 2.7.

2.2 **Publication 2:** *Niobium quantum interference microwave circuits with monolithic three-dimensional nanobridge Junctions*

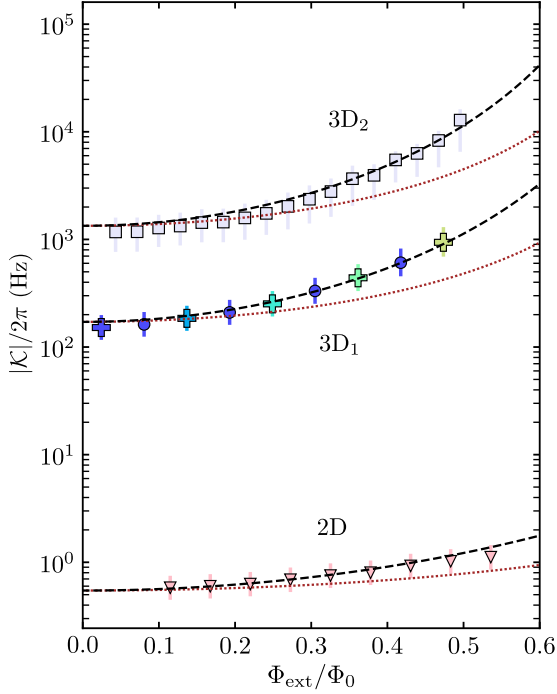


**Figure 2.7: The SQUID-cavity Kerr nonlinearity.** The Kerr nonlinearity  $|\mathcal{K}|$  vs external flux bias  $\Phi_{\text{ext}}/\Phi_0$  determined by probing the transmission response with a weak microwave signal, while a strong microwave pump tone with variable power and fixed frequency is applied slightly blue-detuned at a temperature  $T_s = 2.5$  K. Symbols are data and dashed lines are theoretical curves. © 2024 American Physical Society.

### Contributions

This work was done in cooperation with D. Hackenbeck, J. Peter, R. Kleiner, D. Kölle and D. Bothner. For the publication, I had the leading role in device design, device fabrication, numerical simulations and exper-

## *2 Summary of publications and contributions*

imentation. Additionally, I shared the leading role in data analysis and manuscript composition.

### 2.3 *Publication 3: A flux-tunable $\text{YBa}_2\text{Cu}_3\text{O}_7$ quantum interference microwave circuit*

## 2.3 **Publication 3: A flux-tunable $\text{YBa}_2\text{Cu}_3\text{O}_7$ quantum interference microwave circuit**

This publication presents the realization and characteristics of a flux-tunable  $\text{YBa}_2\text{Cu}_3\text{O}_7$  (YBCO) quantum interference microwave circuit with Josephson junctions patterned by helium focused-ion-beam (He-FIB).

So far, the standard superconducting material for flux-tunable microwave applications has been aluminum due to the high quality and controllability of Al Josephson junctions (JJs). However, experiments in flux-mediated optomechanics [100] and dispersive quantum magnetometry of individual magnetic nanoparticles prefer a high tolerance to external magnetic fields [62, 79]. Microwave resonators fabricated on the high-temperature superconductor like YBCO offer magnetic-field tolerances extending into the Tesla regime and provide the advantage of operating at high temperature up to  $\sim 80$  K [101, 102]. Additionally the usual approaches regarding JJs in Nb (see **publication 1** and **2**) [103], NbN [104] or hybrid JJs based on graphene [105] show potential to be integrated into high-field applications, but come with complications such as non-sinusoidal CPRs or complex fabrication challenges.

Publication 3 presents the realization of a high-temperature superconducting quantum interference microwave cavity utilizing YBCO. The circuit is an inductor-capacitor circuit, that combines two parallel interdigitated capacitors with linear inductors, cf. Fig. 2.8. It is capacitively side-coupled to a coplanar waveguide transmission for driving and readout. A large square-shaped  $11.5 \times 11.5 \mu\text{m}^2$  SQUID loop is integrated into the centre of the circuit. The two Josephson junctions are irradiated using a helium ion microscope (HIM) with a line dose of 900 ions/nm for each JJ.

To obtain information about the frequency-tunability and the screening parameter  $\beta_L$ , the circuit has to be characterized similar to **publication 2**. First, a magnetic field perpendicular to the YBCO thin film plane is applied to introduce an external magnetic flux  $\Phi_{\text{ext}}$  into the SQUID at liquid helium temperature. An observed phenomenon is the shift of the cavity resonance frequency  $\omega_0(\Phi_{\text{ext}})$  to lower values for increasing magnetic flux  $\Phi_{\text{ext}}$ , cf. Fig. 2.9. Moreover, a modulation of  $\omega_0$  with a periodicity of one flux quantum  $\Phi_0$  is observed. The frequency tuning

## 2 Summary of publications and contributions

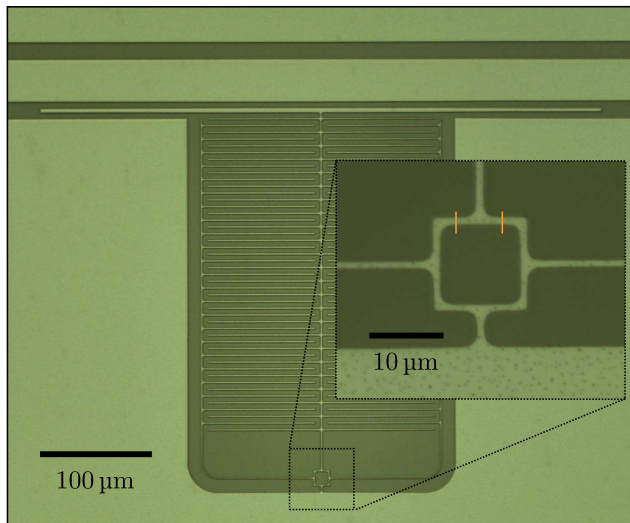


**Figure 2.8: The YBCO SQUID cavity with He-FIB patterned Josephson junctions.** Optical micrograph of the flux-tunable cavity, consisting of two interdigitated capacitors, a linear inductance and a SQUID loop with yellow indicated He-FIB patterned JJs, cf. zoom inset. The circuit is capacitively coupled to a coplanar waveguide feedline. YBCO is bright, the MgO substrate is dark. Adapted © 2023 American Institute of Physics.

range  $\omega_0^{\max} - \omega_0^{\min} \sim 2\pi \cdot 300$  MHz is larger than in similar Dayem-bridge SQUID-cavities reported for Nb (see **publication 1** and **2**) [53] or aluminum [97, 98]. Additionally, there is no hysteretic flux response observed, and a small screening parameter  $\beta_L = 0.33$  is obtained despite our large SQUID loop. This suggests that the He-FIB-JJs add no extra contribution to  $\beta_L$  compared to constriction junction CPRs with non-sinusoidal characteristics [87, 106, 107]. Also it looks like that the performance is even superior to the monolithic 3D constrictions in **publication 2** in terms of tunability, lower  $\beta_L$ , nearly ideal sinusoidal CPR, and the potential for application at higher magnetic fields and temperatures.

2.3 **Publication 3:** A flux-tunable  $\text{YBa}_2\text{Cu}_3\text{O}_7$  quantum interference microwave circuit

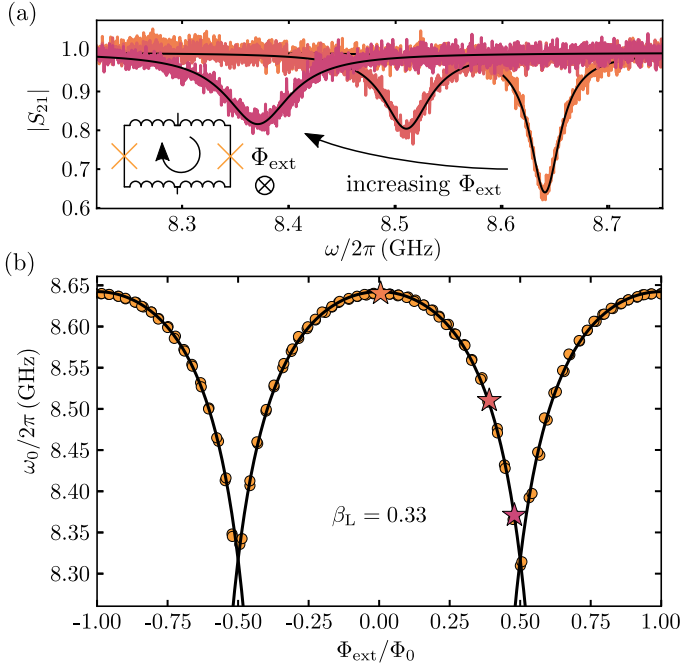


**Figure 2.9: Flux-tuning of the resonance frequency of a YBCO SQUID-cavity.** (a) Transmission response  $|S_{21}|$  of the YBCO-HIM-SQUID cavity at liquid helium temperature for three different bias flux values. With increasing flux in the SQUID, cf. inset schematic, the absorption resonance is shifting towards lower frequencies. In panel (b) the resonance frequency  $\omega_0(\Phi_{\text{ext}})$  is plotted. It modulates periodically with a periodicity of  $\Phi_0$  and the SQUID-cavity has a screening parameter  $\beta_L = 0.33$ . Symbols are data, lines are fits and the star-shaped data points in (b) correspond to curves in (a). © 2023 American Institute of Physics.

To determine the circuit Kerr nonlinearity  $\mathcal{K}$ , which is crucial for radiation-pressure experiments or parametric amplifiers, a two-tone characterization is performed. For this purpose, a continuous pump tone with slightly blue-detuned fixed-frequency and variable pump power is applied

## 2 Summary of publications and contributions

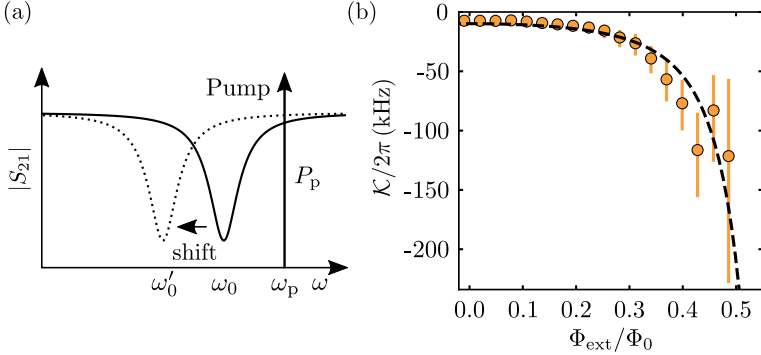


**Figure 2.10: The SQUID-cavity Kerr nonlinearity.** (a) Schematic drawing of the two-tone experiment. A pump tone with power  $P_p$  is applied slightly blue-detuned to the cavity resonance frequency. The transmission response  $|S_{21}|$  of the cavity is then measured using a low-power probe tone. As  $P_p$  increases, and consequently the intracavity photon number, the frequency shifts to lower values. (b) Kerr nonlinearity  $\mathcal{K}$  for different flux values obtained due to the frequency shift by intracavity pump photons. Symbols are data and the dashed line is a theoretical curve. Adapted © 2023 American Institute of Physics.

to the cavity. The response  $S_{21}$  is measured using a low-power probe tone. By increasing the intracircuit photon number through the pump tone, the resonance frequency shifts towards lower frequencies and  $\mathcal{K}$  can be obtained from this shift, cf. Fig. 2.10. The YBCO-SQUID cavity shows values varying from  $-8$  kHz at the zero flux (sweetspot) to  $-120$  kHz, which is sufficiently small to allow for high-power and high dynamic-range applications.

The combination of the huge operation temperature range, high critical magnetic field, low Kerr nonlinearity and high flux tunability opens up a significant parameter space for optomechanical, magnons experiments. Additionally, in future devices, the flexibility in HIM ion dose can be used to vary these parameters by several orders of magnitude.

### 2.3 **Publication 3:** *A flux-tunable $\text{YBa}_2\text{Cu}_3\text{O}_7$ quantum interference microwave circuit*

#### **Contributions**

This work was done in cooperation with D. Hackenbeck, C. Füger, R. Kleiner, D. Kölle and D. Bothner. For the publication, I had the leading role in device design, device fabrication, numerical simulations and experimentation. Additionally, I shared the leading role in data analysis and manuscript composition.

## 2.4 Publication 4: High- $Q$ magnetic levitation and control of superconducting microspheres at millikelvin temperatures

In publication 4, a cryogenic system for the detection and characterization of the motion of a levitating superconducting microsphere in a static magnetic trap is presented. The behaviour of the superconducting lead-tin sphere with 100  $\mu\text{m}$  diameter is observed using a DC-SQUID as well as an optical readout scheme in a dilution refrigerator at 15 mK.

Levitating objects offer a promising platform for conducting quantum experiments with macroscopic, micrometer-sized objects [108, 109], as well as for developing ultrasensitive force sensors [110, 111] and studying thermodynamics in the underdamped regime [112]. Most of these systems are based on an optical system for read out or levitation [46]. This leads to challenges related to heating and damping caused by photon absorption and scattering [46]. In contrast, magnetostatically levitating superconducting objects offers the potential for unachieved long coherence times and the levitation of larger masses [28, 113–115]. A successful implementation will have an immediate implication for testing fundamental physical questions, e.g. at the intersection of gravity with quantum physics. At the same time it will enable applications with unprecedented performance in the domain of magnetic and force sensing, and information processing in hybrid quantum systems.

In the setup, a superconducting sphere, made of a type-II superconductor 90-10 lead-tin alloy with 100  $\mu\text{m}$  diameter, is levitating within a static magnetic quadrupole field trap generated by a superconducting anti-Helmholtz coil formation, cf. Fig. 2.11. The coil is elliptically wound to ensure the center of mass (COM) motion is not degenerate and modes can be classified into  $x$ -,  $y$ - and  $z$ -axis motions. This COM motion is detected by inductively coupling the microsphere to a DC-SQUID current sensor via a planar Nb gradiometric pickup coil. The particle oscillation induces current in the pickup loop, which will be measured by the DC-SQUID. For preparing the levitated sphere there is a small feedback coil below the

2.4 **Publication 4:** *High- $Q$  magnetic levitation and control of superconducting microspheres at millikelvin temperatures*

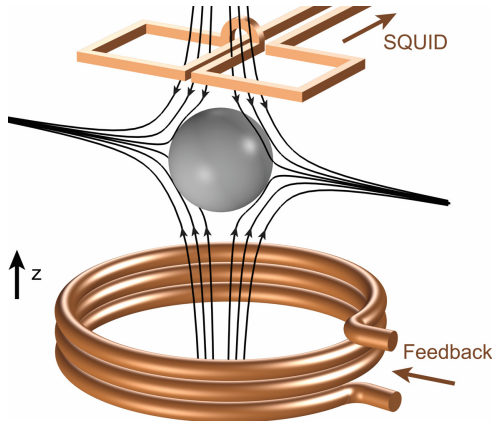


**Figure 2.11: Conceptual representation of the levitation experiment.** Schematic drawing of the levitation setup. The levitated sphere is magnetically trapped and induces magnetic flux by motion into the superconducting pickup coil. At the bottom, a feedback coil is shown, which is for adjusting the amplitudes of oscillation and preparing the sphere for levitation. Black lines show the magnetic trapping quadrupole field generated by an anti-Helmholtz coil pair (coils not shown). © 2023 American Physical Society.

trap centre to apply a magnetic feedback force to the levitated sphere for adjusting the motion amplitude.

The particle's COM frequencies are continuously tunable with a trap current resulting in frequencies for the  $x$ - and  $y$ -modes between  $\sim 50$  and  $\sim 100$ Hz, and for the  $z$ -mode between  $\sim 110$  and  $\sim 240$ Hz, cf. Fig. 2.12. In addition, the quality factor  $Q_{\text{sp}}$  was measured through ring-down measurements, wherein the initial starting amplitude is established by applying an appropriate feedback signal from the feedback coil before characterization. The particle remains stably trapped for several hours in a dilution refrigerator environment and we observe a  $Q_{\text{sp}} \sim 2.6 \cdot 10^7$  at 212Hz for the  $z$ -mode. This high quality factor for the particle mass of  $5.6 \mu\text{g}$  sets the limits for force and acceleration sensing to  $5 \cdot 10^{-19} \text{ N}/\sqrt{\text{Hz}}$  and  $9 \cdot 10^{-12} \text{ g}/\sqrt{\text{Hz}}$ , respectively. This sensitivity is only reached with

## 2 Summary of publications and contributions

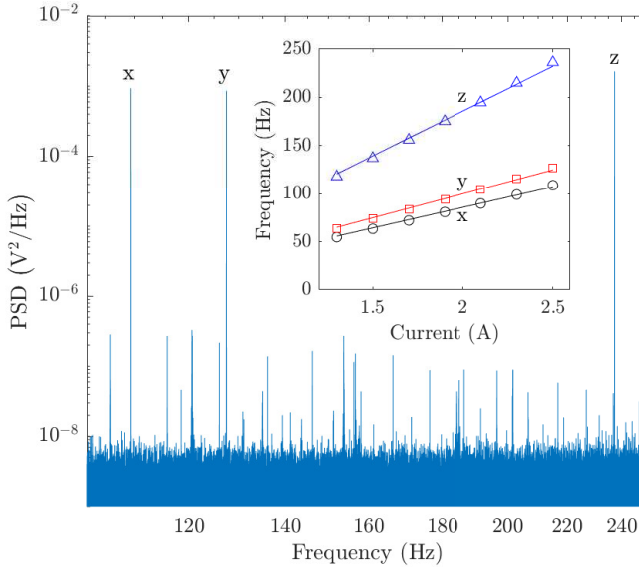


**Figure 2.12: The particle COM modes detected by a SQUID sensor.** The three sphere COM modes,  $x$ -,  $y$ -,  $z$ -mode, in the power spectral density (PSD) of the SQUID signal. Insert shows the linear dependence of the COM frequencies on the trap current of the anti-Helmholtz coil. © 2023 American Physical Society.

much smaller (larger) masses [116, 117]. However, there is much room for experimental improvement. For instance, using a type-I superconducting sphere would avoid dissipation caused by flux creep, which probably limits the quality factor [118]. Additionally, positioning the pickup coil closer to the sphere could significantly increase the magneto-mechanical coupling. In the measurements, the coil was approximately  $400\ \mu\text{m}$  away from the sphere.

However, the experiment shows a promising sensing capability in force and acceleration. With these improvements, the system offers a promis-

2.4 **Publication 4:** *High-Q magnetic levitation and control of superconducting microspheres at millikelvin temperatures*

ing approach for bringing microgram objects into the quantum regime, potentially enabling the probing of quantum effects of gravity.

**Contributions**

This work was done in collaboration with the group of M. Aspelmeyer at the University of Vienna where the levitation measurement was performed. I was responsible for designing the SQUID current sensor and gradiometric pickup coil, conducting coupling simulations, and characterizing the sensor along with the pickup coil prior to their installation in the actual experiment. Additionally, I provided assistance in writing.



### 3 Conclusion and outlook

In this thesis, monolithic 3D niobium constriction junctions patterned by neon focused ion beam have been successfully realized in microwave devices with and without DC access. The performance of these Nb cavities with cJJs are on par with similar aluminium constriction devices regarding circuit capabilities. Moreover, it is worth highlighting that the potential operating temperature and magnetic field tolerance of these devices significantly surpass those of aluminum circuits. This comes with the change in material and the selected type of Josephson junctions for implementation. A remarkable flexibility in dynamic ranges and performance in the Nb devices was demonstrated, which shows considerable promise for applications, including photon-pressure systems, flux-mediated optomechanics, and dispersive SQUID magnetometry.

However, constriction junctions in general are far less understood than conventional Josephson tunnel junctions. Especially the junction nonlinearity, which is related to the current-phase-relation has a major impact on the circuit performance and can limit the device tunability. On the other hand, the CPR is highly sensitive to material properties, constriction dimensions and fabrication method. To adequately improve the circuit design utilizing 3D Ne-FIB cJJs, it was imperative to explore the influence of a single 3D constriction on the microwave circuit properties. A forward-skewed sinusoidal CPR was observed. To validate the analysis, the CPR was examined using two different experimental approaches. One approach focused on precisely measuring the nonlinear inductance tuning, while the other approach centered on studying the Kerr nonlinearity tuning of the cJJ. Additionally, the superconducting-resistive switching current of the constrictions was suppressed by about 20% compared to the critical current. This CPR deviate significantly from the ideal sinusoidal shape and has an impact on the cavity tunability, flux responsivity and screening parameter, when integrated into SQUID devices.

In the second part, a high- $T_c$  superconducting flux tunable microwave circuit using YBCO with Josephson junctions fabricated by helium focused ion beam was successfully realized. In this context, the sinusoidal-like

### 3 Conclusion and outlook

CPR of the HIM-JJs in combination with the high magnetic field tolerance and wide temperature range accessible for YBCO devices, present an exciting opportunity for applications in dispersive SQUID magnetometry and flux-mediated optomechanics.

The last part of the thesis presents the realization of an experimental setup to perform quantum experiments with macroscopic and micrometer-sized levitating superconducting objects. There, a microsphere is trapped at the center of a magnetic quadrupole field, based on the Meißner–Ochsenfeld effect. This setup offers comprehensive control over all modes of particle-motion with a high quality factor  $> 10^7$ . These initial findings constitute the first steps to control objects with large masses and long coherence times in the quantum regime. The system also shows the potential for flux-mediated optomechanics experiments and for sensing ultrasensitive forces.

The comprehensive insights gained from the devices, experimental methodologies, and circuit advancements detailed across the four publications offer promising ways for surpassing current limitations in circuit materials, nonlinearity, fabrication techniques, and experimental levitation control. The results show potentials toward innovative experiments in coupling and sensing across diverse domains, including photons, phonons, magnons, and gravitational forces.

Despite our progress, several open questions remain regarding circuit characteristics, cJJ performance, and optomechanical coupling of levitation. In terms of microwave SQUID cavities, exploring their properties in large, in-plane magnetic fields up to the Tesla regime would be interesting for all high-field applications. Unfortunately, the lack of a suitable experimental setup hindered this exploration to be performed within this thesis. Additionally, understanding the complete temperature dependence, from millikelvin to the critical temperature of the materials and/or junction properties, and also investigating the noise properties of the presented devices in **publication 1-3** for future experiments would be beneficial.

Regarding cJJ performance, one key question revolves around understanding the physical and/or technical origins of premature switching in the constriction. This could be probed by measuring switching statistics as a function of temperature, bias current sweep rates, and various noise

sources. Further experiments could delve into the dependence of the CPR on constriction thickness and ion dose. It would also be great to develop strategies to make the CPR less skewed.

Exploring the coupling of mechanical, levitating oscillators to superconducting circuits represents another avenue of interest. While initial steps have been taken, as described in **publication 4**, there is room for improvement. The next step would be to increase the inductive-coupling between the detector and the sphere, and the mechanical quality factor by using a type-I superconductor. Especially, coupling such a system to a flux-tunable microwave cavity, would enable probing quantum effects of gravity. The first step in this direction is done in **publication 5** (not presented in this thesis), in which the first experimental realization of a levitating flux-mediated optomechanical experiment is presented. Nevertheless, there is still room for improvement in the flux-mediated optomechanical coupling. In **publication 5**, an Al SQUID cavity is used, and due to the lack of magnetic field tolerance of the material, a pickup loop is needed. The discussed SQUID cavities of Nb and YBCO could boost the coupling rates significantly, if the mechanical oscillator were integrated directly into the system. Also, the low Kerr nonlinearity of the devices could allow for many more pump/readout photons compared to the currently Al cavity. This increases the coupling rate further. Future experiments also could focus on enhanced optomechanical coupling aimed for cooling the mechanical motion, achieving mechanical entanglement, and investigating gravitational interaction between two levitating objects.



## 4 Acknowledgements

That's it - this thesis represents the culmination of several years of dedicated work as a PhD candidate, during which I faced numerous challenges. At the outset, I encountered significant obstacles, particularly in navigating the uncharted territory of utilizing flux-tunable cavities, a concept unfamiliar to the research group. Compounding this, I began with an empty measurement room devoid of the necessary equipment for conducting the experiments presented in this thesis. Moreover, there was a lack of expertise in cleanroom procedures at the time, exacerbated by a turnover in the group's member.

However, I am deeply grateful for the invaluable assistance and support I received from numerous outstanding scientists, friends, and family. Without their guidance and encouragement, I would not have been able to overcome these challenges and achieve the milestones detailed in this thesis.

First of all, I want to thank my supervisors, Prof. Reinhold Kleiner and Prof. Dieter Kölle, whose made all of this possible. Joining your group during such an exciting time filled me with gratitude for the trust you placed in me. With that trust, we transformed an empty space into a fully equipped laboratory with multiple measurement setups, including a temperature-controlled liquid-cryostat and basic measurement systems for helium dewars. Thank you for providing me with the support and encouragement to explore superconducting circuits in such depth. Our numerous fruitful discussions and shared insights have been instrumental in my academic journey. Also Your meticulous proofreading of this thesis, papers, presentations have made a profound impact on me.

I am immensely grateful to Dr. Daniel Bothner for his invaluable contributions to the project. He joined the group during my time and without his expertise in experimentation, setup, and theory, I would not have achieved the level of success we did together. Thank you for being an exceptionally PostDoc with great and steady hands-on ideas that made the whole project a success. You contributed in so many ways that it is impossible to list it up here. Thank you, Daniel, for your outstanding

## 4 Acknowledgements

support and collaboration. It has been a pleasure and privilege to work alongside you.

Moreover, I want to thank Dr. Christoph Back for supporting my in navigating cryogenic challenges, electronic troubleshooting, mechanical cleanroom issues, and as a friend. Our interactions were always enjoyable, and I cherished every moment spent in conversation with you. In particular, I fondly recall our humorous discussions during lunchtime and after work. Thank you, Christoph, for your camaraderie and assistance throughout our journey together.

I want to thank Dr. Markus Turad and Dr. Ronny Löffler from the Center for Light-Matter Interaction, Sensors & Analytics (LISA<sup>+</sup>) for introducing me into the cleanroom equipment. I gained proficiency in operating a wide array of instruments, including the SEM, HIM, XRD, surface profilometer,  $\mu$ MLA, wafer dicer, PECVD, UHV-system comprising an Argon, oxygen, and SF<sub>6</sub> etching chamber, PLD, electron evaporation with gold, aluminum, and palladium, and sputter chamber with gold and niobium. Their expertise and patient instruction were instrumental in enhancing my skill set and contributed significantly to the success of my work.

I am immensely grateful to Roy Schilling and Martin Beuter from the mechanical workshop. Their expertise in precision construction, even with challenging materials, has been indispensable in bringing many aspects of my experiments to life. Without their meticulous work, the measurement setup would not have been possible. Working alongside them, I also had the opportunity to enhance my skills in constructing various components, including translating CAD layouts into tangible structures.

I extend my gratitude to Manuel Brandt and Frank Heselschwerdt for their diligent work at the liquid helium station. Every interaction with you guys, whether it was getting or bringing a liquid helium dewar, was a pleasure.

I also want to extend my heartfelt thanks to Marie Luise and Susanne Maier for their invaluable assistance with all the organizational formalities. Their support in navigating through various formal procedures has been deeply appreciated throughout this journey.

Moreover, I would like to express my gratitude to all the working, bachelor, and master students who get supervised from me - Daniel Hackenbeck, Lukas Wolz, Janis Peter, Kenny Fohmann, Emily Guo and Christoph Fuger. Our collaborations have been enriching both scientifically and personally. I have enjoyed our conversations and learned a great deal from each of you, whether it be in the realm of science, friendship, or leadership. Together with Mohamad Kazouini, Benedikt Wilde, and Timo Kern, who were also part of the newly established microwave team, we have achieved remarkable progress in our projects. We have overcome challenges and pushed boundaries in record time. I also want to express my gratitude for your scientific contributions and friendship.

Moreover, I want to thank Joachim Hofer, Dr. Philip Schmidt and Prof. Markus Aspelmeyer for the excellent work at the levitation setup in Vienna for reading the motion with a microwave and DC setup. Also for many fruitful discussions, for implementing the DC-SQUID and pickup loops into the setup, for valuable design ideas, for all the setup improvements, and for creating the great output of the levitation-project.

I want to thank Assoc. Prof. Thilo Bauch for taking his time and reading the thesis.

Furthermore, I want to thank Julian Linek, Christoph Schmid and Timo Ziegler for having nice discussion about electronic setups and science.

At this point, I also want to thank all my friends, who balanced my life so that I would not become crazy in this spooky world of quantum physics. We shared exciting nights at the university and beyond, filled with unforgettable stories and experiences.

Finally, I want to express my deepest gratitude to my parents, Waltraud and Winfried Uhl, and to my sister, Melanie Uhl, for their unwavering support throughout this journey. Thank you for everything.



## Bibliography

- [1] J. Chaste, A. Eichler, J. Moser, G. Ceballos, R. Rurali, and A. Bachtold, “A nanomechanical mass sensor with yoctogram resolution”, *Nature Nanotechnology* **7**, 301–304 (2012).
- [2] M. Gierling, P. Schneeweiss, G. Visanescu, P. Federsel, M. Häffner, D. P. Kern, T. E. Judd, A. Günther, and J. Fortágh, “Cold-atom scanning probe microscopy”, *Nature Nanotechnology* **6**, 446–451 (2011).
- [3] J. Moser, J. Güttinger, A. Eichler, M. J. Esplandiú, D. Liu, M. Dykman, and A. Bachtold, “Ultrasensitive force detection with a nanotube mechanical resonator”, *Nature Nanotechnology* **8**, 493 (2013).
- [4] A. D. O’Connell, M. Hofheinz, M. Ansmann, R. C. Bialczak, M. Lenander, E. Lucero, M. Neeley, D. Sank, H. Wang, M. Weides, J. Wenner, J. M. Martinis, and A. N. Cleland, “Quantum ground state and single-phonon control of a mechanical resonator”, *Nature* **464**, 697–703 (2010).
- [5] J. Chan, T. M. Alegre, A. H. Safavi-Naeini, J. T. Hill, A. Krause, S. Gröblacher, M. Aspelmeyer, and O. Painter, “Laser cooling of a nanomechanical oscillator into its quantum ground state”, *Nature* **478**, 89–92 (2011).
- [6] J. D. Teufel, T. Donner, D. Li, J. W. Harlow, M. Allman, K. Cicak, A. J. Sirois, J. D. Whittaker, K. W. Lehnert, and R. W. Simmonds, “Sideband cooling of micromechanical motion to the quantum ground state”, *Nature* **475**, 359–363 (2011).
- [7] K. C. Schwab and M. L. Roukes, “Putting mechanics into quantum mechanics”, *Physics Today* **58**, 36–42 (2005).
- [8] M. Aspelmeyer, T. J. Kippenberg, and F. Marquardt, “Cavity optomechanics”, *Reviews of Modern Physics* **86**, 1391 (2014).

## Bibliography

- [9] M. R. Islam, M. M. Ali, M.-H. Lai, K.-S. Lim, and H. Ahmad, “Chronology of Fabry-Perot interferometer fiber-optic sensors and their applications: a review”, *Sensors* **14**, 7451–7488 (2014).
- [10] J. Thompson, B. Zwickl, A. Jayich, F. Marquardt, S. Girvin, and J. Harris, “Strong dispersive coupling of a high-finesse cavity to a micromechanical membrane”, *Nature* **452**, 72–75 (2008).
- [11] R. Ma, A. Schliesser, P. Del’Haye, A. Dabirian, G. Anetsberger, and T. J. Kippenberg, “Radiation-pressure-driven vibrational modes in ultrahigh-Q silica microspheres”, *Optics Letters* **32**, 2200–2202 (2007).
- [12] A. Ashkin, “Trapping of atoms by resonance radiation pressure”, *Physical Review Letters* **40**, 729 (1978).
- [13] T. Carmon, H. Rokhsari, L. Yang, T. J. Kippenberg, and K. J. Vahala, “Temporal behavior of radiation-pressure-induced vibrations of an optical microcavity phonon mode”, *Physical Review Letters* **94**, 223902 (2005).
- [14] T. Kippenberg, H. Rokhsari, T. Carmon, A. Scherer, and K. Vahala, “Analysis of radiation-pressure induced mechanical oscillation of an optical microcavity”, *Physical Review Letters* **95**, 033901 (2005).
- [15] A. Schliesser, P. Del’Haye, N. Nooshi, K. Vahala, and T. J. Kippenberg, “Radiation pressure cooling of a micromechanical oscillator using dynamical backaction”, *Physical Review Letters* **97**, 243905 (2006).
- [16] A. Wallraff, D. I. Schuster, A. Blais, L. Frunzio, R.-S. Huang, J. Majer, S. Kumar, S. M. Girvin, and R. J. Schoelkopf, “Strong coupling of a single photon to a superconducting qubit using circuit quantum electrodynamics”, *Nature* **431**, 162–167 (2004).
- [17] V. Braginski and A. Manukin, “Ponderomotive effects of electromagnetic radiation”, *Soviet Physics JETP* **25**, 653–655 (1967).
- [18] B. Cuthbertson, M. Tobar, E. Ivanov, and D. Blair, “Parametric back-action effects in a high-Q cryogenic sapphire transducer”, *Review of Scientific Instruments* **67**, 2435–2442 (1996).

- [19] V. B. Braginskii and A. B. Manukin, “Measurement of weak forces in physics experiments”, University of Chicago Press (1977).
- [20] K. R. Brown, J. Britton, R. Epstein, J. Chiaverini, D. Leibfried, and D. J. Wineland, “Passive cooling of a micromechanical oscillator with a resonant electric circuit”, *Physical Review Letters* **99**, 137205 (2007).
- [21] L. Midolo, A. Schliesser, and A. Fiore, “Nano-opto-electro-mechanical systems”, *Nature Nanotechnology* **13**, 11–18 (2018).
- [22] J. D. Teufel, F. Lecocq, and R. W. Simmonds, “Overwhelming thermomechanical motion with microwave radiation pressure shot noise”, *Physical Review Letters* **116**, 013602 (2016).
- [23] A. Reed, K. Mayer, J. Teufel, L. Burkhardt, W. Pfaff, M. Reagor, L. Sletten, X. Ma, R. Schoelkopf, E. Knill, et al., “Faithful conversion of propagating quantum information to mechanical motion”, *Nature Physics* **13**, 1163–1167 (2017).
- [24] S. Gröblacher, K. Hammerer, M. R. Vanner, and M. Aspelmeyer, “Observation of strong coupling between a micromechanical resonator and an optical cavity field”, *Nature* **460**, 724–727 (2009).
- [25] J. D. Teufel, D. Li, M. Allman, K. Cicak, A. Sirois, J. Whittaker, and R. Simmonds, “Circuit cavity electromechanics in the strong-coupling regime”, *Nature* **471**, 204–208 (2011).
- [26] G. Peterson, S. Kotler, F. Lecocq, K. Cicak, X. Jin, R. Simmonds, J. Aumentado, and J. Teufel, “Ultrastrong parametric coupling between a superconducting cavity and a mechanical resonator”, *Physical Review Letters* **123**, 247701 (2019).
- [27] S. M. Meenehan, J. D. Cohen, S. Gröblacher, J. T. Hill, A. H. Safavi-Naeini, M. Aspelmeyer, and O. Painter, “Silicon optomechanical crystal resonator at millikelvin temperatures”, *Physical Review A* **90**, 011803 (2014).
- [28] O. Romero-Isart, L. Clemente, C. Navau, A. Sanchez, and J. Cirac, “Quantum magnetomechanics with levitating superconducting microspheres”, *Physical Review Letters* **109**, 147205 (2012).

## Bibliography

- [29] M. Yuan, V. Singh, Y. M. Blanter, and G. A. Steele, “Large cooperativity and microkelvin cooling with a three-dimensional optomechanical cavity”, *Nature Communications* **6**, 8491 (2015).
- [30] G. Via, G. Kirchmair, and O. Romero-Isart, “Strong single-photon coupling in superconducting quantum magnetomechanics”, *Physical Review Letters* **114**, 143602 (2015).
- [31] M. Kounalakis, Y. M. Blanter, and G. A. Steele, “Flux-mediated optomechanics with a transmon qubit in the single-photon ultrastrong-coupling regime”, *Physical Review Research* **2**, 023335 (2020).
- [32] L. Grünhaupt, N. Maleeva, S. T. Skacel, M. Calvo, F. Levy-Bertrand, A. V. Ustinov, H. Rotzinger, A. Monfardini, G. Catelani, and I. M. Pop, “Loss mechanisms and quasiparticle dynamics in superconducting microwave resonators made of thin-film granular aluminum”, *Physical Review Letters* **121**, 117001 (2018).
- [33] S. Mahashabde, E. Otto, D. Montemurro, S. de Graaf, S. Kubatkin, and A. Danilov, “Fast tunable high- $Q$ -factor superconducting microwave resonators”, *Physical Review Applied* **14**, 044040 (2020).
- [34] C. R. H. McRae, H. Wang, J. Gao, M. R. Vissers, T. Brecht, A. Dunsworth, D. P. Pappas, and J. Mutus, “Materials loss measurements using superconducting microwave resonators”, *Review of Scientific Instruments* **91**, 091101 (2020).
- [35] P. Nation, J. Suh, and M. Blencowe, “Ultrastrong optomechanics incorporating the dynamical Casimir effect”, *Physical Review A* **93**, 022510 (2016).
- [36] D. Zoepfl, M. Juan, C. Schneider, and G. Kirchmair, “Single-photon cooling in microwave magnetomechanics”, *Physical Review Letters* **125**, 023601 (2020).
- [37] D. Drung, S. Bechstein, K.-P. Franke, M. Scheiner, and T. Schurig, “Improved direct-coupled dc SQUID read-out electronics with automatic bias voltage tuning”, *IEEE transactions on applied superconductivity* **11**, 880–883 (2001).

- [38] T. Bera, S. Majumder, S. K. Sahu, and V. Singh, “Large flux-mediated coupling in hybrid electromechanical system with a transmon qubit”, *Communications Physics* **4**, 12 (2021).
- [39] I. Rodrigues, D. Bothner, and G. Steele, “Coupling microwave photons to a mechanical resonator using quantum interference”, *Nature Communications* **10**, 5359 (2019).
- [40] P. Schmidt, M. T. Amawi, S. Pogorzalek, F. Deppe, A. Marx, R. Gross, and H. Huebl, “Sideband-resolved resonator electromechanics based on a nonlinear Josephson inductance probed on the single-photon level”, *Communications Physics* **3**, 233 (2020).
- [41] J. Millen, T. S. Monteiro, R. Pettit, and A. N. Vamivakas, “Optomechanics with levitated particles”, *Reports on Progress in Physics* **83**, 026401 (2020).
- [42] C. Gonzalez-Ballester, M. Aspelmeyer, L. Novotny, R. Quidant, and O. Romero-Isart, “Levitodynamics: Levitation and control of microscopic objects in vacuum”, *Science* **374**, eabg3027 (2021).
- [43] T. Li and T. Li, *Millikelvin cooling of an optically trapped microsphere in vacuum* (Springer, 2013), pp. 81–110.
- [44] O. Romero-Isart, A. C. Pflanzer, M. L. Juan, R. Quidant, N. Kiesel, M. Aspelmeyer, and J. I. Cirac, “Optically levitating dielectrics in the quantum regime: Theory and protocols”, *Physical Review A* **83**, 013803 (2011).
- [45] D. C. Moore and A. A. Geraci, “Searching for new physics using optically levitated sensors”, *Quantum Science and Technology* **6**, 014008 (2021).
- [46] F. Tebbenjohanns, M. L. Mattana, M. Rossi, M. Frimmer, and L. Novotny, “Quantum control of a nanoparticle optically levitated in cryogenic free space”, *Nature* **595**, 378–382 (2021).
- [47] A. Palacios-Laloy, F. Nguyen, F. Mallet, P. Bertet, D. Vion, and D. Esteve, “Tunable resonators for quantum circuits”, *Journal of Low Temperature Physics* **151**, 1034–1042 (2008).

## Bibliography

- [48] R. Meservey and P. Tedrow, “Properties of very thin aluminum films”, *Journal of Applied Physics* **42**, 51–53 (1971).
- [49] S. E. de Graaf, A. Danilov, A. Adamyan, T. Bauch, and S. Kubatkin, “Magnetic field resilient superconducting fractal resonators for coupling to free spins”, *Journal of Applied Physics* **112**, 123905 (2012).
- [50] N. Samkharadze, A. Bruno, P. Scarlino, G. Zheng, D. DiVincenzo, L. DiCarlo, and L. Vandersypen, “High-kinetic-inductance superconducting nanowire resonators for circuit QED in a magnetic field”, *Physical Review Applied* **5**, 044004 (2016).
- [51] C. W. Zollitsch, J. O’Sullivan, O. Kennedy, G. Dold, and J. J. Morton, “Tuning high- $Q$  superconducting resonators by magnetic field reorientation”, *AIP Advances* **9**, 125225 (2019).
- [52] A. Roitman, A. Shaulov, and Y. Yeshurun, “Characterization of  $\text{YBa}_2\text{Cu}_3\text{O}_{7-\delta}$  coplanar resonator for microwave kinetic inductance detectors”, *Superconductor Science and Technology* **36**, 015002 (2023).
- [53] O. Kennedy, J. Burnett, J. Fenton, N. Constantino, P. Warburton, J. Morton, and E. Dupont-Ferrier, “Tunable Nb superconducting resonator based on a constriction nano-SQUID fabricated with a Ne focused ion beam”, *Physical Review Applied* **11**, 014006 (2019).
- [54] K. Hasselbach, D. Maily, and J. Kirtley, “Micro-superconducting quantum interference device characteristics”, *Journal of Applied Physics* **91**, 4432–4437 (2002).
- [55] E. Tralbaldo, C. Pfeiffer, E. Andersson, R. Arpaia, A. Kalaboukhov, D. Winkler, F. Lombardi, and T. Bauch, “Grooved Dayem nanobridges as building blocks of high-performance  $\text{YBa}_2\text{Cu}_3\text{O}_{7-\delta}$  SQUID magnetometers”, *Nano Letters* **19**, 1902–1907 (2019).
- [56] E. Tralbaldo, S. Ruffieux, E. Andersson, R. Arpaia, D. Montemurro, J. Schneiderman, A. Kalaboukhov, D. Winkler, F. Lombardi, and T. Bauch, “Properties of grooved Dayem bridge based  $\text{YBa}_2\text{Cu}_3\text{O}_{7-\delta}$  superconducting quantum interference devices and magnetometers”, *Applied Physics Letters* **116** (2020).

- [57] Y. Kubo, F. Ong, P. Bertet, D. Vion, V. Jacques, D. Zheng, A. Dréau, J.-F. Roch, A. Auffèves, F. Jelezko, et al., “Strong coupling of a spin ensemble to a superconducting resonator”, *Physical Review Letters* **105**, 140502 (2010).
- [58] Y. Kubo, C. Grezes, A. Dewes, T. Umeda, J. Isoya, H. Sumiya, N. Morishita, H. Abe, S. Onoda, T. Ohshima, et al., “Hybrid quantum circuit with a superconducting qubit coupled to a spin ensemble”, *Physical Review Letters* **107**, 220501 (2011).
- [59] R. Morris, A. Van Loo, S. Kosen, and A. Karenowska, “Strong coupling of magnons in a YIG sphere to photons in a planar superconducting resonator in the quantum limit”, *Scientific Reports* **7**, 11511 (2017).
- [60] B. Z. Rameshti, S. V. Kusminskiy, J. A. Haigh, K. Usami, D. Lachance-Quirion, Y. Nakamura, C.-M. Hu, H. X. Tang, G. E. Bauer, and Y. M. Blanter, “Cavity magnonics”, *Physics Reports* **979**, 1–61 (2022).
- [61] Y.-P. Wang and C.-M. Hu, “Dissipative couplings in cavity magnonics”, *Journal of Applied Physics* **127**, 130901 (2020).
- [62] M. Hatridge, R. Vijay, D. Slichter, J. Clarke, and I. Siddiqi, “Dispersive magnetometry with a quantum limited SQUID parametric amplifier”, *Physical Review B* **83**, 134501 (2011).
- [63] M. A. Castellanos-Beltran, K. Irwin, G. Hilton, L. Vale, and K. Lehnert, “Amplification and squeezing of quantum noise with a tunable Josephson metamaterial”, *Nature Physics* **4**, 929–931 (2008).
- [64] N. Bergeal, F. Schackert, M. Metcalfe, R. Vijay, V. Manucharyan, L. Frunzio, D. Prober, R. Schoelkopf, S. Girvin, and M. Devoret, “Phase-preserving amplification near the quantum limit with a Josephson ring modulator”, *Nature* **465**, 64–68 (2010).
- [65] C. Macklin, K. O’Brien, D. Hover, M. Schwartz, V. Bolkhovsky, X. Zhang, W. Oliver, and I. Siddiqi, “A near-quantum-limited Josephson traveling-wave parametric amplifier”, *Science* **350**, 307–310 (2015).

## Bibliography

- [66] M. W. Doherty, N. B. Manson, P. Delaney, F. Jelezko, J. Wrachtrup, and L. C. Hollenberg, “The nitrogen-vacancy colour centre in diamond”, *Physics Reports* **528**, 1–45 (2013).
- [67] B. Bhoi, B. Kim, S.-H. Jang, J. Kim, J. Yang, Y.-J. Cho, and S.-K. Kim, “Abnormal anticrossing effect in photon-magnon coupling”, *Physical Review B* **99**, 134426 (2019).
- [68] I. Boverter, M. Kläui, R. Macêdo, and M. Weides, “Steering between level repulsion and attraction: broad tunability of two-port driven cavity magnon-polaritons”, *New Journal of Physics* **21**, 125001 (2019).
- [69] X. Zhang, C.-L. Zou, L. Jiang, and H. X. Tang, “Cavity magnomechanics”, *Science Advances* **2**, e1501286 (2016).
- [70] D. Lachance-Quirion, S. P. Wolski, Y. Tabuchi, S. Kono, K. Usami, and Y. Nakamura, “Entanglement-based single-shot detection of a single magnon with a superconducting qubit”, *Science* **367**, 425–428 (2020).
- [71] M. Amazioug, B. Teklu, and M. Asjad, “Enhancement of magnon–photon–phonon entanglement in a cavity magnomechanics with coherent feedback loop”, *Scientific Reports* **13**, 3833 (2023).
- [72] S. Touzard, A. Kou, N. Frattini, V. Sivak, S. Puri, A. Grimm, L. Frunzio, S. Shankar, and M. Devoret, “Gated conditional displacement readout of superconducting qubits”, *Physical Review Letters* **122**, 080502 (2019).
- [73] T. Walter, P. Kurpiers, S. Gasparinetti, P. Magnard, A. Potočník, Y. Salathé, M. Pechal, M. Mondal, M. Oppliger, C. Eichler, et al., “Rapid high-fidelity single-shot dispersive readout of superconducting qubits”, *Physical Review Applied* **7**, 054020 (2017).
- [74] T. Peronnin, D. Marković, Q. Ficheux, and B. Huard, “Sequential dispersive measurement of a superconducting qubit”, *Physical Review Letters* **124**, 180502 (2020).

- [75] J. Aumentado, “Superconducting parametric amplifiers: The state of the art in Josephson parametric amplifiers”, *IEEE Microwave Magazine* **21**, 45–59 (2020).
- [76] E. Del Barco, A. Kent, E. Yang, and D. Hendrickson, “Quantum superposition of high spin states in the single molecule magnet  $\text{Ni}_4$ ”, *Physical Review Letters* **93**, 157202 (2004).
- [77] R. Vijay, J. Sau, M. L. Cohen, and I. Siddiqi, “Optimizing anharmonicity in nanoscale weak link Josephson junction oscillators”, *Physical Review Letters* **103**, 087003 (2009).
- [78] R. Vijay, E. Levenson-Falk, D. Slichter, and I. Siddiqi, “Approaching ideal weak link behavior with three dimensional aluminum nanobridges”, *Applied Physics Letters* **96**, 223112 (2010).
- [79] E. Levenson-Falk, N. Antler, and I. Siddiqi, “Dispersive nanoSQUID magnetometry”, *Superconductor Science and Technology* **29**, 113003 (2016).
- [80] A. Ghirri, C. Bonizzoni, D. Gerace, S. Sanna, A. Cassinese, and M. Affronte, “ $\text{YBa}_2\text{Cu}_3\text{O}_7$  microwave resonators for strong collective coupling with spin ensembles”, *Applied Physics Letters* **106**, 184101 (2015).
- [81] M. Cirio, G. Brennen, and J. Twamley, “Quantum magnetomechanics: ultrahigh- $Q$ -levitated mechanical oscillators”, *Physical Review Letters* **109**, 147206 (2012).
- [82] K. Sliwa, M. Hatridge, A. Narla, S. Shankar, L. Frunzio, R. Schoelkopf, and M. Devoret, “Reconfigurable Josephson circulator/directional amplifier”, *Physical Review X* **5**, 041020 (2015).
- [83] D. Bothner, I. Rodrigues, and G. Steele, “Photon-pressure strong coupling between two superconducting circuits”, *Nature Physics* **17**, 85–91 (2021).
- [84] J. Clarke and A. I. Braginski, *The SQUID handbook. vol. 2 - Applications of SQUIDs and SQUID systems* (Wiley-VCH, Weinheim, 2006).

## Bibliography

- [85] R. Behr, O. Kieler, J. Kohlmann, F. Müller, and L. Palafox, “Development and metrological applications of Josephson arrays at PTB”, *Measurement Science and Technology* **23**, 124002 (2012).
- [86] A. A. Golubov, M. Y. Kupriyanov, and E. Il’Ichev, “The current-phase relation in Josephson junctions”, *Reviews of Modern Physics* **76**, 411 (2004).
- [87] K. Likharev, “Superconducting weak links”, *Reviews of Modern Physics* **51**, 101 (1979).
- [88] F. E. Schmidt, D. Bothner, I. C. Rodrigues, M. F. Gely, M. D. Jenkins, and G. A. Steele, “Current detection using a Josephson parametric upconverter”, *Physical Review Applied* **14**, 024069 (2020).
- [89] R. Haller, G. Fülöp, D. Indolese, J. Ridderbos, R. Kraft, L. Y. Cheung, J. H. Ungerer, K. Watanabe, T. Taniguchi, D. Beckmann, R. Danneau, P. Virtanen, and C. Schönenberger, “Phase-dependent microwave response of a graphene Josephson junction”, *Physical Review Research* **4**, 013198 (2022).
- [90] Y. Wang, L. Chen, Y. Pan, D. Zhang, S. Yu, G. Wu, X. Liu, L. Wu, W. Shi, G. Zhang, et al., “Geometric scaling of the current–phase relation of niobium nanobridge junctions”, *ACS Nano* **17**, 15466–15473 (2023).
- [91] J. Clarke and F. K. Wilhelm, “Superconducting quantum bits”, *Nature* **453**, 1031–1042 (2008).
- [92] E. Levenson-Falk, R. Vijay, N. Antler, and I. Siddiqi, “A dispersive nanoSQUID magnetometer for ultra-low noise, high bandwidth flux detection”, *Superconductor Science and Technology* **26**, 055015 (2013).
- [93] I. C. Rodrigues, G. A. Steele, and D. Bothner, “Parametrically enhanced interactions and nonreciprocal bath dynamics in a photon-pressure Kerr amplifier”, *Science Advances* **8**, eabq1690 (2022).

- [94] V. Bouchiat, M. Faucher, C. Thirion, W. Wernsdorfer, T. Fournier, and B. Pannetier, “Josephson junctions and superconducting quantum interference devices made by local oxidation of niobium ultra-thin films”, *Applied Physics Letters* **79**, 123–125 (2001).
- [95] E. Mitchell and S. Lam, “Niobium dc SQUIDS with nanobridge junctions”, *Physics Procedia* **36**, 382–387 (2012).
- [96] H. Wang, L. Chen, X. Liu, L. Wu, X. Wu, L. You, and Z. Wang, “Fabrication and characterization of miniaturized NbN superconducting quantum interference devices with nanobridge junctions”, *IEEE Transactions on Applied Superconductivity* **27**, 1–5 (2017).
- [97] D. Bothner, I. C. Rodrigues, and G. A. Steele, “Four-wave-cooling to the single phonon level in Kerr optomechanics”, *Communications Physics* **5**, 33 (2022).
- [98] I. C. Rodrigues, D. Bothner, and G. A. Steele, “Cooling photon-pressure circuits into the quantum regime”, *Science Advances* **7**, eabg6653 (2021).
- [99] G. De Simoni, C. Puglia, and F. Giazotto, “Niobium Dayem nanobridge Josephson gate-controlled transistors”, *Applied Physics Letters* **116**, 242601 (2020).
- [100] O. Shevchuk, G. A. Steele, and Y. M. Blanter, “Strong and tunable couplings in flux-mediated optomechanics”, *Physical Review B* **96**, 014508 (2017).
- [101] H. Zeng, J.-Y. Juang, J.-Y. Lin, K.-H. Wu, T. Uen, and Y. Gou, “Temperature dependence of the penetration depth and effective dielectric constant measured by  $\text{YBa}_2\text{Cu}_3\text{O}_{7-\delta}$  microstrip ring resonators”, *Physica C: Superconductivity* **351**, 97–102 (2001).
- [102] E. Tralbaldo, R. Arpaia, M. Arzeo, E. Andersson, D. Golubev, F. Lombardi, and T. Bauch, “Transport and noise properties of YBCO nanowire based nanoSQUIDS”, *Superconductor Science and Technology* **32**, 073001 (2019).

## Bibliography

- [103] E. J. Romans, S. Rozhko, L. Young, A. Blois, L. Hao, D. Cox, and J. C. Gallop, “Noise performance of niobium nano-SQUIDS in applied magnetic fields”, *IEEE Transactions on Applied Superconductivity* **21**, 404–407 (2010).
- [104] M. Xu, R. Cheng, Y. Wu, G. Liu, and H. X. Tang, “Magnetic field-resilient quantum-limited parametric amplifier”, *PRX Quantum* **4**, 010322 (2023).
- [105] J. Kroll, W. Uilhoorn, K. van der Enden, D. de Jong, K. Watanabe, T. Taniguchi, S. Goswami, M. Cassidy, and L. P. Kouwenhoven, “Magnetic field compatible circuit quantum electrodynamics with graphene Josephson junctions”, *Nature Communications* **9**, 4615 (2018).
- [106] S. A. Cybart, E. Cho, T. Wong, B. H. Wehlin, M. K. Ma, C. Huynh, and R. Dynes, “Nano Josephson superconducting tunnel junctions in  $\text{YBa}_2\text{Cu}_3\text{O}_{7-\delta}$  directly patterned with a focused helium ion beam”, *Nature Nanotechnology* **10**, 598–602 (2015).
- [107] B. Müller, M. Karrer, F. Limberger, M. Becker, B. Schröppel, C. Burkhardt, R. Kleiner, E. Goldobin, and D. Koelle, “Josephson junctions and SQUIDS created by focused helium-ion-beam irradiation of  $\text{YBa}_2\text{Cu}_3\text{O}_7$ ”, *Physical Review Applied* **11**, 044082 (2019).
- [108] W. Lechner, S. Habraken, N. Kiesel, M. Aspelmeyer, and P. Zoller, “Cavity optomechanics of levitated nanodumbbells: nonequilibrium phases and self-assembly”, *Physical Review Letters* **110**, 143604 (2013).
- [109] J. Rieser, M. A. Ciampini, H. Rudolph, N. Kiesel, K. Hornberger, B. A. Stickler, M. Aspelmeyer, and U. Delić, “Tunable light-induced dipole-dipole interaction between optically levitated nanoparticles”, *Science* **377**, 987–990 (2022).
- [110] G. Ranjit, M. Cunningham, K. Casey, and A. A. Geraci, “Zeptonewton force sensing with nanospheres in an optical lattice”, *Physical Review A* **93**, 053801 (2016).

- [111] T. Weiss, M. Roda-Llordes, E. Torrontegui, M. Aspelmeyer, and O. Romero-Isart, “Large quantum delocalization of a levitated nanoparticle using optimal control: applications for force sensing and entangling via weak forces”, *Physical Review Letters* **127**, 023601 (2021).
- [112] M. Debiossac, D. Grass, J. J. Alonso, E. Lutz, and N. Kiesel, “Thermodynamics of continuous non-markovian feedback control”, *Nature Communications* **11**, 1360 (2020).
- [113] H. Pino, J. Prat-Camps, K. Sinha, B. P. Venkatesh, and O. Romero-Isart, “On-chip quantum interference of a superconducting microsphere”, *Quantum Science and Technology* **3**, 025001 (2018).
- [114] C. Navau, S. Minniberger, M. Trupke, and A. Sanchez, “Levitation of superconducting microrings for quantum magnetomechanics”, *Physical Review B* **103**, 174436 (2021).
- [115] M. G. Latorre, G. Higgins, A. Paradkar, T. Bauch, and W. Wieczorek, “Superconducting microsphere magnetically levitated in an anharmonic potential with integrated magnetic readout”, *Physical Review Applied* **19**, 054047 (2023).
- [116] J. M. Goodkind, “The superconducting gravimeter”, *Review of Scientific Instruments* **70**, 4131–4152 (1999).
- [117] D. Hempston, J. Vovrosh, M. Toroš, G. Winstone, M. Rashid, and H. Ulbricht, “Force sensing with an optically levitated charged nanoparticle”, *Applied Physics Letters* **111**, 133111 (2017).
- [118] V. Nemoshkalenko, E. Brandt, A. Kordyuk, and B. Nikitin, “Dynamics of a permanent magnet levitating above a high- $T_c$  superconductor”, *Physica C: Superconductivity* **170**, 481–485 (1990).



# Appended publications

© Reprints of the publications are made with permission of the American Physical Society.

© Reprints of the publications are made with permission of the American Institute of Physics.



# Publication 1

# Extracting the current-phase-relation of a monolithic three-dimensional nano-constriction using a DC-current-tunable superconducting microwave cavity

Kevin Uhl,\* Daniel Hackenbeck, Dieter Koelle, Reinhold Kleiner, and Daniel Bothner†  
*Physikalisches Institut, Center for Quantum Science (CQ) and LISA+,  
Universität Tübingen, 72076 Tübingen, Germany*

Superconducting circuits with nonlinear elements such as Josephson tunnel junctions or kinetic inductance nanowires are the workhorse for microwave quantum and superconducting sensing technologies. For devices, which can be operated at high temperatures and large magnetic fields, nano-constrictions as nonlinear elements are recently under intense investigation. Constrictions, however, are far less understood than conventional Josephson tunnel junctions, and their current-phase-relationships (CPRs) – although highly important for device design – are hard to predict. Here, we present a niobium microwave cavity with a monolithically integrated, neon-ion-beam patterned three-dimensional (3D) nano-constriction. By design, we obtain a DC-current-tunable microwave circuit and characterize how the bias-current-dependent constriction properties impact the cavity resonance. Based on the results of these experiments, we reconstruct the CPR of the nano-constriction. Finally, we discuss the Kerr nonlinearity of the device, a parameter important for many high-dynamic-range applications and an experimental probe for the second and third derivatives of the CPR. Our platform provides a useful method to comprehensively characterize nonlinear elements integrated in microwave circuits and could be of interest for current sensors, hybrid quantum systems and parametric amplifiers. Our findings furthermore contribute to a better understanding of nano-fabricated 3D constrictions.

## INTRODUCTION

Josephson junctions (JJs) and nonlinear weak links between two superconducting electrodes form an essential ingredient for a wide variety of groundbreaking technologies, such as superconducting quantum interference devices (SQUIDs) [1, 2], voltage standards [3] or superconducting microwave quantum circuits [4–6]. The main characteristics of a superconducting nonlinear element are its critical current  $I_0$  and its potentially non-trivial current-phase-relation (CPR)  $I(\delta)$ , which relates the phase difference  $\delta$  across it to the current  $I$  flowing through it [7, 8]. These two quantities also determine both the inductance and the anharmonicity of a Josephson microwave circuit, extremely important parameters for engineering high-quality superconducting qubits [9, 10] or Josephson parametric amplifiers [11–13]. For standard superconductor-insulator-superconductor (SIS) Josephson junctions, the CPR usually has the ideal sinusoidal form  $I = I_0 \sin \delta$  and the only remaining design parameter for particular applications is the critical current. Other types of JJs, for example trilayer junctions with normal-conducting (SNS) or ferromagnetic (SFS) barriers as well as constriction-type junctions (cJJs) in many cases exhibit a significant deviation of their CPR from the ideal sinusoidal shape [8]. To properly design devices and technologies based on these non-sinusoidal Josephson elements, it is therefore of utmost importance to gather knowledge about  $I_0$  and the CPR.

Lately, there has been growing interest in constriction type Josephson junctions. Those cJJs have been

already investigated in the early days of superconducting weak links [14], they have been implemented into DC-SQUID magnetometers and nanoSQUIDs [15–20, 22] and more recently into superconducting field-effect transistors [23, 24] and superconducting microwave circuits [25–27]. The latter – nano-constriction microwave circuits – are used for dispersive magnetometry [28, 29], microwave optomechanics [30, 31], photon-pressure devices [32, 33], parametric amplifiers [34], current detectors [35], and quantum bits [36]. Constrictions are interesting for these applications, since they combine a small junction area with high critical current densities but without adding large capacitances or lossy materials. Hence, they are ideal for experiments in large magnetic fields and for microwave circuits with small anharmonicity. On the other hand, the exact constriction CPR depends quite strongly on the material properties, the constriction dimensions as well as the fabrication method [8, 14]. Therefore, a platform for investigating simultaneously the transport characteristics, the constriction CPR and the cJJ impact on the microwave circuit properties such as frequency tunability, Kerr anharmonicity and change of decay rates would be ideal. Some experiments in that direction have already been realized in the past [37–40], none of which checking all the boxes on the wishlist though.

Here, we present a superconducting microwave cavity with an integrated 3D niobium nano-constriction, which has been monolithically cut into the cavity by using the focused ion beam (FIB) of a neon (Ne) ion microscope (NIM). Our particular choice of cavity layout allows simultaneous DC current-voltage access to the cJJ and microwave characterization of the DC-current-biased cavity using microwave reflectometry [35, 41]. Compared to similar experiments with different types of JJs [35, 38, 40], the monolithic approach – in which the cJJ

\* kevin.uhl@pit.uni-tuebingen.de

† daniel.bothner@uni-tuebingen.de

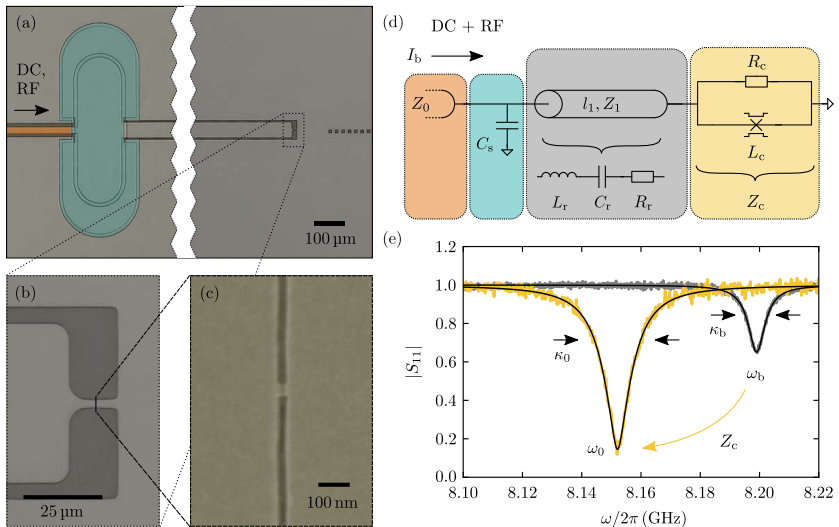


FIG. 1. **A superconducting microwave cavity with integrated niobium nano-constriction and direct current access.** (a) False-color optical micrograph of the  $\lambda/2$  transmission line cavity. At the input port, the cavity is shunt-coupled by a large parallel-plate shunt capacitance  $C_s$  (Nb-Si<sub>3</sub>N<sub>4</sub>-Nb, colored in teal) to a  $Z_0 = 50\ \Omega$  feedline (center conductor colored in orange) for simultaneous microwave (RF) and direct current (DC) probing of cavity and integrated nano-constriction. The cavity itself has a characteristic impedance  $Z_1 = 32\ \Omega$  and a length of  $l_1 \approx 7200\ \mu\text{m}$  (the zigzag lines indicate that most of the cavity length is omitted here). At the far end (far from the input), close to the connection to ground, a monolithic 3D niobium nano-constriction-type Josephson junction (cJJ) is patterned into the center conductor of the coplanar waveguide cavity by means of a focused neon ion beam. Bright and colored parts are niobium, dark parts are silicon substrate. (b) Zoom to the end part of the resonator; (c) False-color scanning electron microscopy image of the 3D cJJ. (d) Circuit equivalent of the cavity with the cJJ at the end, which is modelled as a parallel combination of a loss channel (resistor  $R_c$ ) and a reactive channel (inductance  $L_c$ ), in total described by the impedance  $Z_c$ ; the coplanar waveguide part of the cavity can be described by a lumped element series equivalent with an inductor  $L_r$ , a capacitor  $C_r$ , and a resistor  $R_r$ , respectively. (e) Reflection response  $S_{11}$  of the cavity before (gray) and after (yellow) cutting the constriction, measured at  $T_s = 3.9\ \text{K}$ . From the change in resonance frequency  $\omega_b \rightarrow \omega_0$  and linewidth  $\kappa_b \rightarrow \kappa_0$  induced by the added constriction impedance  $Z_c$ , the cJJ elements  $R_c$  and  $L_c$  can be determined. Gray and yellow noisy lines are data, black smooth lines are fits.

is cut into the cavity at the very end of the fabrication – has the advantage that one and the same cavity can be characterized without and with the cJJ. From the change of cavity resonance frequency and linewidth by the current-biased cJJ, we reconstruct the constriction CPR and observe that it considerably deviates from the simple sinusoidal shape and that it gets more linear with decreasing temperature. Finally, we measure the cavity Kerr anharmonicity, and demonstrate that it is both in good agreement with calculations based on the forward-skewed CPR found beforehand and sufficiently small for high-dynamic range applications. Our analysis also reveals, that very small deviations in the second and third derivatives of the CPR can considerably impact the value of the Kerr constant, even at zero bias current. Overall, our results show that the cavity-integrated characterization of nonlinear superconducting inductances can be used to reconstruct the CPR of familiar and novel weak

links, to deepen the understanding of Ne-FIB patterned cJJs and that 3D niobium cJJs are promising for applications in superconducting microwave circuits, radiation-pressure systems and current sensors.

## RESULTS

### The Device

Our device is presented in Fig. 1 and it is based on a  $\lambda/2$  (half wavelength) coplanar waveguide cavity, near-shortened to ground at both ends. The cavity is patterned from a 90-nm-thick DC-magnetron-sputtered niobium film on high-resistivity silicon substrate, it has a characteristic impedance  $Z_1 \approx 32\ \Omega$  and a total length  $l_1 \approx 7200\ \mu\text{m}$ . The niobium film has a critical temperature  $T_c \sim 9.0\ \text{K}$  and a residual resistivity of  $\rho \sim 7.3\ \mu\Omega\text{-cm}$  at 10 K. At its input port, the cavity is shunt-coupled to a  $Z_0 = 50\ \Omega$  coplanar waveguide feedline for microwave

driving and readout via a three-layer parallel plate capacitance  $C_s \approx 17.5$  pF to ground. Due to this particular coupling scheme, the center conductor remains uninterrupted and we can pass a DC bias current along the waveguide from the feedline all the way through the cavity [41]. At the far end of the cavity, the center conductor has a narrower part, into which the cJJ is cut with a Ne-FIB after a first round of basic cavity characterization experiments. The cJJ has a length of  $\sim 25$  nm, a width of  $\sim 40$  nm and a thickness of  $\sim 40$  nm, cf. Fig. 1(c). For more details on the sample fabrication, cf. Supplementary Note I.

All experiments, before and after the junction cutting, are performed in the vacuum chamber of a liquid helium cryostat. For the measurements, the  $10 \times 10$  mm<sup>2</sup> large chip containing the constriction-cavity is mounted on and wirebonded to a microwave printed circuit board (PCB), which is connected to a coaxial microwave cable. Close to the sample, a bias-tee is connected to the coaxial cable to combine the DC and microwave inputs, and a 10 dB directional coupler is added to split microwave input and output signals. The microwave input line is strongly attenuated to thermalize the input noise to the sample temperature, and the output line is connected to a cryogenic  $\sim 35$  dB HEMT (high-electron-mobility transistor) amplifier. The DC cables are two cryogenically low-pass-filtered twisted pair copper wires. For a stable temperature control between  $T_{\min} \approx 2.5$  K and  $T_{\max} \approx 6$  K (range of the experiments presented here), a vacuum pump is connected to the liquid helium container of the cryostat and a feedback-loop-controlled heating resistor is included in the vacuum sample chamber. More details on the experimental setup and a corresponding schematic can be found in Supplementary Note II.

As any Josephson element at temperatures of few kelvin typically has a reactive and a resistive part to its impedance, we model the cJJ as a parallel combination of an inductor  $L_c$  and a resistor  $R_c$  similar to the two-fluid model, cf. Fig. 1(d). We omit the additional junction capacitance here as well as a possible quasiparticle inductance in the resistive branch, since according to our estimates both are negligible at the frequencies relevant for this work. In order to model the cJJ-shortened transmission line resonator with analytic expressions, we use a lumped element equivalent of the resonator with resistor  $R_r$ , inductor  $L_r$  and capacitor  $C_r$ , cf. Fig. 1(d), which is a very good approximation near the resonance frequency (cf. Supplementary Notes III and IV) and simplifies the calculations.

For sufficiently low excitation powers to be safely in the linear response regime, the resonance frequency of the cavity after junction cutting is in good approximation given by

$$\omega_0 = \frac{\omega_b}{1 + \frac{L_c}{2L_r}} \quad (1)$$

with the resonance frequency before the cutting  $\omega_b = 1/\sqrt{L_r C_{\text{tot}}}$  and  $C_{\text{tot}} = C_r C_s / (C_r + C_s)$ . The resonator

inductance is given by

$$L_r = \frac{\pi Z_1}{2\omega_1} \quad (2)$$

with the shunt-capacitor-less resonance frequency  $\omega_1$  (cf. Supplementary Note III). From Eqs. (1) and (2) it also becomes clear why we chose  $Z_1$  to be smaller than the usual  $50 \Omega$ , since a smaller  $L_r$  increases the device sensitivity to changes in  $L_c^*$ . The resonance linewidth after constriction cutting is

$$\kappa_0 \approx \kappa_b + \omega_0^2 R_c^* C_{\text{tot}} \quad (3)$$

with the total linewidth before cutting  $\kappa_b$ . The two effective lumped elements  $R_c^*$  and  $L_c^*$  are related to the actual junction resistance and inductance  $R_c$  and  $L_c$ , respectively, via

$$R_c^* = \frac{R_c \omega_0^2 L_c^2}{R_c^2 + \omega_0^2 L_c^2}, \quad L_c^* = \frac{L_c R_c^2}{R_c^2 + \omega_0^2 L_c^2} \quad (4)$$

and after finding the values for  $R_c^*$  and  $L_c^*$  from the properties of the cavity, we invert these relations and obtain the values for  $R_c$  and  $L_c$ .

To demonstrate the effect of cutting the cJJ into the resonator and to analyze the unbiased constriction properties, we show in Fig. 1(e) the reflection response  $S_{11}$  around resonance of the cavity without and with the junction, i.e., before and after constriction cutting. As always in this work, the response was measured by means of a vector network analyzer (VNA). Before cutting the junction, the cavity has a resonance frequency  $\omega_b \approx 2\pi \cdot 8.199$  GHz and a total linewidth of  $\kappa_b = 2\pi \cdot 7.6$  MHz with internal and external contributions  $\kappa_{i,b} = 2\pi \cdot 1.3$  MHz and  $\kappa_{e,b} = 2\pi \cdot 6.3$  MHz, respectively. After the junction is cut into the cavity, the resonance frequency has shifted to  $\omega_0 \approx 2\pi \cdot 8.152$  GHz and the linewidth to  $\kappa_0 \approx 2\pi \cdot 15.6$  MHz. Here, the junction-induced decay rate is  $\kappa_c = \omega_0^2 R_c^* C_{\text{tot}} \approx 2\pi \cdot 8.0$  MHz. Using relations Eq. (4) we obtain  $L_c = 11.9$  pH and  $R_c = 7.4 \Omega$ . Note that we only show the resonance lines for a single sample temperature  $T_s = 3.9$  K here, but in Supplementary Notes III and VII more data on the temperature dependence of the junction-less cavity and the cavity with constriction can be found.

### Tuning the cavity with a DC current

As a next step, we investigate the impact of a DC bias current  $I_b$  through the cJJ on the cavity properties  $\omega_0(I_b)$  and  $\kappa_i(I_b)$ , respectively. The experiment and the results are presented in Fig. 2. Again, we show exemplarily the data for a single sample temperature  $T_s = 3.9$  K, but more analogous data for different temperatures are presented and discussed in Supplementary Note VII. First, we measure the current-voltage characteristic (IVC) of the cJJ without any microwave tone by sending a DC current through the junction and tracking the corresponding DC voltage. We observe switching from the zero-voltage-

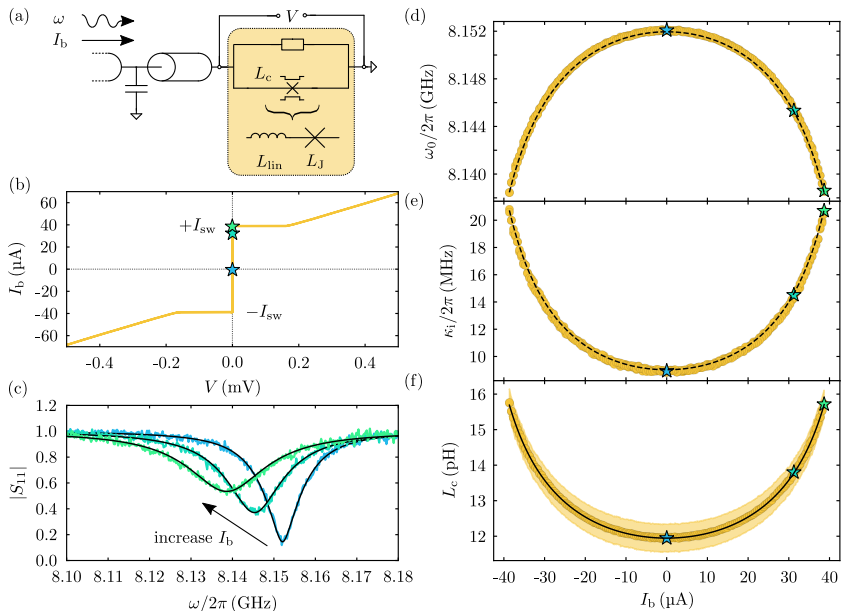


**FIG. 2. Tuning microwave cavity and constriction inductance with a sub-critical DC current.** (a) Schematic of the experiment. A DC bias current  $I_b$  is sent through the feedline and the cavity center conductor to the cJJ and the corresponding (time-averaged) voltage  $V$  is detected. For various DC currents, the resonator reflection  $S_{11}$  is measured with a vector network analyzer. For the analysis, we split the constriction inductance  $L_c$  into a linear part  $L_{lin}$  and a Josephson part  $L_J$ . All data in this figure were taken at  $T_s = 3.9$  K. (b) shows a typical non-hysteretic current-voltage characteristic (IVC) of the constriction with a switching current of  $I_{sw} \sim \pm 39 \mu\text{A}$ . The three stars mark the bias current values  $I_b = 0$ ,  $I_b \sim 0.8I_{sw}$  and  $I_b \sim 0.99I_{sw}$ , for which we show the corresponding cavity reflection response  $S_{11}$  in panel (c). With increasing DC current, the resonance frequency shifts to lower values and the cavity linewidth increases. Colored noisy lines are data, black smooth lines are fits. From the fits to each reflection measurement, the resonance frequency  $\omega_0(I_b)$  and the internal decay rate  $\kappa_i(I_b)$  are extracted, the results are shown in panels (d) and (e), respectively. We attribute the frequency shift to a change of the nonlinear constriction inductance  $L_c(I_b)$  and the change in linewidth to a current-dependent loss channel  $R_c(I_b)$ . The values we extract for the current-dependent junction inductance  $L_c$  are shown in panel (f). In (d)-(f), symbols are data, solid lines are fits, dashed lines are calculated from theory expressions and fit values, and star symbols correspond to the resonances shown in (c). The color-shaded area around the data points in (f) corresponds to the estimated error due to uncertainties of the constriction-free cavity parameters as discussed in Supplementary Note VII.

to a finite-voltage-state at a current of  $I_{sw} \approx 39 \mu\text{A}$  in both current directions. We also find a non-hysteretic IVC indicating that the constriction is in the overdamped regime, and we observe a considerable excess current of  $I_{ex} \sim 23.7 \mu\text{A}$ , possibly related to self-heating or to Andreev reflections [42, 43]. Overall, the IVCs behave very much as expected from earlier experiments and observations in niobium constrictions [18, 44]. The (differential) DC resistance that we determine from the slope of the linear part of the voltage-branch is  $R_{lin} = 11 \Omega$ , so slightly larger than the  $R_c \approx 7.4 \Omega$  we got from the microwave experiment. They are also not expected to coincide, however, since heating effects for instance can significantly impact the measured DC resistance.

To investigate the microwave properties of the current-biased cavity in the sub-critical  $I_b$  regime, we then measure the reflection response  $S_{11}$  for varying bias currents  $I_b < I_{sw}$  and extract  $\omega_0(I_b)$  and  $\kappa_i(I_b)$  from fits to the reflection data. The equations and fitting routines used are detailed in Supplementary Notes V and VI. Here, we use sufficiently low microwave probe powers to keep the cavity in the linear response regime, which we ensure by staying far below the input powers needed to observe nonlinearities in the resonance lineshape. With increasing bias current, the resonance frequency is shifting to lower values as observed also in earlier experiments [35, 38] and expected from the nature of a superconducting nonlinear inductance, which usually increases with

increasing bias current. The total frequency range that we can cover with the bias-current-tuning is strongly temperature-dependent (see Supplementary Note VII), but for  $T_s = 3.9$  K it is  $\sim 13.5$  MHz. The internal linewidth on the other hand is increasing with increasing bias current, from  $\kappa_i \sim 2\pi \cdot 8.9$  MHz at zero bias current to  $\kappa_i \sim 2\pi \cdot 20.7$  MHz at  $I_b \sim I_{sw}$ . For currents larger than the switching current the resonance vanishes abruptly, as the losses in the constriction and the internal linewidth get so high that the resonance cannot be discriminated from the background anymore. Both effects the decrease in resonance frequency and the increase in linewidth can ultimately be attributed to a bias-current-dependent decrease of Cooper pair density and an increase of quasiparticle density inside the cJJ. A reduced Cooper pair density leads to an increase of the kinetic supercurrent inductance  $L_c$ . Simultaneously, it leads to a reduced value for  $R_c$ , i.e., more and more of the microwave current is passing through the resistor (quasiparticle current) instead of the inductor (Cooper pair current).

By applying the same data extraction routine as discussed in the context of Fig. 1, we can determine for all bias currents the value of  $L_c$ , the result is plotted in Fig. 2(f). The constriction inductance increases from around 12 pH at zero bias current to around 15.8 pH at  $I_b \sim I_{sw}$ . We perform a fit of the data by assuming that the inductance of the constriction  $L_c$  can be described by a series combination of a linear inductance  $L_{lin}$  and an ideal Josephson inductance  $L_J$ , an often surprisingly accurate model for nano-constrictions, that has already been discussed in Ref. [14] and more recently in Ref. [45]. The dependence of the total inductance on the bias current in this case is given by

$$L_c(I_b) = L_{lin} + L_J(I_b) \quad (5)$$

$$= L_{lin} + \frac{L_{J0}}{\sqrt{1 - \frac{I_b^2}{I_0^2}}} \quad (6)$$

with the zero-bias-current Josephson inductance  $L_{J0} = \Phi_0/(2\pi I_0)$  and the theoretical critical current  $I_0$ . The latter can be different from the experimental switching current  $I_{sw}$ , for instance due to thermal or quantum activated escape, phase diffusion or electronic noise coupling into the device. And indeed, as indicated by the black fit line in Fig. 2(f), this approach works very well with the fit parameters  $L_{lin} = 5.55$  pH and  $I_0 = 50.5$   $\mu$ A, which corresponds to  $L_{J0} = 6.5$  pH. From this fit it indeed seems that the critical current  $I_0$  is significantly larger than the experimental switching current  $I_{sw}$  and we will discuss this effect further for various sample temperatures in the next sections and in Supplementary Note VII. Regarding the extracted resistance  $R_c$  we do not have a clear microscopic or intuitive physical model for the functional bias-current dependence, but we can fit it with an even fourth order polynomial for all temperatures, cf. also Supplementary Note VII. Re-inserting the obtained fit curves for  $L_c(I_b)$  and  $R_c(I_b)$  back into the equations for the reso-

nance frequency and linewidths leads to the black dashed lines in panels (d) and (e), showing excellent agreement with the data.

### Extracting the constriction current-phase relation

Once we know the cJJ inductance for each bias current, we can reconstruct the current-phase-relation (CPR) of the constriction and in what follows we will describe the relation between  $L_c$  and  $I(\delta)$  in more detail. We have treated the cJJ so far as a bias-current-dependent but microwave-linear inductance, which was justified by the low powers used in the experiment. But what exactly does that mean and how is it related to the CPR of the cJJ? In circuit theory, a linear inductance  $L$  is directly related to a harmonic potential, where the potential energy is given by  $E_{pot} = \frac{\Phi^2}{2L}$  with the generalized flux through the inductor  $\Phi$ . A Josephson-like element now usually has an anharmonic and  $2\pi$ -periodic potential, e.g., a cosine-shaped potential  $E_{pot} = E_J(1 - \cos \delta)$  in the case of a standard junction, which is expressed in terms of the phase difference across the junction  $\delta = 2\pi \frac{\Phi}{\Phi_0}$  instead of the flux and where  $E_J = \frac{\Phi_0 I_0}{2\pi}$  is the Josephson energy. For a linear inductance, the potential can therefore be expressed in terms of the phase as  $E_{pot} = \frac{\Phi_0^2 \delta^2}{4\pi^2 2L}$ . At the same time, such a quadratic term is also the first dynamically relevant term in a Taylor expansion of a nonlinear  $2\pi$ -periodic potential around the equilibrium phase  $\delta_0$ , which explains why for small phase oscillations (=low microwave excitation powers) we can also treat the nano-constriction as a linear inductance. In both cases, the current-phase relation is given by

$$I(\delta) = \frac{2\pi}{\Phi_0} \frac{\partial E_{pot}}{\partial \delta} \quad (7)$$

and the linear inductance of the element is expressed as

$$\frac{1}{L} = \frac{4\pi^2}{\Phi_0^2} \left. \frac{\partial^2 E_{pot}}{\partial \delta^2} \right|_{\delta_0} \quad (8)$$

where the equilibrium phase is defined via  $I(\delta_0) = I_b$ . Hence, there is a direct relation between the CPR and  $L$ , which reads in terms of our device variables

$$L_c = \frac{\Phi_0}{2\pi} \left( \left. \frac{\partial I}{\partial \delta} \right|_{\delta_0} \right)^{-1}. \quad (9)$$

In other words, the constriction inductance is identical to the reciprocal of the slope of the CPR at any bias point and we can obtain the phase for any given bias current by

$$\delta = \frac{2\pi}{\Phi_0} \int_0^{I_b} L_c dI_b', \quad (10)$$

given that we have tracked the inductance for all currents up to  $I_b$ . Since of course we only have a finite number

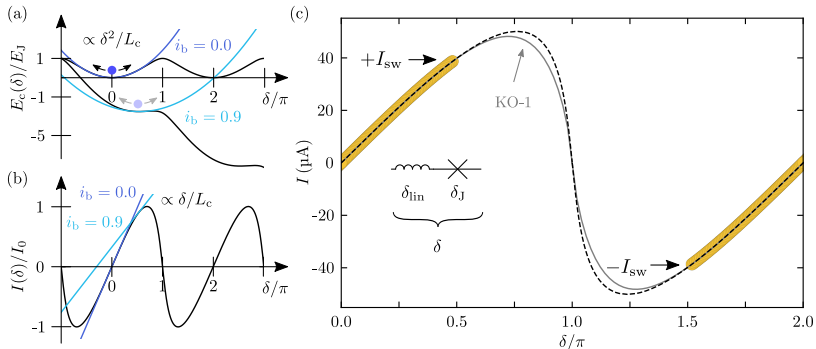


FIG. 3. **Reconstructing the current-phase-relation of the nano-constriction from microwave data.** (a) Schematic drawing of a  $2\pi$ -phase-periodic constriction potential  $E_c(\delta)$ , in which the superconducting phase particle can oscillate around its equilibrium position  $\delta_0$ . We show the two exemplary cases  $\delta_0 = 0$  for  $i_b = I_b/I_0 = 0$  and  $\delta_0 > 0$  for  $i_b = 0.9$ , where  $I_0$  is the critical current. For small oscillation amplitudes, the potential can be approximated by a parabola  $\propto \delta^2/L_c$ . A bias current  $i_b > 0$  is equivalent to a potential tilt, which reduces the curvature in the minimum. (b) The schematic current-phase-relation (CPR) can be obtained from the potential by differentiation and the slope of the CPR at the equilibrium position of the particle is  $\propto 1/L_c$ . Hence, from knowing the inductance  $L_c$  for many bias currents  $I_b$ , the CPR can be reconstructed by integration (see main text). We perform this integration here for the dataset discussed in Fig. 2(f) and the result is plotted in (c) as yellow circles. Temperature is  $T_s = 3.9$  K and data points extend to  $\pm I_{sw}$ . Data points for  $I < 0$  have been manually shifted by  $+2\pi$  in phase. By describing  $L_c$  as a linear-plus-Josephson inductance, the CPR  $I(\delta)$  can be modeled with a total phase  $\delta = \delta_{lin} + \delta_J$  with the phase across the linear part  $\delta_{lin}$ , the result is shown as black dashed line and resembles a forward-skewed sinusoidal shape. Here  $\delta_{lin}$  and  $\delta_J$  describe the individual phases across each component, linear and sinusoidal part, respectively. For comparison an exemplary CPR based on the KO-1 model is shown as gray fit line.

$N$  of discrete current and inductance values, we have to replace the integration by summation

$$\delta_j = \frac{2\pi}{\Phi_0} \sum_j^N L_{c,j} \Delta I_j \quad (11)$$

with  $j > 0$  and  $\Delta I_j = I_{b,j} - I_{b,j-1}$ . Figure 3 summarizes and illustrates these ideas and the result of our CPR reconstruction using this method for the data presented and discussed already in Fig. 2.

What we find when performing this discrete integration is shown in Fig. 3(c): we obtain a rather linear dependence  $I(\delta)$  for  $\delta \leq \pi/4$ , which starts to bend towards smaller slopes for higher currents and then suddenly stops at around  $\delta \approx \pi/2$ , when  $I_b = I_{sw}$ . Very clearly, this CPR deviates significantly from the sinusoidal shape of an ideal Josephson tunnel junction, which would have a maximum and zero slope at  $\delta = \pi/2$ . In our data, we do not reach a point where the slope approaches zero, which is typically the case when  $I_b \sim I_0$ . When we add the theoretical curve for the CPR of a series combination of  $L_{lin}$  and an ideal Josephson element  $L_J$  though, shown as dashed line, the picture seems to match quite perfectly. The theoretical CPR is piecewise calculated using

$$\delta = (-1)^n \arcsin\left(\frac{I}{I_0}\right) + \frac{2\pi}{\Phi_0} L_{lin} I + n\pi \quad (12)$$

and inversely plotted for  $n \in \{-1, 0, 1\}$ . Note that we used exactly the values for  $L_{lin}$  and  $I_0$ , that we obtained from the fit in Fig. 2(f), and so the agreement is not a complete surprise.

Such a forward-skewed CPR has been found in many papers for constriction junctions and generalized weak links before [8, 14, 16, 25, 44, 45], in particular for niobium constrictions, but also for aluminum and other materials. Similar CPRs are also predicted by different theoretical models, such as for instance the Kulik-Omelyanchuk (KO-1) model [14], Ginzburg-Landau models [45] and others, for a review cf. Refs. [8, 14]. Of course, we cannot be completely certain how the experimental CPR will continue beyond  $\pi/2$ , where we do not have further experimental data points. However, it has been demonstrated in previous studies that the linear-plus-Josephson-inductance model matches numerically calculated CPRs with high accuracy, see e.g. the very recent work by Wang *et al.* on 3D niobium constrictions [45]. The forward-skewed CPRs of analytical models are furthermore indeed quite similar in shape, and for a qualitative comparison we show a KO-1 fit of our data, although strictly speaking we are most likely not in the regime of validity of this theory with our device properties. According to Ref. [8], the KO-1 model is valid in the regime where the length of the constriction  $l_c \ll \sqrt{\xi_0 l_e}$  and the transverse size  $w_c \ll l_c$ . Both conditions are not

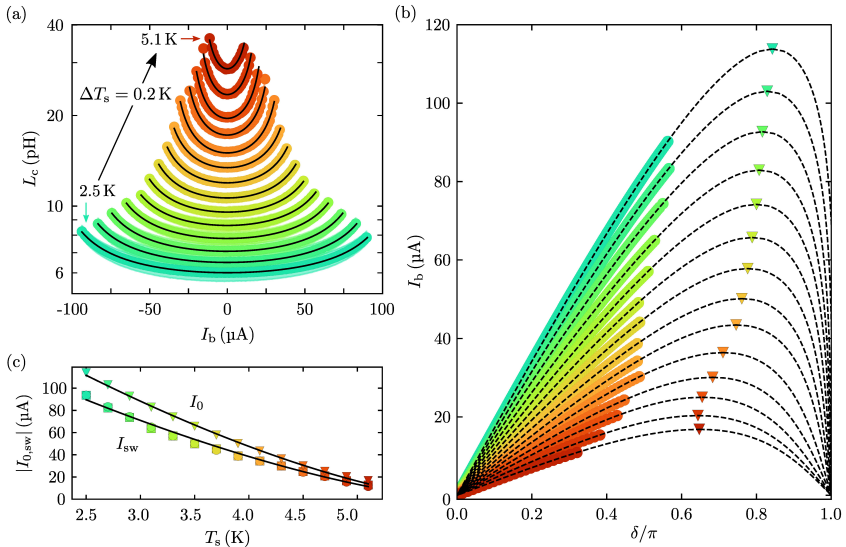


FIG. 4. **Change of the constriction properties with sample temperature.** (a) The constriction inductance  $L_c(I_b)$  for several different sample temperatures  $T_s$ . Lowest temperature is  $T_s^{\min} = 2.5$  K (cyan data, lowest  $L_c$ ), highest temperature  $T_s^{\max} = 5.1$  K (dark red data, highest  $L_c$ ), increased in steps of  $\Delta T_s = 0.2$  K. The inductance increases with both increasing bias current  $I_b$  and with increasing temperature. Circles are data, lines are fits using Eq. (6), and colored shades around the data points correspond to the error range analogous to the one in Fig. 3(f). By integrating the inductance  $L_c$ , the corresponding constriction CPR can be reconstructed for each  $T_s$ . The result is plotted in (b), circles are data, dashed lines are theoretical CPRs with the two-inductor-model and based on the fits of (a). With increasing temperature, the CPRs get less skewed and less linear in the regime  $\delta \leq \pi/2$ . For all curves (except for the highest few temperatures)  $I_{sw} \sim 0.8I_0$ , but the phase for which either of them is reached gets smaller with increasing  $T_s$ . The CPR critical currents  $I_0$  are marked with triangles at the maximum of each dashed line. (c) Critical current  $I_0$  and switching current  $I_{sw}$  vs temperature in the range  $T_s = 2.5$  K–5.1 K. Circles and squares are  $I_{sw}$  data obtained by microwave and IV-measurements, respectively. Triangles are the theoretical critical currents  $I_0$ , which we get from the fits of  $L_c$ . Solid lines in (c) are fits with Eq. (13).

fulfilled in our device since the BCS coherence length is  $\xi_0 = 38$  nm for niobium, the electron mean free path in our device is  $l_e \approx 5.7$  nm (cf. Supplementary Note VII) and  $l_c = 25$  nm,  $w_c = 40$  nm. Nevertheless does the KO-1 fit resemble both, the skewedness and the critical current  $I_0$  in good approximation and at the same time demonstrates that small deviations in the CPR are well possible in the regime  $I \sim I_0$  without compromising the behaviour for  $I < I_{sw}$ .

Since we have the possibility to vary the sample temperature between  $T_s^{\min} \sim 2.5$  K and  $T_s^{\max} > T_c \approx 9$  K, we will use this opportunity to study the temperature-dependence of cavity and constriction properties and of the resulting CPR in the next part.

#### Change of CPR with sample temperature

To this end, we repeat all the measurements and data analyses discussed above for  $T_s = 3.9$  K for all temper-

atures  $2.5 \text{ K} \leq T_s \leq 5.1 \text{ K}$  in steps of  $\Delta T_s = 0.2$  K. In Supplementary Note VII a collection of all cavity resonance frequencies and internal linewidths as function of  $I_b$  and  $T_s$  is presented. Here, we want to focus on the resulting constriction inductances  $L_c$ , the re-constructed current-phase-relationships and the constriction currents  $I_{sw}$  and  $I_0$ .

Our main findings are collected and presented in Fig. 4. The constriction inductance  $L_c$  is increasing with both, temperature and bias current, and over all temperatures the minimum and maximum values are  $\sim 6$  pH and  $36$  pH, respectively. With decreasing temperature, the inductance tunes faster with increasing  $I_b$ , a signature for a decreasing  $I_0$ . The relative tuning range however, i.e., the ratio of maximum to minimum inductance for a fixed  $T_s$  seems to be rather constant, except for the highest temperatures, where the range decreases somewhat. For a further quantitative analysis and the extraction of the CPRs, we again fit the measured inductances with

our linear-plus-sinusoidal inductance model Eq. (6) and it gives excellent agreement for all temperatures.

Then, we integrate the data points of  $L_c$  over the bias current  $I_b$  for each  $T_s$  and plot the resulting CPRs in panel (b) in direct comparison with the curves calculated through the two-inductance model and the corresponding fit. There are several important observations we can make in this representation.

Firstly, the integrated CPRs are always in excellent agreement with the calculated ones, there is no indication of deviations in the experimentally accessible regime. This shows that the inductance model we applied to obtain the fits is well-applicable over the complete temperature and bias-current range.

Secondly, the CPR skewedness is getting reduced with increasing temperature, an effect that has already been observed earlier for superconducting junctions with skewed CPRs [44] and which is also an intrinsic property of theories like the KO-1 model for instance [8, 14]. One way of intuitively interpreting this is that the constriction inductance becomes more linear with decreasing temperature and deviates stronger from that of an ideal tunnel junction. Ultimately, it is defined by a competition of different length scales such as the constriction dimensions, the electron mean free path and the superconducting coherence length [8], some of which are temperature-dependent. Importantly, however, we do not observe any multi-valued CPRs as in many earlier studies on niobium constrictions [16, 44], which is a signature of the high quality of our devices [25]. Since for the lowest temperatures used here the CPR slope around  $\delta = \pi$  is approaching very large values, it could, however, be that for even lower temperatures the single-valuedness vanishes and that the critical current is maybe even shifted to  $\delta_{I_0} > \pi$ .

Finally, we observe that the switching current for all temperatures except for the very highest ones is reached at  $\delta \sim \pi/2$  and that the ratio  $I_{sw}/I_0$  does not show a strong temperature dependence, cf. also panel (c) and Supplementary Note VII. In fact, the ratio  $I_{sw}/I_0$  stays nearly constant for all temperatures at around  $0.8 \pm 0.05$ , except for the highest  $T_s = 5.1$  K, where the switching happens even earlier, cf. also Supplementary Note VII. Although we do not know the exact origin of the premature switching, we believe we can exclude several possible suspects due to the constant value of  $I_{sw}/I_0$ . If the switching was triggered by an external noise source with a constant noise amplitude or by thermal noise, the suppression of the switching current would increase with increasing  $T_s$  or remain constant in units of  $\mu$ A. Also, the switching is not induced by the microwave probe signals, except maybe for the highest  $T_s$ . In panel (c) we show both, the switching currents determined from the IV characteristics in absence of any microwave signals (circles) and the switching currents observed in the experiment, in which we stepwise increase  $I_b$  and probe the cavity for each value (squares). The results do not show any remarkable difference. It is however, not unusual

that in experiments with superconducting nanowires and constrictions the switching current is considerably lower than the critical current. It has been attributed to phase slips and phase diffusion in the past [46–49], which can be thermally activated or by quantum tunneling, and the level of suppression can depend on the bias current sweep rate (here 22.5 nA/ms), on the thermalization and heating details of the sample and on the current-phase-relation of the system under consideration. To illuminate and analyze this premature switching in more detail, further experiments and systematic investigations will be necessary, for instance through measuring switching statistics as function of bias-current sweep rate and temperature.

To gain further insights from the data we do have, we fit the temperature dependence of both  $I_{sw}$  and  $I_0$  with a function

$$I_x(T_s) = I_{c,x} \left( 1 - \frac{T_s}{T_{c,x}} \right)^{\frac{3}{2}} \quad (13)$$

where  $x = \{0, sw\}$ . Although not based on a specific theory for constrictions, such a temperature-dependence reproduces very well the experimentally observed behaviour, cf. panel (c) in Fig. 4. Here, the fit parameters are the critical/switching current at zero temperature  $I_{c,x}$ , and the constriction critical temperature  $T_{c,x}$ . We find  $T_{cc,0} = 5.96$  K and  $T_{cc,sw} = 5.98$  K, so the two values are very close together, but quite different from  $T_c \approx 9.0$  K of the superconducting film. This demonstrates that our device corresponds to a so-called SS'S constriction, where the superconductor in the leads (S) is different from the superconductor forming the constriction itself (S'). The exact reason for both the reduction of  $T_{cc}$  compared to  $T_c$  and the difference between similar samples are currently not completely clear, but we suspect neon ion implantation or the creation of a thin normal-conducting surface layer to be the origin [50].

### Characterizing the nonlinear CPR corrections

So far, we have operated in all experiments and analyses with low microwave powers and assuming the constriction to be a linear microwave inductance. With higher microwave powers, however, we can also gather information about higher-order corrections to the periodic and non-parabolic constriction potential, and compare these higher-order corrections with the ones obtained from our CPR model. The picture is simple: when we apply a microwave signal to the cavity, the phase particle in the anharmonic potential is oscillating around the minimum, and the oscillation amplitude depends on microwave excitation power and frequency. For very small oscillations, the particle only feels a parabolic term, for higher powers the particle will experience the deviations, cf. also Fig. 5(a). Experimentally, these deviations will be observable by a dependence of the cavity resonance frequency on intracavity microwave photon number, which originates from a change of the time-averaged

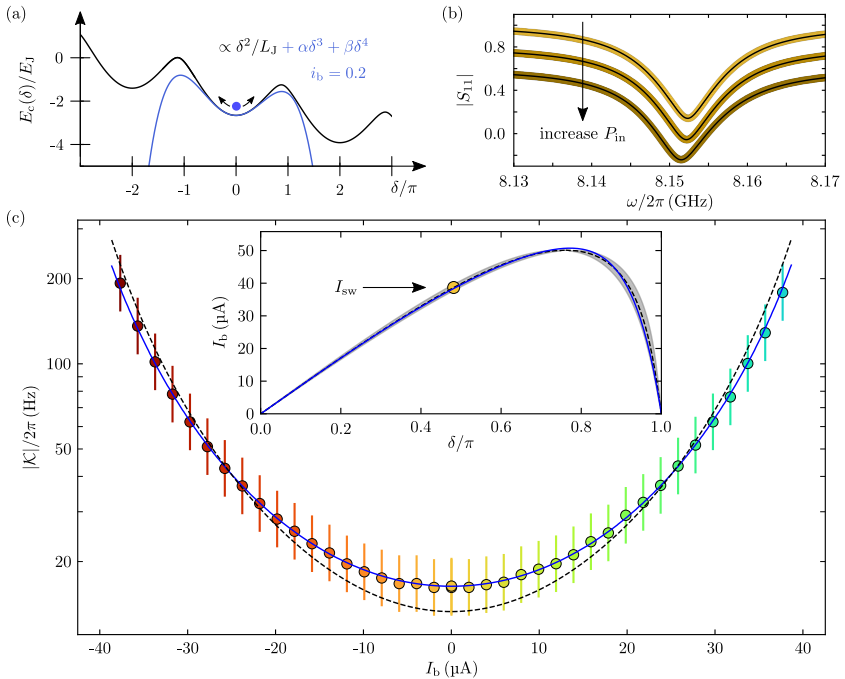


FIG. 5. **Higher order derivatives of the CPR shape the Kerr anharmonicity.** (a) Schematic of a particle in a  $2\pi$ -periodic potential, which is oscillating with large amplitudes. For larger oscillation amplitudes than considered so far, the particle will experience a deviation from the harmonic approximation and the next relevant contribution in a Taylor-expansion of the potential is  $\propto \delta^4$  for the case of  $I_b = 0$  or both third order and fourth order corrections  $\propto \delta^3$  and  $\propto \delta^4$  for  $I_b > 0$ , respectively. Shown is the case for  $i_b = 0.2$ . The Taylor-coefficients  $\alpha$  and  $\beta$  are proportional to the second and third derivatives of the CPR, respectively. (b) Reflection data  $S_{11}$  of the cavity for three different microwave probe tone powers  $P_{in}$ . Subsequent curves are offset by  $-0.2$  each for better visibility. For the larger powers, the resonance shifts to lower frequencies and deviates from the Lorentzian lineshape. We fit the data using a nonlinear model (black lines), from which we obtain the Kerr constant  $\mathcal{K}$ , which has contributions from both the third order and the fourth order correction terms, see Supplementary Note IV for details. The values of  $|\mathcal{K}| = -\mathcal{K}$  for multiple bias currents are shown in panel (c), they increase in magnitude with increasing bias current from around  $\mathcal{K} \approx 2\pi \cdot 18$  Hz for  $I_b = 0$  to  $\mathcal{K} \approx 2\pi \cdot 190$  Hz for  $I_b \sim \pm I_{sw}$ . Error bars consider a  $\pm 1$  dB uncertainty in on-chip power of the microwave tone. For comparison we plot two different theory lines based on nonlinear current-conservation calculations; the black dashed one takes as input the second and third derivatives of the experimentally determined CPRs (linear-plus-sinusoidal model), the blue solid one is based on an artificially created CPR, that resembles very closely the one based on the linear-plus-sinusoidal-inductance model for  $I_b < I_0$ . Both CPRs are shown in direct comparison in the inset. The switching current in the experiment is marked by a yellow circle, the uncertainty in the linear-plus-sinusoidal CPR is shown as gray shade. Sample temperature for experimental data was  $T_s = 3.9$  K.

constriction inductance with higher powers. It has been demonstrated, that both third order and fourth order nonlinearities in the potential lead to a shift of the resonance frequency proportional to intracavity photon number and that the shift of both terms can be condensed into a single effective Kerr constant  $\mathcal{K}$  [51]. The total cavity frequency shift is then  $\mathcal{K}n_c$  with the intracavity photon number  $n_c$ .

We determine the effective Kerr constant by measur-

ing the power-dependence of the resonance line up to the regime where the nonlinearities kick in. In this regime, the cavity lineshape begins to deform towards the famous shark-fin resonance of Duffing oscillators, i.e., it becomes asymmetric and the minimum moves towards lower frequencies, cf. Fig. 5(b) and Supplementary Note VIII. We also observe a small nonlinear damping effect, i.e., both the amplitude of  $S_{11}$  in the minimum and the total linewidth increase with microwave power, most likely due

to an increase of the time-averaged quasiparticle density. We fit the experimentally obtained dataset based on the solution of the nonlinear cavity equation of motion [52]

$$\dot{\alpha} = \left[ i(\omega_0 + \mathcal{K}|\alpha|^2) - \frac{\kappa_0 + \kappa_{nl}|\alpha|^2}{2} \right] \alpha + i\sqrt{\kappa_c} S_{in} \quad (14)$$

where  $\alpha$  is the complex cavity field amplitude, which is normalized such that  $|\alpha|^2 = n_c$  is the intracavity photon number. The microwave input field  $S_{in}$  is normalized such that  $|S_{in}|^2 = P_{in}/(\hbar\omega)$  with the on-chip input power  $P_{in}$ , the probe frequency  $\omega$  and the reduced Planck constant  $\hbar$ . As main fit parameter we obtain the Kerr constant  $\mathcal{K}$  for each bias current  $I_b$ . More details on the fitting procedure, the free and fixed parameters during the fit, and on the error estimates can be found in Supplementary Note VIII.

The obtained Kerr anharmonicity  $\mathcal{K}$  increases strongly with increasing bias current  $I_b$ , from  $\sim 2\pi \cdot 18$  Hz at  $I_b = 0$  to  $\sim 2\pi \cdot 190$  Hz at  $I_b \lesssim \pm I_{sw}$ , cf. Fig. 5(c). The theoretical relation between the CPR and the  $\mathcal{K}$  is given by

$$\mathcal{K} = \frac{e^2}{2\hbar C_{tot}} p_c^3 \left[ \frac{g_4}{g_2} - \frac{3g_3^2}{g_2^2} (1 - p_c) - \frac{5}{3} \frac{g_3^2}{g_2^2} p_c \right] \quad (15)$$

where the coefficients

$$g_n = \frac{\partial^{n-1} J}{\partial \delta^{n-1}} \Big|_{\delta_0} \quad (16)$$

encode the  $(n-1)$ -th derivatives of the CPR with respect to phase at the equilibrium phase  $\delta_0$ , and

$$p_c = \frac{L_c(I_b)}{L_r + L_c(I_b)} \quad (17)$$

is the constriction inductance participation ratio, cf. also Supplementary Note IV for the derivation. Using the CPR, which we obtained from the linear-plus-sinusoidal model, we can easily calculate the theoretical Kerr constant now and the result is in acceptable agreement with the data. There are, however, also some deviations at the lowest and at the highest bias currents, the theoretical line is underestimating the Kerr constant at low currents and overestimating it at high currents. Certainly, there are some simple possible explanations for these deviations such as uncertainties in on-chip microwave power (error bars account for  $\pm 1$  dB), and fitting errors in external and internal cavity linewidths. But there is also another, more interesting possibility: very small differences between the CPR fit-curve and the actual CPR.

To demonstrate how tiny differences in the CPR can have a large impact on the Kerr constant, we have therefore constructed an artificial CPR  $I_{ar}(\delta)$  based on an odd polynomial function (details in Supplementary Note VIII). We then do a simultaneous fit of this new CPR to both the experimental CPR data and to the experimental Kerr data. The result is shown as blue lines in Fig. 5(c) and shows excellent agreement with both datasets. The

relative deviation  $[I_{ar}(\delta) - I(\delta)]/I(\delta)$  between this constructed CPR and the linear-plus-sinusoidal CPR  $I(\delta)$  is smaller than 1% in the complete range covered by our experiment ( $I_b \lesssim 40 \mu\text{A}$ ,  $\delta \lesssim \pi/2$ ). It also falls completely into the error range of the experimental CPR (gray-shaded area) for all phases except for a small region around  $I_0$ . So even for nearly identical CPRs and very similar critical currents, the tiny details of the shape of the CPR, encoded in the  $g_n$  coefficients, can have a strong impact on the actual experimental nonlinearities. Most strikingly, and in stark contrast to perfectly sinusoidal CPR Josephson junctions, is there no unique relation between the junction inductance and the Kerr constant anymore, as can be seen from the values at  $I_b = 0$ . Both CPRs have identical first derivatives (=inductances) there, but Kerr constants that differ by  $\sim 20\%$  due to the third derivatives being different.

Regarding possible applications, such small nonlinearities are well-suited for high dynamic range devices such as parametric amplifiers [11, 12, 34], current detectors [35] or photon-pressure systems [32, 53]. If desired, the Kerr constant could also be made much larger by simple adjustments, for instance by either making the constriction critical current smaller by milling it thinner [27], or by changing the circuit layout to a lumped element version with a very different  $L_r$ . One could even imagine to characterize the cJJ just as we did here and then remove the cavity and circuitry around the cJJ again to replace it with a tailored target layout, optimized for exactly the existing junction.

## DISCUSSION

In conclusion, we have reported a superconducting half-wavelength microwave cavity with bias-current access, that has enabled us to comprehensively characterize the properties of a monolithically patterned 3D nano-constriction. To this end we used a combination of microwave reflectometry and DC biasing of the device. We demonstrated that we can tune both resonance frequency and cavity linewidth by biasing the nano-constriction with small currents in the  $\mu\text{A}$  regime, a property potentially very useful for current detectors, parametric amplifiers or photon-pressure systems. From the analysis of the bias-current- and temperature-dependent constriction-cavity properties, we were able to extract the constriction inductance and to reconstruct the constriction current-phase-relation for a wide range of temperatures. We found a forward-skewed sinusoidal function, which is characteristic for nano-constrictions, and observed that the skewedness decreases with increasing temperature. Furthermore, we found that the superconducting-resistive switching current of the constrictions is suppressed by about 20% compared to the critical current and that the critical temperature of the constriction is considerably reduced compared to the bare niobium film.

On one hand our approach of measuring the CPR of

a nonlinear superconducting inductance with DC-plus-microwave excitation has the disadvantage that we are limited to phases below the switching phase and cannot observe its behaviour in the regime of negative inductance (negative slope of the CPR). This is possible in DC-SQUID experiments for instance [45, 54–56]. On the other hand, however, can we directly compare and analyze switching current and critical current, and our approach allows us to characterize how the integration of the constriction into a microwave cavity impacts the circuit properties, in both cases biased and unbiased. Our approach furthermore enables us to extract a value for the sub-switching constriction resistance, and by characterizing the Kerr constant we finally gain access to the derivatives of the CPR, something which is only possible in DC experiments by differentiating the resulting CPR

dataset by hand. Here, we could demonstrate by measuring and modeling the Kerr anharmonicity of the cavity, that very small changes of the absolute values of the CPR can lead to large differences in the higher order potential corrections though.

Interesting open questions are how exactly the constriction and cavity properties will behave at lower temperatures in the mK regime, and what the physical and/or technical origin is for the premature switching of the constriction. The latter could be investigated by measuring switching statistics as a function of temperature, bias current sweep rates and in presence of various noise sources. Further experiments could also be dedicated to investigate the origin of the suppression of  $T_{C_c}$  compared to  $T_c$  and to the question if and how the CPR depends on constriction thickness and ion dose.

## References

- [1] Kleiner, R., Koelle, D., Ludwig, F., and Clarke, J., **Superconducting quantum interference devices: State of the art and applications**. Proceedings of the IEEE **92**, 1534–1548 (2004)
- [2] Clarke, J. and Braginski, A. I., *The SQUID Handbook*. Wiley-VCH, Weinheim, Germany (2004)
- [3] Hamilton, C. A., **Josephson voltage standard**. Review of Scientific Instruments **71**, 3611 (2000)
- [4] Nakamura, Y., Pashkin, Yu. A., and Tsai, J. S., **Coherent control of macroscopic quantum states in a single-Cooper-pair box**. Nature **398**, 786–788 (1999)
- [5] Clarke, J. and Wilhelm, F. K., **Superconducting quantum bits**. Nature **453**, 1031–1042 (2008)
- [6] You, J. Q. and Nori, Franco, **Atomic physics and quantum optics using superconducting circuits**. Nature **474**, 589–597 (2011)
- [7] Josephson, B. D., **Possible new effects in superconductive tunnelling**. Physics Letters **1**, 251–253 (1962)
- [8] Golubov, A. A., Kupriyanov, M. Yu., and Il'ichev, E., **The current-phase relation in Josephson junctions**. Reviews of Modern Physics **76**, 411 (2004)
- [9] Krantz, P., Kjaergaard, M., Yan, F., Orlando, T. P., Gustavsson, S., and Oliver, W. D., **A quantum engineer's guide to superconducting qubits**. Applied Physics Reviews **6**, 021318 (2019)
- [10] Willsch, D., Rieger, D., Winkel, P., Willsch, M., Dickel, C., Krause, J., Ando, Y., Lescanne, R., Leghtas, Z., Bronn, N. T., Deb, P., Lanes, O., Mineev, Z. K., Dennig, B., Geisert, S., Günzler, S., Ihssen, S., Paluch, P., Reisinger, T., Hanna, R., Bae, J. H., Schüffelgen, P., Grützmacher, D., Buimaga-larina, L., Morari, C., Wernsdorfer, W., DiVincenzo, D. P., Michielens, K., Catelan, G., and Pop, I. M., **Observation of Josephson Harmonics in Tunnel Junctions**. arXiv:2302.09192 (2023)
- [11] Castellanos-Beltran, M. A., Irwin, K. D., Hilton, G. C., Vale, L. R., and Lehnert, K. W., **Amplification and squeezing of quantum noise with a tunable Josephson metamaterial**. Nature Physics **4**, 929–931 (2008)
- [12] Bergeal, N., Schackert, F., Metcalfe, M., Vijay, R., Manucharyan, V. E., Frunzio, L., Prober, D. E., Schoelkopf, R. J., Girvin, S. M., and Devoret, M. H., **Phase-preserving amplification near the quantum limit with a Josephson ring modulator**. Nature **465**, 64–68 (2010)
- [13] Macklin, C., O'Brien, K., Hover, D., Schwartz, M. E., Bolkhovskoy, V., Zhang, X., Oliver, W. D., and Siddiqi, I., **A near-quantum-limited Josephson traveling-wave parametric amplifier**. Science **350**, 307–310 (2015)
- [14] Likharev, K. K., **Superconducting weak links**. Reviews of Modern Physics **51**, 101 (1979)
- [15] Bouchiat, V., Faucher, M., Thirion, C., Wernsdorfer, W., Fournier, T., and Pannetier, B., **Josephson junctions and superconducting quantum interference devices made by local oxidation of niobium ultrathin films**. Applied Physics Letters **79**, 123 (2001)
- [16] Hasselbach, K., Maily, D., and Kirtley, J. R., **Microsuperconducting quantum interference device characteristics**. Journal of Applied Physics **91**, 4432 (2002)
- [17] Mitchell, E. E. and Lam, S. K. H., **Niobium dc SQUIDS with Nanobridge Junctions**. Physics Procedia **36**, 382–387 (2012)
- [18] Chen, L., Wang, H., Liu, X., Wu, L., and Wang, Z., **A High-Performance Nb Nano-Superconducting Quantum Interference Device with a Three-Dimensional Structure**. Nano Letters **16**, 7726–7730 (2016)
- [19] Wang, H., Chen, L., Liu, X., Wu, L., Wu, X., You, L., and Wang, Z., **Fabrication and Characterization of Miniaturized NbN Superconducting Quantum Interference Devices With Nanobridge Junctions**. IEEE Transactions on Applied Superconductivity **27**, 1601905 (2017)
- [20] Martínez-Pérez, M. J. and Koelle, D., **NanoSQUIDS: Basics & recent advances**. Physical Sciences Reviews **2**, 20175001 (2017)
- [21] Trabaldo, E., Ruffieux, S., Andersson, E., Arpaia, R., Montemurro, D., Schneiderman, J. F., Kalaboukhov, A., Winkler, D., Lombardi, F., and Bauch, T., **Properties of grooved Dayem bridge based  $YBa_2Cu_3O_{7-\delta}$  superconducting quantum interference devices and magnetometers**. Applied Physics Letters **116**, 132601 (2020)
- [22] Wyss, M., Bagani, K., Jetter, D., Marchiori, E., Vervelaki, A., Gross, B., Ridderbos, J., Gliga, S., Schönenberger, C., and Poggio, M., **Magnetic, Ther-**

- mal, and Topographic Imaging with a Nanometer-Scale SQUID-On-Lever Scanning Probe. *Physical Review Applied* **17**, 034002 (2022)
- [23] De Simoni, G., Paolucci, F., Solinas, P., Strambini, E., and Giazotto, F., **Metallic superconducting field-effect transistor**. *Nature Nanotechnology* **13**, 802-805 (2018)
- [24] Paolucci, F., De Simoni, G., Strambini, E., Solinas, P., and Giazotto, F., **Ultra-Efficient Superconducting Dayem Bridge Field-Effect Transistor**. *Nano Letters* **18**, 4195-4199 (2018)
- [25] Vijay, R., Levenson-Falk, E. M., Slichter, D. H., and Siddiqi, I., **Approaching ideal weak link behavior with three dimensional aluminum nanobridges**. *Applied Physics Letters* **96**, 223112 (2010)
- [26] Kennedy, O. W., Burnett, J., Fenton, J. C., Constantino, N. G. N., Warburton, P. A., Morton, J. J. L., and Dupont-Ferrier, E., **Tunable Nb superconducting resonator based on a constriction nano-SQUID fabricated with a Ne focused ion beam**. *Physical Review Applied* **11**, 014006 (2019)
- [27] Uhl, K., Hackenbeck, D., Peter, J., Kleiner, R., Koelle, D., and Bothner, D., **Niobium Quantum Interference Microwave Circuits with Monolithic Three-Dimensional (3D) Nanobridge Junctions**. arXiv:2305.16276 (2023)
- [28] Hatridge, M., Vijay, R., Slichter, D. H., Clarke, J., and Siddiqi, I., **Dispersive magnetometry with a quantum limited SQUID parametric amplifier**. *Physical Review B* **83**, 134501 (2011)
- [29] Levenson-Falk, E. M., Antl, N., and Siddiqi, I., **Dispersive nanoSQUID magnetometry**. *Superconductor Science and Technology* **29**, 113003 (2016)
- [30] Rodrigues, I. C., Bothner, D., and Steele, G. A., **Coupling microwave photons to a mechanical resonator using quantum interference**. *Nature Communications* **10**, 5359 (2019)
- [31] Bothner, D., Rodrigues, I. C., and Steele, G. A., **Four-wave-cooling to the single phonon level in Kerr optomechanics**. *Communications Physics* **5**, 33 (2022)
- [32] Bothner, D., Rodrigues, I. C., and Steele, G. A., **Photon-pressure strong coupling between two superconducting circuits**. *Nature Physics* **17**, 85-91 (2021)
- [33] Rodrigues, I. C., Bothner, D., and Steele, G. A., **Cooling photon-pressure circuits into the quantum regime**. *Science Advances* **7**, eabg6653 (2021)
- [34] Xu, M., Cheng, R., Wu, Y., Liu, G., and Tang, H. X., **Magnetic Field-Resilient Quantum-Limited Parametric Amplifier**. *PRX Quantum* **4**, 010322 (2023)
- [35] Schmidt, F. E., Bothner, D., Rodrigues, I. C., Gely, M. F., Jenkins, M. D., and Steele, G. A., **Current Detection Using a Josephson Parametric Upconverter**. *Physical Review Applied* **14**, 024069 (2020)
- [36] Rieger, D., Günzler, S., Spiecker, M., Paluch, P., Winkel, P., Hahn, L., Hohmann, J. K., Bacher, A., Wernsdorfer, W., and Pop, I. M., **Granular aluminum nanojunction fluxonium qubit**. *Nature Materials* **22**, 194-199 (2023)
- [37] Rifkin, R. and Deaver, Jr., B. S., **Current-phase relation and phase-dependent conductance of superconducting point contacts from rf impedance measurements**. *Physical Review B* **13**, 3894 (1976)
- [38] Schmidt, F. E., Jenkins, M. D., Watanabe, K., Taniguchi, T., and Steele, G. A., **Probing the current-phase relation of graphene Josephson junctions using microwave measurements**. arXiv:2007.09795 (2020)
- [39] Dou, Z., Wakamura, T., Virtanen, P., Wu, N.-J., Deblock, R., Autier-Laurent, S., Watanabe, K., Taniguchi, T., Gueron, S., Bouchiat, H., and Ferrier, M., **Microwave photoassisted dissipation and supercurrent of a phase-biased graphene-superconductor ring**. *Physical Review Research* **3**, L032009 (2021)
- [40] Haller, R., Fülöp, G., Indolese, D., Ridderbos, J., Kraft, R., Cheung, L. Y., Ungerer, J. H., Watanabe, K., Taniguchi, T., Beckmann, D., Danneau, R., Virtanen, P., and Schönenberger, C., **Phase-dependent microwave response of a graphene Josephson junction**. *Physical Review Research* **4**, 013198 (2022)
- [41] Bosman, S. J., Singh, V., Bruno, A., and Steele, G. A., **Broadband architecture for galvanically accessible superconducting microwave resonators**. *Applied Physics Letters* **107**, 192602 (2015)
- [42] Blonder, G. E., Tinkham, M., and Klapwijk, T. M., **Transition from metallic to tunneling regimes in superconducting microconstrictions: Excess current, charge imbalance, and supercurrent conversion**. *Physical Review B* **25**, 4515 (1982)
- [43] Tinkham, M., Free, J. U., Lau, C. N., and Markovic, N., **Hysteretic  $I - V$  curves of superconducting nanowires**. *Physical Review B* **68**, 134515 (2003)
- [44] Troeman, A. G. P., van der Ploeg, S. H. W., Il'ichev, E., Meyer, H.-G., Golubov, A. A., Kupriyanov, M. Yu., and Hilgenkamp, H., **Temperature dependence measurements of the supercurrent-phase relationship in niobium nanobridges**. *Physical Review B* **77**, 024509 (2008)
- [45] Wang, Y., Chen, L., Pan, Y., Zhang, D., Yu, S., Wu, G., Liu, X., Wu, L., Shi, W., Zhang, G., Zhang, L., Peng, W., Ren, J., and Wang, Z., **Geometric Scaling of the Current-Phase Relation of Niobium Nanobridge Junctions**. *ACS Nano* **17**, 15466-15473 (2023)
- [46] Pekker, D., Shah, N., Sahu, M., Bezryadin, A., and Goldbart, P. M., **Stochastic dynamics of phase-slip trains and superconductive-resistive switching in current-biased nanowires**. *Physical Review B* **80**, 214525 (2009)
- [47] Li, P., Wu, P. M., Bonze, Y., Borzenets, I. V., Finkelstein, G., and Chang, A. M., **Switching Currents Limited by Single Phase Slips in One-Dimensional Superconducting Al Nanowires**. *Physical Review Letters* **107**, 137004 (2011)
- [48] Baumans, X. D. A., Zharinov, V. S., Raymenants, E., Blanco Alvarez, S., Scheerder, J. E., Brisbois, J., Massarotti, D., Caruso, R., Tafuri, F., Janssens, E., Moshchalkov, V. V., Van de Vondel, J., and Silhanek, A. V., **Statistics of localized phase slips in tunable width planar point contacts**. *Scientific Reports* **7**, 44569 (2017)
- [49] Friedrich, F., Winkel, P., Borisov, K., Seeger, H., Sürgers, C., Pop, I. M., and Wernsdorfer, W., **Onset of phase diffusion in high kinetic inductance granular aluminum micro-SQUIDS**. *Superconductor Science and Technology* **32**, 125008 (2019)
- [50] Troeman, A. G. P., Derking, H., Borger, B., Pleikies, J., Veldhuis, D., and Hilgenkamp, H., **NanoSQUIDS Based on Niobium Constrictions**. *Nano Letters* **7**, 2152-2156 (2007)
- [51] Frattini, N. E., Sivak, V. V., Lingenfelter, A., Shankar, S., and Devoret, M. H., **Optimizing the Nonlinearity and Dissipation of a SNAIL Parametric Amplifier for Dynamic Range**. *Physical Review Applied* **10**, 054020 (2017)

- (2018)
- [52] Gely, M. F., Sanz Mora, A., Yanai, S., van der Spek, R., Bothner, D., and Steele, G. A., **Apparent nonlinear damping triggered by quantum fluctuations**. *Nature Communications* **14**, 7566 (2023)
  - [53] Rodrigues, I. C., Steele, G. A., and Bothner, D., **Parametrically enhanced interactions and nonreciprocal bath dynamics in a photon-pressure Kerr amplifier**. *Science Advances* **8**, eabq1690 (2022)
  - [54] Koops, M. C., van Duyneveldt, G. V., and de Bruyn Ouboter, R., **Direct Observation of the Current-Phase Relation of an Adjustable Superconducting Point Contact**. *Physical Review Letters* **77**, 2542 (1996)
  - [55] Della Rocca, M. L., Chauvin, M., Huard, B., Pothier, H., Esteve, D., and Urbina, C., **Measurement of the Current-Phase Relation of Superconducting Atomic Contacts**. *Physical Review Letters* **99**, 127005 (2007)
  - [56] Nanda, G., Aguilera-Servin, J. L., Rakyta, P., Kormanyos, A., Kleiner, R., Koelle, D., Watanabe, K., Taniguchi, T., Vandersypen, L. M. K., and Goswami, S., **Current-Phase Relation of Ballistic Graphene Josephson Junctions**. *Nano Letters* **417**, 3396-3401 (2017)

#### Acknowledgements

The authors thank Markus Turad, Ronny Löffler (both LISA<sup>+</sup>) and Christoph Back for technical support. This research was supported by the Deutsche Forschungsgemeinschaft (DFG) via grant numbers BO 6068/1-1, BO 6068/2-1 and KO 1303/13-2. We also gratefully acknowledge support by the COST actions NANOCOHYBRI (CA16218) and SUPERQUMAP (CA21144).

#### Data and code availability

All data and processing scripts presented in this paper will be available via zenodo upon publication of this work.

#### Competing interest

The authors declare no competing interests.

**Supplementary Material for:**  
**Extracting the current-phase-relation of a monolithic three-dimensional nano-constriction using a DC-current-tunable superconducting microwave cavity**

K. Uhl *et al.*

**CONTENTS**

I. Supplementary Note I: Device fabrication	15
II. Supplementary Note II: Measurement setup	15
III. Supplementary Note III: The cavity model without constrictions	17
A. Bare transmission line resonator	17
B. Shunt-coupled transmission line resonator	18
C. Circuit parameters and measurements	18
IV. Supplementary Note IV: The cavity model with constrictions	21
A. The nano-constriction: Potential, current-phase-relation and inductance	21
B. Shunt-coupled transmission line resonator with nano-constriction	22
C. Getting the CPR from the constriction inductance	23
D. Kerr anharmonicity of the circuit	24
V. Supplementary Note V: Circuit response model	25
A. Equation of motion and general considerations	25
B. The linear single-tone regime	26
C. The nonlinear single-tone regime	26
VI. Supplementary Note VI: $S$ -parameter background correction and fitting	27
A. The real-world reflection function and fit-based background correction	27
B. Data-based background correction	28
VII. Supplementary Note VII: Additional data and analyses	28
A. Properties of the superconducting niobium film	28
B. Impact of junction cutting to a reference cavity and constriction parameter uncertainty	29
C. Bias current-tuning curves of $\omega_0$ and constriction inductance $L_c$ for all sample temperatures	30
D. Internal linewidth $\kappa_i$ and resistance $R_c$ vs bias current and temperature	32
E. The ratio $I_{sw}/I_0$ and comparison with SQUID circuits	34
VIII. Supplementary Note VIII: Additional data and theory for the extraction of the Kerr constant	35
A. Observation of cavity response nonlinearities and fits in the weakly nonlinear regime	35
B. Construction of an artificial CPR	37
IX. Supplementary References	38

## I. SUPPLEMENTARY NOTE I: DEVICE FABRICATION

- **Step 1: Microwave cavity patterning.**

The fabrication starts with sputtering 90-nm-thick niobium (Nb) on top of a high-resistivity ( $\rho > 10\text{ k}\Omega\cdot\text{m}$ ) intrinsic two inch silicon wafer. The thickness of the wafer is  $\sim 500\ \mu\text{m}$ . Then, the complete wafer is covered with ma-P 1205 photoresist by spin-coating (resist thickness  $\sim 600\ \text{nm}$ ) and structured by means of maskless scanning laser photolithography ( $\lambda_{\text{Laser}} = 365\ \text{nm}$ ). After development of the resist in ma-D 331/S for 25 s, the Nb film is dry etched by means of reactive ion etching using  $\text{SF}_6$ . For cleaning, the wafer gets finally rinsed in multiple subsequent baths of acetone and isopropanol.

- **Step 2: Dielectric layer for the shunt capacitor.**

As a second step, we again perform maskless scanning laser photolithography to define the areas on the chip, which will be covered with the dielectric for the parallel plate input shunt capacitor of the cavity. After resist development identical to step 1, the wafer with the patterned resist structures is placed inside the vacuum chamber of a plasma-enhanced chemical vapour deposition (PECVD) system and is covered with 150 nm of silicon-nitride ( $\text{Si}_3\text{N}_4$ ). Afterwards an ultrasonic-assisted lift-off procedure is performed in acetone, which removes the resist and all the  $\text{Si}_3\text{N}_4$  except for the ellipsoidal plates on the parallel plate shunt capacitors, cf. Fig. 1 of the main paper. Finally, the wafer is rinsed in multiple baths of acetone and isopropanol again.

- **Step 3: Superconducting shunt capacitor top plate.**

The third step is fully equivalent to step 2, but instead of PECVD-grown  $\text{Si}_3\text{N}_4$ , a 70 nm thick layer of niobium is deposited by magnetron sputtering. After liftoff in acetone, this second Nb layer is only covering the dielectric ellipse of the shunt capacitor and is removed at all other locations. To avoid getting shorts between the first and second niobium layers at the edge of the capacitor, the ellipsoid of the niobium top-layer is smaller than the corresponding  $\text{Si}_3\text{N}_4$  ellipsoid by about  $10\ \mu\text{m}$  along all edges.

- **Step 4: Dicing and mounting for pre-characterization.**

At the end of the cavity fabrication, the wafer gets diced into individual  $10 \times 10\ \text{mm}^2$  chips, and one chip at a time is mounted on a printed circuit board (PCB), where it is wirebonded to microwave feedlines and ground, and packaged in a radiation-tight copper housing. After mounting into the measurement setup, the pre-characterization of the device is performed.

- **Step 5: 3D constriction fabrication.**

Each pre-characterized standing wave cavity contains a narrow part at its far end, where the constriction junction is placed after pre-characterization. To cut the constriction into the  $\sim 3\ \mu\text{m}$  wide bridge, the sample is removed from the PCB and sample box again and mounted into a neon ion microscope (NIM). The NIM allows one to perform high-precision milling with a nano-scaled spot-size focused neon beam (Ne-FIB). The 3D constriction patterning is performed by cutting two  $\sim 25\ \text{nm}$  narrow slot-shaped rectangles from both sides into the bridge, and by additionally and simultaneously milling the constriction from the top with a third rectangle, but with a lower dose. The dose for the cut-through rectangles was chosen to be  $18000\ \text{ions}/\text{nm}^2$  and on top of the constriction the dose was  $6500\ \text{ions}/\text{nm}^2$ . For this dose and an accelerating voltage of 20 kV, we expect a remaining constriction thickness of  $\sim 40\ \text{nm}$ .

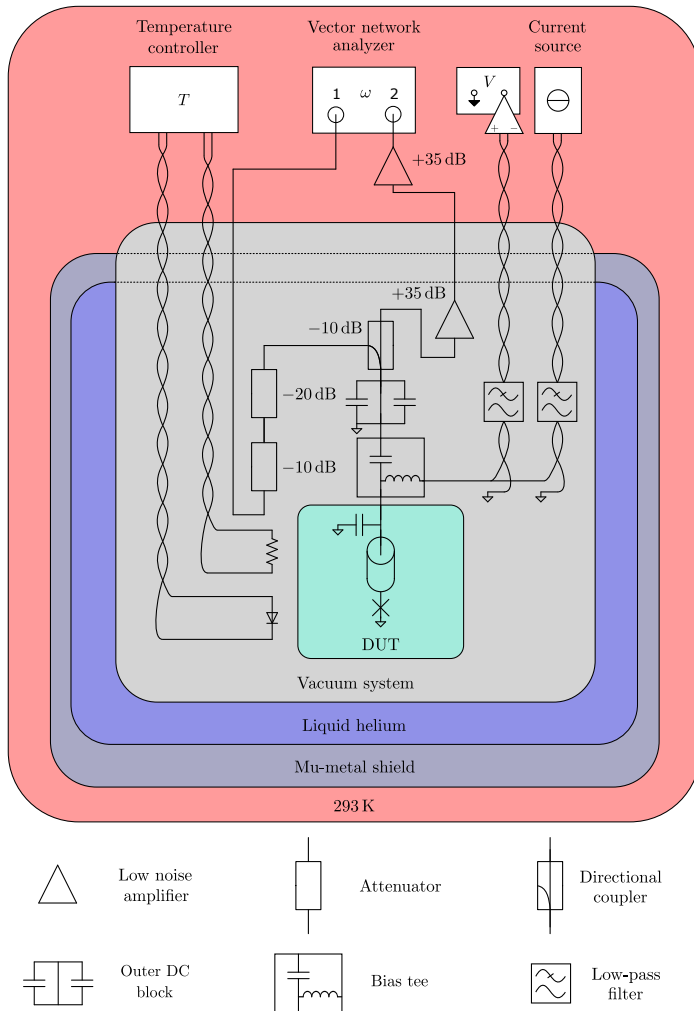
- **Step 6: Dicing and mounting.**

After the Ne-FIB cutting process the sample is mounted in the same way as in Step 4.

## II. SUPPLEMENTARY NOTE II: MEASUREMENT SETUP

A schematic illustration of the measurement setup is shown in Supplementary Fig. 1. Both the junction-less cavity and the cavity with constriction, here generically labeled as device under test (DUT), are characterized in an evacuated sample space located at the end of a cryostat dipstick, which is introduced into a liquid helium bath. The cryostat is surrounded by a double-layer room-temperature mu-metal shield to provide magnetic shielding for the whole sample space. The DUT inside the copper housing is attached to an L-shaped copper mounting bracket, which is screwed to one of two circular mounting plates inside the evacuated sample volume.

The DUT is connected to a single coaxial cable for input and output of the microwave (measured in reflection) and the direct current (DC) signals (combined via bias-tee). The microwave input and output signals, however, are sent and received through two separate coaxial lines, that are only combined via a directional coupler close to the device, in order to measure the reflection  $S_{11}$  as transmission  $S_{21}$  by a vector network analyzer (VNA). This way, the input



Supplementary Figure 1. **Schematic of the measurement setup.** Detailed information is given in the text.

signal can be strongly attenuated without any signal loss on the output line. The input line is attenuated by 30 dB in order to balance the thermal radiation from room temperature to the cryostat temperature. The directional coupler adds another 10 dB of input attenuation, as the input signal enters through the coupled port and the reflected signal propagates straight through it. Including the cables, attenuators, couplers and all other components, we estimate the total attenuation between the VNA output and the device to be  $\sim 53 \pm 1$  dB. The attenuators are mounted in close proximity to the sample in the sample vacuum space and we assume them to have a temperature  $T_{\text{att}} \approx T_s$ , where  $T_s$  is the temperature of the sample. For amplification of the weak microwave signal used here, a cryogenic

high electron mobility transistor (HEMT) amplifier and a room temperature amplifier are mounted to the output line. The cryogenic HEMT is placed close to the DUT in order to minimize signal losses in between the sample and the amplifier chain.

In order to inject the DC current into the cavity and to measure the voltage in a near-ideal four-terminal configuration, a microwave bias-tee is added to the coaxial microwave lines just before the microwave signal reaches the device. The DC port of the bias-tee and the ground are connected to two pairs of twisted copper wires by solder joints, one pair for the current and the other pair to measure the corresponding voltage. Both twisted pairs are low pass filtered close to the microwave bias-tee with a cutoff frequency of  $\sim 1.5$  kHz in order to prevent noise in the kHz to MHz range from entering the device. In order to minimize the low-frequency current and voltage noise entering the device through other channels, a ground-DC block is added in front of the bias-tee, which in combination with the bias-tee and the usage of non-conducting pieces and screws interrupts all galvanic connections between the cryostat/microwave lines and the sample box including the sample. By these measures, we completely separate the cryostat/dipstick ground from the sample ground (the latter being highlighted with the empty triangular ground symbols in Supplementary Fig. 1). The DC electronics are controlled via a National Instruments DAC/ADC measurement card, the current source has a floating ground and the voltage  $V$  is preamplified by a room-temperature low-noise amplifier with a gain of  $10^4$ .

A temperature diode is attached to the sample housing/the mounting bracket in close proximity to the actual sample and both are coupled to the liquid helium bath via the copper mounting bracket and through a small amount of helium exchange gas. For controlling the sample temperature  $T_s$ , the diode is glued with varnish to the DUT copper housing and a manganin heating resistor (made of a twisted pair wire to avoid stray magnetic fields) is placed nearby. Both the temperature diode (4 wires) and the heating resistor (2 wires) are also connected via twisted pairs of copper wire to a temperature controller. For cooling the device to temperatures below that of liquid helium (4.2 K), we pump at the helium dewar of the cryostat and reach down to  $T_{s,\min} \lesssim 2.4$  K. To achieve high-stability temperature control ( $\Delta T_s < 1$  mK) in the most relevant range for this work  $2.4 \text{ K} \lesssim T_s \lesssim 6.5$  K, we use the helium pumping and additionally heat the sample with the heating resistor, whose power is controlled via a PID feedback loop by the temperature controller.

### III. SUPPLEMENTARY NOTE III: THE CAVITY MODEL WITHOUT CONSTRICTIONS

#### A. Bare transmission line resonator

Our device is based on a short-ended half wavelength coplanar waveguide cavity with a characteristic impedance  $Z_1 = 32 \Omega$  and a length of  $l_1 = 7200 \mu\text{m}$ . The complex propagation constant along the transmission line resonator is given by  $\gamma = \alpha + i\beta$  with the attenuation constant  $\alpha$  and the phase constant  $\beta = \omega/v_\phi$ . Here  $\omega$  is the angular frequency of the propagating wave on the line and  $v_\phi = 1/\sqrt{L'C'}$  is the phase velocity, where  $C'$  is the capacitance per unit length and  $L'$  is the total inductance per unit length. Note that  $L'$  has both a geometric contribution  $L'_g$  and a kinetic contribution  $L'_k$  with  $L' = L'_g + L'_k$ . We can deduce the resonance frequency of the fundamental mode (without shunt capacitor and before junction cutting) as  $\omega_1 = \pi v_\phi/l_1$ .

For the input impedance of a short-ended and lossy transmission line at a distance  $l_1$  from its shorted end, we have

$$Z_{\text{in}}^{\text{TL}} = Z_1 \frac{\tanh \alpha l_1 + i \tan \beta l_1}{1 + i \tan \beta l_1 \tanh \alpha l_1} \quad (\text{S1})$$

which for small losses  $\alpha l_1 \ll 1$  and close to its fundamental mode resonance  $\omega \approx \omega_1$  can be Taylor-approximated as

$$Z_{\text{in}}^{\text{TL}} \approx Z_1 \alpha l_1 + i Z_1 \pi \frac{\Delta_1}{\omega_1} \quad (\text{S2})$$

where  $\Delta_1 = \omega - \omega_1$ . When we compare this with the Taylor-approximated input impedance of a series RLC circuit

$$Z_{\text{in}}^{\text{RLC}} \approx R_r + 2iL_r \Delta_1 \quad (\text{S3})$$

we recognize that they actually look identical for

$$R_r = Z_1 \alpha l_1, \quad L_r = \frac{Z_1 \pi}{2\omega_1} = \frac{L'l_1}{2}, \quad C_r = \frac{2}{\pi\omega_1 Z_1} = \frac{2C'l_1}{\pi^2}. \quad (\text{S4})$$

From the lumped element equivalents, we can also now give expressions for the internal linewidth  $\kappa_{i,1}$  and the internal quality factor  $Q_{i,1} = \omega_1/\kappa_{i,1}$  of the resonator. They are given as

$$\kappa_{i,1} = \frac{R_r}{L_r} = \frac{2\omega_1 \alpha l_1}{\pi}, \quad Q_{i,1} = \frac{\pi}{2\alpha l_1}. \quad (\text{S5})$$

### B. Shunt-coupled transmission line resonator

When we couple the short-ended transmission line cavity to a microwave feedline with characteristic impedance  $Z_0$  by means of a shunt capacitor to ground  $C_s$  as in our device, we need to consider a change in total capacitance as well as a splitting of the linewidth and quality factor into internal and external contributions. To do this, we first consider the input impedance of the shunt-capacitor-and-feedline parallel combination as seen from the cavity, which is

$$Z_e = \left( \frac{1}{Z_0} + i\omega C_s \right)^{-1} = \frac{Z_0}{1 + i\omega C_s Z_0}. \quad (\text{S6})$$

We can split this into its real and imaginary part and then write it as a combination of an effective frequency-dependent series combination of a resistor  $R^*$  and capacitor  $C^*$

$$Z_e = \frac{Z_0}{1 + \omega^2 C_s^2 Z_0^2} + \frac{1}{i\omega} \frac{\omega^2 C_s Z_0^2}{1 + \omega^2 C_s^2 Z_0^2} = R^* + \frac{1}{i\omega C^*}. \quad (\text{S7})$$

Next, we perform two approximations by using  $\omega \approx \omega_b$  and  $\omega_b^2 C_s^2 Z_0^2 \gg 1$  and get

$$R^* \approx \frac{1}{\omega_b^2 C_s^2 Z_0}, \quad C^* \approx C_s \quad (\text{S8})$$

which allows us to find the total capacitance

$$C_{\text{tot}} = \frac{C_r C_s}{C_r + C_s}, \quad (\text{S9})$$

the new resonance frequency

$$\omega_b = \frac{1}{\sqrt{L_r C_{\text{tot}}}}, \quad (\text{S10})$$

the coupled resistance

$$R_b = R_r + R^*, \quad (\text{S11})$$

and finally the total linewidth, which we can split into internal and external contributions

$$\begin{aligned} \kappa_b &= \omega_b^2 R_b C_{\text{tot}} \\ &= \omega_b^2 R_r C_{\text{tot}} + \omega_b^2 R^* C_{\text{tot}} \\ &= \frac{\omega_b^2 R_r C_r C_s}{C_r + C_s} + \frac{C_r}{Z_0 C_s (C_r + C_s)} \\ &= \kappa_{i,b} + \kappa_{e,b}. \end{aligned} \quad (\text{S12})$$

The linewidths are related to the corresponding quality factors via  $Q_{i,b} = \omega_b / \kappa_{i,b}$  and  $Q_{e,b} = \omega_b / \kappa_{e,b}$ .

### C. Circuit parameters and measurements

The parameters we need for our circuit are the total capacitance  $C_{\text{tot}}$  and the total inductance  $L_r = L_g + L_k$ , which has a geometric and a kinetic contribution. What makes things more complicated on one hand but also experimentally accessible on the other hand is that the kinetic contributions are dependent on the niobium London penetration depth  $\lambda_L$ , which is a function of sample temperature  $T_s$ .

We start our parameter extraction procedure by calculating the geometric inductance per unit length

$$L'_g = \frac{\mu_0}{4} \frac{K(k'_1)}{K(k_1)}, \quad (\text{S13})$$

where  $\mu_0$  is the vacuum permittivity,  $K(k)$  is the complete elliptic integral of the first kind and

$$k_1 = \frac{S_1}{S_1 + 2W_1}, \quad k'_1 = 1 - k_1^2. \quad (\text{S14})$$

here, the width of the coplanar waveguide center conductor is  $S_1 = 50 \mu\text{m}$  and the gap between ground and center conductor is  $W_1 = 5 \mu\text{m}$ . As result we obtain  $L'_g = 261 \text{ nH/m}$ , a value that we also obtain with less than 1% deviation by numerical simulations. In addition to the geometric inductance we need to take the kinetic inductance into account. The relation between  $\lambda_L$  and the kinetic inductance per unit length is given by [S1]

$$L'_k = \mu_0 g \frac{\lambda_{\text{eff}}}{S_1}, \quad (\text{S15})$$

where  $d_{\text{Nb}}$  is the film thickness,  $g$  is a geometrical, dimensionless factor taking into account the details of the transmission line cavity by [S1, S2]

$$g = \frac{1}{2 [k'_1 K(k_1)]^2} \left[ -\ln\left(\frac{d_{\text{Nb}}}{4S_1}\right) - k_1 \ln\left(\frac{d_{\text{Nb}}}{4(S_1 + 2W_1)}\right) + 2 \frac{S_1 + W_1}{S_1 + 2W_1} \ln\left(\frac{W_1}{S_1 + W_1}\right) \right] \quad (\text{S16})$$

and the effective penetration depth  $\lambda_{\text{eff}}$  of a thin film  $d_{\text{Nb}} \lesssim \lambda_L$  is [S3]

$$\lambda_{\text{eff}} = \lambda_L \coth \frac{d_{\text{Nb}}}{\lambda_L}. \quad (\text{S17})$$

Then the total inductance per unit length is

$$L' = L'_g + \mu_0 g \frac{\lambda_L \coth \frac{d_{\text{Nb}}}{\lambda_L}}{S_1}. \quad (\text{S18})$$

In the experiment, we do not vary directly  $\lambda_L$  but the sample temperatur  $T_s$ , the relation between the two is given by

$$\lambda_L(T_s) = \frac{\lambda_0}{\sqrt{1 - \left(\frac{T_s}{T_c}\right)^4}} \quad (\text{S19})$$

where  $\lambda_0$  is the zero-temperature penetration depth and  $T_c$  is the critical temperature. We measure the cavity resonance frequency  $\omega_b(T_s)$  and fit the experimentally obtained data with

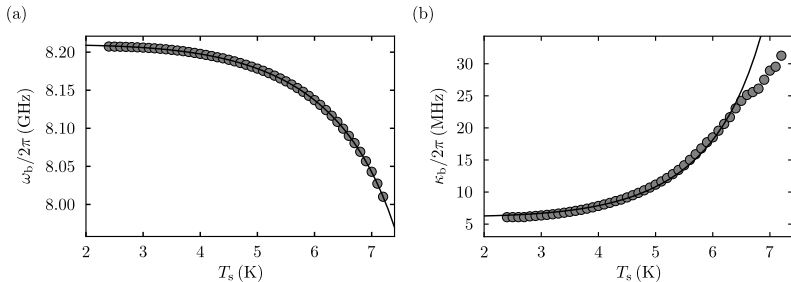
$$\begin{aligned} \omega_b(T_s) &= \frac{1}{\sqrt{C_{\text{tot}} L_r(T_s)}} \\ &= \frac{1}{\sqrt{C_{\text{tot}} \frac{l_1}{2} \left[ L'_g + \frac{\mu_0 g}{S_1} \frac{\lambda_0}{\sqrt{1 - \left(\frac{T_s}{T_c}\right)^4}} \coth \left[ \frac{d_{\text{Nb}}}{\lambda_0} \sqrt{1 - \left(\frac{T_s}{T_c}\right)^4} \right] \right]}} \end{aligned} \quad (\text{S20})$$

with the geometrical parameters  $S_1 = 50 \mu\text{m}$ ,  $W_1 = 5 \mu\text{m}$ ,  $d_{\text{Nb}} = 90 \text{ nm}$ ,  $g = 3.8$ ,  $l_1 = 7200 \text{ nm}$  and  $L'_g = 261 \text{ nH}\cdot\text{m}^{-1}$  as constants and with  $C_{\text{tot}} = 367 \text{ fF}$ ,  $\lambda_0 = 141 \text{ nm}$  and  $T_c = 9.0 \text{ K}$  as fit parameters. The result is shown in Supplementary Fig. 2(a).

The next relevant parameter is the effective shunt capacitance  $C_s$ , which we obtain from measurement of the external linewidth  $\kappa_{e,b} = 2\pi \cdot 6.3 \text{ MHz}$  and the knowledge of  $Z_0 = 50 \Omega$  and  $C_{\text{tot}}$ . By using Eqs. (S9) and (S12) we obtain for the coupling shunt capacitance  $C_s = 17.5 \text{ pF}$  and  $C_r = 375 \text{ fF}$  for the cavity capacitance at  $T_s = 3.9 \text{ K}$ . We can compare this with the theoretical value for  $C_r^{\text{theo}} = 388 \text{ fF}$ , where we used

$$C' = 4\epsilon_0 \epsilon_{\text{eff}} \frac{K(k_1)}{K(k'_1)} \quad (\text{S21})$$

with  $\epsilon_{\text{eff}} = (\epsilon_{\text{Si}} + 1)/2$  and  $\epsilon_{\text{Si}} = 11.5$ , and find reasonable agreement. Similarly, we get for the shunt capacitance  $C_s^{\text{theo}} = 12.4 \text{ pF}$ , which we obtain by calculating  $C_{s1}^{\text{theo}} = \epsilon_0 \epsilon_{\text{SiN}} A_1 / d_{\text{SiN}} = 24.9 \text{ pF}$  and  $C_{s2}^{\text{theo}} = \epsilon_0 \epsilon_{\text{SiN}} A_2 / d_{\text{SiN}} = 24.9 \text{ pF}$ . Here, we used  $\epsilon_{\text{SiN}} = 7$ ,  $A_1 = 0.06 \text{ mm}^2$ ,  $A_2 = 0.06 \text{ mm}^2$  and  $d_{\text{SiN}} = 150 \text{ nm}$ . The two capacitances  $C_{s1}^{\text{theo}}$  and  $C_{s2}^{\text{theo}}$  are the capacitances between center conductor and top shunt electrode and between top shunt electrode and the ground planes, respectively, which in series result in  $C_s^{\text{theo}} = C_{s1}^{\text{theo}} C_{s2}^{\text{theo}} / (C_{s1}^{\text{theo}} + C_{s2}^{\text{theo}})$ . Again, we find acceptable agreement, and possible deviations originate most likely from variations in  $d_{\text{SiN}}$  and  $\epsilon_{\text{SiN}}$ , but possibly also from inductive contributions in the shunt capacitor plates or from the feedline input impedance deviating from  $Z_0$  due to cable resonances and parasitic reflections.



Supplementary Figure 2. **Temperature dependence of cavity parameters before junction cutting.** In (a) we show the cavity resonance frequency  $\omega_b$  vs sample temperature  $T_s$ . The shift in frequency with increasing temperature occurs due to a change of the total circuit inductance  $L_r(T_s) = L_g + L_k(T_s)$ . Circles are data, line is a fit using Eq. (S20) and with  $T_c = 9.0$  K,  $C_{tot} = 367$  fF and  $\lambda_0 = 141$  nm as fit parameters. In panel (b), the total circuit linewidth  $\kappa_b/2\pi$  vs  $T_s$  is shown. The linewidth increases with increasing temperature, indicating growing losses by thermal quasiparticles in the superconductor. Circles are data, line is a fit using Eq. (S25) with  $\kappa_{0,b} = 2\pi \cdot 6.2$  MHz and  $A_\kappa = 4.1 \cdot 10^{-15}$  s<sup>3</sup>/m<sup>3</sup> as fit parameter.

In addition to the resonance frequency, we also extract the total resonance linewidth  $\kappa_b$  as a function of temperature, data are shown in Supplementary Fig. 2(b). At the elevated temperatures we are operating here  $T_s \gtrsim T_c/4$ , the internal decay rate will be dominated by quasiparticle losses. From the two-fluid model, the effective surface resistance of a superconductor with the corresponding correction factor for thin films and around the cavity resonance frequency is given by [S3]

$$R_{s,\text{eff}} = \frac{1}{2} \omega_b^2 \mu_0^2 \lambda_L^3 \sigma_n \frac{n_n}{n} \left[ \coth\left(\frac{d_{\text{Nb}}}{\lambda_L}\right) + \frac{d_{\text{Nb}}/\lambda_L}{\sinh^2\left(\frac{d_{\text{Nb}}}{\lambda_L}\right)} \right], \quad (\text{S22})$$

where  $\sigma_n$  is the normal state conductivity,  $n_n$  is the quasiparticle density and  $n = n_n + n_s$  is the total electron density with  $n_s$  being the superconducting charge carrier density (twice the Cooper pair density). The temperature dependence of the quasiparticle density is given by

$$\frac{n_n(T_s)}{n} = \left(\frac{T_s}{T_c}\right)^4. \quad (\text{S23})$$

Since the quasiparticle loss channel is equivalent to the kinetic inductance channel in terms of current density distribution, the resulting circuit model lumped element resistance  $R_r \propto R_{s,\text{eff}}$  is expected to be in series with  $L_r$ . Combining this result with Eq. (S12) we get

$$\begin{aligned} \kappa_{i,b}(T_s) &= \omega_b^2(T_s) R_r(T_s) C_{\text{tot}} \\ &= A_\kappa \omega_b^4(T_s) \lambda_L^3(T_s) \left(\frac{T_s}{T_c}\right)^4 \left[ \coth\left(\frac{d_{\text{Nb}}}{\lambda_L(T_s)}\right) + \frac{d_{\text{Nb}}/\lambda_L(T_s)}{\sinh^2\left(\frac{d_{\text{Nb}}}{\lambda_L(T_s)}\right)} \right] \end{aligned} \quad (\text{S24})$$

with the fit parameter  $A_\kappa$  that contains geometry, material properties and other temperature-independent contributions. Since we are not certain that we can reliably discriminate between  $\kappa_{i,b}$  and  $\kappa_{e,b}$  due to cable resonances and impedance mismatches in the setup leading to Fano interferences, we fit the temperature dependence of the total linewidth using

$$\kappa_b(T_s) = \kappa_{0,b} + \kappa_{i,b}(T_s) \quad (\text{S25})$$

with  $\kappa_{0,b}$  as second fit parameter. The agreement between the experimental data and the fit line is very good, cf. Supplementary Fig. 2(b), with considerable deviations only appearing for  $T_s \gtrsim 6.5$  K. Note also that the fit value  $\kappa_{0,b} = 2\pi \cdot 6.2$  MHz is very close to  $\kappa_{e,b} = 2\pi \cdot 6.3$  MHz obtained at  $T_s = 3.9$  K.

Supplementary Table I summarizes all relevant cavity parameters before constriction cutting again in a single spot.

Supplementary Table I. **Circuit parameters before cutting the nanobridge junction.** The geometric inductance  $L_g$  is obtained using  $L_g = L'_g l_1/2$ . From a fit to the temperature-dependence of  $\omega_b$  we obtain the zero-temperature penetration depth  $\lambda_0$ , the critical temperature  $T_c$  and the total capacitance  $C_{\text{tot}}$ . Additionally we get the kinetic inductance  $L_k = L'_k l_1/2$  and therefore the circuit inductance  $L_r = L_g + L_k$ . From the measured external linewidth  $\kappa_{e,b}$  we subsequently find the coupling capacitance  $C_s$  and the circuit capacitance  $C_r$ . For completeness we also give  $\kappa_{i,b}$ . All experimental values are given for  $T_s = 3.9$  K.

$l_1$ (nm)	$L_g$ (pH)	$L_k$ (pH)	$L_r$ (pH)	$C_r$ (fF)	$C_s$ (pF)	$C_{\text{tot}}$ (fF)	$\lambda_0$ (nm)	$T_c$ (K)	$\frac{\omega_b}{2\pi}$ (GHz)	$\frac{\kappa_{e,b}}{2\pi}$ (MHz)	$\frac{\kappa_{i,b}}{2\pi}$ (MHz)
7200	939.4	87.4	1026.8	375	17.5	367	141	9	8.199	6.3	1.3

#### IV. SUPPLEMENTARY NOTE IV: THE CAVITY MODEL WITH CONSTRICTIONS

##### A. The nano-constriction: Potential, current-phase-relation and inductance

We model the constriction similar to an ideal Josephson junction by assuming a  $2\pi$ -periodic current-phase-relation (CPR)  $I(\delta)$  and a  $2\pi$ -periodic corresponding potential energy  $E_c(\delta)$ . The relation between the two can be established by

$$E_c(\delta) = \int_0^\delta I(\delta') V(\delta') d\delta'. \quad (\text{S26})$$

With the voltage

$$V(t) = \frac{\Phi_0}{2\pi} \dot{\delta} \quad (\text{S27})$$

this can be written as

$$E_c(\delta) = \frac{\Phi_0}{2\pi} \int I(\delta) d\delta, \quad (\text{S28})$$

i.e., the CPR is essentially the derivative of the potential energy

$$I(\delta) = \frac{2\pi}{\Phi_0} \frac{\partial E_c}{\partial \delta}. \quad (\text{S29})$$

We can Taylor-expand the total potential up to fourth order around the equilibrium phase  $\delta_0$  and get

$$E(\delta) = E_c(\delta_0) + \left. \frac{\partial E_c}{\partial \delta} \right|_{\delta_0} \delta + \frac{1}{2} \left. \frac{\partial^2 E_c}{\partial \delta^2} \right|_{\delta_0} \delta^2 + \frac{1}{6} \left. \frac{\partial^3 E_c}{\partial \delta^3} \right|_{\delta_0} \delta^3 + \frac{1}{24} \left. \frac{\partial^4 E_c}{\partial \delta^4} \right|_{\delta_0} \delta^4 - \frac{\Phi_0 I_b}{2\pi} \delta \quad (\text{S30})$$

where we also included a tilt of the potential  $E_c$  by the bias current  $I_b$  and where  $\delta$  (kept the same for simplicity) is the new dynamical variable around the equilibrium phase  $\delta_0$ . For very small  $\delta$ , we can drop the third and fourth order terms as well as the constant offset and get

$$E(\delta) \approx \left. \frac{\partial E_c}{\partial \delta} \right|_{\delta_0} \delta + \frac{1}{2} \left. \frac{\partial^2 E_c}{\partial \delta^2} \right|_{\delta_0} \delta^2 - \frac{\Phi_0 I_b}{2\pi} \delta. \quad (\text{S31})$$

From here we find the equilibrium position  $\delta_0$  from the condition  $\partial E/\partial \delta = 0$ , i.e., by

$$\left. \frac{\partial E_c}{\partial \delta} \right|_{\delta_0} = \frac{\Phi_0 I_b}{2\pi} \quad (\text{S32})$$

or

$$I(\delta_0) = I_b. \quad (\text{S33})$$

Using the generalized flux  $\Phi = \frac{\Phi_0}{2\pi} \delta$ , we can write the last remaining term in the potential as an inductive energy

$$E_c(\Phi) \approx \frac{\Phi^2}{2L_c} \quad (\text{S34})$$

with the constriction inductance

$$L_c = \frac{\Phi_0^2}{4\pi^2} \left( \frac{\partial^2 E_c}{\partial \delta^2} \Big|_{\delta_0} \right)^{-1}. \quad (\text{S35})$$

In the next subsection, we will discuss how to model the overall cavity when including this inductance as well as a corresponding resistor, then how to reconstruct the CPR from the measurement of  $L_c$  for different  $I_b$ , and finally we will discuss the consequences of the higher order terms to the high-power dynamics of the resonator.

### B. Shunt-coupled transmission line resonator with nano-constriction

We observe that cutting the constrictions into the circuit leads to a shift of the resonance frequency and to a broadening of the resonance linewidth. Similar to the two-fluid model and following our considerations in the previous subsection, we therefore model the circuit elements introduced by the junction for low powers as a constriction inductance  $L_c$  in parallel with a constriction resistance  $R_c$ . We note that we omit any additional capacitance, as according to our simulations the impedance of a possible constriction capacitance is negligible compared to its inductance impedance. For the parallel combination of  $R_c$  and  $L_c$  near the relevant frequency  $\omega_0$ , we get the input impedance

$$\begin{aligned} Z_c &= \frac{i\omega L_c R_c}{R_c + i\omega L_c} \\ &\approx \frac{R_c \omega_0^2 L_c^2}{R_c^2 + \omega_0^2 L_c^2} + i\omega \frac{L_c R_c^2}{R_c^2 + \omega_0^2 L_c^2} \\ &= R_c^* + i\omega L_c^*. \end{aligned} \quad (\text{S36})$$

Unfortunately, we cannot do any approximation here, as a priori we cannot assume anything for the ratio  $\omega_0 L_c / R_c$ . However, adding these new series elements to the circuit, we get the final resonator elements

$$R_{\text{tot}} = R_r + R^* + R_c^* \quad (\text{S37})$$

$$L_{\text{tot}} = L_r + L_c^* \quad (\text{S38})$$

$$C_{\text{tot}} = \frac{C_r C_s}{C_r + C_s}. \quad (\text{S39})$$

and we can express the final resonance frequency as

$$\begin{aligned} \omega_0 &= \frac{1}{\sqrt{C_{\text{tot}}(L_r + L_c^*)}} \\ &\approx \frac{\omega_b}{1 + \frac{L_c^*}{2L_r}} \end{aligned} \quad (\text{S40})$$

where the approximation is valid for  $L_c^* \ll L_r$ , a condition safely fulfilled in our device.

For the linewidth we find

$$\begin{aligned} \kappa_0 &= \omega_0^2 R_{\text{tot}} C_{\text{tot}} \\ &= \omega_0^2 R_r C_{\text{tot}} + \omega_0^2 R_c^* C_{\text{tot}} + \omega_0^2 R^* C_{\text{tot}} \\ &= \kappa_i + \kappa_e. \end{aligned} \quad (\text{S41})$$

where

$$\kappa_i = \omega_0^2 R_r C_{\text{tot}} + \omega_0^2 R_c^* C_{\text{tot}} \quad (\text{S42})$$

contains also the junction contribution from  $R_c$ .

An alternative route to finding expressions for  $\omega_0$  and  $\kappa_i$  starts with equalizing the input impedances of the transmission line resonator at the point of the constriction and the input impedance of the cJJ

$$Z_1 \alpha_1 + i Z_1 \tan \beta l_1 = -R_c^* - i\omega L_c^* \quad (\text{S43})$$

where the minus signs on the right hand side stem from the opposite current directions in the two parts. When we use our expressions for  $R_r$  and  $L_r$  and Taylor-expand the tangent function around the first mode, we obtain

$$R_r + i \frac{2L_r \omega_1}{\pi} (\beta l_1 - \pi) = -R_c^* - i\omega L_c^*. \quad (\text{S44})$$

Now we use  $\beta = \omega/v_\phi$  and look for a complex-valued solution for  $\omega$ , that we call  $\tilde{\omega}_0 = \omega_0 + i \frac{\kappa_i}{2}$ . We get

$$\tilde{\omega}_0 = \frac{\omega_1}{1 + \frac{L_c^*}{2L_r}} + i \frac{R_r + R_c^*}{2L_r + L_c^*}. \quad (\text{S45})$$

This is equivalent to

$$\omega_0 = \frac{\omega_1}{1 + \frac{L_c^*}{2L_r}} \quad (\text{S46})$$

$$\kappa_i = \frac{R_r + R_c^*}{L_r + L_c^*/2} \quad (\text{S47})$$

which is slightly different from our earlier obtained lumped element expression, since we did not take the shunt capacitance into account and that it leads to a shift from  $\omega_1$  to  $\omega_b$  already. If we replace the constriction-less resonance frequency  $\omega_1$  by  $\omega_b$ , though, we get for the resonance frequency the above result

$$\omega_0 = \frac{\omega_b}{1 + \frac{L_c^*}{2L_r}}. \quad (\text{S48})$$

The deviation in  $\kappa_i$  is given by the ratio  $(L_r + L_c^*)/(L_r + L_c^*/2)$ , which is one the order of  $\omega_b/\omega_0 \lesssim 1.01$ .

### C. Getting the CPR from the constriction inductance

Based on our above considerations, we can use that the second derivative of the potential is the first derivative of the CPR

$$\frac{\partial^2 E_c}{\partial \delta^2} = \frac{\Phi_0}{2\pi} \frac{\partial I}{\partial \delta} \quad (\text{S49})$$

and insert this into our equation for the constriction inductance

$$L_c = \frac{\Phi_0}{2\pi} \left( \frac{\partial I}{\partial \delta} \Big|_{\delta_0} \right)^{-1}. \quad (\text{S50})$$

So once we know the constriction inductance  $L_c$  for each bias current and corresponding equilibrium phase, we can invert this relation to get

$$\delta = \frac{2\pi}{\Phi_0} \int_0^{I_b} L_c dI + \delta_{\text{off}}. \quad (\text{S51})$$

We assume the offset phase  $\delta_{\text{off}} = 0$ . In practice, we have a finite number of points and do

$$\delta_j = \frac{2\pi}{\Phi_0} \sum_j^N L_{c,j} \Delta I. \quad (\text{S52})$$

instead with  $j > 0$ ,  $N$  the total number of bias-current values and  $\Delta I = I_{b,j} - I_{b,j-1}$ . Finally, we can plot pairwise values for  $(\delta_j, I_{b,j})$ , i.e., the experimentally determined CPR.

#### D. Kerr anharmonicity of the circuit

So far, we have neglected the third and fourth order terms of the Taylor series of  $E_c$ . We will now derive the resulting Kerr constant  $\mathcal{K}$  in two different ways. In one derivation, we will not make any assumptions about the shape of the CPR, except that it is  $2\pi$ -periodic and single-valued. In the second derivation further below, we will assume the constriction to be a series combination of a linear inductance and an ideal Josephson inductance with a sinusoidal CPR. Both derivations lead to the same  $\mathcal{K}$  here.

In the first derivation, we start by assuming that the potential can be described by a prefactor  $E_J$  multiplied by a  $2\pi$ -periodic function. Then, we can write the Taylor series as

$$\frac{E(\delta)}{E_J} = \bar{g}_0 + \bar{g}_1\delta + \frac{1}{2}\bar{g}_2\delta^2 + \frac{1}{6}\bar{g}_3\delta^3 + \frac{1}{24}\bar{g}_4\delta^4 - \frac{\Phi_0 I_b}{2\pi E_J}\delta \quad (\text{S53})$$

where the coefficients are given by

$$\bar{g}_n = \frac{1}{E_J} \left. \frac{\partial^n E_c}{\partial \delta^n} \right|_{\delta_0}. \quad (\text{S54})$$

Of course, we can also write the coefficients for  $n > 0$  as

$$\bar{g}_n = \frac{\Phi_0}{2\pi E_J} \left. \frac{\partial^{n-1} I}{\partial \delta^{n-1}} \right|_{\delta_0}, \quad (\text{S55})$$

which gives a much more direct relation to the CPR. The minimum phase is determined by  $\bar{g}_1 = \frac{\Phi_0 I_b}{2\pi E_J}$ , or just by  $I(\delta_0) = I_b$ . We can also obtain  $\delta_0$  experimentally as described above for the reconstruction of the CPR, when we just integrate up to  $I_b$ .

Taking also into account the additional linear inductance of the cavity  $L_r$  and following Ref. [S4] now, we find that we need to define a total phase variable  $\delta_{\text{tot}}$ , that describes the phase across the series combination of  $L_r$  and the constriction. With the linear inductive energy  $E_L = \frac{\Phi_0^2}{4\pi^2 L_r}$ , the total inductive energy is given by

$$E_{\text{tot}}(\delta_{\text{tot}}, \delta) = \frac{1}{2}E_L(\delta_{\text{tot}} - \delta)^2 + E_c(\delta) - \frac{\Phi_0 I_b}{2\pi}\delta_{\text{tot}}. \quad (\text{S56})$$

From the condition  $\partial E_{\text{tot}}/\partial \delta = 0$  we find the current-conservation condition [S4]

$$0 = E_L(\delta - \delta_{\text{tot}}) + \frac{\partial E_c}{\partial \delta} \quad (\text{S57})$$

which defines  $\delta$  as a function of  $\delta_{\text{tot}}$ , i.e.,  $\delta[\delta_{\text{tot}}]$ . This function allows us to calculate the derivative now

$$\frac{\partial \delta}{\partial \delta_{\text{tot}}} = \frac{E_L}{E_L + \frac{\partial^2 E_c}{\partial \delta^2}} \quad (\text{S58})$$

as well as the corresponding higher order derivatives  $\partial^2 \delta / \partial \delta_{\text{tot}}^2$  and  $\partial^3 \delta / \partial \delta_{\text{tot}}^3$ .

Similarly to above, we now Taylor-expand the total potential as

$$\frac{E_{\text{tot}}(\delta_{\text{tot}})}{E_J} = \tilde{G}_0 + \tilde{G}_1\delta_{\text{tot}} + \frac{1}{2}\tilde{G}_2\delta_{\text{tot}}^2 + \frac{1}{6}\tilde{G}_3\delta_{\text{tot}}^3 + \frac{1}{24}\tilde{G}_4\delta_{\text{tot}}^4 - \frac{\Phi_0 I_b}{2\pi E_J}\delta_{\text{tot}} \quad (\text{S59})$$

where the new coefficients (for  $n \geq 2$ ) are given by

$$\tilde{G}_2 = \frac{E_L}{E_J} \left( 1 - \frac{\partial \delta}{\partial \delta_{\text{tot}}} \right) \quad (\text{S60})$$

$$\tilde{G}_3 = -\frac{E_L}{E_J} \frac{\partial^2 \delta}{\partial \delta_{\text{tot}}^2} \quad (\text{S61})$$

$$\tilde{G}_4 = -\frac{E_L}{E_J} \frac{\partial^3 \delta}{\partial \delta_{\text{tot}}^3} \quad (\text{S62})$$

After some algebra and using

$$p_c = \frac{L_c}{L_r + L_c} \quad (\text{S63})$$

we find that the coefficients can be expressed as

$$\tilde{G}_2 = p_c \tilde{g}_2 \quad (\text{S64})$$

$$\tilde{G}_3 = p_c^3 \tilde{g}_3 \quad (\text{S65})$$

$$\tilde{G}_4 = p_c^4 \left[ \tilde{g}_4 - \frac{3\tilde{g}_3^2}{\tilde{g}_2} (1 - p_c) \right] \quad (\text{S66})$$

and that the Kerr constant in the end is given by [S4]

$$\mathcal{K} = \frac{e^2}{2\hbar C_{\text{tot}}} p_c^3 \left[ \frac{\tilde{g}_4}{\tilde{g}_2} - \frac{3\tilde{g}_3^2}{\tilde{g}_2^2} (1 - p_c) - \frac{5}{3} \frac{\tilde{g}_3^2}{\tilde{g}_2^2} p_c \right]. \quad (\text{S67})$$

In order to make the very close connection to the system CPR obvious again, we define new coefficients in terms of the CPR  $I(\delta)$  as

$$g_2 = \frac{\partial I}{\partial \delta} \quad (\text{S68})$$

$$g_3 = \frac{\partial^2 I}{\partial \delta^2} \quad (\text{S69})$$

$$g_4 = \frac{\partial^3 I}{\partial \delta^3}. \quad (\text{S70})$$

These are connected to the previous coefficients by  $g_n = 2\pi E_J \tilde{g}_n / \Phi_0$  and lead to the Kerr constant

$$\mathcal{K} = \frac{e^2}{2\hbar C_{\text{tot}}} p_c^3 \left[ \frac{g_4}{g_2} - \frac{3g_3^2}{g_2^2} (1 - p_c) - \frac{5}{3} \frac{g_3^2}{g_2^2} p_c \right]. \quad (\text{S71})$$

In the second variant we split the constriction inductance into a linear part  $L_{\text{lin}}$  and the Josephson part  $L_J$ . As phase variables we consider the phase  $\delta_J$  across the Josephson part  $L_J$  with a sinusoidal CPR  $I = I_0 \sin \delta_J$  and the total phase  $\delta_{\text{tot}}$ . The total linear inductance is the given by  $L'_t = L_t + L_{\text{lin}}$ . The equilibrium phase is given by

$$\delta_{J,0} = \arcsin \frac{I_b}{I_0} \quad (\text{S72})$$

and the Josephson energy by  $E_J = \frac{\Phi_0 I_0}{2\pi}$ . With the modified coefficients

$$c_n = \frac{1}{E_J} \left. \frac{\partial^n E_{\text{cos}}}{\partial \delta_J^n} \right|_{\delta_{J,0}} \quad (\text{S73})$$

and  $E_{\text{cos}} = E_J (1 - \cos \delta_J)$  we follow the same derivation steps as above and find the Kerr constant as

$$\mathcal{K} = \frac{e^2}{2\hbar C_{\text{tot}}} p_J^3 \left[ \frac{c_4}{c_2} - \frac{3c_3^2}{c_2^2} (1 - p_J) - \frac{5}{3} \frac{c_3^2}{c_2^2} p_J \right] \quad (\text{S74})$$

where

$$p_J = \frac{L_J}{L'_t + L_J}, \quad L_J = \frac{\Phi_0}{2\pi I_0 \cos \delta_{J,0}}. \quad (\text{S75})$$

## V. SUPPLEMENTARY NOTE V: CIRCUIT RESPONSE MODEL

### A. Equation of motion and general considerations

We model the classical intracavity field  $\alpha$  of the constriction cavity with effective Kerr nonlinearity and nonlinear damping using the equation of motion [S5]

$$\dot{\alpha} = \left[ i(\omega_c + \mathcal{K}|\alpha|^2) - \frac{\kappa + \kappa_{\text{nl}}|\alpha|^2}{2} \right] \alpha + i\sqrt{\kappa_c} S_{\text{in}}. \quad (\text{S76})$$

Here,  $\omega_c$  is the cavity resonance frequency ( $= \omega_b$  before cutting and  $= \omega_0$  after),  $\mathcal{K}$  is the Kerr nonlinearity (frequency shift per photon),  $\kappa$  is the bare total linewidth ( $= \kappa_b$  before cutting and  $= \kappa_0$  after),  $\kappa_{nl}$  is the nonlinear damping constant,  $\kappa_e$  is the external linewidth ( $= \kappa_{e,b}$  before cutting) and  $S_{in}$  is the input field. The intracavity field is normalized such that  $|\alpha|^2 = n_c$  corresponds to the intracavity photon number  $n_c$  and  $|S_{in}|^2$  to the input photon flux (photons per second) on the coplanar waveguide feedline. We do not explicitly take into account the third order nonlinearity here, but the nonlinear frequency shift that results from its existence is contained in  $\mathcal{K}$  as described above.

The solution of this equation of motion depends significantly on the input power. The ideal reflection response function, however, will always be of the form

$$S_{11}^{\text{ideal}} = -1 - i\sqrt{\kappa_e} \frac{\alpha}{S_{in}} \quad (S77)$$

with the solution of interest  $\alpha$ .

### B. The linear single-tone regime

In the linear single-tone regime, valid for low microwave-probing powers, we set  $\mathcal{K} = \kappa_{nl} = 0$ . Then, we can solve the remaining equation by Fourier transform and obtain

$$\alpha = \frac{i\sqrt{\kappa_e}}{\frac{\kappa}{2} + i(\omega - \omega_c)} S_{in}. \quad (S78)$$

The ideal reflection response is then given by

$$S_{11}^{\text{ideal}} = -1 + \frac{2\kappa_e}{\kappa + 2i(\omega - \omega_c)}. \quad (S79)$$

### C. The nonlinear single-tone regime

In the nonlinear single-tone regime, we have to solve the full equation of motion and start by setting the input field to  $S_{in} = S_0 e^{i\phi} e^{i\omega t}$  with real-valued  $S_0$ . For the intracavity field, we make the Ansatz  $\alpha(t) = \alpha_0 e^{i\omega t}$  with real-valued  $\alpha_0$ . The phase delay between input and response is fully encoded in  $\phi$ . Then the equation of motion reads

$$i\omega\alpha_0 = \left[ i(\omega_c + \mathcal{K}\alpha_0^2) - \frac{\kappa + \kappa_{nl}\alpha_0^2}{2} \right] \alpha_0 + i\sqrt{\kappa_e} S_0 e^{i\phi} \quad (S80)$$

which after multiplication with its complex conjugate yields the characteristic polynomial for the intracircuit photon number  $n_c = \alpha_0^2$

$$n_c^3 \left[ \mathcal{K}^2 + \frac{\kappa_{nl}^2}{4} \right] + n_c^2 \left[ \frac{\kappa\kappa_{nl}}{2} - 2\mathcal{K}\Delta \right] + n_c \left[ \Delta^2 + \frac{\kappa^2}{4} \right] - \kappa_e S_0^2 = 0. \quad (S81)$$

Here  $\Delta = \omega - \omega_c$  is the detuning between the microwave input tone and the bare cavity resonance. The real-valued roots of this polynomial correspond to the physical solutions for the amplitude  $\alpha_0$ , the highest and lowest amplitudes are the stable states in the case of three real-valued roots.

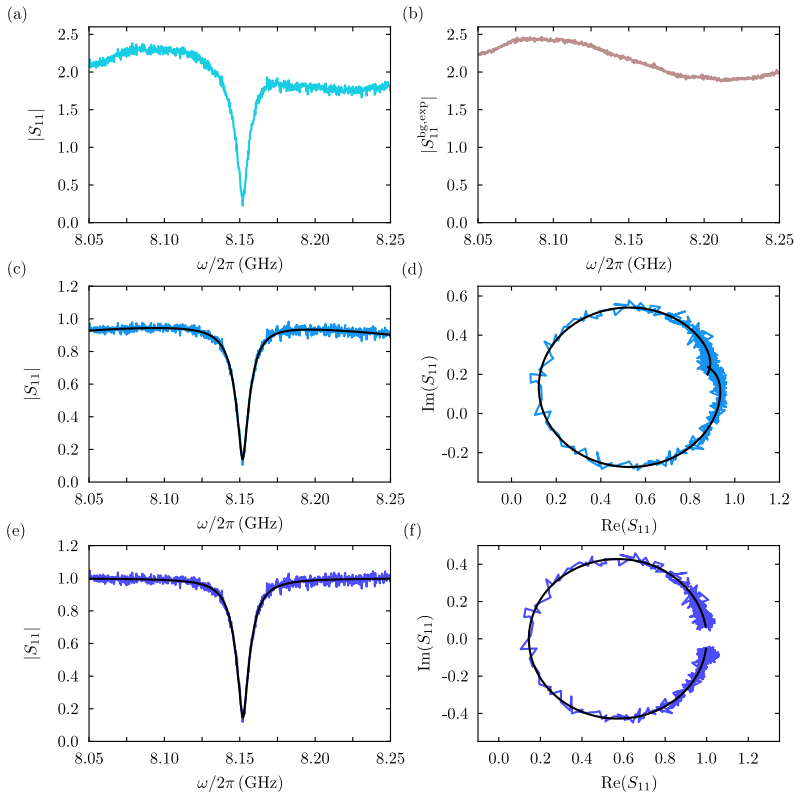
For the complete complex reflection, we also need the phase  $\phi$ , which we obtain via

$$\phi = \text{atan2} \left( -\frac{\kappa + \kappa_{nl}n_c}{2}, \Delta - \mathcal{K}n_c \right) \quad (S82)$$

Having both parts of the complex field solution at hand, we can also calculate the reflection

$$\begin{aligned} S_{11, \text{nl}}^{\text{ideal}} &= -1 - i\sqrt{\kappa_e} \frac{\alpha}{S_{in}} \\ &= -1 - i\sqrt{\kappa_e} \frac{\alpha_0}{S_0} e^{-i\phi}. \end{aligned} \quad (S83)$$

We use this equation to fit the nonlinear response curves in the higher-power regime, from which we determine the Kerr nonlinearity, cf. Fig. 5 of the main paper and Supplementary Note VIII.



Supplementary Figure 3. **Background correction and fitting routine.** (a) Reflection  $|S_{11}|$  vs probe frequency of the constriction cavity for a current bias value  $I_b = 0$ . The absorption resonance dip around 8.15 GHz is clearly visible, the measurement temperature is  $T_s = 3.9$  K. (b) Identical to (a), but at an elevated temperature  $T_s = 8.1$  K. What we detect here is the experimental background  $S_{11}^{\text{bg,exp}}$ , slightly modified by temperature-dependent signal propagation on the chip and in the coldest parts of the microwave cables. We measure not only the amplitude, but also the phase of  $S_{11}$  and  $S_{11}^{\text{bg,exp}}$ . (c) shows the magnitude of  $S_{11}/S_{11}^{\text{bg,exp}}$ , the background is nearly a flat line, but not yet at  $|S_{11}| = 1$  as expected for an ideal reflection. (d) shows the imaginary part of the background-divided reflection vs the real part. Noisy light blue lines in (c) and (d) are data, black smooth lines are a fit with Eq. (S84). (e) and (f) show the final background-corrected data, where also the remaining background from the fit is divided off and the resonance circle is corrected by the Fano rotation  $\theta$ . Noisy blue lines in (e) and (f) are data, black smooth lines are the fits.

## VI. SUPPLEMENTARY NOTE VI: S-PARAMETER BACKGROUND CORRECTION AND FITTING

### A. The real-world reflection function and fit-based background correction

Due to impedance imperfections in both, the input and output lines, the ideal response is modified by cable resonances and interferences within the setup [S6, S7]. Origin of these imperfections are connectors, attenuators, wirebonds, transitions to or from the PCB etc. in the signal lines. In addition, the cabling has a frequency-dependent attenuation. To take all these modifications into account, we model the final reflection parameter  $S_{11}^{\text{real}}$  by

$$S_{11}^{\text{real}} = (a_0 + a_1\omega + a_2\omega^2) [-1 + f(\omega)e^{i\theta}] e^{i(\phi_0 + \phi_1\omega)} \quad (\text{S84})$$

when the ideal response would be given by

$$S_{11}^{\text{ideal}} = -1 + f(\omega). \quad (\text{S85})$$

The real-valued numbers  $a_0, a_1, a_2, \phi_0, \phi_1$  describe a frequency dependent modification of the background reflection, and the phase factor  $\theta$  takes into account possible interferences such as parasitic reflection just before the device or interferences from e.g. imperfect isolation in the directional coupler.

Our standard fitting routine begins with removing the actual resonance signal from the measured  $S_{11}$ , leaving us with a gapped background reflection, which we fit using

$$S_{11}^{\text{bg}} = (a_0 + a_1\omega + a_2\omega^2) e^{i(\phi_0 + \phi_1\omega)}. \quad (\text{S86})$$

Subsequently, we remove this background function from all measurement traces by complex division. The resonance circle rotation angle  $\theta$  is then rotated off additionally. The result of both corrections is what we present as background-corrected data or reflection/response data in all figures. For the power dependence measurements, we determine the background from the measurement in the linear regime and perform a background correction based on that single linear response line for all powers.

### B. Data-based background correction

As the cavity in our experiment has a rather large linewidth of tens of MHz and as the background reflection often cannot be described over such a large frequency span with a simple second order polynomial as suggested by Eq. (S84), we perform a two-step background correction to obtain as clean  $S$ -parameters as possible. The procedure is exemplarily shown for one resonance of the constriction cavity in Supplementary Fig. 3.

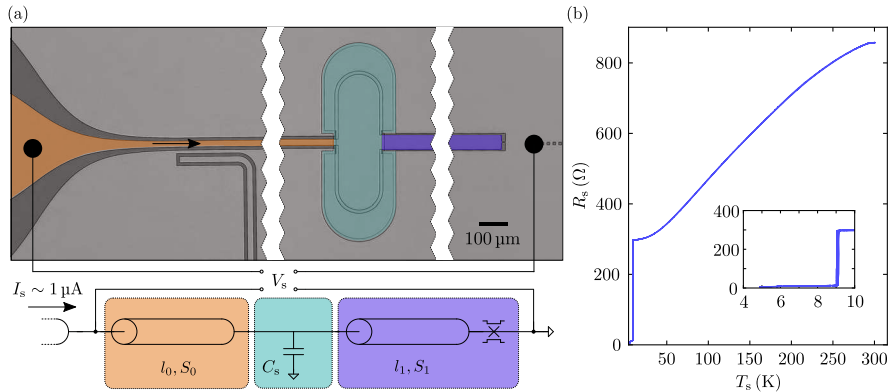
In the first step, we record for each measurement (e.g. the one in panel (a)) also the resonance-less reflection function as shown in panel (b). The resonance-less  $S_{11}$  is obtained by increasing the sample temperature to about  $T_s = 8.1$  K, where the resonance frequency is out of the measurement window and  $\kappa_i$  is so large that the resonance is not impacting the data anymore. The elevated temperature leads to a slight upshift of the overall background, but since its frequency-dependence is not modified and since we perform a second-step-correction, this is not impacting the final result. Then we perform a complex division of the full  $S_{11}$  signal by the bare background signal  $S_{11}^{\text{bg,exp}}$ , the result is a resonance with a nearly flat background as shown in (c), the complex-valued version can be seen in (d). Subsequently, we perform a fit using Eq. (S84) from which we obtain a second background function as well as a Fano rotation angle  $\theta$ . We divide off the fit-background, again by complex division, and finally rotate the resonance circle by  $\theta$  around its anchor point. The final result including the corresponding fits can be seen in panels (e) and (f). For the circuits with constrictions, we perform this data processing with all  $S_{11}$  spectra used for the data analysis and all shown resonances have been treated this way. For the data before constriction cutting, we do only the fit-based background-correction.

## VII. SUPPLEMENTARY NOTE VII: ADDITIONAL DATA AND ANALYSES

### A. Properties of the superconducting niobium film

For analyzing the characteristics of the niobium film additionally from transport data, the complete feedline-plus-cavity resistance  $R_c$  is tracked via a DC 4-point measurement, while slowly changing the sample temperature  $T_s$  between room temperature and  $\sim 5$  K. The resistance  $R_s = V_s/I_s$  is obtained by sending a current  $I_s = 1 \mu\text{A}$  and by measuring the corresponding voltage  $V_s$ . For the 4-point measurement, two wirebonds are attached to the microwave launcher of the cavity feedline and two are attached to the ground plane near the end of the cavity, where also the constriction is placed. One pair is sending the current and the second pair is detecting the voltage. The experiment is conducted in a separate dipstick with a stepper motor, that is slowly immersing the sample into liquid helium.

Supplementary Fig. 4 shows a schematic of the DC measurement and the resulting resistance  $R_s(T_s)$ . We find a sudden and large drop of  $R_s$  at the critical temperature of the niobium film  $T_{c,4p} = 9.08 \pm 0.04$  K, which is in a good agreement with the result obtained from the microwave data in Supplementary Note III C. The remaining resistance for  $T_s < T_{c,4p}$  is attributed to the residual resistance of the constriction, which has a considerably reduced transition temperature  $T_{cc}$ . The fact that there is not a second sharp step in the resistance at  $T_s \approx T_{cc}$  indicates that there might be a wider  $T_{cc}$ -distribution in and around the constriction, possibly induced by ion implantation or surface damage.



Supplementary Figure 4. **Temperature dependence of film resistance.** (a) Schematic of the experiment; top: false-color optical images, bottom: circuit equivalent. By implementing a four-probe measurement we measure the voltage  $V_s$  across the whole feedline-cavity center conductor when sending a current  $I_s = 1 \mu\text{A}$  for varying sample temperature  $T_s$ . The feedline has a length  $l_0$  and a cross-section  $A_0 = S_0 d_{\text{Nb}}$ ; the cavity has the length  $l_1$  and the cross-section  $A_1 = S_1 d_{\text{Nb}}$ . The circuit is slowly moving into a helium bath for changing the temperature  $T_c$  and measuring the voltage after every 0.005 s. (b) Resistance  $R_s = V_s/I_s$  vs temperature  $T_s$ . We obtain a critical temperature  $T_{c,4p} = 9.08 \pm 0.04$  K, a resistance  $R_s(10\text{ K}) = 297.6 \Omega$  at 10 K, a resistance  $R_{c,4p}(8.9\text{ K}) = 12.8 \Omega$  and a residual film resistivity  $\rho = 7.3 \mu\Omega\text{-cm}$ , see main text for more details. Inset shows a zoom-in to temperatures around and below the superconducting transition.

To evaluate the film properties further, we calculate the resistance drop at  $T_{c,4p}$  as  $R_{\text{Nb}} = R_s(T_s = 10\text{ K}) - R_s(T_s = 8.9\text{ K}) \approx 284.8 \Omega$ . The residual resistivity of the film at  $T_s = 10\text{ K}$  (without constriction) is then determined by

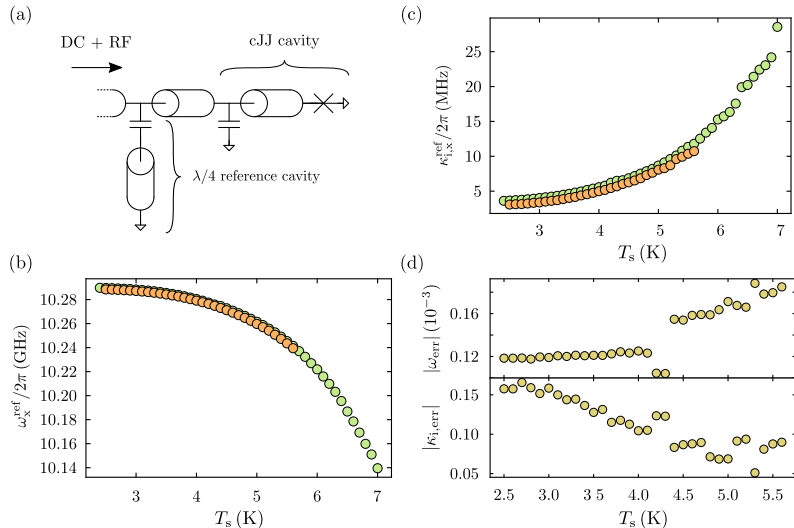
$$\rho = \frac{d_{\text{Nb}} R_{\text{Nb}}}{\left(\frac{l_1}{S_1} + \frac{l_0}{S_0}\right)}, \quad (\text{S87})$$

where  $l_1 = 7200 \mu\text{m}$  and  $S_1 = 50 \mu\text{m}$  are length and center conductor width, respectively, of the cavity, and where  $l_0 = 4416 \mu\text{m}$  and  $S_0 = 20 \mu\text{m}$  are the corresponding values of the feedline. We obtain  $\rho = 7.3 \mu\Omega\text{-cm}$ . In addition, we estimate the electron mean free path  $l_e = 5.7\text{ nm}$  using the material constant  $\rho l_e = 3.72 \cdot 10^{-6} \mu\Omega\text{-cm}^2$  [88]. This shows, that our films are well-described by the so-called dirty limit, where  $l_e \ll \xi_0$  with the BCS coherence length  $\xi_0 = 38\text{ nm}$ .

## B. Impact of junction cutting to a reference cavity and constriction parameter uncertainty

In main paper Fig. 1(e), we present the resonances of the transmission line cavity before and after cutting the nano-constrictions and discuss their impact on the cavity at  $T_s = 3.9\text{ K}$ . In fact, for all our data regarding the constriction inductance and current-phase-relation, the knowledge of the cavity parameters before cutting  $\omega_b, \kappa_b, L_T, C_s$  is crucial. The reliable determination of the junction properties therefore requires that the niobium film itself or the bare cavity are not impacted by the ion-beam-cutting procedure and by exposing the chip to air, nitrogen atmosphere and room-temperature vacuum for some time (on the order of hours to days). Otherwise for instance the kinetic inductance might change between the two measurements, which would impact the apparent junction properties extracted from the comparison of  $\omega_b, \kappa_b$  and  $\omega_0, \kappa_0$ .

In order to estimate the impact of the additional nano-patterning step to the unirradiated parts of the niobium film as precisely as possible, we add a  $\lambda/4$  reference resonator with higher resonance frequency than the constriction-cavity to the same feedline, cf. Supplementary Fig 5(a). The coupler of the hanger-type  $\lambda/4$ -cavity can also be seen in the optical image in the top left part of Supplementary Fig. 4. The reference cavity is capacitively side-coupled with  $\kappa_{c,x}^{\text{ref}} \lesssim 2\pi \cdot 0.9\text{ MHz}$  ( $x$  stands for 'b' or '0', i.e., indicates whether before and after cutting) to the transmission line and it is shorted to ground at the opposite end, forming a  $\lambda/4$  transmission line cavity. Similar to the constriction-cavity, we characterize the reference cavity before and after constriction cutting, although it does not contain any



Supplementary Figure 5. **Side-coupled  $\lambda/4$  reference-resonator properties before and after the neon-ion-beam process.** (a) Circuit equivalent of the complete feedline and cavities, including the side-coupled  $\lambda/4$  reference cavity and the transmission line cavity with cJJ at the end. The reflection of both cavities is measured with a vector network analyzer. (b) shows the resonance frequency  $\omega_x^{\text{ref}}$  of the  $\lambda/4$  reference cavity before and after cJJ cutting (into the cJJ cavity only) vs temperature. Green circles are before cutting and orange after. In panel (c) the internal linewidth of the  $\lambda/4$  reference cavity  $\kappa_{i,x}^{\text{ref}}/2\pi$  vs temperature is shown. Color of datapoints is equivalent to (b). In (d) we show the normalized change of the resonance frequency  $|\omega_{\text{err}}| = |(\omega_0^{\text{ref}} - \omega_b^{\text{ref}})/\omega_b^{\text{ref}}|$  and of the internal linewidth  $|\kappa_{i,\text{err}}| = |(\kappa_i^{\text{ref}} - \kappa_{i,b}^{\text{ref}})/\kappa_{i,b}^{\text{ref}}|$  vs temperature in the range of  $2.5 \text{ K} \leq T_s \leq 5.6 \text{ K}$ .

constrictions. Except for the Ne ion irradiation, it has experienced the same environments as the constriction-cavity and we can estimate the uncertainty in constriction-cavity parameters from its property changes.

In Supplementary Fig. 5(b)-(d) we discuss how resonance frequency and internal linewidth of the reference cavity changed between the two measurements for several temperatures. The resonance frequency has shifted by  $\Delta\omega^{\text{ref}} = \omega_0^{\text{ref}} - \omega_b^{\text{ref}} \lesssim -2\pi \cdot 1.1 \text{ MHz}$  to lower frequencies. The total linewidth and therefore the internal linewidth has decreased by  $\Delta\kappa_i^{\text{ref}} = \kappa_i^{\text{ref}} - \kappa_{i,b}^{\text{ref}} \lesssim -2\pi \cdot 0.6 \text{ MHz}$ . The knowledge of these slight changes allows us to estimate an analog inaccuracy for the resonance frequency and linewidth of the cJJ cavity before cutting. To do so, we introduce the normalized deviation of the frequency as  $|\omega_{\text{err}}| = |(\omega_0^{\text{ref}} - \omega_b^{\text{ref}})/\omega_b^{\text{ref}}| \leq 0.19 \cdot 10^{-3}$  and of the internal linewidth as  $|\kappa_{i,\text{err}}| = |(\kappa_i^{\text{ref}} - \kappa_{i,b}^{\text{ref}})/\kappa_{i,b}^{\text{ref}}| \leq 0.17$ . Although the exact numbers depend on the temperature, we take the maximum value as upper threshold for all temperatures and integrate it into our analysis of the constriction properties. To be more precise, we assume, that the parameters before cutting are given by

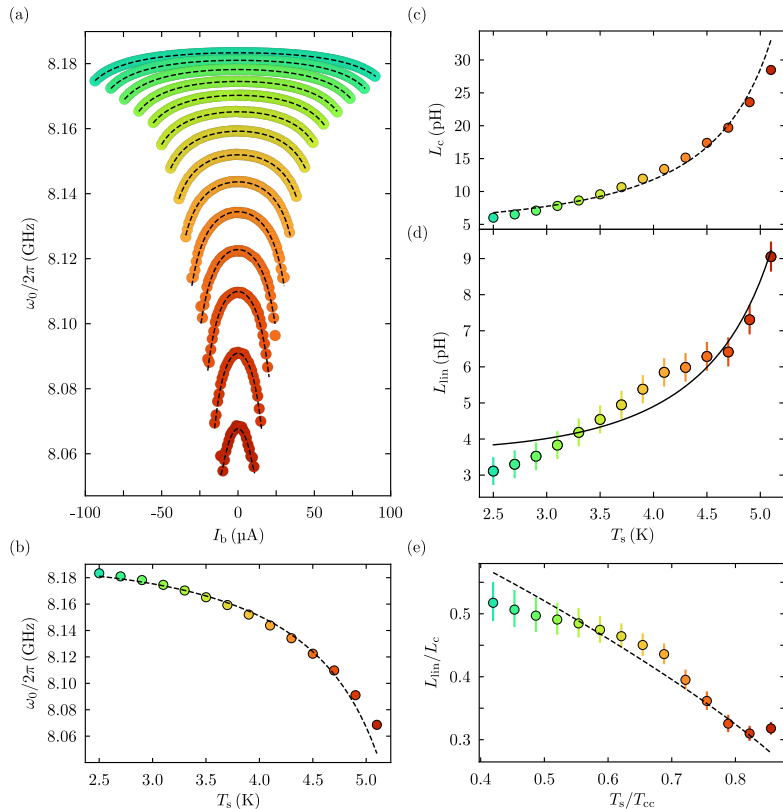
$$\omega_{b,\text{err}} = \omega_b (1 \pm |\omega_{\text{err}}|) \quad (\text{S88})$$

$$\kappa_{i,b,\text{err}} = \kappa_{i,b} (1 \pm |\kappa_{i,\text{err}}|) \quad (\text{S89})$$

and carry these errors through the data analysis and parameter extraction. This leads to the shaded areas around the constriction inductance shown in main paper Fig. 2(e) and main paper Fig. 4(a), and to the areas around the resistances shown in Supplementary Fig. 7. It also leads to the error bars in the inductances and resistances in Supplementary Figs. 6 and 7. The error is furthermore included in all experimental CPRs, but too small to be visible.

### C. Bias current-tuning curves of $\omega_0$ and constriction inductance $L_c$ for all sample temperatures

In main paper Fig. 2 we show the bias current-tuning curve of the resonance frequency  $\omega_0(I_b)$  for the sample temperature  $T_s = 3.9 \text{ K}$ . For completeness and for additional analyses of the constriction temperature-dependence,



Supplementary Figure 6. **Bias-current tunability of resonance frequency  $\omega_0$  and analysis of constriction inductances vs  $T_s$ .** (a) shows the cavity resonance frequency vs bias current  $\omega_0(I_b)$  for temperatures 2.5 – 5.1 K. Temperature increases from top curve to bottom curve in steps of 0.2 K. In (b) we show the resonance frequency at zero bias current vs temperature  $T_s$ . For (a) and (b), symbols are data and dashed lines are calculated using Eq. (S94) in combination with fit curves of the constriction inductances  $L_c(I_b)$ ,  $L_J(T_s)$  and  $L_{\text{lin}}(T_s)$ . In panel (c) we show  $L_c$  for zero bias current ( $I_b = 0$ ) vs sample temperature. Symbols are data, the dashed theory line is calculated from the individual fits of  $L_{\text{lin}}(T_s)$  and  $I_0(T_s)$ . (d) Linear constriction inductance contribution  $L_{\text{lin}}$  as obtained from the  $L_c(I_b)$ -tuning curve fits vs sample temperature  $T_s$ . Symbols are data, the solid black line is a fit using Eq. (S92) (e) shows the participation ratio of the linear inductance  $L_{\text{lin}}$  to the total constriction inductance  $L_c$  vs reduced temperature  $T_s/T_{cc}$ , demonstrating that with increasing temperature the linear contribution gets less significant, i.e., that the CPR gets less skewed. Symbols are data, the dashed line is calculated from the individual fits of  $L_{\text{lin}}(T_s)$  and  $I_0(T_s)$ .

we present in Supplementary Fig. 6(a) and (b) the bias-current tuning-curves for all measured temperatures and the temperature-dependence of the resonance frequency at zero bias current, respectively.

The resonance frequency at  $I_b = 0$  decreases with increasing  $T_s$ , most dominantly due to the increasing constriction inductance. At the same time, the bias-current tuning range  $\omega_0^{\text{max}} - \omega_0^{\text{min}}$  increases with  $T_s$  until 4.7 K is reached, and decreases again for even higher  $T_s$ . The trend for increasing tuning range with increasing  $T_s$  originates from a larger participation ratio of the constriction inductance with increasing temperature, which is closely related to  $T_{cc} < T_c$ . In other words, the constriction inductance grows faster with absolute temperature than the total inductance of the remaining cavity. The observation that for the highest temperatures the tuning range decreases again is related to the

constriction switching current being more suppressed compared to  $I_0$  when its temperature approaches  $T_{cc}$ , possibly induced by thermal current noise.

For a more quantitative discussion of the constriction inductance, we extract  $L_c$  and the constriction resistance  $R_c$  (which will be discussed in the next subsection) by using the coupled Eqs. (S40) and (S41) and as also described in the main paper. We model the bias-current-dependence by

$$\begin{aligned} L_c(I_b) &= L_{\text{lin}} + L_J \\ &= L_{\text{lin}} + \frac{L_{J0}}{\cos \delta_J} \\ &= L_{\text{lin}} + \frac{\Phi_0}{2\pi\sqrt{I_0^2 - I_b^2}}, \end{aligned} \quad (\text{S90})$$

i.e., by the total inductance being a series combination of an ideal Josephson inductance  $L_J$  with a sinusoidal current-phase-relation (CPR) and a linear inductance  $L_{\text{lin}}$ . Here,  $\delta_J$  is the phase difference across the Josephson element,  $L_{J0} = \Phi_0 \cdot (2\pi I_0)^{-1}$  with  $\Phi_0 \approx 2.068 \cdot 10^{-15} \text{ Tm}^2$  the flux quantum and  $I_0$  the critical current of the junction.

For all temperatures the experimental data can be fitted with high reliability using that simple model, cf. panel (a) in main paper Fig. 4. From the fits to the  $L_c(I_b)$  data for all temperatures we obtain as fit parameters the values for  $L_{\text{lin}}(T_s)$  as well as  $I_0(T_s)$ . The latter is already discussed in the main paper (cf. main paper Fig. 4(c)) and can be well described by

$$I_0(T_s) = I_{c,0} \left(1 - \frac{T_s}{T_{cc}}\right)^{3/2} \quad (\text{S91})$$

in the temperature range relevant here, despite the fact that most likely there is a  $T_{cc}$ -distribution present instead of a single sharp value. The fit parameters are the critical current at zero temperature  $I_{c,0} = 252 \mu\text{A}$  and the constriction critical temperature  $T_{cc} = 6.0 \text{ K}$ . The values for  $L_{\text{lin}}(T_s)$  increase with temperature from about 3 pH at the lowest  $T_s$  to around 9 pH at the highest  $T_s$ . Since the linear contribution is likely a predominantly kinetic inductance (the geometric inductance of a constriction is very small), we model its temperature dependence by

$$L_{\text{lin}}(T_s) = L_{\text{off}} + \frac{L_{\text{lin},0}}{1 - \left(\frac{T_s}{T_{cc}}\right)^4}, \quad (\text{S92})$$

where  $L_{\text{lin},0}$  is the inductance at zero temperature,  $T_{cc}$  is the constriction critical temperature and  $L_{\text{off}}$  a possible temperature-independent offset. Although the data points suggest a more complicated temperature dependence, possibly due to a  $T_{cc}$  distribution in the constriction or to cavity-width fitting errors, the overall trend is described acceptably by this simple model with the fit parameters  $L_{\text{off}} = -1.0 \text{ pH}$  and  $L_{\text{lin},0} = 4.8 \text{ pH}$ . The negative offset is small and most likely does not have a physical meaning. Using the two fits for  $I_0(T_s)$  and  $L_{\text{lin}}(T_s)$ , we can also calculate the expected curves for  $\omega_0(T_s)$ ,  $L_c(T_s)$ , and  $L_{\text{lin}}(T_s)/L_c(T_s)$ , cf. dashed lines in panels (b), (c), and (e), respectively. The latter,  $L_{\text{lin}}/L_c$ , shows a clear trend for a decrease with increasing temperature, indicating again that the CPR gets less skewed with increasing  $T_s$ , cf. also main paper Fig. 4. The calculation of  $L_c(I_b, T_s)$  and  $\omega_0(I_b, T_s)$  is done via

$$L_c(I_b, T_s) = L_{\text{lin}}(T_s) + \frac{\Phi_0}{2\pi\sqrt{I_0(T_s)^2 - I_b^2}} \quad (\text{S93})$$

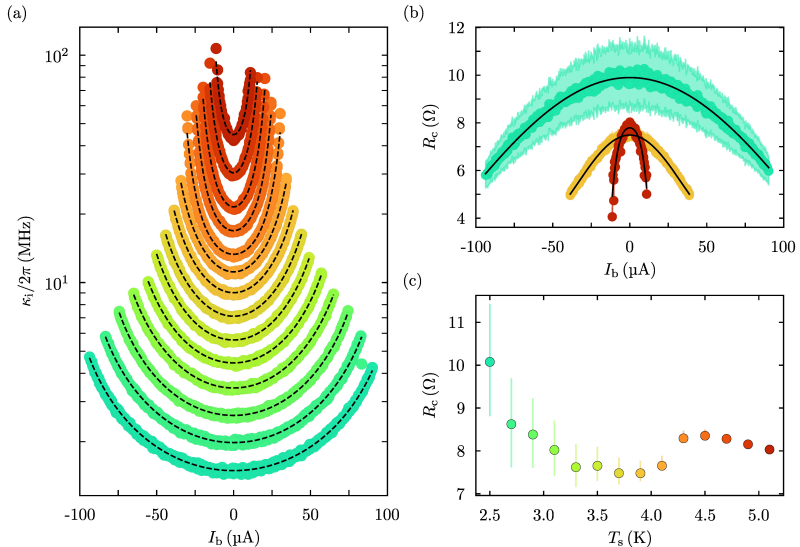
and

$$\begin{aligned} \omega_0(I_b, T_s) &= \frac{\omega_b(T_s)}{\sqrt{1 + \frac{L_c(I_b, T_s)}{2L_r(T_s)}}} \\ &= \frac{1}{C_{\text{tot}}L_r(T_s)} \frac{1}{\sqrt{1 + L_{\text{lin}}(T_s) + \frac{L_{J0}}{\sqrt{I_0(T_s)^2 - I_b^2}} \frac{1}{2L_r(T_s)}}} \end{aligned} \quad (\text{S94})$$

where in the latter we used the approximation  $R_J \gg \omega_b L_J$ , i.e.,  $L_c \approx L_c^*$ .

#### D. Internal linewidth $\kappa_i$ and resistance $R_c$ vs bias current and temperature

In main paper Fig. 4(a) we show the bias current-tuning curves of the cJJ inductance  $L_c$  for varying sample temperature  $T_s$ . For the determination of  $L_c$  we use the coupled Eqs. (S40) and (S41). Therefore, we obtain also



Supplementary Figure 7. **Internal linewidth  $\kappa_i$  and resistance  $R_c$  for varying bias current and sample temperatures.** (a) Internal linewidth  $\kappa_i$  vs bias current  $I_b$  for all measurement temperatures  $T_s$  in the range from 2.5 K to 5.1 K. Points are data and dashed lines are calculated theory lines using Eq. (S96). In panel (b) the constriction resistance  $R_c$  vs bias current for three different temperatures  $T_s = (2.5, 3.9, 5.1)$  K is shown. Points are data and the solid black lines are fits using Eq. (S95). In (c) we show  $R_c$  at zero bias current vs temperature  $T_s$ . Points are data. The uncertainties in (a)-(c), shown as shaded areas and error bars, respectively, are related to the uncertainties in  $\kappa_{i,b}$  and  $\omega_b$ , cf. Supplementary Note VII B.

the constriction resistance  $R_c$  from the microwave behaviour by considering the internal linewidth  $\kappa_i$ . The internal linewidth for all  $I_b$  and  $T_s$  is shown in Supplementary Fig. 7(a). The device shows a strong dependence of  $\kappa_i$  on both  $I_b$  and  $T_s$ , and increases with both. The linewidth tuning range follows similar trends as the resonance frequency equivalent and grows with increasing temperature. At the lowest temperature, the circuit has a linewidth tuning range of  $\sim 3$  MHz, which increases up to  $\sim 65$  MHz for highest  $T_s$ . We believe the increase of internal loss rate with both bias current and temperature is related to a locally reduced superconducting energy gap and therefore to an increased quasiparticle density in the constriction, mainly due to a reduced critical temperature compared to the rest of the niobium film. It will be interesting to analyze the losses at much lower temperatures in future experiments, since currently we do not have a solid model to understand the temperature and bias current dependence of  $\kappa_i$ .

How does this dependence translate to the constriction resistance  $R_c(I_b, T_s)$  now? Some examples for its bias-current-dependence  $R_c(I_b)$  are shown in Supplementary Fig. 7(b), the values change by about 3 – 4  $\Omega$ , interestingly nearly independent of temperature. The temperature only modifies moderately the zero-bias-current value of  $R_c$  and the bias current required for a certain change. In panel (c) we show the slight variations of  $R_c$  at zero bias current as a function of temperature, all values are between 10  $\Omega$  and 7.5  $\Omega$  with more of an oscillating behaviour than a strong trend towards decreasing or increasing. The values are close to the resistances  $R_{dc}$  measured in the IV-characteristics and have a deviation of  $(R_{dc} - R_c)/R_{dc} \sim 0.02 - 0.38$ .

As an easy approach to obtain a function for  $\kappa_i(I_b)$ , we fit the resistance with a polynomial

$$R_c(I_b) = R_0 + R_1 I_b^2 + R_2 I_b^4 \quad (\text{S95})$$

with  $R_0$ ,  $R_1$  and  $R_2$  as fit parameter. The bias-current-dependent internal linewidth can then be written as

$$\kappa_i(I_b) = \kappa_{i,b} + \frac{R_c(I_b)\omega_b^2 L_c(I_b)^2}{R_c(I_b)^2 + \omega_b^2 L_c(I_b)^2} C_{\text{tot}} \left( \frac{\omega_b}{1 + \frac{L_c(I_b)R_c(I_b)^2}{R_c(I_b)^2 + \omega_b^2 L_c(I_b)^2} \frac{1}{2L_r}} \right)^2, \quad (\text{S96})$$

where  $L_c(I_b)$  is the constriction inductance,  $\omega_b$  is the frequency before cutting,  $C_{\text{tot}}$  is the total cavity capacitance and  $L_r$  is the linear inductance of the cavity without the constriction. The curves we obtain from this agree very well with the experimental data, cf. dashed lines in Supplementary Fig. 7. The inaccuracy in  $R_c$  is due to the inaccuracy of  $\kappa_{i,b}$  obtained from analyzing the reference cavity before and after cutting with NIM as described in Supplementary Note VIII B.

### E. The ratio $I_{\text{sw}}/I_0$ and comparison with SQUID circuits

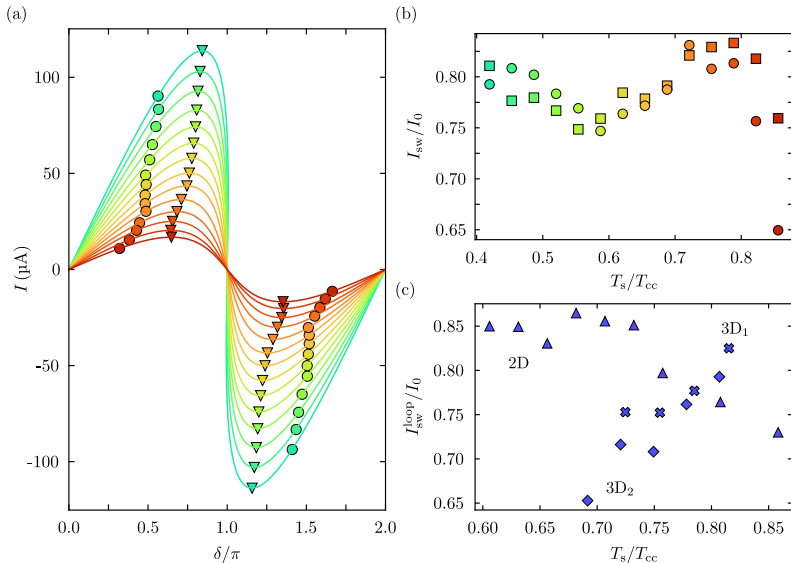
To (piecewise) calculate the theoretical curves for the linear-plus-sinusoidal CPRs as shown in main paper Figs. 3 and 4, we use the total phase  $\delta$  as function of the current  $I \leq I_0$

$$\begin{aligned} \delta &= \delta_J + \delta_{\text{lin}} \\ &= (-1)^n \arcsin\left(\frac{I}{I_0}\right) + \frac{2\pi}{\Phi_0} L_{\text{lin}} I + n\pi. \end{aligned} \quad (\text{S97})$$

and plot the result inverted as  $I(\delta)$ . The corresponding curves for all measurement temperatures relevant in this paper are shown in main paper Fig. 4 and again in Supplementary Fig. 8(a) for further discussions. Note that there are also other ways for plotting the CPR, for instance as numerical derivative of the potential  $E_c(\delta)$ , which leads to exactly the same curves. The measured switching current  $I_{\text{sw}}$  from the IV-characteristics and from the corresponding bias-current-tuning of the resonance frequency deviate both considerably from the (expected) critical current  $I_0$ , that we obtain from the fit of  $L_c(I_b)$ . In Supplementary Fig. 8(a), we added as circles the switching current measured in the microwave experiment and as triangles we highlight the points of  $I = I_0$ . In panel (b) we plot the ratio  $I_{\text{sw}}/I_0$  for both IV-switching-currents and microwave-switching-currents. The two values are very similar, although for the highest temperature there seems to be a deviation and the microwave-switching currents are somewhat lower, possibly due to microwave-activated escape of the phase particle from the potential minimum. For the ratio  $I_{\text{sw}}/I_0$  we find values in the range  $\sim 0.65 - 0.84$  in the reduced-temperature range  $0.42 < T_s/T_{\text{cc}} < 0.86$ . Except for the value obtained at the highest temperature in the microwave experiment, there is not a clear trend towards increasing or decreasing values and the ratio is nearly constant and oscillating around  $\sim 0.8$ . This indicates that most likely constant-amplitude current noise or a thermal current noise (whose amplitude increases with  $T_s$ ) cannot be responsible for the observation of premature switching. Due to this observation we believe that noise by the HEMT, thermal cavity noise, and environmental noise (e.g. 50 Hz noise) are not the culprits.

Interestingly, however, we realized that an almost identical deviation is observable when analyzing the data in Ref. [S9]. In that work, we have investigated microwave circuits with integrated superconducting quantum interference devices (SQUIDs) and with no DC bias-current access. The SQUIDs there are also based on niobium and on neon-ion-beam-patterned nano-constrictions, they even have the same film thickness of  $\sim 90$  nm. Regarding the constrictions, we have investigated three different types in Ref. [S9]. One of the three is a 2D cJJ with thickness equal to the leads (90 nm), and the other two are 3D versions, where the constrictions are thinner than the superconducting leads, similar to the constrictions studied in the present work. The 3D cJJs only differ in the thickness  $\sim 30$  nm (3D<sub>1</sub>) and  $\sim 20$  nm (3D<sub>2</sub>). All three types had a length of  $\sim 20$  nm and a width of  $\sim 40$  nm, i.e., they are very comparable to the one described here. By applying an external magnetic field to the circuits, that introduces magnetic flux into the SQUIDs, the flux-tunability of the resonance frequencies was studied. From a careful analysis of the resulting data, we determined the circulating ring current  $I_{\text{loop}}$  in the SQUID, the switching ring-current  $I_{\text{loop}}^{\text{sw}}$ , where the number of flux quanta in the loop is jumping, and the theoretical critical current  $I_0$  of a single cJJ in the SQUID. We find that  $I_{\text{loop}}^{\text{sw}}/I_0$  for all three SQUID devices lie in the same range as for the single-cJJ device of the current paper. For the 2D-SQUID device, the values seem rather constant at lower  $T_s$  with a tendency to decrease for the higher temperatures. For the 3D-SQUIDs the trend suggests that the ratio is actually increasing with temperature, which would in agreement with the data from the current system. In any case does this similarity in values, but also in trends for the 3D-cJJs, support the idea that the premature switching has an origin in the intrinsic constriction properties rather in external source. It would be highly unlikely that an external noise source would couple equally into both systems.

We believe that the suppressed critical current of the constrictions and therefore the premature switching into the normal state is related to phase slips, and very similar  $I_{\text{sw}}/I_0$  values have been reported by both experiments and theoretical works in the past [S10–S14]. To illuminate the current switching in detail, however, further experiments, e.g. measuring switching statistics for varying current sweep rates and experiments at lower temperatures, will be necessary.



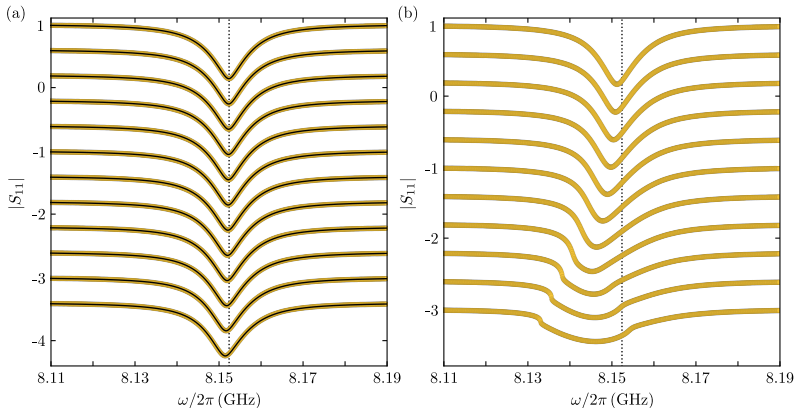
Supplementary Figure 8. **Discussion of  $I_{sw}/I_0$  and a comparison with the same quantity from SQUID circuits.** (a) CPRs for all measurement temperatures  $T_s$ , calculated via  $L_{lin}$  and expected critical current  $I_0$ , for details cf. text. Increasing  $T_s$  corresponds to decreasing  $I_0$  and decreasing forward-skewedness of the CPR, which can be seen from the maximum of the curves  $I_0$  (triangular symbols) shifting to smaller phases. Circles are the switching current  $I_{sw}$  measured by using microwave reflectometry. (b) Ratio of measured switching current to CPR critical current  $I_{sw}/I_0$  using the data from  $\omega_0(I_0)$  (circles) and from IV-characteristics (squares). In panel (c) we show data of  $I_{sw}^{loop}/I_0$ , obtained from experiments with niobium SQUID microwave circuits [S9], where  $I_{sw}^{loop}$  is the maximum circulating ring current in the SQUID loop. The ring current is induced by applying external magnetic flux. Switching loop currents are observed through flux hysteresis jumps of the circuit resonance frequencies, and the  $I_0$  are obtained similarly to here by a linear-plus-sinusoidal inductance model and by fitting the measured resonance-frequency shifts with magnetic field. There are data for three different types of cJJs. The cJJ types are a 2D (thickness  $\sim 90$  nm equal for the leads and cJJ) and two 3D (constriction thinner than the superconducting leads) versions (thicknesses  $\sim 30$  nm for 3D<sub>1</sub> and  $\sim 20$  nm for 3D<sub>2</sub>). Interestingly,  $I_{sw}^{loop}/I_0$  for all three devices lies in the same range as for the device of the present work, although the trends with reduced temperature slightly differ.

## VIII. SUPPLEMENTARY NOTE VIII: ADDITIONAL DATA AND THEORY FOR THE EXTRACTION OF THE KERR CONSTANT

### A. Observation of cavity response nonlinearities and fits in the weakly nonlinear regime

In Supplementary Fig. 9, we show reflection data and corresponding fits of the cavity response around the onset of nonlinearities in (a) and data only for even higher powers in (b). For the determination of the Kerr anharmonicity  $\mathcal{K}$ , we use the reflection data in the weakly nonlinear regime shown in (a), since the data for the higher powers shown in (b) are beyond the validity of our simple nonlinear model. They show features that cannot be reproduced by our theory.

In the weakly nonlinear regime, the resonance minimum shifts slightly to lower values with increasing microwave input power, the total linewidth increases and the resonance shape becomes slightly asymmetric towards the shape of a Duffing resonance. After a background correction, we use Eqs. (S80)-(S83) to fit the data in two steps. In the first step, we fit all curves simultaneously with a single  $\mathcal{K}$ , a single  $\kappa_0$  and a single  $\kappa_{nl}$  as fit parameters. For  $\kappa_e$  and  $\omega_0$  we use a constant average value, which we obtained from multiple resonances below the nonlinear regime, and for  $P_{in}^{av}$  we use the on-chip input power calculated from the VNA output power and the cable attenuation. This first fit gives already a very good agreement with the data. We use a second round of fitting afterwards to improve the



Supplementary Figure 9. **Cavity resonances in the nonlinear regime.** (a) Cavity reflection  $|S_{11}|$  in the weakly nonlinear regime. We define the weakly nonlinear regime as the power range in which the data can be well-described by our model. Input power increases in steps of 1 dB; top curve: lowest power, bottom curve: highest power. Subsequent datasets are offset by  $-0.4$  dB for clarity, colored points are data, black smooth lines are fits. (b) Cavity reflection  $|S_{11}|$  for input powers beyond the weakly nonlinear regime. Data only (no fits), since our model is not able to capture the resonance shapes anymore. Temperature for both panels is  $T_s = 3.9$  K and bias current is  $I_b = 0$ . In (a) and (b) the vertical dotted line shows the resonance frequency in the linear regime

fits of panel (a), in which we allow each individual resonance dataset to have its own  $\kappa_{nl}$ . The result of this second round is shown as lines overlaid to the data in Supplementary Fig. 9(a). Strictly speaking this approach is somehow in contradiction to the model itself, since if the model was completely valid, we would only get a single  $\kappa_{nl}$  for all curves. However, due to the large total cavity linewidth we believe that the background correction is prone to having small frequency-dependent uncertainties, the external linewidth is also not a constant over the complete resonance line since it is frequency-dependent, and there might be other contributions to the nonlinearity of  $\kappa$  and  $\kappa_e$  present at low powers, e.g. due to nonlinear dielectric losses and two-level systems in the shunt capacitor. The resulting  $\kappa_{nl}$  and the injected  $\kappa_e$  are shown in Supplementary Fig. 10. We emphasize, that this second round of fitting is not really necessary and not changing the value of  $\mathcal{K}$ , its purpose is merely to demonstrate that the resonances can be well-explained by a single Kerr constant and power-dependent decay rates, although the exact power-dependence of the decay rates is somewhat obscured when each line gets its own  $\kappa_{nl}$ .

To calculate the possible deviation of the fit parameters due to uncertainties in the on-chip input power, we repeat this procedure for  $P_{in}^{min} = P_{in}^{av} - 1$  dB and  $P_{in}^{max} = P_{in}^{av} + 1$  dB. The resulting values for  $\mathcal{K}_+$  and  $\mathcal{K}_-$  represent the tips of the error bars in main paper Fig. 5. We repeat the same routine for each bias current and obtain the values for  $\mathcal{K}$  (as well as  $\mathcal{K}_+$  and  $\mathcal{K}_-$ ) plotted in main paper Fig. 5. For higher input powers, cf. data in panel (b), we observe that the resonances deviate strongly from Duffing resonances. For this reason we exclude the higher powers from the extraction of  $\mathcal{K}$ .

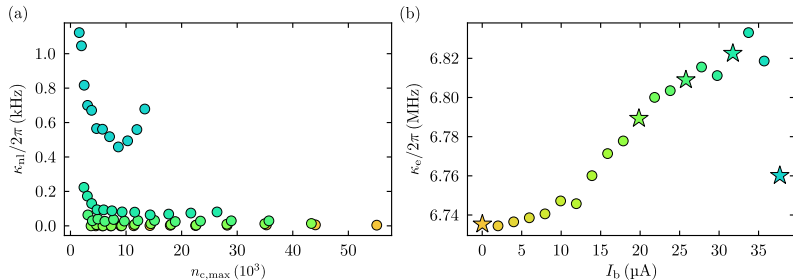
To double-check the results for  $\mathcal{K}$ , that we obtained by this full-model fitting, we also implement a more common and simple routine for finding  $\mathcal{K}$ . We know that within our model the microwave probe tone with frequency  $\omega$  is on the shifted resonance frequency  $\omega'_0$  of the cavity when  $\Delta = \mathcal{K}n_{c,max}$  with  $\Delta = \omega - \omega_0$ . The resonance intracavity photon number  $n_{c,max}$  is the maximum photon number achieved with a constant input power during the frequency sweep at  $\omega'_0$ . Equation (S80) then becomes

$$\frac{\kappa_{eff}}{2} \alpha_{0,max} = i\sqrt{\kappa_e} S_0 e^{i\phi} \quad (S98)$$

with  $\kappa_{eff} = \kappa_0 + \kappa_{nl}n_{c,max}$ . To calculate  $n_{c,max}$ , we then get the magnitude squared of this equation, re-sort some factors and arrive at

$$n_{c,max} = \frac{4P_{in}^{av}}{\hbar\omega} \frac{\kappa_e}{\kappa_{eff}^2}. \quad (S99)$$

The only unknown in this relation is then the effective decay rate  $\kappa_{eff}$ , but we can easily find its value by the reflection response  $S_{11}$  at this particular frequency. It can be calculated from (valid in the effective undercoupled regime



Supplementary Figure 10. **The nonlinear damping and external linewidth of the Kerr fitting.** (a) Nonlinear damping parameter  $\kappa_{nl}$  for 5 different bias-currents (color-coded) and plotted vs the maximum intracavity photon number on resonance, as obtained from the second round of fitting, cf. text. (b) the external linewidth  $\kappa_e$  vs bias-current  $I_b$  used for the nonlinear fits and obtained as average value from multiple resonances in the linear regime. The bias-current-dependence originates most likely from a frequency-dependence  $\kappa_w(\omega)$  and could be explained by parasitic reflections in the setup or by fitting errors due to Fano resonances. The star symbols correspond to the 5 bias currents, that are also displayed in (a).

$$\kappa_e < \kappa_{\text{eff}}/2$$

$$|S_{11}| = 1 - \frac{2\kappa_e}{\kappa_{\text{eff}}}. \quad (\text{S100})$$

without the knowledge of  $\kappa_{nl}$  or  $n_{c,max}$ .

We obtain both  $\delta\omega_0 = \omega'_0 - \omega_0$  and  $\kappa_e/\kappa_{\text{eff}}$  from the data by fitting the resonance minimum with a simple parabola as shown exemplarily in the inset of Supplementary Fig. 11(a). The shifted resonance frequency  $\omega'_0$  is just given by the frequency coordinate of the parabola minimum and the corresponding  $|S_{11}|$  by the corresponding  $y$ -axis value of the minimum. Finally we calculate  $n_{c,max}$ .

We repeat this procedure for all powers at a fixed bias current, and then perform a linear fit of  $\delta\omega_0 = \mathcal{K}n_{c,max}$  with  $\mathcal{K}$  as fit parameter. Doing the same for all bias-currents then gives us the anharmonicity as a function of current. To consider a  $\pm 1$  dB uncertainty in input power, which then translates to an error in the intracavity photon number and finally to an error in anharmonicity, we repeat the same procedure for  $P_{in}^{\text{min}/\text{max}} = P_{in}^{\text{av}} \pm 1$  dB. In Supplementary Fig. 11 we show the result of these fits in comparison with the results obtained from the full response fit explained above. The short conclusion is that the two approaches lead to nearly identical values for  $\mathcal{K}$ .

## B. Construction of an artificial CPR

To construct the artificial CPR used in main paper Fig. 5 for the calculation of the alternative Kerr constant and shown in the inset of panel (c), we use the Ansatz of an odd polynomial function

$$I_{\text{ar}}(\delta) = \sum_{n>0} \alpha_{2n-1} \delta^{2n-1} \quad (\text{S101})$$

and the validity of the function is  $\delta \in [-\pi, \pi]$ . Outside of the intervall, the function will then be just set to be periodically repeating. After trying for a bit by hand, we found that restricting ourselves to a few term is sufficient to model CPR and Kerr simultaneously and we use

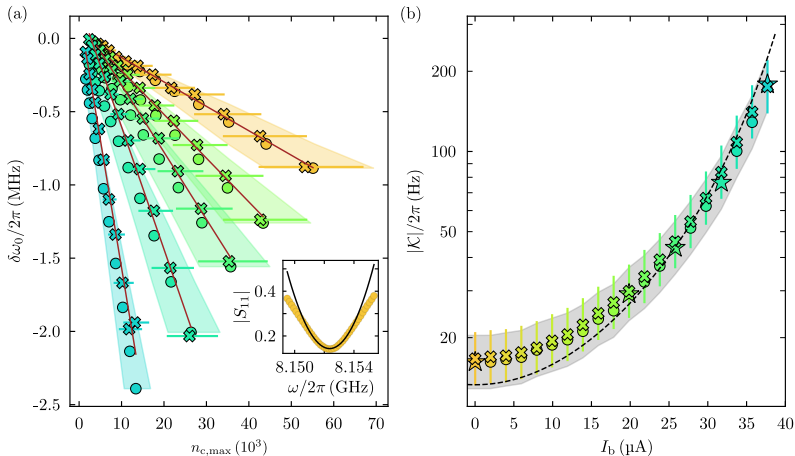
$$I_{\text{ar}}(\delta) = \alpha_1 \delta + \alpha_3 \delta^3 + \alpha_7 \delta^7 + \alpha_{15} \delta^{15} \quad (\text{S102})$$

For the first coefficient, we use the actual slope

$$\alpha_1 = \frac{\Phi_0}{2\pi(L_{J0} + L_{\text{lin}})} \quad (\text{S103})$$

to ensure that the zero bias-current inductance is not changed by a modified CPR. The second and third coefficients  $\alpha_3$  and  $\alpha_7$  are used as fit parameters, and the final coefficient  $\alpha_{15}$  is set to be

$$\alpha_{15} = -\frac{\alpha_1 \pi + \alpha_3 \pi^3 + \alpha_7 \pi^7}{\pi^{15}} \quad (\text{S104})$$



Supplementary Figure 11. **Comparing full-model Kerr anharmonicity with the one obtained by a linear-fit approach.** (a) Frequency shift  $\delta\omega_0 = \omega'_0 - \omega_0$  of the cavity as function of intracavity photon number at the power-shifted resonance frequency  $\omega'_0$ . Data are shown for five values of the bias current (color-coded). Circles are obtained from fitting the nonlinear resonances with the full response model for  $S_{11}(\omega)$  and naturally lie on a straight line due to the underlying model. Crosses are the result of measuring just the position of the nonlinear resonance minima and calculating from that the corresponding intracavity photon number  $n_{c,\max}$  by hand, cf. text for details and inset for a parabolic fit around one of the resonance minima. Error bars to the crosses consider  $\pm 1$  dB uncertainty in input power, error shades are the analogous quantity for the full response model. Brown solid lines are linear fits  $\delta\omega_0 = \mathcal{K}n_{c,\max}$  with  $\mathcal{K}$  as single fit parameter. The values for the extracted  $\mathcal{K}$  are plotted in (b) as  $|\mathcal{K}| = -\mathcal{K}$ . Circles are the values of the full response model, crosses from the linear fit, star shaped symbols in the full response data correspond to the bias currents discussed in (a). Error bars belong to the circles and correspond to the color shades in (a), error shade in gray belongs to the crosses and corresponds to the error bars in (a). The dashed line is the theoretical curve based on the linear-plus-sinusoidal model for the CPR. All values lie within the error range of the experiment.

to ensure that  $I_{\text{ar}}(\pi) = 0$ , i.e., that the CPR goes to zero at  $\delta = \pi$ . We use this function to fit simultaneously the CPR and the Kerr data. Most likely there are even better fitting polynomial curves, when allowing more or different terms, but this one is sufficient to demonstrate the principle.

## IX. SUPPLEMENTARY REFERENCES

- [S1] Watanabe, K., Yoshida, K., Aoki, T., and Kohjiro, S., *Kinetic Inductance of Superconducting Coplanar Waveguides*. Japanese Journal of Applied Physics **33**, 5708 (1994)
- [S2] Clem, John R., *Inductances and attenuation constant for a thin-film superconducting coplanar waveguide resonator*. Journal of Applied Physics **113**, 013910 (2013)
- [S3] Klein, N., Chaloupka, H., Müller, G., Orbach, S., and Piel, H., *The effective microwave surface impedance of high- $T_c$  thin films*. Journal of Applied Physics **67**, 6940 (1990)
- [S4] Frattini, N. E., Sivak, V. V., Lingenfelter, A., Shankar, S., and Devoret, M. H., *Optimizing the Nonlinearity and Dissipation of a SNAIL Parametric Amplifier for Dynamic Range*. Physical Review Applied **10**, 054020 (2018)
- [S5] Gely, M. F., Sanz Mora, A., Yanai, S., van der Spek, R., Bothner, D., and Steele, G. A., *Apparent nonlinear damping triggered by quantum fluctuations*. Nature Communications **14**, 7566 (2023)
- [S6] Wenner, J., Neeley, M., Bialczak, Radoslaw C., Lenander, M., Lucero, E., O'Connell, A. D., Sank, D., Wang, H., Weides, M., Cleland, A. N., and Martinis, J. M., *Wirebond crosstalk and cavity modes in large chip mounts for superconducting qubits*. Superconductor Science and Technology **24**, 065001 (2011)
- [S7] Rieger, D., Günzler, S., Spiecker, M., Nambisan, A., Wernsdorfer, W., and Pop, I. M., *Fano Interference in Microwave Resonator Measurements*, Physical Review Applied **20**, 014059 (2023).

- [S8] Mayadas, A. F., Laibowitz, R. B., and Cuomo, J. J., **Electrical Characteristics of rf-Sputtered Single-Crystal Niobium Films**, *Journal of Applied Physics* **43**, 1287-1289 (1972).
- [S9] Uhl, K., Hackenbeck, D., Peter, J., Kleiner, R., Koelle, D., and Bothner, D., **Niobium Quantum Interference Microwave Circuits with Monolithic Three-Dimensional (3D) Nanobridge Junctions**, arXiv:2305.16276 (2023).
- [S10] Pekker, D., Shah, N., Sahu, M., Bezryadin, A., and Goldbart, P. M., **Stochastic dynamics of phase-slip trains and superconductive-resistive switching in current-biased nanowires**. *Physical Review B* **80**, 214525 (2009)
- [S11] Li, P., Wu, P. M., Bomze, Y., Borzenets, I. V., Finkelstein, G., and Chang, A. M., **Switching Currents Limited by Single Phase Slips in One-Dimensional Superconducting Al Nanowires**. *Physical Review Letters* **107**, 137004 (2011)
- [S12] Aref, T., Levchenko, A., Vakaryuk, V., and Bezryadin, A., **Quantitative analysis of quantum phase slips in superconducting Mo<sub>76</sub>Ge<sub>24</sub> nanowires revealed by switching-current statistics**. *Physical Review B* **86**, 024507 (2012)
- [S13] Baumans, X. D. A., Zharinov, V. S., Raymenants, E., Blanco Alvarez, S., Scheerder, J. E., Brisbois, J., Massarotti, D., Caruso, R., Tafuri, F., Janssens, E., Moshchalkov, V. V., Van de Vondel, J., and Silhanek, A. V., **Statistics of localized phase slips in tunable width planar point contacts**. *Scientific Reports* **7**, 44569 (2017)
- [S14] Friedrich, F., Winkel, P., Borisov, K., Seeger, H., Sürgers, C., Pop, I. M., and Wernsdorfer, W., **Onset of phase diffusion in high kinetic inductance granular aluminum micro-SQUIDS**. *Superconductor Science and Technology* **32**, 125008 (2019)

# Publication 2

## Niobium quantum interference microwave circuits with monolithic three-dimensional nanobridge junctions

Kevin Uhl<sup>✉,\*</sup>, Daniel Hackenbeck, Janis Peter<sup>✉</sup>, Reinhold Kleiner<sup>✉</sup>, Dieter Koelle<sup>✉</sup>, and Daniel Bothner<sup>✉,†</sup>

*Physikalisches Institut, Center for Quantum Science (CQ) and LISA<sup>+</sup>, Universität Tübingen, Tübingen 72076, Germany*

 (Received 26 May 2023; revised 10 November 2023; accepted 25 January 2024; published 27 February 2024)

Nonlinear microwave circuits are key elements for many groundbreaking research directions and technologies, such as quantum computation and quantum sensing. The majority of microwave circuits with Josephson nonlinearities to date are based on aluminum thin films; therefore, they are severely restricted in their operation range regarding temperatures and external magnetic fields. Here, we present the realization of superconducting niobium microwave resonators with integrated, three-dimensional (3D) nanobridge-based superconducting quantum interference devices. The 3D nanobridges (constriction weak links) are monolithically patterned into prefabricated microwave *LC* circuits using neon focused-ion-beam milling, and the resulting quantum interference circuits show frequency tunabilities, flux responsivities, and Kerr nonlinearities on par with comparable aluminum nanobridge devices, but with the perspective of a much larger operation parameter regime. Our results demonstrate that neon focused-ion-beam milling is a promising method for fabricating 3D constriction junctions with flexible parameters and reveal great potential for application of the resulting microwave circuits in hybrid systems with, e.g., magnons and spin ensembles or in flux-mediated optomechanics.

DOI: [10.1103/PhysRevApplied.21.024051](https://doi.org/10.1103/PhysRevApplied.21.024051)

### I. INTRODUCTION

Superconducting microwave circuits with integrated Josephson junctions (JJs) and superconducting quantum interference devices (SQUIDs) have led to groundbreaking experimental and technological developments in recent decades. Both single JJs and SQUIDs constitute a flexible and designable Josephson or Kerr nonlinearity, while a SQUID additionally provides *in situ* tunability of the resonance frequency by external magnetic flux. Circuits with large nonlinearities originating from the Josephson element form artificial atoms and qubits [1,2], which have been used for spectacular experiments in circuit quantum electrodynamics [3] and quantum information processing [4]. Frequency-tunable devices with a small nonlinearity are highly relevant for quantum-limited Josephson parametric amplifiers [5–7], tunable microwave cavities for hybrid systems with spin ensembles and magnons, dispersive SQUID magnetometry [8,9], photon-pressure systems [10–13], and microwave optomechanics [14–17].

In many of these currently active research fields, such as flux-mediated optomechanics, hybrid quantum devices with magnonic oscillators and dispersive SQUID

magnetometry, it is highly desirable to have frequency-tunable microwave circuits with small nonlinearity, high magnetic field tolerance, and (in some cases) a critical temperature significantly above that of aluminum. The vast majority of frequency-tunable and nonlinear circuits, however, use Josephson junctions and SQUIDs made of aluminum thin films [18,19], a superconducting material with a critical magnetic field of only  $B_c \sim 10\text{--}100$  mT and a critical temperature  $T_c \approx 1.2\text{--}1.5$  K for convenient film thicknesses  $\gtrsim 100$  nm [20]. For much thinner films or material variations such as granular aluminum, the critical fields and temperatures can be considerably higher [20–22], but at the expense of a very high kinetic inductance, a property often detrimental to high-performance SQUID operation. An approach that could fulfil the aforementioned wish list is the implementation of microwave circuits made of niobium [23], niobium alloys [24,25], or even a high- $T_c$  superconductor such as YBCO [26–28] with high critical current density and high-field-compatible Josephson elements such as nanoconstrictions [29–31]. In most efforts so far, however, it has proven difficult to obtain large-tunability constriction-junction SQUIDs made of these materials, both in the direct-current (dc) operation mode and in the microwave domain [30,32–35].

Here, we report the realization of niobium superconducting quantum interference microwave circuits based on

\*kevin.uhl@pit.uni-tuebingen.de

†daniel.bothner@uni-tuebingen.de

neon focused-ion-beam (Ne-FIB) patterned monolithic 3D nanobridge junctions. Although the SQUIDs in our devices have a large effective area of about  $72 \mu\text{m}^2$ , we achieve smaller screening parameters than previous 2D niobium nanobridge SQUID circuits with much smaller loops [30]. A small screening parameter is an important prerequisite for stable flux tunability of the circuit resonance frequency and large flux responsivities [36]. In addition, we characterize our nanobridge quantum interference circuits at varying temperatures in the regime  $2.4 < T_s < 3.4 \text{ K}$  and demonstrate that they have a small Kerr nonlinearity of  $|\mathcal{K}|/2\pi \lesssim 10 \text{ kHz}$ , ideal for large dynamic range applications. Our devices and results show great potential for dispersive SQUID magnetometry, hybrid systems with spin ensembles, magnons or cold atoms, and flux-mediated optomechanics.

## II. DEVICES

Our devices are lumped-element microwave circuits, patterned from a  $d_{\text{Nb}} = 90\text{-nm}$ -thick layer of dc magnetron sputtered niobium on top of a high-resistivity silicon substrate with thickness  $d_{\text{Si}} = 500 \mu\text{m}$ . The niobium film has a transition temperature  $T_c \approx 8.6 \text{ K}$  and a zero-temperature penetration depth  $\lambda_0 \approx 155 \text{ nm}$  (see Note II within the Supplemental Material [37]), and comparable films show residual normal-state resistivities of  $\rho_{\text{Nb}} \sim 8\text{--}10 \mu\Omega \text{ cm}$  at  $10 \text{ K}$ . The circuits consist of two interdigitated capacitors (IDCs) combined in parallel and several linear inductors, and they are capacitively side coupled to a  $Z_0 \approx 50 \Omega$  coplanar waveguide transmission line by means of a coupling capacitance  $C_c$  for driving and readout. One of the devices and its circuit equivalent are shown in Figs. 1(a) and 1(b), respectively. The width of all lines (fingers and inductor wires) and the gaps in between two adjacent IDC fingers is  $W = 3 \mu\text{m}$ . At the connection point between the capacitors and the inductor wires, a square-shaped loop with an effective area of about  $8.5 \times 8.5 \mu\text{m}^2$  (hole size  $6 \times 6 \mu\text{m}^2$ ) is embedded into the circuit, which forms the SQUID once the nanoconstrictions are introduced; see Figs. 1(c) and 1(d).

After patterning the circuit itself by means of optical lithography and reactive ion etching using  $\text{SF}_6$ , the nanoconstrictions are fabricated into the center of the two loop arms using a neon focused ion beam. For the simplest constrictions, we cut a narrow  $20\text{-nm}$ -wide slot from both sides into each of the two loop arms, leaving only a  $40\text{-nm}$ -wide constriction in the center of each arm. This type of constriction (thickness equal for the leads and the constriction) has been referred to as 2D constriction and has been implemented for both dc and microwave SQUIDs in the past [30,32,33]. It has also been demonstrated, however, that 3D versions, i.e., constrictions that are thinner than the superconducting leads connected to them, can have superior properties such as less skewed

current-phase relations, smaller critical currents, and lower flux noise [9,32,38,39]. Furthermore, implementing 3D constrictions, although usually very challenging to fabricate, allows one to keep the circuit film thickness large, i.e., the circuit and loop kinetic inductance small, while at the same time getting a critical junction current  $I_0 \sim 10 \mu\text{A}$ , a highly desirable range for simultaneously achieving a large frequency tunability and a small circuit nonlinearity.

For implementation of the 3D versions, we therefore modify our ion beam scan pattern in a way that the constriction is thinned down during the cutting procedure [see Fig. 1(e)]; more details can be found in Appendix A. Such a monolithic and so far unexplored Ne-FIB-based approach for the generation of 3D nanobridges circumvents some of the challenges and possible problems of previously implemented multilayer deposition processes, such as guaranteeing good galvanic contact between the layers or dealing with thin additional edges at the bottom of the microwave structures [38,39], two problems that get increasingly challenging with decreasing constriction thickness. Single-layer processes using electron-beam lithography (EBL) and reactive ion etching or lift-off on the other hand cannot be used for the fabrication of 3D bridges. Ne FIB furthermore allows one to retrim prepatterned nanoconstrictions with relative ease compared to EBL due to the limited multilayer alignment accuracy of typical EBL machines and the inevitable resist involved. FIB techniques can finally be used on very uneven samples, something hard to implement with classical lithography techniques. In principle, our fabrication method for 3D constrictions can also be implemented using other materials such as aluminum, lead, titanium, or niobium alloys, and it will be interesting to study the properties of such circuits nanopatterned by Ne FIB and to compare them with those obtained using established techniques.

In addition to the manufacturing advantages, our approach offers the unique opportunity to characterize one and the same microwave circuit both without and with the junctions, i.e., one can experimentally determine the impact of the junctions on the circuit properties. In reverse, we can also extract with high reliability the properties of the constrictions themselves, such as the critical currents as a function of temperature or the linear contribution to the total junction inductance, which is closely related to the constriction current-phase relation. We perform these analyses in more detail below and in the Supplemental Material [37].

We combine several  $LC$  circuits on a single coplanar waveguide feedline, more specifically four circuits with a SQUID and three circuits without a SQUID for reference. The base circuits only differ in the number of fingers in the IDCs and in the corresponding resonance frequencies between 3 and 7 GHz. We present data for three of the SQUID resonators with three different constriction types; one resonator has 2D constrictions (junction thickness

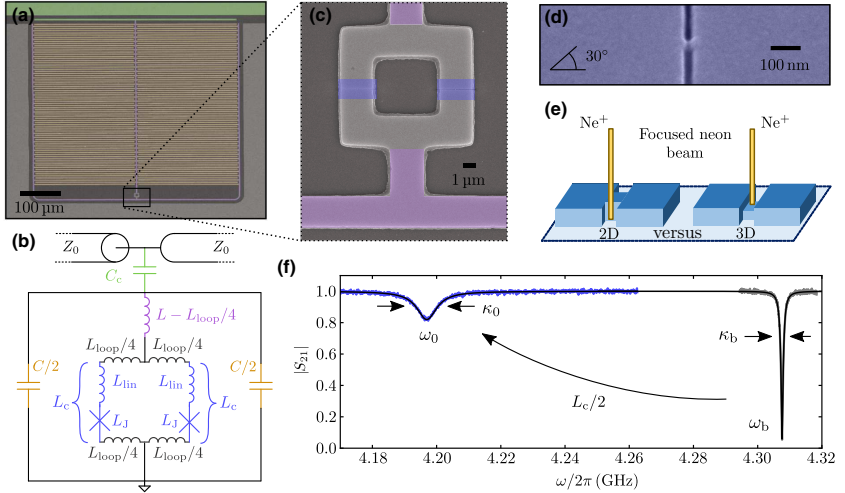


FIG. 1. A niobium-based quantum interference microwave circuit with monolithic three-dimensional nanobridge junctions. (a) False-color optical micrograph and (b) equivalent circuit of a typical device. The main circuit inductance (purple) is modeled by a linear inductor  $L - L_{\text{loop}}/4$  and the two interdigitated capacitors (IDCs; orange) have a total capacitance of  $C$ . Each of the two IDCs has  $N_{\text{idc}}$  (here  $N_{\text{idc}} = 46$ ) fingers with a length of  $l = 250 \mu\text{m}$  and a width of  $W = 3 \mu\text{m}$ . In the center of the circuit is a loop structure for the SQUID. The square-shaped loop has a total loop inductance  $L_{\text{loop}} \approx 17 \text{ pH}$  and the nanobridges (blue) have a constriction inductance  $L_c$  (only  $\neq 0$  after junction patterning). The resonant circuit is capacitively coupled to a coplanar waveguide transmission line with a characteristic impedance of  $Z_0 \approx 50 \Omega$  by means of a coupling capacitance  $C_c$  (coupling elements green). (c) False-color scanning electron microscopy (SEM) image of the loop after constriction cutting; (d) enlarged view of a 3D constriction after cutting. In (a), (c), and (d) niobium is bright gray and colored. The silicon substrate is dark gray. Panel (e) schematically illustrates the nanoconstriction fabrication. For the 2D constrictions, two narrow slits are patterned into each of the SQUID arms by a neon focused ion beam; for the 3D constrictions, the nanobridges are additionally thinned down from the top by the neon beam. (f) Transmission  $|S_{21}|$  of one of the circuits (device 3D<sub>1</sub>) at  $T_s = 2.5 \text{ K}$  before (gray) and after (blue) the constriction cutting; black lines are fits to the data. Before the junction cutting, the circuit has a resonance frequency  $\omega_b$  and a linewidth  $\kappa_b$ ; after the cutting the circuit has a resonance frequency  $\omega_0$  and a linewidth  $\kappa_0$ . Values can be found in the main text. From the shift of the resonance frequency induced by the cutting, we determine the total additional inductance of the constrictions  $L_c/2$ .

$d_{\text{JJ}} = 90 \text{ nm}$ ) and two resonators have 3D constrictions with  $d_{\text{JJ}} \approx 30 \text{ nm}$  (3D<sub>1</sub>) and with  $d_{\text{JJ}} \approx 20 \text{ nm}$  (3D<sub>2</sub>) (thicknesses are estimated from the neon ion dose). The chip is  $10 \times 10 \text{ mm}^2$  large and is mounted onto a printed circuit board (PCB), to which both the ground planes and the coplanar waveguide feedlines are connected through wirebonds. The chip and PCB are placed in a radiation-tight copper housing and the package—including a magnet coil fixed to the box—is mounted inside the vacuum chamber of a dipstick that can be inserted into a liquid helium cryostat. The cryostat allows for high-stability temperature control in the range  $2.4 < T < 7.5 \text{ K}$  by a combination of pumping on the liquid helium container and a feedback loop using a temperature diode and a heating resistor in the vacuum compartment where the sample is mounted. The sample box including the magnet is additionally placed

into a cryoperm magnetic shield and the whole cryostat is packed into a double-layer room-temperature mu-metal shield. The microwave input line is strongly attenuated by 30 dB to equilibrate the incoming noise to the sample temperature and the output line is connected to a cryogenic high-electron-mobility-transistor amplifier. More details on the experimental setup are given in Appendix B and Note I within the Supplemental Material [37].

### III. IMPACT OF JUNCTION CUTTING

As first step in our device characterization, we measure the transmission coefficient  $S_{21}$  with a vector network analyzer (VNA) once before the constriction patterning and once after. For all data presented here, below, and in the Supplemental Material [37], the VNA probe tone power

is chosen to be sufficiently weak, such that all nanoconstriction circuits are always in the linear response regime. This corresponds to intracircuit probe photon numbers  $n_{\text{pr}}^{2\text{D}} < 70$ ,  $n_{\text{pr}}^{3\text{D}1} < 10$  and  $n_{\text{pr}}^{3\text{D}2} < 2$  for all VNA measurements. In Fig. 1(f), the transmission  $|S_{21}|$  at 2.5 K for device 3D<sub>1</sub> is shown in direct comparison for both cases. From the fits, we obtain the resonance frequencies  $\omega_b = 2\pi \cdot 4.308$  GHz (no constrictions) and  $\omega_0 = 2\pi \cdot 4.197$  GHz (with constrictions) and therefore we can calculate the single-constriction inductance from the constriction-induced frequency shift via

$$\omega_0 = \frac{\omega_b}{\sqrt{1 + L_c/(2L)}}. \quad (1)$$

Here and for all further analyses in this work, we assume two identical constrictions in each SQUID. Using  $L = 568$  pH, as obtained from a combination of measuring the temperature dependence of the resonance frequency and numerical simulations with the software package 3D-MLSI [40] (see Note II within the Supplemental Material [37] for all device parameters), we get  $L_c^{3\text{D}1} = 61$  pH for device 3D<sub>1</sub>.

Additionally, we extract the internal (subscript “i”) and external (subscript “e”) linewidths from the fit before and after nanobridge patterning and obtain  $\kappa_{i,b} = 2\pi \cdot 73$  kHz,  $\kappa_{e,b} = 2\pi \cdot 1.2$  MHz without and  $\kappa_i = 2\pi \cdot 6.5$  MHz,  $\kappa_e = 2\pi \cdot 1.4$  MHz with the constriction junctions. Here  $\kappa_b = \kappa_{i,b} + \kappa_{e,b}$  and  $\kappa_0 = \kappa_i + \kappa_e$ .

The slight increase in the external linewidth could be caused by parasitic reflections in the microwave feedlines and/or cables and by the resulting partial standing wave pattern, which will lead to the input impedance of the feedline at the location of the resonator being different from  $50 \Omega$  in a possibly frequency-dependent fashion. Other possible causes are parasitic signal paths, e.g., around the chip [41], leading to frequency-dependent Fano interferences and fitting errors as described in Ref. [42]. Both effects could be different before and after the Ne-FIB step due to the chip being wirebonded for a second time after the constriction nanopatterning.

The considerable increase in the internal linewidth on the other hand indicates that cutting the junction has introduced an additional loss channel and we believe that it is related to an increased quasiparticle density inside the constriction. First, it has been observed that ion-milled constrictions have a reduced critical temperature compared to the rest of the niobium film [43–46], which locally decreases the superconducting gap and increases the intrinsic thermal quasiparticle density; see also the later discussion of the temperature dependence of the devices. Based on this reduced gap, the local quasiparticle density could even be further increased, since the constriction with the reduced gap might act as a potential well or trap for thermal quasiparticles from the leads, similar to what has

been observed in aluminum constrictions or vortex cores [47,48]. We note that the increase in losses could also be partly related to generating some normal-conducting niobium at the surface or at the edges of the constriction by the neon ions. To illuminate the exact loss mechanisms in detail, however, further and dedicated experiments will be necessary in the future.

By performing completely analogous experiments and data analyses for the 2D and 3D<sub>2</sub> circuits (see Appendix D), we extract the corresponding constriction inductances to be  $L_c^{2\text{D}} = 8$  pH and  $L_c^{3\text{D}2} = 103$  pH. More details regarding the three circuits and their basic parameters,  $L$ ,  $C$ ,  $L_{\text{loop}}$ ,  $C_c$ , and  $\kappa_{i/e}$ , can be found in Note II within the Supplemental Material [37].

#### IV. FLUX TUNING

In order to learn more about the nature of the constrictions and how our SQUID circuits perform in terms of frequency tunability, flux responsivity, and the screening parameter, we apply an external magnetic field to the circuits that introduces magnetic flux  $\Phi_{\text{ext}}$  into the SQUIDs. The constriction inductance  $L_c$  we obtained above is not necessarily a purely nonlinear Josephson inductance, but might have a linear contribution as well. In many cases, nanoconstrictions have been found to have forward-skewed sinusoidal current-phase relationships (CPRs) [33, 38,49–51] and such a skewed sine function can also be modeled approximately as a series combination of an ideal Josephson inductance  $L_J$  with sinusoidal CPR and a linear inductance  $L_{\text{lin}}$  [49], i.e.,  $L_c = L_J + L_{\text{lin}}$ ; see Fig. 2(a). Here, the ideal Josephson inductance would be given by  $L_J = L_{J0}/\cos\varphi$ , where  $\varphi$  is the phase difference across the junction,  $L_{J0} = \Phi_0(2\pi I_0)^{-1}$ , and  $I_0$  is the critical current of the junction. The Josephson phase  $\varphi$  of each junction in a symmetric SQUID without bias current is related to the total flux  $\Phi$  in the loop via  $\varphi = \pi\Phi/\Phi_0$ . To change the magnetic flux through the loop, we sweep a dc current through the magnet coil attached to the backside of the chip housing, which generates a nearly homogeneous out-of-plane magnetic field at the position of the SQUIDs.

Figure 2(b) shows the circuit response  $|S_{21}|$  of the 3D<sub>1</sub> SQUID circuit for several bias fluxes  $\Phi_{\text{ext}}$ . We observe that the resonance dip moves to lower frequencies, i.e., that the resonance frequency is shifted downwards with flux, and that the depth of the dip decreases while the linewidth increases, at least as long as  $\Phi_{\text{ext}} < \Phi_0/2$  with the flux quantum  $\Phi_0 \approx 2.068 \times 10^{-15}$  Tm<sup>2</sup>. Over larger flux ranges, we in fact observe an oscillating behavior of the resonance frequency  $\omega_0(\Phi_{\text{ext}})$  with a periodicity of  $\Phi_0$ , reflecting fluxoid quantization in the SQUID loop; see Fig. 2(c). Very much as suggested by previous reports [36,38] and as intuitively expected, we observe that the resonance frequency tuning range (difference

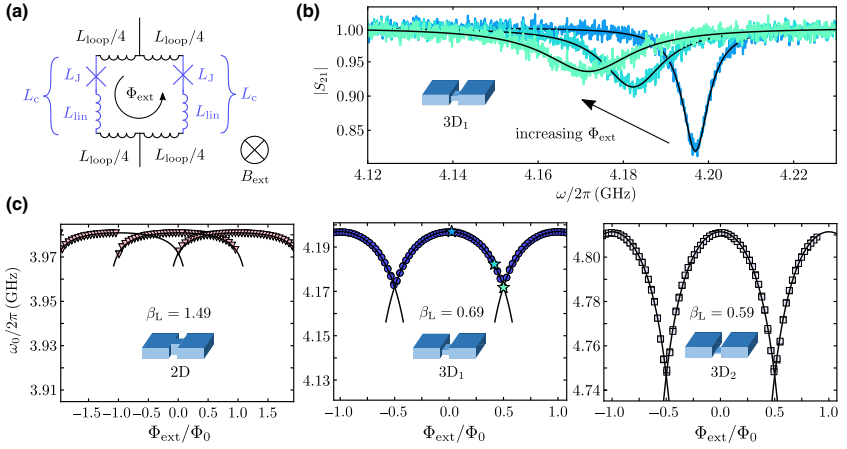


**FIG. 2.** Flux tuning the resonance frequency of niobium quantum interference circuits with 2D and 3D constriction junctions. (a) Circuit equivalent of the SQUID with a linear loop inductance  $L_{\text{loop}}/2$  in each arm and a constriction inductance  $L_c$ , modeled by a linear contribution  $L_{\text{lin}}$  and a sinusoidal Josephson contribution  $L_J$ . We apply an external magnetic field  $B_{\text{ext}}$  perpendicular to the SQUID loop to change the inductances  $L_J(\Phi_{\text{ext}})$  with the externally applied magnetic flux  $\Phi_{\text{ext}}$  and with it the resonance frequency of the circuit. (b) Transmission response  $|S_{21}|$  of the 3D<sub>1</sub> constriction SQUID circuit for three different external fluxes  $\Phi_{\text{ext}}$  and  $T_s = 2.5$  K. With increasing  $\Phi_{\text{ext}}$ , the resonance shifts towards lower frequencies, indicating an increase in the constriction inductance by flux. Colored noisy lines are data and black smooth lines are fits. The flux values are  $\Phi_{\text{ext}}/\Phi_0 = 0, 0.4, 0.5$ . From the fits, we extract the resonance frequency  $\omega_0(\Phi_{\text{ext}})$ , which is shown as a function of flux in panel (c) for the three different circuits with three different constrictions. Insets show sketches of the junction type. Symbols are data and lines are fits from which we extract the screening parameter  $\beta_L$ . Left: 2D constriction with a thickness of about 90 nm. Middle: 3D constriction 3D<sub>1</sub> with a thickness of about 30 nm; star-shaped data points correspond to the data sets in (b). Right: 3D constriction 3D<sub>2</sub> with a thickness of about 20 nm. With decreasing thickness of the constriction, the tuning range gets larger and the screening parameter  $\beta_L$  and flux hysteresis (overlap of adjacent flux arches) decrease.

between the maximum and minimum resonance frequencies) gets larger with decreasing constriction thickness. For the 2D junctions [left plot in Fig. 2(c)], the total resonance frequency tuning range that we can achieve is only about 10 MHz and the individual flux arches strongly overlap with a total observable width of each arch of about  $2\Phi_0$ . For the 3D<sub>2</sub> device [right plot in Fig. 2(c)], the tuning range is about 65 MHz and a flux hysteresis (two possible resonance frequencies for a single flux value as in the 2D circuit) is not observable in the data. The 3D<sub>1</sub> circuit is somewhere in between, just as it is positioned in Fig. 2(c).

To quantitatively model the flux dependence of the resonance frequency and gather information about  $L_J$  and  $L_{\text{lin}}$ , we consider a flux-dependent resonance frequency

$$\omega_0(\Phi_{\text{ext}}) = \frac{\omega_b}{\sqrt{1 + \frac{1}{2L} \left( L_{\text{lin}} + \frac{L_{J0}}{\cos(\pi \frac{\Phi}{\Phi_0})} \right)}}. \quad (2)$$

The relation between the total flux in the SQUID  $\Phi$  and the external flux  $\Phi_{\text{ext}}$  is given by

$$\frac{\Phi}{\Phi_0} = \frac{\Phi_{\text{ext}}}{\Phi_0} - \frac{\beta_L}{2} \sin\left(\pi \frac{\Phi}{\Phi_0}\right), \quad (3)$$

where

$$\beta_L = \frac{2I_0(L_{\text{loop}} + 2L_{\text{lin}})}{\Phi_0} = \frac{L_{\text{loop}} + 2L_{\text{lin}}}{\pi L_{J0}} \quad (4)$$

is the effective SQUID screening parameter. The result of fitting the flux dependence of the resonance frequency with Eqs. (2) and (3) is shown as lines in Fig. 2(c) and shows good agreement with the experimental data for all three circuits.

The fit parameters we obtain for the single-junction sweetspot inductance  $L_{J0}$ , the single-junction critical current  $I_0$ , the linear inductance contribution  $L_{\text{lin}}$ , and the screening parameter  $\beta_L$  are summarized in Table I. Interestingly, the extracted inductances do not show the somewhat expected tendency that  $L_{\text{lin}}/L_{J0}$ , representing the

TABLE I. Nanobridge and SQUID parameters for the three circuits. Parameters are the same as those for the flux-tuning curve fits of Fig. 2(c) at  $T_s = 2.5$  K.

Circuit	$I_0$ ( $\mu\text{A}$ )	$L_{J0}$ (pH)	$L_{\text{lin}}$ (pH)	$\beta_L$
2D	65	5	3	1.49
3D <sub>1</sub>	10	33	28	0.69
3D <sub>2</sub>	6	58	45	0.59

skewedness of the CPR, decreases with  $d_{J1}$  and  $I_0$ . As a consequence of the low critical current in the 3D<sub>2</sub> device, however, we obtain a small screening parameter  $\beta_L = 0.59$  despite our large SQUID loop and a maximum flux responsivity  $\partial\omega_0/\partial\Phi_{\text{ext}} \approx 2\pi \cdot 400$  MHz/ $\Phi_0$ , on par with similar aluminum constriction devices [52,53] and highly promising for applications in photon-pressure systems and flux-mediated optomechanics. The screening parameters in the optimized aluminum-constriction circuits in Refs. [52,53] for 50–100- $\mu\text{m}^2$ -large SQUIDs have been obtained as  $\beta_L = 0.7$  and  $\beta_L = 1.1$ , respectively, and the flux responsivities used in these experiments have been between  $\partial\omega_0/\partial\Phi_{\text{ext}} \approx 2\pi \cdot 250$  MHz/ $\Phi_0$  and  $\partial\omega_0/\partial\Phi_{\text{ext}} \approx 2\pi \cdot 520$  MHz/ $\Phi_0$ . Therefore, it is now possible to work with comparable circuits, responsivities, and screening parameters as before, but at a considerably higher temperature (here  $T_s \sim 2.5$  K) and presumably at much larger magnetic in-plane fields. Note also that the flux responsivities strongly depend on the linear inductance of the circuit  $L$ , which is highly designable and is currently about 500 pH. With a different circuit layout such as that in, e.g., Ref. [54] and an even thicker film,  $L$  could be reduced by up to one order of magnitude, thereby also increasing the tuning range and the flux responsivity by a factor of about 5 compared to now.

Regarding the increase in the linewidth with flux, which is visible in the data of Fig. 2(b), we believe that it is related to a reduction in the superconducting gap with increasing current in the constriction [50], and the corresponding increase in local quasiparticle density, both by the reduction of the gap itself, but also by trapping more quasiparticles from the leads. Most likely, there are additional contributions due to internal and external low-frequency flux noise and thermal photon occupation of a nonlinear resonator [19], which at  $T_s = 2.5$ –3.5 K is  $\bar{n}_{\text{th}} \sim 10$ –20 photons for an 4–5 GHz mode based on the Bose distribution  $\bar{n}_{\text{th}} = (e^{\hbar\omega_0/k_B T_s} - 1)^{-1}$ .

## V. TEMPERATURE DEPENDENCE

An interesting question when characterizing and operating superconducting microwave devices and SQUIDs at a temperature several tens of percent of the critical temperature  $T_c$  is how the properties depend on the sample temperature  $T_s$  in that regime and if we can extrapolate to the properties at lower temperatures from that. The most

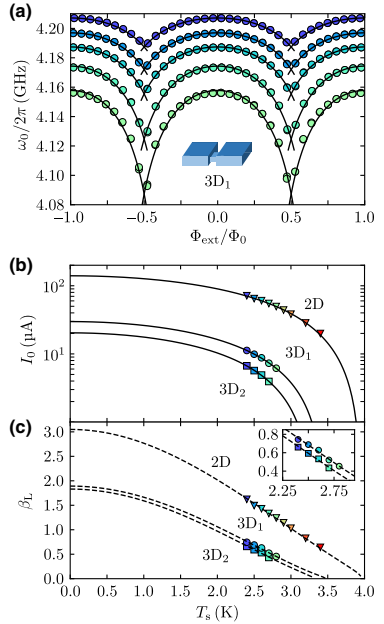


FIG. 3. Temperature dependence of the circuit and SQUID. (a) Flux-tuning curve  $\omega_0(\Phi_{\text{ext}})$  of device 3D<sub>1</sub> for several different sample temperatures  $T_s = 2.4$ –2.8 K in steps of 0.1 K. Top curve: lowest temperature. Bottom curve: highest temperature. Circles are data and lines are fits to Eqs. (2) and (3). From the fits we extract the critical current of the constriction  $I_0$  and the screening parameter  $\beta_L$ ; the obtained values for both are shown as circles in (b) and (c), respectively. (b) Critical current  $I_0$  versus the sample temperature  $T_s$  for all three constriction SQUID cavities as extracted from the corresponding flux-tuning curves. Symbols are data and lines are fits. From the theoretical fit curves (see the main text), we can extrapolate to the critical current at millikelvin temperatures and obtain the critical temperatures of the constrictions  $T_{\text{cc}}^{2\text{D}} = 3.96$  K,  $T_{\text{cc}}^{3\text{D}1} = 3.47$  K, and  $T_{\text{cc}}^{3\text{D}2} = 3.31$  K. In combination with the temperature dependencies of  $L_{\text{loop}}$  and  $L_{\text{lin}}$ , we can calculate theoretical lines for  $\beta_L(T_s)$ , as shown in panel (c), for all three circuits in comparison to the experimental data. Inset shows an enlarged view of the data for the 3D samples.

relevant parameters we are going to consider here are the cavity resonance frequency  $\omega_0(T_s)$ , the constriction critical current  $I_0(T_s)$ , and the SQUID screening parameter  $\beta_L(T_s)$  for all three circuits.

The main results are summarized in Fig. 3. We repeat the experiment of flux tuning presented in the previous section for different sample temperatures  $T_s$ . From the transmission curves  $S_{21}$  for varying external flux we extract

$\omega_0(T_s, \Phi_{\text{ext}})$  [see Fig. 3(a) for a corresponding dataset of sample 3D<sub>1</sub>]. Corresponding datasets for 2D and 3D<sub>2</sub> can be found in Appendix D. For each temperature  $T_s$ , we also measured  $\omega_b(T_s)$ , so we have a reference resonance frequency from before neon irradiation; see also Note II within the Supplemental Material [37] for the temperature dependence of the constrictionless 3D<sub>1</sub>.

We observe in the resonance frequency tuning curves that with decreasing temperature the zero-flux resonance frequency gets shifted to larger values, a clear indication for a reduction of the kinetic inductance both in the constrictions and in the rest of the circuit. Furthermore, we find that the tuning range of the resonance frequency grows with increasing temperature, indicating that the constriction inductance increases faster than the remaining circuit inductance, and we observe that the screening parameter  $\beta_L$  decreases, since  $L_{J0}$  is increasing faster with  $T_s$  than the effective loop inductance  $L_{\text{loop}} + 2L_{\text{lin}}$ .

For a quantification of these effects, we fit the flux-tuning data again with the same equations and procedure as described in the previous section. As a result, we obtain for each sample  $L_{J0}(T_s)$  and  $L_{\text{lin}}(T_s)$  (see Note V within the Supplemental Material [37]), and from the former we calculate  $I_0(T_s) = \Phi_0[2\pi L_{J0}(T_s)]^{-1}$ . The critical currents obtained from this are shown for all three circuits in Fig. 3(b). We model the data with the theoretical Bardeen expression for the critical current of a constriction [44,55]

$$I_0(T_s) = I_c \left[ 1 - \left( \frac{T_s}{T_{cc}} \right)^2 \right]^{3/2}, \quad (5)$$

and find as fitting parameters the critical current at zero temperature  $I_c$  as well as the constriction critical temperature  $T_{cc}$ . As we have already speculated above, the critical temperature  $T_{cc}$  of the constrictions is considerably reduced compared to the niobium film to values between  $T_{cc}^{\text{2D}} = 3.96$  K and  $T_{cc}^{\text{3D2}} = 3.31$  K according to these fits. Interestingly, similar  $T_{cc}$  values have also been observed for electron-beam-patterned niobium nanobridges with comparable critical currents [44]; therefore, the reduced transition temperature might not actually be related to an impact of the neon ions. Since according to this fit our data are taken at  $T_s > 0.5T_{cc}$ , we find that the critical currents still increase by a factor of 2 in the 2D constrictions and by about a factor of 3 in the 3D constrictions when approaching  $T_s \rightarrow 0$  and with respect to the smallest experimental temperature  $T_s^{\text{min}} = 2.4$  K.

It is also interesting to discuss the temperature dependence of  $\beta_L$  and its projected values in the millikelvin regime, although this is a bit speculative due to the limited range of data available. The experimental data shown in Fig. 4(c) for all three circuits have been obtained from the flux-tuning fits. For the 2D sample, the values for  $\beta_L$  are found to be between 0.6 and 1.6 in the measured regime and, for the 3D samples, between 0.4 and 0.8. To

model the temperature dependence, we take into account the fit curves for  $I_0(T_s)$  as shown in panel (b), the temperature dependence of the loop inductance  $L_{\text{loop}}(T_s)$  as discussed in Note II within the Supplemental Material [37], and the temperature dependence of  $L_{\text{lin}}(T_s)$  that we obtain by a fit of the experimentally obtained values (see Note V within the Supplemental Material [37]). We find curves that coincide very well with the experimental data in the measured range of  $T_s$  and that predict screening parameters for  $T_s \rightarrow 0$  saturating around 3.1 for the 2D constrictions and around 1.8 and 1.9 for the 3D SQUIDs. All these values are still smaller than or comparable to the millikelvin screening parameter  $\beta_L > 3.4$  given in Ref. [30] for 2D niobium constrictions, despite the fact that our SQUID areas are almost a factor 20 larger.

It seems that the non sinusoidal CPR of the constrictions is currently the main limiting factor for  $\beta_L$  in the 3D samples, while in the 2D sample  $2L_{\text{lin}}^{\text{2D}} \approx 6$  pH and the screening parameter is limited by the actual  $L_{\text{loop}}$ . It will be interesting to see in future experiments in the millikelvin temperature regime if these predictions are valid or if so far neglected effects will emerge and lead to a different behavior than expected. With lower-temperature experimental possibilities, it will also be interesting to further reduce the thickness and critical current of the 3D junctions, which in the current setup with  $T_s^{\text{min}} \approx 2.4$  K was not possible, as can be seen from the very limited temperature range already accessible in the existing 3D devices with  $T_{cc} < 3.5$  K.

## VI. KERR NONLINEARITY OF THE CIRCUITS

As a final experiment, we determine a very important parameter of Josephson-based microwave circuits—their Kerr constant  $\mathcal{K}$ , also called the anharmonicity or Kerr nonlinearity, which is equivalent to the circuit resonance frequency shift per intracavity photon. For many applications, a small Kerr nonlinearity is highly desired, as it increases the dynamic range or maximum intracavity photon number of the device. This is important, for instance, in parametric amplifiers [5–7,56] and in cavity-based detection techniques such as dispersive SQUID readout [8,9,54], SQUID optomechanics [15,57], and photon-pressure sensing [11,12], where the signal of interest is proportional to the intracavity photon number  $n_c$  and therefore profits from high-power detection tones. The origin of the nonlinearity in our SQUID circuits is the nonlinear inductance of the nanoconstrictions. In order to access  $\mathcal{K}$  experimentally, we implement a two-tone protocol, (see, e.g., Refs. [56,58]), and measure the equivalent of the ac Stark shift in the driven circuits. The first microwave tone of the two-tone scheme is a fixed-frequency pump tone with variable power  $P_p$  and a frequency  $\omega_p$  slightly blue detuned from the undriven cavity resonance  $\omega_p = \omega_0 + \Delta_p$  with  $\Delta_p \sim \kappa$ . For each pump power, we then measure the

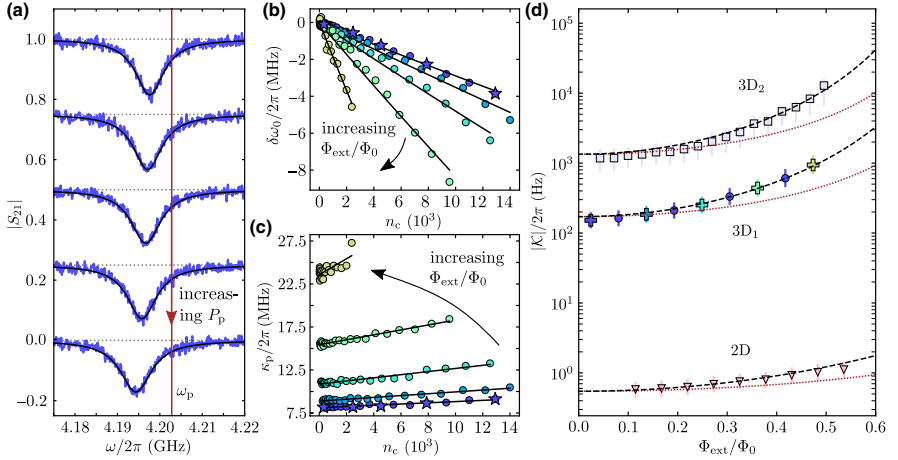


FIG. 4. Two-tone characterization of the SQUID-circuit Kerr nonlinearity. (a) The SQUID circuit transmission response  $S_{21}$  is probed with a weak microwave signal, while a strong microwave pump tone with fixed frequency  $\omega_p$  and variable power  $P_p$  is applied slightly blue detuned from the cavity resonance  $\omega_p - \omega_0 = \Delta_p \sim \kappa$ . With increasing  $P_p$ , the dressed circuit resonance frequency shifts towards lower frequencies and the linewidth increases. Five datasets for five different  $P_p$  are shown; subsequent datasets are offset by  $-0.25$  for clarity. From fits (black lines) to the data (blue noisy lines) we calculate the resonance frequency shift  $\delta\omega_0 = \omega_0(P_p) - \omega_0(0)$  and the linewidth  $\kappa_p$ . The results are shown in panels (b) and (c) for different  $\Phi_{\text{ext}}$ , temperature  $T_s = 2.5$  K, and sample 3D1. Circles are data and lines are fits. Star symbols are data points that correspond to the five datasets shown in panel (a). From the fits, we determine the Kerr nonlinearity  $\mathcal{K}(\Phi_{\text{ext}})$ . We perform this characterization for all three circuits; the result is shown in panel (d) versus the external flux bias  $\Phi_{\text{ext}}/\Phi_0$ . Symbols are data and dashed lines are theoretical curves based on the flux-tuning curve and Eq. (9), but without free parameters. Dotted red lines are theoretical curves without the correction factor arising from  $\beta_1 \neq 0$ . Cross symbols in the data of 3D1 correspond to the extracted values from the datasets shown in panels (b) and (c). Error bars take into account uncertainties in the intracavity photon number  $n_c$ ; see Note VI within the Supplemental Material [37].

pump-dressed device transmission  $S_{21}$  with a small probe tone; see Fig. 4(a).

What we find qualitatively in this experiment is that, with increasing pump power, the dressed circuit resonance frequency shifts towards lower frequencies and that the internal linewidth of the mode increases; see Fig. 4(a). For a quantitative analysis, we fit each pump-dressed resonance with a linear cavity response for  $S_{21}$  (see Appendix C and Note IV within the Supplemental Material [37]), from which we extract the pump-shifted resonance frequency  $\omega'_0$  and the pump-broadened total linewidth  $\kappa_p$ .

To model the circuit and the results and to extract  $\mathcal{K}$ , we use the equation of motion for the complex intracavity field  $\alpha$ :

$$\dot{\alpha} = \left[ i(\omega_0 + \mathcal{K}|\alpha|^2) - \frac{\kappa_0 + \kappa_{\text{nl}}|\alpha|^2}{2} \right] \alpha + i\sqrt{\frac{\kappa_c}{2}} S_{\text{in}} \quad (6)$$

with a nonlinear damping parameter  $\kappa_{\text{nl}}$ , the total input field  $S_{\text{in}}$ , and a normalization such that  $|\alpha|^2 = n_c$  is the total intracircuit photon number. In the linearized two-tone

regime (pump power  $\gg$  probe power; see Appendix C for details), for the pump-broadened linewidth and the pump-induced frequency shift  $\delta\omega_0 = \omega_0 - \omega'_0$ , we find the relations

$$\kappa_p = \kappa_0 + 2\kappa_{\text{nl}}n_c, \quad (7)$$

$$\delta\omega_0 = \Delta_p - \sqrt{(\Delta_p - \mathcal{K}n_c)(\Delta_p - 3\mathcal{K}n_c) - \frac{\kappa_{\text{nl}}^2 n_c^2}{4}}. \quad (8)$$

Subsequently, we use the  $\delta\omega_0$  and  $\kappa_p$  as obtained from the measurements to determine the intracavity photon number  $n_c$  for each  $P_p$  without any knowledge of  $\mathcal{K}$ ; see Appendix C, in particular Eq. (C25). In Figs. 4(b) and 4(c), the extracted values  $\delta\omega_0$  and  $\kappa_p$  are shown for various bias flux values and plotted versus the intracircuit pump photon number  $n_c$  in device 3D1 at a sample temperature  $T_s = 2.5$  K. Both quantities show a nearly linear dependence on the pump photon number as implemented by our model and the corresponding slope depends in turn on the bias flux

$\Phi_{\text{ext}}$ . We fit the data using Eqs. (7) and (8) and obtain  $\mathcal{K}(\Phi_{\text{ext}})$  for all three devices.

For all circuits, the nonlinearity shown in Fig. 4(d) increases with increasing flux, but the absolute values differ by several orders of magnitude. While the 2D circuit has a Kerr constant of about only 1 Hz, the 3D circuits possess nonlinearities of  $10^2$  to  $10^3$  Hz in 3D<sub>1</sub> and up to  $10^3$  to  $10^4$  Hz in 3D<sub>2</sub>. All nonlinearities can still be considered small though and are in particular several orders of magnitude smaller than the cavity linewidths  $\mathcal{K} \ll \kappa_0$ . We also observe very good agreement with the theoretical expression for the Kerr nonlinearity

$$\mathcal{K} = -\frac{e^2}{2\hbar C_{\text{tot}}} \left( \frac{L_J}{2L + L_{\text{lin}} + L_J} \right)^3 \left[ 1 + 3\Lambda \tan^2 \left( \pi \frac{\Phi}{\Phi_0} \right) \right] \quad (9)$$

with electron charge  $e$ , total circuit capacitance  $C_{\text{tot}} = C + C_c$ , reduced Planck constant  $\hbar$ , and  $\Lambda = (L_{\text{lin}} + L_{\text{loop}}/2)/(L_{\text{lin}} + L_{\text{loop}}/2 + L_J)$ . Note that we apply the method of nonlinear current conservation discussed in Ref. [56] to obtain this theoretical expression; see Appendix E. The unusual  $\tan^2$  term in the square brackets of Eq. (9) is, however, not stemming from an asymmetry or a hidden third-order nonlinearity, it is a correction factor for perfectly symmetric SQUIDs with screening parameter  $\beta_L > 0$ . How necessary it is to consider this extra term is revealed by the difference to the simple participation ratio expression [Eq. (9) with  $\Lambda = 0$ ], which is also shown in Fig. 4(d) as dotted lines and that, for large flux bias values, differs from the exact result and the data by up to a factor of about 4. The excellent agreement between the data and the theory curves also supports our initial assumption of (nearly) identical constrictions in each SQUID, since a junction asymmetry would lead to the flux-tuning curves of either the resonance frequency or the Kerr anharmonicity to deviate from the theory assuming symmetric SQUIDs.

## VII. DISCUSSION

In summary, we have reported niobium-based superconducting quantum interference microwave circuits with integrated, monolithically fabricated 2D and 3D nanoconstriction SQUIDs. The successful implementation of 3D constrictions nanopatterned with a Ne FIB constitutes a promising addition to the notoriously difficult patterning methods of such devices, and can also be applied to other materials such as aluminum or niobium alloys in the future. Our experimental results revealed that the tuning range and the flux responsivity of the circuits increase with decreasing constriction thickness and critical current. Strikingly, our circuits can be operated at temperatures up to about 4 K though, nearly an order-of-magnitude enhancement over comparable aluminum realizations. The critical currents we obtained strongly depend on constriction type

and thickness as well as on sample temperature, and we found values between  $I_{0,\text{min}} \sim 4 \mu\text{A}$  and  $I_{0,\text{max}} \sim 80 \mu\text{A}$  in the investigated temperature range. We believe that in the future we can even achieve critical currents as low as  $1 \mu\text{A}$ , possibly even in the millikelvin regime. We have also extracted and modeled the Kerr anharmonicity of all circuits and found values between 0.5 Hz for the 2D circuits and 10 kHz for the 3D circuit with the lowest critical current junctions. The overall characteristics of the circuits make them highly promising candidates for quantum circuit and quantum sensing applications, in particular when a high dynamic range and high magnetic fields will be important such as in spin-qubit circuit quantum electrodynamics, hybrid quantum devices with magnonic oscillators, dispersive magnetometry, or flux-mediated optomechanics.

Depending on the exact requirements of each hybrid system and experiment, the parameters of the embedding circuits can be easily adjusted in the future to obtain much larger (or smaller) frequency tuning ranges, larger (or smaller) flux responsivities, and larger (or smaller) Kerr nonlinearities. A good example for how strongly the embedding circuit impacts these properties is given in Ref. [54], where two very different resulting circuits are obtained from identical aluminum constriction SQUIDs by just choosing very different values for  $C$  and  $L$ . One of the circuits can be flux tuned by about 2 GHz, while the other has a tuning range of about 90 MHz. Using similar approaches and combining them with the possibility to adjust the SQUID size, the desired critical currents, and the operation temperature by at least one order of magnitude opens a very large parameter space for the design of nonlinearities, flux tunabilities, and responsivities.

The most interesting open questions to be investigated in future experiments are the circuit characteristics at temperatures in the millikelvin regime and in large magnetic fields, the exact origin of the microwave losses in the nanoconstriction circuits, and possibilities to reduce them, as well as a theoretical and experimental investigation of the noise characteristics in such devices. Finally, it will be interesting to investigate possibilities to further reduce the critical currents and the screening parameters, by potentially further reducing the size of the nanoconstrictions in all three dimensions.

All data presented in this paper and the corresponding processing scripts used during the analysis are publicly available online [59].

## ACKNOWLEDGMENTS

We gratefully acknowledge technical support by M. Turad and R. Löffler (both LISA<sup>+</sup>) and by C. Back. We acknowledge funding by the Deutsche Forschungsgemeinschaft (DFG) via Grants No. BO 6068/1-1, No. BO 6068/2-1, and No. KO 1303/13-2, and support from

the COST actions NANOCOBYBRI (CA16218) and SUPERQUMAP (CA21144). J.P. acknowledges support from the Cusanuswerk, Bischöfliche Studienförderung.

## APPENDIX A: DEVICE FABRICATION

In this appendix, the sample fabrication is described step by step, and a schematic representation of the nanoconstriction fabrication based on Ne-FIB milling is shown in Fig. 5.

**Step 1: microwave cavity patterning.** The fabrication starts with sputtering 90-nm niobium (Nb) on top of a high-resistivity ( $\rho > 10 \text{ k}\Omega \text{ m}$ ) intrinsic 2-in. silicon wafer. The wafer thickness is 500  $\mu\text{m}$ . Then, the complete wafer is covered with a 600-nm-thick layer of ma-P 1205 photoresist by spin coating and structured by means of maskless scanning laser photolithography ( $\lambda_{\text{Laser}} = 365 \text{ nm}$ ). After development of the resist in ma-D 331/S for 40 s, the patterned side of the wafer is etched by means of reactive ion etching using  $\text{SF}_6$ . For cleaning, the wafer is finally rinsed in multiple subsequent baths of acetone and isopropanol.

**Step 2: dicing and mounting for precharacterization.** At the end of the microwave cavity fabrication, the wafer is diced into individual  $10 \times 10 \text{ mm}^2$  chips. These chips are individually mounted onto a PCB, where they are wirebonded to microwave feedlines and ground, and the complete set of chip and PCB is packaged into a radiation-tight copper housing. After mounting into the measurement setup, the precharacterization of the device is performed.

**Step 3: 2D and 3D constriction fabrications.** Each precharacterized LC circuit contains a square-shaped Nb loop structure with inner dimensions of  $6 \times 6 \mu\text{m}^2$  and a conductor strip width of 3  $\mu\text{m}$ ; see Fig. 1. Two nanoconstrictions are patterned into the opposite sides of the loops using the focused ion beam of a neon ion microscope (NIM). The NIM allows for high-precision milling with a nanoscaled spot-size Ne FIB. For the 2D constrictions, two approximately 20-nm-wide slot-shaped rectangles are ion milled simultaneously from both sides into each loop strip with a dose of 20 000 ions/ $\text{nm}^2$  and an accelerating voltage of 20 kV. Simultaneous here means that the neon beam is scanned in a pattern that alternates repeatedly between the left and the right slots. In between the two slots, a milling gap of 40 nm is left untouched, where the 2D constriction is formed. The 3D constriction patterning is performed in the same way, but additionally and again simultaneously to the slot rectangles the constriction is milled from the top with a third rectangle, but with a lower ion dose. The exact value of the constriction dose defines its remaining thickness. For the 3D<sub>1</sub> and 3D<sub>2</sub> samples, the doses were 7500 and 8500 ions/ $\text{nm}^2$ , respectively.

**Step 4: device mounting.** After the Ne-FIB cutting process the sample is mounted in the same way as in step 2.

## APPENDIX B: MEASUREMENT SETUP

Both the junctionless circuits and the SQUID cavities, here generically labeled as the devices under test (DUTs), are characterized in an evacuated sample space located at the end of a cryostat dipstick, which is introduced into

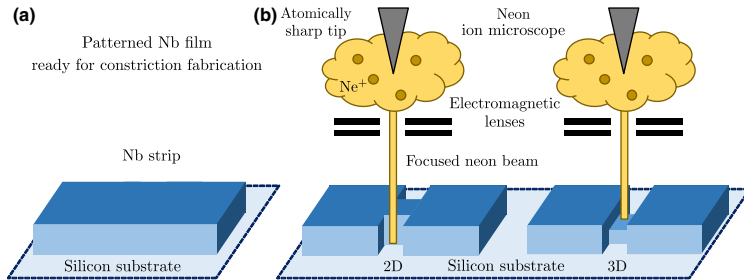


FIG. 5. Schematic niobium nanoconstriction fabrication using a neon focused ion beam. (a) Niobium (Nb) strip on a silicon substrate prepared for cutting a nanoconstriction into it. (b) Fabrication of the two different constriction types discussed in this study using a neon ion microscope (NIM): left, 2D constriction; right, 3D constriction. The NIM has an atomically sharp beam source (tip) maintained at a high voltage of 20 kV. Neon gas around the tip gets ionized and the ions are accelerated and focused through several electromagnetic lenses to form a Ne FIB with a nanoscaled spot size (about 0.5 nm). For the 2D constrictions, the strip is patterned by cutting two narrow slots from both sides into the strip. Therefore, the nanobridge has the same height as the remaining niobium leads. For the 3D constrictions, the constriction is also milled and thinned down from the top simultaneously with the slot cutting, just with a smaller ion dose.

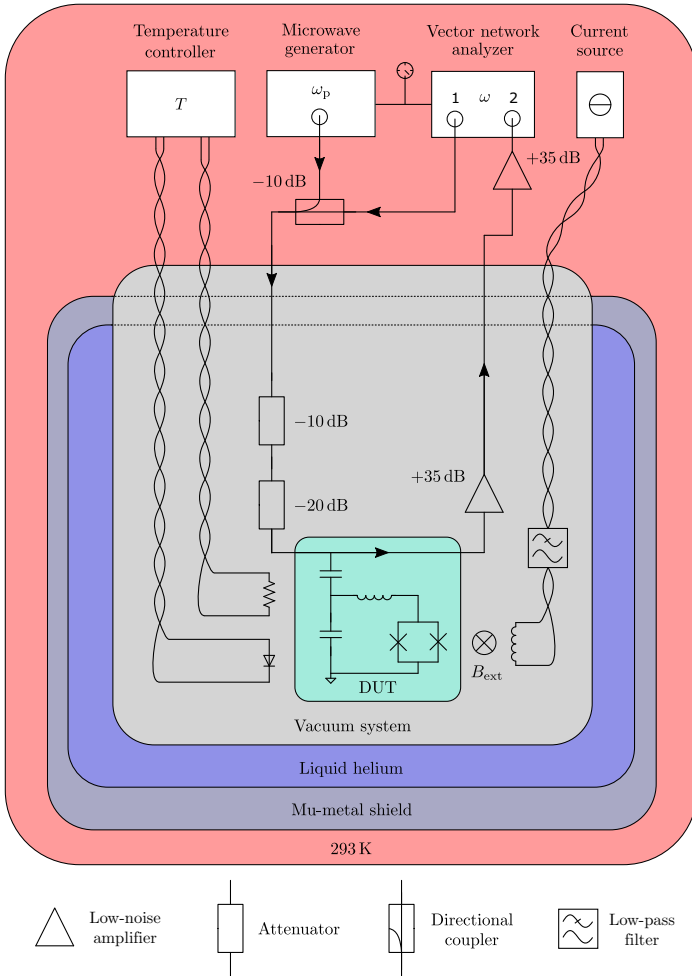


FIG. 6. Schematic of the measurement setup. In the drawing, the isolation vacuum shield in between the helium container and the outer world is omitted. Detailed information is given in the text.

a liquid helium cryostat. The cryostat is covered by a double-layer room-temperature mu-metal shield to provide magnetic shielding for the whole sample space. A schematic illustration of the measurement setup is shown in Fig. 6. The DUT inside the copper housing is attached to a copper mounting bracket and a magnet coil for the

application of a magnetic field perpendicular to the chip surface  $B_{ext}$ . The magnet coil is connected to a low-noise current source at room temperature with a twisted pair of copper wires. The magnet wires are low-pass filtered at cryogenic temperature with a cutoff frequency at about 3 kHz. Additionally, the DUT is connected to two coaxial

lines for input and output of the microwave signals. A temperature diode is attached to the sample housing in close proximity to the sample and both are coupled to the liquid helium bath via the copper mounting bracket and through helium exchange gas. For controlling the sample temperature  $T_s$ , the diode is glued with varnish to the DUT copper housing and a manganin heating resistor (made of a twisted wire pair to avoid stray magnetic fields) is placed nearby. Both the temperature diode (four wires) and the heating resistor (two wires) are also connected via twisted pairs of copper wire to a temperature controller.

The SQUID cavities are designed in a side-coupled geometry. Therefore, the input and output signals are sent and received through two separate coaxial lines in order to measure the transmission spectrum  $S_{21}$  of the DUT by a VNA. The input line is attenuated by  $-30$  dB in order to balance the thermal radiation from room temperature to the cryostat temperature. The attenuators are mounted in close proximity to the sample in the sample vacuum space and we assume that they have a temperature  $T_{\text{att}} \approx T_s$ . For amplification of the weak microwave signal used here, a cryogenic high-electron-mobility-transistor (HEMT) amplifier and a room-temperature amplifier are mounted in the output line. The cryogenic HEMT is placed close to the DUT in order to minimize signal losses in between the sample and the amplifier chain.

For the two-tone experiment, an additional fixed-frequency microwave pump tone with frequency  $\omega_p$  and power  $P_p$  is sent to the DUT. This pump tone is generated by a microwave generator and combined via a 10-dB directional coupler with the VNA signal before entering the cryostat. In the experiment the VNA and microwave generator are both referenced to the 10-MHz clock of the generator.

For cooling the device to temperatures below that of liquid helium  $T_{\text{He}} = 4.2$  K, we pump at the helium dewar of the cryostat and reach down to  $T_{s,\text{min}} \lesssim 2.4$  K with the current setup. To achieve high-stability ( $\Delta T_s < 1$  mK) temperature control in the most relevant range for this work,  $2.4 \lesssim T_s \lesssim 3.5$  K, we use the helium pumping and additionally heat the sample with the heating resistor whose power is controlled via a proportional–integral–derivative feedback loop by the temperature controller.

## APPENDIX C: CIRCUIT RESPONSE MODEL

### 1. Equation of motion and general considerations

We model the classical intracavity field  $\alpha$  of the SQUID circuits with Kerr nonlinearity and nonlinear damping using the equation of motion [28,60]

$$\dot{\alpha} = \left[ i(\omega_c + \mathcal{K}|\alpha|^2) - \frac{\kappa + \kappa_{\text{nl}}|\alpha|^2}{2} \right] \alpha + i\sqrt{\frac{\kappa_c}{2}} S_{\text{in}}. \quad (\text{C1})$$

Here,  $\omega_c$  is the cavity resonance frequency ( $= \omega_b$  before cutting and  $= \omega_0$  after),  $\mathcal{K}$  is the Kerr nonlinearity (frequency shift per photon),  $\kappa$  is the bare total linewidth ( $= \kappa_b$  before cutting and  $= \kappa_0$  after),  $\kappa_{\text{nl}}$  is the nonlinear damping constant,  $\kappa_c$  is the external linewidth ( $= \kappa_{c,b}$  before cutting), and  $S_{\text{in}}$  is the input field. The intracavity field is normalized such that  $|\alpha|^2 = n_c$  corresponds to the intracavity photon number  $n_c$  and  $|S_{\text{in}}|^2$  to the input photon flux (photons per second) on the coplanar waveguide feedline.

The solution of this equation of motion significantly depends on the pump power and the number of tones sent to the cavity. The ideal transmission response function, however, will always be of the form

$$S_{21}^{\text{ideal}} = 1 + i\sqrt{\frac{\kappa_c}{2}} \frac{\alpha}{S_{\text{in}}} \quad (\text{C2})$$

with the solution of interest  $\alpha$ .

### 2. The linear single-tone regime

In the linear single-tone regime, we set  $\mathcal{K} = \kappa_{\text{nl}} = 0$ . Then, we can solve the remaining equation by Fourier transformation and obtain

$$\alpha = \frac{i\sqrt{\kappa_c/2}}{\kappa/2 + i(\omega - \omega_c)} S_{\text{in}}. \quad (\text{C3})$$

The ideal transmission response of a capacitively side-coupled and linear  $LC$  circuit is then given by

$$S_{21}^{\text{ideal}} = 1 - \frac{\kappa_c}{\kappa + 2i(\omega - \omega_c)}. \quad (\text{C4})$$

### 3. The nonlinear single-tone regime

In the nonlinear single-tone regime, we have to solve the full equation of motion and start by setting the input field to  $S_{\text{in,st}} = S_0 e^{i\phi_p} e^{i\omega t}$  with real valued  $S_0$ . For the intracavity field, we make the ansatz  $\alpha(t) = \alpha_0 e^{i\omega t}$  with real valued  $\alpha_0$ . The phase delay between input and response is encoded in  $\phi_p$ . Then the equation of motion reads

$$i\omega\alpha_0 = \left[ i(\omega_c + \mathcal{K}\alpha_0^2) - \frac{\kappa + \kappa_{\text{nl}}\alpha_0^2}{2} \right] \alpha_0 + i\sqrt{\frac{\kappa_c}{2}} S_0 e^{i\phi_p}, \quad (\text{C5})$$

which after multiplication with its complex conjugate yields the characteristic polynomial for the intracircuit photon number  $n_c = \alpha_0^2$ :

$$n_c^3 \left[ \mathcal{K}^2 + \frac{\kappa_{\text{nl}}^2}{4} \right] + n_c^2 \left[ \frac{\kappa\kappa_{\text{nl}}}{2} - 2\mathcal{K}\Delta \right] + n_c \left[ \Delta^2 + \frac{\kappa^2}{4} \right] - \frac{\kappa_c}{2} S_0^2 = 0. \quad (\text{C6})$$

Here  $\Delta = \omega - \omega_c$  is the detuning between the microwave input tone and the bare cavity resonance. The real-valued

roots of this polynomial correspond to the physical solutions for the amplitude  $\alpha_0$ ; the highest and lowest amplitudes are the stable states in the case of three real-valued roots.

For the complete complex transmission, we also need the phase  $\phi_p$ , which we obtain via

$$\phi_p = \text{atan2}\left(-\frac{\kappa + \kappa_{\text{nl}} n_c}{2}, \Delta - \mathcal{K} n_c\right). \quad (C7)$$

Having both parts of the complex field solution at hand, we can also calculate the transmission

$$S_{21,\text{nl}}^{\text{ideal}} = 1 + i\sqrt{\frac{\kappa_c}{2}} \frac{\alpha_0}{S_0} e^{-i\phi_p}. \quad (C8)$$

Note that we do not use these equations for any data analysis in this manuscript, but we include them for pedagogical reasons, since they facilitate understanding the two-tone regime.

#### 4. The linearized two-tone regime

In the two-tone experiments, we apply a strong pump tone with fixed frequency  $\omega_p$  and fixed power  $P_p$  and probe the cavity response with a weak additional scanning tone; the total input is then  $S_{\text{in,tt}} = S_0 e^{i\phi_p} e^{i\omega_p t} + S_{\text{pr}}(t) e^{i\omega_p t}$ . The probe input amplitude  $S_{\text{pr}}(t)$  is time dependent and complex valued. As an ansatz for the intracavity field, we choose  $\alpha(t) = \alpha_0 e^{i\omega_p t} + \alpha_{\text{pr}}(t) e^{i\omega_p t}$  with a complex and time dependent  $\alpha_{\text{pr}}(t)$  and obtain the equation of motion

$$\begin{aligned} i\omega_p \alpha_0 + i\omega_p \alpha_{\text{pr}} + \dot{\alpha}_{\text{pr}} &= i[\omega_c + \mathcal{K}(\alpha_0^2 + \alpha_0(\alpha_{\text{pr}} + \alpha_{\text{pr}}^*) + |\alpha_{\text{pr}}|^2)]\alpha_0 \\ &+ i[\omega_c + \mathcal{K}(\alpha_0^2 + \alpha_0(\alpha_{\text{pr}} + \alpha_{\text{pr}}^*) + |\alpha_{\text{pr}}|^2)]\alpha_{\text{pr}} \\ &- \left[\frac{\kappa}{2} + \frac{\kappa_{\text{nl}}}{2}(\alpha_0^2 + \alpha_0(\alpha_{\text{pr}} + \alpha_{\text{pr}}^*) + |\alpha_{\text{pr}}|^2)\right]\alpha_0 \\ &- \left[\frac{\kappa}{2} + \frac{\kappa_{\text{nl}}}{2}(\alpha_0^2 + \alpha_0(\alpha_{\text{pr}} + \alpha_{\text{pr}}^*) + |\alpha_{\text{pr}}|^2)\right]\alpha_{\text{pr}} \\ &+ i\sqrt{\frac{\kappa_c}{2}} S_0 e^{i\phi_p} + i\sqrt{\frac{\kappa_c}{2}} S_{\text{pr}}. \end{aligned} \quad (C9)$$

Now we perform the linearization, i.e., we drop all terms not linear in the small quantity  $\alpha_{\text{pr}}$  and get

$$\begin{aligned} i\omega_p \alpha_0 + i\omega_p \alpha_{\text{pr}} + \dot{\alpha}_{\text{pr}} &= \left[i(\omega_c + \mathcal{K} n_c) - \frac{\kappa + \kappa_{\text{nl}} n_c}{2}\right]\alpha_0 \\ &+ \left[i\mathcal{K} - \frac{\kappa_{\text{nl}}}{2}\right]n_c \alpha_{\text{pr}} + i\sqrt{\frac{\kappa_c}{2}} S_0 e^{i\phi_p} + i\sqrt{\frac{\kappa_c}{2}} S_{\text{pr}}. \end{aligned} \quad (C10)$$

The time-independent terms are identical to Eq. (C6) of the nonlinear single-tone experiment and allow one to determine  $\alpha_0$  and  $n_c$  via the characteristic polynomial now. The remaining equation can be Fourier transformed to give

$$\frac{\alpha_{\text{pr}}}{\chi_{\text{pr}}} = \left[i\mathcal{K} - \frac{\kappa_{\text{nl}}}{2}\right]n_c \bar{\alpha}_{\text{pr}} + i\sqrt{\frac{\kappa_c}{2}} S_{\text{pr}}, \quad (C11)$$

where

$$\chi_{\text{pr}} = \frac{1}{(\kappa + 2\kappa_{\text{nl}} n_c)/2 + i(\Delta_p - 2\mathcal{K} n_c + \Omega)} \quad (C12)$$

with  $\bar{\alpha}_{\text{pr}} = \alpha_{\text{pr}}^*(-\Omega)$ , the detuning between the pump and bare cavity resonance  $\Delta_p = \omega_p - \omega_c$ , and the probe frequency with respect to the pump  $\Omega = \omega - \omega_p$ .

Using the equivalent equation for  $\bar{\alpha}_{\text{pr}}$  with  $\bar{S}_{\text{pr}} = 0$ , we get

$$\alpha_{\text{pr}} = i\chi_{\text{g}} \sqrt{\frac{\kappa_c}{2}} S_{\text{pr}} \quad (C13)$$

with

$$\chi_{\text{g}} = \frac{\chi_{\text{pr}}}{1 - [\mathcal{K}^2 + \kappa_{\text{nl}}^2/4]n_c^2 \chi_{\text{pr}} \bar{\chi}_{\text{pr}}}, \quad (C14)$$

and, for the two-tone transmission parameter,

$$S_{21,\text{tt}}^{\text{ideal}} = 1 - \frac{\kappa_c}{2} \chi_{\text{g}}. \quad (C15)$$

#### 5. The pumped Kerr modes

To find the resonance frequencies of the susceptibility  $\chi_{\text{g}}$ , we solve the complex frequency for which  $\chi_{\text{g}}^{-1} = 0$ . The condition is

$$1 - \left[\mathcal{K}^2 + \frac{\kappa_{\text{nl}}^2}{4}\right]n_c^2 \chi_{\text{pr}} \bar{\chi}_{\text{pr}} = 0, \quad (C16)$$

which is solved by

$$\begin{aligned} \tilde{\omega}_{1,2} &= \omega_p + i\frac{\kappa + 2\kappa_{\text{nl}} n_c}{2} \\ &\pm \sqrt{(\Delta_p - \mathcal{K} n_c)(\Delta_p - 3\mathcal{K} n_c) - \kappa_{\text{nl}}^2 n_c^2/4}. \end{aligned} \quad (C17)$$

The real part corresponds to the resonance frequency  $\omega_{1,2} = \text{Re}(\tilde{\omega}_{1,2})$  and the imaginary part corresponds to half

the mode linewidth  $\kappa_{1,2} = 2 \text{Im}(\tilde{\omega}_{1,2})$ . So, in the regime where the argument of the square root is  $> 0$  (always true for our experimental parameters), the system has two resonances

$$\omega_{1,2} = \omega_p \pm \sqrt{(\Delta_p - \mathcal{K}n_c)(\Delta_p - 3\mathcal{K}n_c) - \frac{\kappa_{nl}^2 n_c^2}{4}}, \quad (\text{C18})$$

split symmetrically around the pump frequency. In the experiment and with the parameters we are using, we observe only one of the two modes though, the one at  $\omega_2 = \omega'_0$ . The shift of this mode with respect to its unpumped frequency  $\omega_0$  is given by

$$\delta\omega_0 = \Delta_p - \sqrt{(\Delta_p - \mathcal{K}n_c)(\Delta_p - 3\mathcal{K}n_c) - \frac{\kappa_{nl}^2 n_c^2}{4}}. \quad (\text{C19})$$

When we measure the pumped resonance, we also extract the pumped linewidth

$$\kappa_p = \kappa_0 + 2\kappa_{nl}n_c, \quad (\text{C20})$$

and so the only free parameter when fitting the resonance frequency shift versus pump photon number (see the next subsection) using Eq. (C19) is the Kerr constant  $\mathcal{K}$ . For brevity, we also introduce the short version

$$\kappa_1 = \kappa_{nl}n_c. \quad (\text{C21})$$

## 6. The intracircuit pump photon number

One might expect that we need to know the value of  $\mathcal{K}$  to calculate the intracircuit pump photon number from the pump-induced frequency shift and linewidth broadening. This is not the case though, which allows us to first determine  $n_c$  and subsequently fit the frequency shift  $\delta\omega_0$  as a function of  $n_c$  to extract  $\mathcal{K}$  from the data. We start by setting  $\mathcal{K}n_c = x$  and then solving the characteristic polynomial equation (C6) for  $x$ . We get (assuming that  $n_c > 0$ )

$$x_{1/2} = \Delta_p \pm \sqrt{\frac{\kappa_e n_{in}}{2} - \frac{\kappa_{\text{eff}}^2}{4}}, \quad (\text{C22})$$

where  $n_{in} = S_0^2$  and  $\kappa_{\text{eff}} = \kappa_0 + \kappa_1$ . The solution we are interested in is  $x_2$ . Substituting this into Eq. (C19), the frequency relative to the drive

$$\delta = \sqrt{(\Delta_p - x_2)(\Delta_p - 3x_2) - \frac{\kappa_1^2}{4}} \quad (\text{C23})$$

leads to

$$\delta^2 = \sqrt{\frac{\kappa_e n_{in}}{2} - \frac{\kappa_{\text{eff}}^2}{4}} \left( 3\sqrt{\frac{\kappa_e n_{in}}{2} - \frac{\kappa_{\text{eff}}^2}{4}} - 2\Delta_p \right) - \frac{\kappa_1^2}{4}. \quad (\text{C24})$$

We can solve this equation for  $n_c$ , finding that

$$n_c = \frac{2P_p}{\hbar\omega_p} \frac{\kappa_e}{\kappa_{\text{eff}}^2 + 4\Delta^2} \quad (\text{C25})$$

with the effective detuning

$$\Delta^2 = \frac{2}{9} \left[ \Delta_p^2 + \Delta_p \sqrt{\Delta_p^2 + 3\delta_k^2} + \frac{3}{2}\delta_k^2 \right] \quad (\text{C26})$$

and

$$\delta_k^2 = \delta^2 + \frac{\kappa_1^2}{4}. \quad (\text{C27})$$

## APPENDIX D: ADDITIONAL DATA

### 1. Impact of junction cutting in devices 2D and 3D<sub>2</sub>

In Fig. 1(f), we present the resonances of device 3D<sub>1</sub> before and after cutting the nanoconstrictions at  $T_s = 2.5$  K. From the resonance frequencies before and after cutting,  $\omega_b$  and  $\omega_0$ , respectively, we determine the inductance of a single constriction  $L_c$  in the device via

$$L_c = 2L \left( \frac{\omega_b^2}{\omega_0^2} - 1 \right); \quad (\text{D1})$$

see Notes II and III within the Supplemental Material [37]. In Fig. 7 we show the analogous data for the other two devices of this work, circuits 2D and 3D<sub>2</sub>.

The resonance frequency of device 2D has shifted by the cutting from  $\omega_b = 2\pi \cdot 3.995$  GHz to  $\omega_0 = 2\pi \cdot 3.981$  GHz, which corresponds to a constriction inductance  $L_c^{2D} \approx 8.4$  pH. The total linewidth has increased from  $\kappa_b = 2\pi \cdot 1.5$  MHz to  $\kappa_0 = 2\pi \cdot 2.4$  MHz. In device 3D<sub>2</sub> the impact of the shift was much larger: the resonance frequency shifted from  $\omega_b = 2\pi \cdot 5.047$  GHz to  $\omega_0 = 2\pi \cdot 4.811$  GHz, which corresponds to  $L_c^{3D2} \approx 103$  pH. The linewidth increased from  $\kappa_b = 2\pi \cdot 2.3$  MHz to  $\kappa_0 = 2\pi \cdot 24.2$  MHz. The observation that the increase in the linewidths  $\kappa$  is stronger for a larger constriction inductance is not surprising. As we have shown in Fig. 3, the critical temperature of the constrictions is more suppressed for thinner constrictions, and so at the fixed temperature 2.5 K the thinner constrictions presumably have a higher thermal quasiparticle density and at the same time a higher microwave current density. At this point we cannot exclude that there are also other mechanisms at play such as normal conducting contributions at the surfaces or edges of the constrictions that might increase with neon ion milling time, but the overall trend is understandable quite intuitively from the critical temperature suppression. In Note V within the Supplemental Material [37], we also discuss the dependence of the linewidths on the magnetic flux through the SQUIDS.

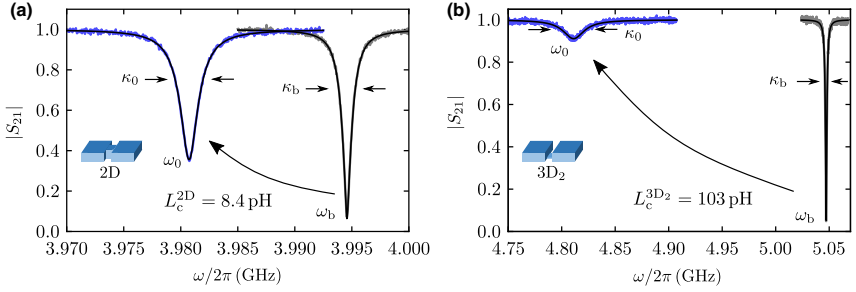


FIG. 7. Impact of constriction cutting in the 2D and 3D<sub>2</sub> circuits. (a) Transmission  $|S_{21}|$  versus the probe frequency of circuit 2D before junction cutting (right, gray noisy line) and after junction cutting at the flux sweetspot (left, blue noisy line). (b) Equivalent to (a), but for the 3D<sub>2</sub> circuit. Both panels: noisy lines are data and black smooth lines are fits. Measurement temperature  $T_s = 2.5$  K. The resonance frequency and linewidth are  $\omega_b$  and  $\kappa_b$  before cutting and  $\omega_0$  and  $\kappa_0$  after cutting. From the shift, we determine the additional inductance in the circuit  $L_c/2$  (two constrictions in parallel). Values for  $\omega_b, \kappa_b, \omega_0, \kappa_0$  can be found in the text.

## 2. Flux-tuning curves versus the sample temperature in devices 2D and 3D<sub>2</sub>

In Fig. 3(a) we show flux-tuning curves of the resonance frequency  $\omega_0(\Phi_{\text{ext}})$  for varying sample temperature  $T_s$  in circuit 3D<sub>1</sub> and derive from those the critical currents  $I_0(T_s)$  and the screening parameters  $\beta_L(T_s)$ . Since we also show  $I_0(T_s)$  and  $\beta_L(T_s)$  for the 2D and 3D<sub>2</sub> devices, we present in Figs. 8(a) and 8(b) the corresponding flux-tuning curves for completeness. For both devices, the sweetspot frequency at  $\Phi_{\text{ext}} = 0$  decreases with increasing  $T_s$  due to the increasing constriction inductance. At the same time the flux-tuning arches get narrower due to a decreasing screening parameter  $\beta_L$  and an increasing inductance participation ratio  $L_c/L$ , and the flux-tuning range  $\omega_0^{\text{max}} - \omega_0^{\text{min}}$  increases for the same reasons. At the highest temperatures, circuit 2D has a tuning range of about 13 MHz and circuit 3D<sub>2</sub> of about 150 MHz. From the fits to the data, we extract the screening parameter  $\beta_L$  and the linear constriction contribution  $L_{\text{lin}}$  and calculate the critical current  $I_0$ . The screening parameter  $\beta_L$  and the critical current  $I_0$  are shown in Figs. 3(b) and 3(c); the linear inductance contributions  $L_{\text{lin}}$  for all three circuits are shown and discussed in Note V within the Supplemental Material [37].

Since the linear inductances in the circuit have a kinetic contribution, the temperature-dependent resonance frequency at the flux sweetspot can be written as

$$\omega_0(T_s) = \frac{1}{\sqrt{C_{\text{tot}}[(L(T_s) + L_{J0}(T_s) + L_{\text{lin}}(T_s))]}}, \quad (\text{D2})$$

where  $L_{J0} = \Phi_0[2\pi I_0(T_s)]^{-1}$ . In Fig. 8(c), we show the resonance frequency at the sweetspot of all three devices.

## APPENDIX E: CALCULATION OF THE KERR NONLINEARITY

For the calculation of the Kerr nonlinearity  $\mathcal{K}$ , we follow the method described in Ref. [56] and start with the effective one-dimensional potential for the SQUID, in which each SQUID arm is considered individually (see also Ref. [28]):

$$U = \frac{1}{2}E_{\text{arm}}(\varphi_{\text{left}} - \varphi_1)^2 + \frac{1}{2}E_{\text{arm}}(\varphi_{\text{right}} - \varphi_2)^2 - E_J \cos \varphi_1 - E_J \cos \varphi_2. \quad (\text{E1})$$

Here  $\varphi_1, \varphi_2$  are the phase differences of the two Josephson junctions,  $\varphi_{\text{left}}$  and  $\varphi_{\text{right}}$  are the total phase differences of the left half and the right half of the SQUID loop including the JJs, and the energies are given by

$$E_J = \frac{\Phi_0 I_0}{2\pi}, \quad E_{\text{arm}} = \frac{\Phi_0^2}{4\pi^2 L_{\text{arm}}} \quad (\text{E2})$$

with  $L_{\text{arm}} = L_{\text{loop}}/2 + L_{\text{lin}}$ . From fluxoid quantization in the SQUID, it follows that

$$\varphi_{\text{right}} - \varphi_{\text{left}} = \varphi_{\text{ext}}, \quad (\text{E3})$$

where  $\varphi_{\text{ext}} = 2\pi \Phi_{\text{ext}}/\Phi_0$  is the phase introduced by the external flux. For a visualization of all variables used in this appendix, see Fig. 9.

Then, the potential can be written as a function of a single phase variable  $\varphi_s = \varphi_{\text{left}}$  as

$$U[\varphi_s] = \frac{1}{2}E_{\text{arm}}(\varphi_s - \varphi_1[\varphi_s])^2 + \frac{1}{2}E_{\text{arm}}(\varphi_s - \varphi_2[\varphi_s] - \varphi_{\text{ext}})^2 - E_J \cos \varphi_1[\varphi_s] - E_J \cos \varphi_2[\varphi_s], \quad (\text{E4})$$

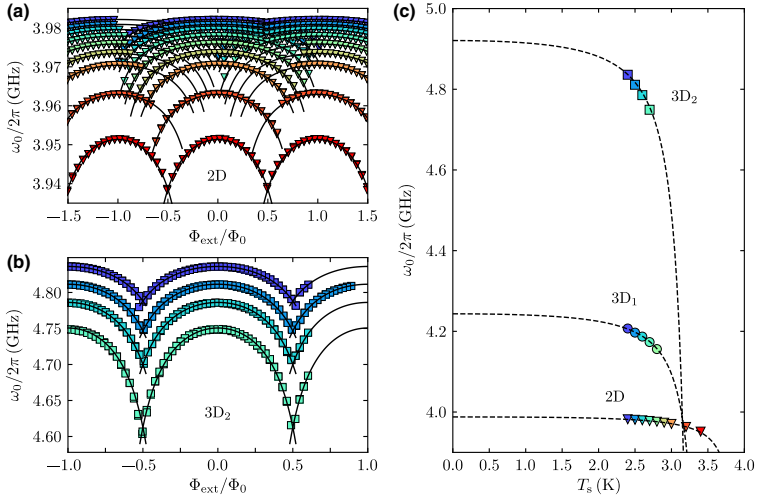


FIG. 8. Temperature dependence of the flux-tuning curves and the sweetspot resonance frequencies. (a) Resonance frequency versus the external bias flux  $\omega_0(\Phi_{\text{ext}})$  in device 2D; symbols are data and lines are fits. Data have been taken at temperatures  $T_s = (2.4, 2.5, 2.6, 2.7, 2.8, 2.9, 3.0, 3.2, 3.4)$  K (in order from top to bottom). (b) Equivalent of (a), but for device 3D<sub>2</sub>. Temperatures are  $T_s = (2.4, 2.5, 2.6, 2.7)$  K. Data are partly incomplete due to hysteretic jumps (device 2D) and due to insufficient flux data ( $\Phi_{\text{ext}}/\Phi_0 > 0.65$  in device 3D<sub>2</sub>). (c) Resonance frequency of all three circuits at the sweetspot frequency ( $\Phi_{\text{ext}} = 0$ ) versus the temperature  $T_s$ . Symbols are data and the dashed lines are calculated theory lines using Eq. (D2).

and as boundary conditions we have the current conservation relations [56]

$$\varphi_s = \varphi_1 + \zeta \sin \varphi_1, \quad (\text{E5})$$

$$\varphi_s = \varphi_2 + \zeta \sin \varphi_2 - \varphi_{\text{ext}}, \quad (\text{E6})$$

where  $\zeta = E_{\text{arm}}/E_J = L_{J0}/L_{\text{arm}}$ .

In order to find the Kerr nonlinearity, we have to Taylor expand the potential up to fourth order, i.e.,

$$\begin{aligned} \frac{U(\varphi_s)}{E_J} &= c_0 + c_1(\varphi_s - \varphi_{s,\text{min}}) + \frac{c_2}{2}(\varphi_s - \varphi_{s,\text{min}})^2 \\ &+ \frac{c_3}{6}(\varphi_s - \varphi_{s,\text{min}})^3 + \frac{c_4}{24}(\varphi_s - \varphi_{s,\text{min}})^4, \quad (\text{E7}) \end{aligned}$$

where the coefficients are determined by the  $n$ th derivative of the potential evaluated at the phase at the potential well minimum  $\varphi_{s,\text{min}}$ :

$$c_n = \frac{1}{E_J} \left. \frac{\partial^n U}{\partial \varphi_s^n} \right|_{\varphi_{s,\text{min}}}. \quad (\text{E8})$$

To find the value for  $\varphi_{s,\text{min}}$ , we demand that in the minimum we have  $c_1 = 0$  and, as a result, we get

$$\varphi_{s,\text{min}} = \frac{1}{2}(\varphi_{1,\text{min}} + \varphi_{2,\text{min}} - \varphi_{\text{ext}}). \quad (\text{E9})$$

In the potential minimum, however, i.e., without any phase excitation, we also have

$$\sin \varphi_{1,\text{min}} = -\sin \varphi_{2,\text{min}} \implies \varphi_{1,\text{min}} = -\varphi_{2,\text{min}}, \quad (\text{E10})$$

since the same SQUID circulating current  $J = -I_0 \sin \varphi_1 = I_0 \sin \varphi_2$  is flowing through both JJs in opposite directions. Then, using Eq. (E9), we can conclude that

$$\varphi_{s,\text{min}} = -\frac{\varphi_{\text{ext}}}{2}, \quad (\text{E11})$$

and using Eq. (E5), we arrive at

$$\varphi_{1,\text{min}} + \zeta \sin \varphi_{1,\text{min}} + \frac{\varphi_{\text{ext}}}{2} = 0, \quad (\text{E12})$$

which is completely equivalent to

$$\frac{\Phi}{\Phi_0} = \frac{\Phi_{\text{ext}}}{\Phi_0} - \frac{\beta_L}{2} \sin \left( \pi \frac{\Phi}{\Phi_0} \right) \quad (\text{E13})$$

with screening parameter  $\beta_L$ , total flux in the SQUID  $\Phi$ , and using the relation  $\varphi_{1,\text{min}} = -\pi(\Phi)/\Phi_0$ . For the

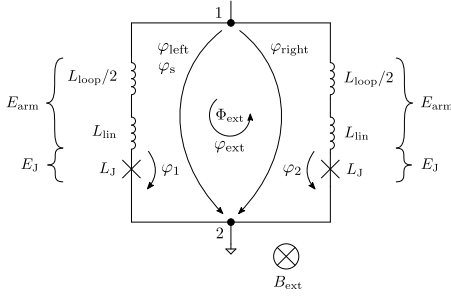


FIG. 9. Schematic SQUID circuit with definitions of all variables used for the calculation of the Kerr constant. Circuit equivalent of the SQUID with a linear loop inductance  $L_{\text{loop}}/2$  in each arm and a constriction modeled by a linear inductance  $L_{\text{lin}}$  and a sinusoidal Josephson contribution  $L_J$ . In each arm the energy  $E_J + E_{\text{arm}}$  is stored, where  $E_J$  is the Josephson energy and  $E_{\text{arm}}$  is the energy stored in the linear contribution. Nodes 1 and 2 subdivide the loop into a left half and right half with total phase differences  $\varphi_{\text{left}}$  and  $\varphi_{\text{right}}$  between the nodes. The single phase variable  $\varphi_s$  is identical to  $\varphi_{\text{left}}$ . The Josephson contributions of the arms have phase differences  $\varphi_1$  and  $\varphi_2$ , respectively. By applying an external magnetic field  $B_{\text{ext}}$  perpendicular to the SQUID loop, an external phase  $\varphi_{\text{ext}}$  is introduced by the external flux  $\Phi_{\text{ext}}$ .

derivatives, we get

$$\frac{\partial U}{\partial \varphi_s} = E_{\text{arm}}(2\varphi_s - \varphi_1[\varphi_s] - \varphi_2[\varphi_s] + \varphi_{\text{ext}}), \quad (\text{E14})$$

$$\frac{\partial^2 U}{\partial \varphi_s^2} = E_{\text{arm}} \left( 2 - \frac{\partial \varphi_1}{\partial \varphi_s} - \frac{\partial \varphi_2}{\partial \varphi_s} \right), \quad (\text{E15})$$

$$\frac{\partial^3 U}{\partial \varphi_s^3} = -E_{\text{arm}} \left( \frac{\partial^2 \varphi_1}{\partial \varphi_s^2} + \frac{\partial^2 \varphi_2}{\partial \varphi_s^2} \right), \quad (\text{E16})$$

$$\frac{\partial^4 U}{\partial \varphi_s^4} = -E_{\text{arm}} \left( \frac{\partial^3 \varphi_1}{\partial \varphi_s^3} + \frac{\partial^3 \varphi_2}{\partial \varphi_s^3} \right), \quad (\text{E17})$$

and we can obtain the phase derivatives from Eqs. (E5) and (E6) as

$$\frac{\partial \varphi_s}{\partial \varphi_1} = 1 + \zeta \cos \varphi_1, \quad (\text{E18})$$

$$\frac{\partial \varphi_s}{\partial \varphi_2} = 1 + \zeta \cos \varphi_2, \quad (\text{E19})$$

which can be inverted as

$$\frac{\partial \varphi_1}{\partial \varphi_s} = \frac{1}{1 + \zeta \cos \varphi_1}, \quad (\text{E20})$$

$$\frac{\partial \varphi_2}{\partial \varphi_s} = \frac{1}{1 + \zeta \cos \varphi_2}. \quad (\text{E21})$$

The consecutive derivatives are, for  $j = 1, 2$ ,

$$\frac{\partial^2 \varphi_j}{\partial \varphi_s^2} = \frac{\zeta \sin \varphi_j}{(1 + \zeta \cos \varphi_j)^3}, \quad (\text{E22})$$

$$\frac{\partial^3 \varphi_j}{\partial \varphi_s^3} = \frac{\zeta \cos \varphi_j (1 + \zeta \cos \varphi_j) + 3\zeta^2 \sin^2 \varphi_j}{(1 + \zeta \cos \varphi_j)^5}, \quad (\text{E23})$$

which we can finally use to express our Taylor coefficients with  $\varphi_0 = -\varphi_{1,\text{min}} = \pi(\Phi)/\Phi_0$  as

$$c_2 = \frac{2 \cos \varphi_0}{1 + \zeta \cos \varphi_0}, \quad (\text{E24})$$

$$c_3 = 0, \quad (\text{E25})$$

$$c_4 = -2 \frac{\cos \varphi_0 (1 + \zeta \cos \varphi_0) + 3\zeta \sin^2 \varphi_0}{(1 + \zeta \cos \varphi_0)^5}. \quad (\text{E26})$$

The SQUID inductance and Kerr nonlinearity of the SQUID, when shunted with  $C_{\text{tot}}$ , are now given by [56]

$$L_s = \frac{L_{J0}}{c_2} = \frac{1}{2} (L_J + L_{\text{arm}}) \quad (\text{E27})$$

and

$$\begin{aligned} \mathcal{K}_s &= \frac{e^2}{2\hbar C_{\text{tot}}} \frac{c_4}{c_2} \\ &= -\frac{e^2}{2\hbar C_{\text{tot}}} \left( \frac{L_J}{L_{\text{arm}} + L_J} \right)^3 \left[ 1 + 3 \frac{L_{\text{arm}}}{L_{\text{arm}} + L_J} \tan^2 \varphi_0 \right], \end{aligned} \quad (\text{E28})$$

where  $L_J = L_{J0}/\cos \varphi_0$ ,  $e$  is the elementary charge, and  $\hbar$  is the reduced Planck number.

When we add a linear inductance  $L - L_{\text{loop}}/4$  in series, we get the modified parameters [56]

$$\tilde{c}_2 = p c_2, \quad (\text{E29})$$

$$L_{\text{tot}} = \frac{L_s}{p}, \quad (\text{E30})$$

$$\tilde{c}_4 = p^4 c_4, \quad (\text{E31})$$

$$\mathcal{K} = p^3 \mathcal{K}_s, \quad (\text{E32})$$

where  $p$  is the inductance participation ratio

$$p = \frac{L_s}{L - L_{\text{loop}}/4 + L_s}. \quad (\text{E33})$$

Then, we finally have the explicit expression for the circuit Kerr nonlinearity

$$\mathcal{K} = -\frac{e^2}{2\hbar C_{\text{tot}}} \left( \frac{L_J}{2L + L_{\text{lin}} + L_J} \right)^3 \left[ 1 + 3 \frac{L_{\text{arm}}}{L_{\text{arm}} + L_J} \tan^2 \varphi_0 \right]. \quad (\text{E34})$$

- [1] J. Clarke and F. K. Wilhelm, Superconducting quantum bits, *Nature* **453**, 1031 (2008).
- [2] J. Q. You and Franco Nori, Atomic physics and quantum optics using superconducting circuits, *Nature* **474**, 589 (2011).
- [3] A. Blais, A. L. Grimsmo, S. M. Girvin, and A. Wallraff, Circuit quantum electrodynamics, *Rev. Mod. Phys.* **93**, 025005 (2021).
- [4] F. Arute *et al.*, Quantum supremacy using a programmable superconducting processor, *Nature* **574**, 505 (2019).
- [5] M. A. Castellanos-Beltran, K. D. Irwin, G. C. Hilton, L. R. Vale, and K. W. Lehnert, Amplification and squeezing of quantum noise with a tunable Josephson metamaterial, *Nat. Phys.* **4**, 929 (2008).
- [6] N. Bergeal, F. Schackert, M. Metcalfe, R. Vijay, V. E. Manucharyan, L. Frunzio, D. E. Prober, R. J. Schoelkopf, S. M. Girvin, and M. H. Devoret, Phase-preserving amplification near the quantum limit with a Josephson ring modulator, *Nature* **465**, 64 (2010).
- [7] C. Macklin, K. O'Brien, D. Hover, M. E. Schwartz, V. Bolkhovsky, X. Zhang, W. D. Oliver, and I. Siddiqi, A near-quantum-limited Josephson traveling-wave parametric amplifier, *Science* **350**, 307 (2015).
- [8] M. Hatridge, R. Vijay, D. H. Slichter, J. Clarke, and I. Siddiqi, Dispersive magnetometry with a quantum limited SQUID parametric amplifier, *Phys. Rev. B* **83**, 134501 (2011).
- [9] E. M. Levenson-Falk, N. Antler, and I. Siddiqi, Dispersive nanoSQUID magnetometry, *Supercond. Sci. Technol.* **29**, 113003 (2016).
- [10] J. R. Johansson, G. Johansson, and F. Nori, Optomechanical-like coupling between superconducting resonators, *Phys. Rev. A* **90**, 053833 (2014).
- [11] C. Eichler and J. R. Petta, Realizing a circuit analog of an optomechanical system with longitudinally coupled superconducting resonators, *Phys. Rev. Lett.* **120**, 227702 (2018).
- [12] D. Bothner, I. C. Rodrigues, and G. A. Steele, Photon-pressure strong coupling between two superconducting circuits, *Nat. Phys.* **17**, 85 (2021).
- [13] I. C. Rodrigues, G. A. Steele, and D. Bothner, Parametrically enhanced interactions and nonreciprocal bath dynamics in a photon-pressure Kerr amplifier, *Sci. Adv.* **8**, eabq1690 (2022).
- [14] O. Shevchuk, G. A. Steele, and Ya. M. Blanter, Strong and tunable couplings in flux-mediated optomechanics, *Phys. Rev. B* **96**, 014508 (2017).
- [15] I. C. Rodrigues, D. Bothner, and G. A. Steele, Coupling microwave photons to a mechanical resonator using quantum interference, *Nat. Commun.* **10**, 5359 (2019).
- [16] P. Schmidt, M. T. Amawi, S. Pogorzalek, F. Deppe, A. Marx, R. Gross, and H. Huebl, Sideband-resolved resonator electromechanics based on a nonlinear Josephson inductance probed on the single-photon level, *Commun. Phys.* **3**, 233 (2020).
- [17] D. Zoepfl, M. L. Juan, N. Diaz-Naufal, C. M. F. Schneider, L. F. Deeg, A. Sharafiev, A. Metelmann, and G. Kirchmair, Kerr enhanced backaction cooling in magnetomechanics, *Phys. Rev. Lett.* **130**, 033601 (2023).
- [18] Y. Nakamura, Yu. A. Pashkin, and J. S. Tsai, Coherent control of macroscopic quantum states in a single-Cooper-pair box, *Nature* **398**, 786 (1999).
- [19] A. Palacios-Laloy, F. Nguyen, F. Mallet, P. Bertet, D. Vion, and D. Esteve, Tunable resonators for quantum circuits, *J. Low Temp. Phys.* **151**, 1034 (2008).
- [20] R. Meservey and P. M. Tedrow, Properties of very thin aluminum films, *J. Appl. Phys.* **42**, 51 (1971).
- [21] K. Borisov, D. Rieger, P. Winkel, F. Henriques, F. Valenti, A. Ionita, M. Wessbecher, M. Spiecker, D. Gusenkova, I. M. Pop, and W. Wernsdorfer, Superconducting granular aluminum resonators resilient to magnetic fields up to 1 Tesla, *Appl. Phys. Lett.* **117**, 120502 (2020).
- [22] J. Krause, C. Dieckel, E. Vaal, M. Vielmetter, J. Feng, R. Bounds, G. Catelani, J. M. Fink, and Y. Ando, Magnetic field resilience of three-dimensional transmons with thin-film Al/AIO<sub>x</sub>/Al Josephson junctions approaching 1 T, *Phys. Rev. Appl.* **17**, 034032 (2022).
- [23] S. E. de Graaf, A. V. Danilov, A. Adamyan, T. Bauch, and S. E. Kubatkin, Magnetic field resilient superconducting fractal resonators for coupling to free spins, *J. Appl. Phys.* **112**, 123905 (2012).
- [24] N. Samkharadze, A. Bruno, P. Scarlino, G. Zheng, D. P. DiVincenzo, L. DiCarlo, and L. M. K. Vandersypen, High-kinetic-inductance superconducting nanowire resonators for circuit QED in a magnetic field, *Phys. Rev. Appl.* **5**, 044004 (2016).
- [25] C. W. Zollitsch, J. O'Sullivan, O. Kennedy, G. Dold, and J. J. L. Morton, Tuning high-Q superconducting resonators by magnetic field reorientation, *AIP Adv.* **9**, 125225 (2019).
- [26] A. Ghirri, C. Bonizzoni, D. Gerace, S. Sanna, A. Cassinese, and M. Affronte, YBa<sub>2</sub>Cu<sub>3</sub>O<sub>7</sub> microwave resonators for strong collective coupling with spin ensembles, *Appl. Phys. Lett.* **106**, 184101 (2015).
- [27] A. Roitman, A. Shaulov, and Y. Yeshurun, Characterization of YBa<sub>2</sub>Cu<sub>3</sub>O<sub>7- $\delta$</sub>  coplanar resonator for microwave kinetic inductance detectors, *Supercond. Sci. Technol.* **36**, 015002 (2023).
- [28] K. Uhl, D. Hackenbeck, C. Fuger, R. Kleiner, D. Koelle, and D. Bothner, A flux-tunable YBa<sub>2</sub>Cu<sub>3</sub>O<sub>7</sub> quantum interference microwave circuit, *Appl. Phys. Lett.* **122**, 182603 (2023).
- [29] E. J. Romans, S. Rozhko, L. Young, A. Blois, L. Hao, D. Cox, and J. C. Gallop, Noise performance of niobium nano-SQUIDs in applied magnetic fields, *IEEE Trans. Appl. Supercond.* **21**, 404 (2011).
- [30] O. W. Kennedy, J. Burnett, J. C. Fenton, N. G. N. Constantino, P. A. Warburton, J. J. L. Morton, and E. Dupont-Ferrier, Tunable Nb superconducting resonator based on a constriction nano-SQUID fabricated with a Ne focused ion beam, *Phys. Rev. Appl.* **11**, 014006 (2019).
- [31] M. Xu, R. Cheng, Y. Wu, G. Liu, and H. X. Tang, Magnetic field-resilient quantum-limited parametric amplifier, *PRX Quantum* **4**, 010322 (2023).
- [32] V. Bouchiat, M. Faucher, C. Thirion, W. Wernsdorfer, T. Fournier, and B. Pannetier, Josephson junctions and superconducting quantum interference devices made by local oxidation of niobium ultrathin films, *Appl. Phys. Lett.* **79**, 123 (2001).

[33] K. Hasselbach, D. Mailly, and J. R. Kirtley, Microsuperconducting quantum interference device characteristics, *J. Appl. Phys.* **91**, 4432 (2002).

[34] E. E. Mitchell and S. K. H. Lam, Niobium dc SQUIDS with nanobridge junctions, *Phys. Procedia* **36**, 382 (2012).

[35] H. Wang, L. Chen, X. Liu, L. Wu, X. Wu, L. You, and Z. Wang, Fabrication and characterization of miniaturized NbN superconducting quantum interference devices with nanobridge junctions, *IEEE Trans. Appl. Supercond.* **27**, 1601905 (2017).

[36] S. Pogorzalek, K. G. Fedorov, L. Zhong, J. Goetz, F. Wulschner, M. Fischer, P. Eder, E. Xie, K. Inomata, T. Yamamoto, Y. Nakamura, A. Marx, F. Deppe, and R. Gross, Hysteretic flux response and nondegenerate gain of flux-driven Josephson parametric amplifiers, *Phys. Rev. Appl.* **8**, 024012 (2017).

[37] See Supplemental Material at <http://link.aps.org/supplemental/10.1103/PhysRevApplied.21.024051> for further details about the power calibration, the theoretical device description, the fitting routine, the error bar calculation, and additional data, which also includes Refs. [61,62].

[38] R. Vijay, E. M. Levenson-Falk, D. H. Slichter, and I. Siddiqi, Approaching ideal weak link behavior with three dimensional aluminum nanobridges, *Appl. Phys. Lett.* **96**, 223112 (2010).

[39] L. Chen, H. Wang, X. Liu, L. Wu, and Z. Wang, A high-performance Nb nano-superconducting quantum interference device with a three-dimensional structure, *Nano Lett.* **16**, 7726 (2016).

[40] M. M. Khapaev, A. Yu. Kidiyarova-Shevchenko, P. Magnelind, and M. Yu. Kupriyanov, 3D-MLSI: Software package for inductance calculation in multilayer superconducting integrated circuits, *IEEE Trans. Appl. Supercond.* **11**, 1090 (2001).

[41] J. Wenner, M. Neeley, Radoslav C. Bialczak, M. Lenander, E. Lucero, A. D. O'Connell, D. Sank, H. Wang, M. Weides, A. N. Cleland, and J. M. Martinis, Wirebond crosstalk and cavity modes in large chip mounts for superconducting qubits, *Supercond. Sci. Technol.* **24**, 065001 (2011).

[42] D. Rieger, S. Günzler, M. Specker, A. Nambisan, W. Wernsdorfer, and I. M. Pop, Fano interference in microwave resonator measurements, *Phys. Rev. Appl.* **20**, 014059 (2023).

[43] D. Hazra, J. R. Kirtley, and K. Hasselbach, Retrapping current in bridge-type nano-SQUIDS, *Phys. Rev. Appl.* **4**, 024021 (2015).

[44] G. De Simoni, C. Puglia, and F. Giazotto, Niobium Dayem nano-bridge Josephson gate-controlled transistors, *Appl. Phys. Lett.* **116**, 242601 (2020).

[45] Z. Qing, T. Yuchien, L. Jinjin, L. Hao, J. Kaili, Z. Yuan, C. Wenhui, M. Zhang, and W. Xueshen, High transfer coefficient niobium nano-SQUID integrated with a nanogap modulation flux line, *Meas. Sci. Technol.* **32**, 025001 (2021).

[46] M. Wyss, K. Bagani, D. Jetter, E. Marchiori, A. Vervelaki, B. Gross, J. Ridderbos, S. Gliga, C. Schönenberger, and M. Poggio, Magnetic, thermal, and topographic imaging with a nanometer-scale SQUID-on-lever scanning probe, *Phys. Rev. Appl.* **17**, 034002 (2022).

[47] E. M. Levenson-Falk, F. Kos, R. Vijay, L. Glazman, and I. Siddiqi, Single-quasiparticle trapping in aluminum nanobridge Josephson junctions, *Phys. Rev. Lett.* **112**, 047002 (2014).

[48] I. Nsanzeza and B. L. T. Plourde, Trapping a single vortex and reducing quasiparticles in a superconducting resonator, *Phys. Rev. Lett.* **113**, 117002 (2014).

[49] K. K. Likharev, Superconducting weak links, *Rev. Mod. Phys.* **51**, 101 (1979).

[50] A. Gumann, T. Dahm, and N. Schopohl, Microscopic theory of superconductor-constriction-superconductor Josephson junctions in a magnetic field, *Phys. Rev. B* **76**, 064529 (2007).

[51] A. G. P. Troeman, S. H. W. van der Ploeg, E. Il'ichev, H.-G. Meyer, A. A. Golubov, M. Yu. Kupriyanov, and H. Hilgenkamp, Temperature dependence measurements of the supercurrent-phase relationship in niobium nanobridges, *Phys. Rev. B* **77**, 024509 (2008).

[52] D. Bothner, I. C. Rodrigues, and G. A. Steele, Four-wave-cooling to the single phonon level in Kerr optomechanics, *Commun. Phys.* **5**, 33 (2022).

[53] I. C. Rodrigues, D. Bothner, and G. A. Steele, Cooling photon-pressure circuits into the quantum regime, *Sci. Adv.* **7**, eabg6653 (2021).

[54] E. M. Levenson-Falk, R. Vijay, and I. Siddiqi, Nonlinear microwave response of aluminum weak-link Josephson oscillators, *Appl. Phys. Lett.* **98**, 123115 (2011).

[55] J. Bardeen, Critical fields and currents in superconductors, *Rev. Mod. Phys.* **34**, 667 (1962).

[56] N. E. Frattini, V. V. Sivak, A. Lingenfelter, S. Shankar, and M. H. Devoret, Optimizing the nonlinearity and dissipation of a SNAIL parametric amplifier for dynamic range, *Phys. Rev. Appl.* **10**, 054020 (2018).

[57] D. Zoeffl, M. L. Juan, C. M. F. Schneider, and G. Kirchmair, Single-photon cooling in microwave magnetomechanics, *Phys. Rev. Lett.* **125**, 023601 (2020).

[58] F. Fani Sani, I. C. Rodrigues, D. Bothner, and G. A. Steele, Level attraction and idler resonance in a strongly driven Josephson cavity, *Phys. Rev. Res.* **3**, 043111 (2021), [www.zenodo.org/records/10618057](http://www.zenodo.org/records/10618057).

[59] M. F. Gely, A. Sanz Mora, S. Yanai, R. van der Spek, D. Bothner, and G. A. Steele, Apparent nonlinear damping triggered by quantum fluctuations, *Nat. Commun.* **14**, 7566 (2023).

[60] N. Klein, H. Chaloupka, G. Müller, S. Orbach, and H. Piel, The effective microwave surface impedance of high- $T_c$  thin films, *J. Appl. Phys.* **67**, 6940 (1990).

[62] R. Igreja and C. J. Dias, Analytical evaluation of the interdigital electrodes capacitance for a multi-layered structure, *Sens. Actuators A* **112**, 291 (2004).

**Supplemental Material for:**  
**Niobium Quantum Interference Microwave Circuits**  
**with Monolithic Three-Dimensional (3D) Nanobridge Junctions**

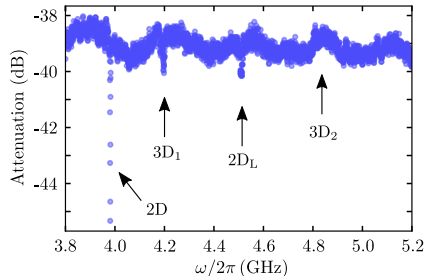
K. Uhl *et al.*

**CONTENTS**

I. Supplemental Note I: Power calibration	2
II. Supplemental Note II: The circuits without constrictions	2
A. The lumped element circuit equivalent without the constrictions	2
B. Circuit parameters from simulations and measurements	3
III. Supplemental Note III: The circuits with constrictions	6
A. The lumped element circuit equivalent with the constrictions	6
IV. Supplemental Note IV: <i>S</i> -parameter background correction and fitting	7
A. The real transmission function and fit-based background correction	7
B. Data-based background correction	7
V. Supplemental Note V: Further data and analyses	9
A. The linear inductance contribution $L_{\text{lin}}$ for all three devices	9
B. The inferred current-phase-relation for all three constriction types	10
C. Flux responsivity $\partial\omega_0/\partial\Phi_{\text{ext}}$ for all devices vs temperature	10
D. Internal linewidth $\kappa_i$ for all devices vs temperature and flux	10
VI. Supplemental Note VI: Error bars	12
A. Error bars for the determination of the Kerr constant $\mathcal{K}$	12
VII. Supplemental References	13

**Note:** Parts of this Supplemental Material (Notes II-IV) overlap with and are based on similar considerations presented in the Supplementary Material of Ref. [28] by (almost) the same authors.

## I. SUPPLEMENTAL NOTE I: POWER CALIBRATION



Supplemental Figure 1. **Frequency dependence of the input line attenuation.** The attenuation is obtained by measuring 200 independent traces in the shown frequency range using the VNA and at  $T_s = 2.5$  K. For each frequency point, the signal-to-noise ratio is determined as the mean-to-standard-deviation-ratio out of the 200 traces. In combination with the frequency-dependent HEMT noise temperature, the sample temperature and an estimated 1 dB loss between the sample and the HEMT, we obtain the shown  $\sim -39 \pm 1$  dB of attenuation between the VNA output and the sample. The frequency range contains the resonance frequencies of the three SQUID cavities 2D, 3D<sub>1</sub> and 3D<sub>2</sub> presented in the main manuscript and that of an additional cavity 2D<sub>L</sub> not discussed here. The resonance of 3D<sub>2</sub> is not visible without raw data processing here, cf. also Supplemental Note IV.

We use the input noise of the cryogenic HEMT amplifier in combination with the knowledge of the sample temperature (more precisely the temperature of the 20 dB attenuator, which is the one closer to the sample) as a calibration method for the attenuation between the VNA output and the superconducting chip. This allows us to estimate the resulting input power on the on-chip feedline based on the set VNA output power. For each frequency point in the relevant frequency range  $\frac{\Delta\omega_{\text{att}}}{2\pi} = 3.8 - 5.2$  GHz the signal-to-noise ratio is determined from finding the mean and the standard deviation of 200 VNA traces. The total thermal noise power referenced to the input of the HEMT is given by

$$P_{\text{HEMT}} = 10 \log \left( \frac{k_B [T_{\text{HEMT}} + T_s]}{1 \text{ mW}} \right) + 10 \log \left( \frac{f_{\text{IFBW}}}{\text{Hz}} \right) \quad (\text{S1})$$

where  $k_B$  is the Boltzmann constant,  $T_{\text{HEMT}}(\omega) = 7.46 \text{ K} - \frac{3}{7\pi} \frac{\omega}{\text{GHz}} \text{ K}$  is the noise temperature of the amplifier according to the specification datasheet in the frequency window  $\Delta\omega_{\text{att}}$ , and  $f_{\text{IFBW}}$  is the measurement intermediate frequency bandwidth (IFBW). We also estimate the loss between sample and HEMT to be  $\sim 1$  dB. In combination, we get the frequency-dependent input line attenuation as shown in Supplemental Fig. 1. Note that the frequency range  $\Delta\omega_{\text{att}}$  contains four resonance dips, three belonging to the SQUID cavities 2D, 3D<sub>1</sub> and 3D<sub>2</sub> presented in the main manuscript and one additional SQUID cavity 2D<sub>L</sub> with long 2D nano-constrictions that is not discussed here ( $\omega_0 \approx 2\pi \cdot 4.52$  GHz). The resonance of 3D<sub>2</sub> is not easily visible without a raw data processing, cf. Supplemental Note IV.

## II. SUPPLEMENTAL NOTE II: THE CIRCUITS WITHOUT CONSTRICTIONS

### A. The lumped element circuit equivalent without the constrictions

In the main manuscript, we discuss data from three distinct microwave circuits, one with 2D nanobridges and two devices with 3D nanobridges. The basic design of the circuits comprises two interdigitated capacitors with multiple linear inductors, that are combined into a single one in our model for the sake of simplicity. The interdigitated capacitors in all circuits have a finger length of 250  $\mu\text{m}$ , and a finger and gap width of 3  $\mu\text{m}$ . Only the number of fingers  $N_{\text{Idc}}$  differs between the circuits. Note that the finger number  $N_{\text{Idc}}$  here refers to the total number of fingers in an IDC, not to the fingers per electrode. We also remark that such a circuit has actually more than one mode, but we are only focusing on the fundamental mode here, i.e., the one with the lowest resonance frequency.

We model the circuit (before the constriction cutting) by a parallel RLC circuit with the inductance  $L$ , the capacitance  $C$  and the resistance  $R$ . The inductance has both a geometric contribution  $L_g$  and a kinetic contribution  $L_k$  with  $L = L_g + L_k$ , as it is common for superconducting thin film circuits. The parallel RLC circuit is coupled via a coupling capacitance  $C_c$  to the microwave feedline, which is a coplanar waveguide with characteristic impedance  $Z_0 \approx 50 \Omega$ . The total inductance  $L$  contains also the contribution from the SQUID loop self inductance  $L_{\text{loop}}$  and so the circuit inductance without the loop would be given by  $L - L_{\text{loop}}/4$ , for a schematic of the circuit (including the constriction inductances  $L_c$ ) see main paper Fig. 1(b). The circuit resonance frequency before introducing the constrictions is given by

$$\omega_b = \frac{1}{\sqrt{L(C + C_c)}} \quad (\text{S2})$$

and the internal and external linewidths are

$$\kappa_{i,b} = \frac{1}{R(C + C_c)}, \quad \kappa_{e,b} = \frac{\omega_b^2 C_c^2 Z_0}{2(C + C_c)} \quad (\text{S3})$$

which are related to the corresponding quality factors via  $Q_{i,b} = \omega_b/\kappa_{i,b}$  and  $Q_{e,b} = \omega_b/\kappa_{e,b}$ .

## B. Circuit parameters from simulations and measurements

The parameters we need for our circuits are the capacitances  $C$  and  $C_c$ , which in sum give  $C_{\text{tot}} = C + C_c$ . On the inductive side, we need the total inductance  $L$  and the loop inductance  $L_{\text{loop}}$ . The inductances, however, are both the sum of a geometric contribution and a kinetic contribution and for the case of the total inductance we get  $L = L_g + L_k$  (analogously of course for the loop inductance). What makes things even more complicated on one hand but also experimentally accessible on the other hand is that the kinetic contributions are dependent on the niobium London penetration depth  $\lambda_L$ , which is a function of sample temperature  $T_s$ .

We start our parameter extraction procedure by calculating the total linear inductance  $L(\lambda_L) = L_g + L_k(\lambda_L)$  with the software package 3D-MLSI [40] for the range  $90 \text{ nm} \leq \lambda_L \leq 250 \text{ nm}$  as this is typically the regime of the penetration depth of our sputtered  $d_{\text{Nb}} = 90 \text{ nm}$  thick niobium films. The relation between the penetration depth and the kinetic inductance is given by [61]

$$L_k = \mu_0 g \lambda_{\text{eff}} \quad (\text{S4})$$

where  $\mu_0$  is the vacuum permittivity,  $g$  is a geometrical dimensionless factor taking into account the details of the superconducting structures and the effective penetration depth  $\lambda_{\text{eff}}$  of a thin film  $d_{\text{Nb}} \lesssim \lambda_L$  is [61]

$$\lambda_{\text{eff}} = \lambda_L \coth \frac{d_{\text{Nb}}}{\lambda_L}. \quad (\text{S5})$$

Then the total inductance is

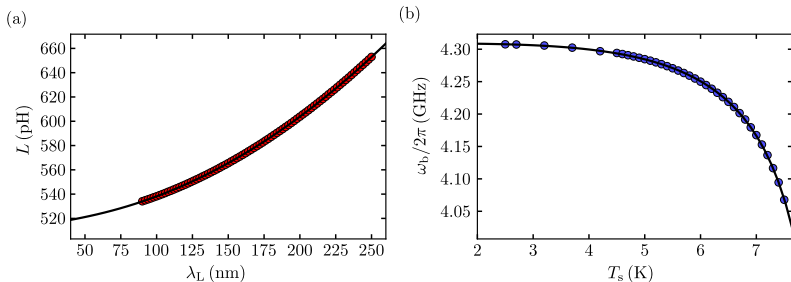
$$L = L_g + \mu_0 g \lambda_L \coth \frac{d_{\text{Nb}}}{\lambda_L} \quad (\text{S6})$$

which we use to fit the numerically obtained  $L(\lambda_L)$  with  $g$  and  $L_g$  as fit parameters, cf. Supplemental Fig. 2(a). In the experiment, we do not vary directly  $\lambda_L$  but the sample temperature  $T_s$ , the relation between the two is given by

$$\lambda_L(T_s) = \frac{\lambda_0}{\sqrt{1 - \left(\frac{T_s}{T_c}\right)^4}} \quad (\text{S7})$$

where  $\lambda_0$  is the zero-temperature penetration depth and  $T_c$  is the critical temperature. We measure the cavity resonance frequency  $\omega_b(T_s)$  and hence fit the experimentally obtained data with

$$\begin{aligned} \omega_b(T_s) &= \frac{1}{\sqrt{C_{\text{tot}} L(T_s)}} \\ &= \frac{1}{\sqrt{C_{\text{tot}} \left[ L_g + \mu_0 g \frac{\lambda_0}{\sqrt{1 - \left(\frac{T_s}{T_c}\right)^4}} \coth \left[ \frac{d_{\text{Nb}}}{\lambda_0} \sqrt{1 - \left(\frac{T_s}{T_c}\right)^4} \right] \right]}} \end{aligned} \quad (\text{S8})$$



Supplemental Figure 2. **Temperature dependence before junction cutting.** In (a) we show the total inductance  $L(\lambda_L)$  of the cavity vs the London penetration depth  $\lambda_L$ . The red circles are data obtained from 3D-MLSI simulations using different  $\lambda_L$  and the line is a fit using Eq. (S6) with  $L_g = 511$  pH and  $g = 156$  as fit parameter. In panel (b), the cavity resonance frequency  $\omega_b$  is shown vs sample temperature  $T_s$ . The shift in frequency with increasing temperature occurs due to a change of the total circuit inductance  $L(T_s) = L_g + L_k(T_s)$ . Circles are data, line is a fit using Eq. (S8) and with  $T_c = 8.6$  K,  $C_{\text{tot}} = 2.404$  pF and  $\lambda_0 = 153$  nm as fit parameters. All data correspond to the circuit 3D<sub>1</sub>.

with  $L_g$  and  $g$  as fixed parameters obtained as described above,  $\mu_0 = 4\pi \cdot 10^{-7}$  H/m,  $d_{\text{Nb}} = 90$  nm, and  $C_{\text{tot}}$ ,  $\lambda_0$  and  $T_c$  as fit parameters.

Once we know  $\lambda_0$ , we can also calculate the loop inductance

$$L_{\text{loop}}(T_s) = L_{\text{loop},g} + \mu_0 g_{\text{loop}} \lambda_{\text{eff}}(T_s) \quad (\text{S9})$$

for all measurement temperatures. Using 3D-MLSI the same way as for  $L$  of the cavity, we obtain  $L_{\text{loop},g} = 12.8$  pH and  $g_{\text{loop}} = 12$ . For  $T_s = 2.5$  K this means  $L_{\text{loop}} = 17$  pH.

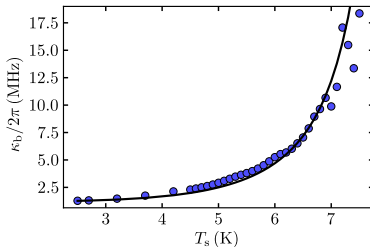
The next relevant parameter is the coupling capacitance  $C_c$ , which we obtain from the measurement of the external linewidth  $\kappa_{e,b}$ , the knowledge of  $Z_0 \approx 50 \Omega$ ,  $\omega_b$  and  $C_{\text{tot}} = C + C_c$  by using Eq. (S3). Finally, we can also obtain  $C = C_{\text{tot}} - C_c$ . To cross-check the values we obtain by this procedure, we also calculate the capacitances (I) by using the analytical expression derived in Ref. [62] as well as (II) by doing Comsol Multiphysics simulations. We find moderate deviations of  $< 10\%$  between the experimental values (based on the inductance simulation) and the analytical expression and of  $< 20\%$  between the experimental values and the Comsol simulations. Since both, the analytical and the Comsol results overestimate the capacitance we obtain by the procedure described here, we think that over-etching into the Si substrate when doing the SF<sub>6</sub>-etch of the Nb (especially in between the fingers), as well as a finger width slightly smaller than  $3 \mu\text{m}$ , can be identified as the source of these deviations. Supplemental Table I summarizes all relevant parameters of the three circuits, the temperature-dependent quantities  $\omega_b$ ,  $\kappa_{e,b}$  and  $\kappa_{i,b}$  are given at  $T_s = 2.5$  K.

Supplemental Table I. **Simulated and experimental parameters of the three circuits before cutting the nanobridge junctions.**

The finger number  $N_{\text{idc}}$  refers to the total number of fingers in each IDC. The geometric inductance  $L_g$  and the kinetic geometry factor  $g$  are obtained from simulations with 3D-MLSI [40]. From a fit to the temperature-dependence of  $\omega_b$  we obtain the zero-temperature penetration depth  $\lambda_0$ , the critical temperature  $T_c$  and the total capacitance  $C_{\text{tot}}$ . From the measured external linewidth  $\kappa_{e,b}$  we subsequently find the coupling capacitance  $C_c$  and the circuit capacitance  $C$ . For completeness we also give  $\kappa_{i,b}$ . All experimental values are given for  $T_s = 2.5$  K.

Resonator	$N_{\text{idc}}$	$L_g$ (pH)	$g$	$\lambda_0$ (nm)	$T_c$ (K)	$C_{\text{tot}}$ (pF)	$C$ (pF)	$C_c$ (fF)	$\frac{\omega_b}{2\pi}$ (GHz)	$\frac{\kappa_{e,b}}{2\pi}$ (MHz)	$\frac{\kappa_{i,b}}{2\pi}$ (kHz)
2D	100	535	164	157	8.6	2.652	2.613	38	3.994	1.4	89
3D <sub>1</sub>	92	511	156	153	8.6	2.404	2.373	31	4.308	1.2	73
3D <sub>2</sub>	76	462	141	153	8.6	1.936	1.903	33	5.047	2.2	120

In addition to the resonance frequency, we also extract the total resonance linewidth  $\kappa_b$  as a function of temperature, data for circuit 3D<sub>1</sub> are shown in Supplemental Fig. 3. At the elevated temperatures we are operating here  $T_s \gtrsim 0.3T_c$ ,



Supplemental Figure 3. **Temperature dependence of linewidth indicates quasiparticle losses.** Total circuit linewidth  $\kappa_{i,b}/2\pi$  vs sample temperature  $T_s$  before cutting the nano-constrictions. The linewidth increases with increasing temperature, indicating growing losses by thermal quasiparticles in the superconductor. Circles are data for device 3D<sub>1</sub>, line is a fit using Eqs. (S13, S14) with  $A_\kappa$  as single fit parameter.

the internal decay rate will be dominated by quasiparticle losses. From the two-fluid model, the effective surface resistance of a superconductor with the corresponding correction factor for thin films and around the cavity resonance frequency is given by [61]

$$R_{s,\text{eff}} = \frac{1}{2} \omega_b^2 \mu_0^2 \lambda_L^3 \sigma_n \frac{n_n}{n} \left[ \coth \left( \frac{d_{\text{Nb}}}{\lambda_L} \right) + \frac{d_{\text{Nb}}/\lambda_L}{\sinh^2 \left( \frac{d_{\text{Nb}}}{\lambda_L} \right)} \right], \quad (\text{S10})$$

where  $\sigma_n$  is the normal state conductivity,  $n_n$  is the quasiparticle density and  $n = n_n + n_s$  is the total electron density with  $n_s$  being the superconducting charge carrier density (twice the Cooper pair density). The temperature dependence of the quasiparticle density is given by

$$\frac{n_n(T_s)}{n} = \left( \frac{T_s}{T_c} \right)^4. \quad (\text{S11})$$

Since the quasiparticle loss channel is equivalent to the inductive channel, the resulting circuit model lumped element resistance  $R' \propto R_{s,\text{eff}}$  is expected to be in series with  $L$ . We can, however, transform this into the parallel resistor  $R$  via

$$R = \frac{R'^2 + \omega_b^2 L^2}{R'} \approx \frac{\omega_b^2 L^2}{R'} \quad (\text{S12})$$

where we used  $\omega_b^2 L^2 \gg R'^2$ .

Combining this result with Eq. (S3) we get

$$\begin{aligned} \kappa_{i,b}(T_s) &= \omega_b^2(T_s) R'(T_s) C_{\text{tot}} \\ &= A_\kappa \omega_b^4(T_s) \lambda_L^3(T_s) \left( \frac{T_s}{T_c} \right)^4 \left[ \coth \left( \frac{d_{\text{Nb}}}{\lambda_L(T_s)} \right) + \frac{d_{\text{Nb}}/\lambda_L(T_s)}{\sinh^2 \left( \frac{d_{\text{Nb}}}{\lambda_L(T_s)} \right)} \right] \end{aligned} \quad (\text{S13})$$

with the fit parameter  $A_\kappa$  that contains geometry, material properties and other temperature-independent contributions.

Since we are not certain that we can reliably discriminate between  $\kappa_{i,b}$  and  $\kappa_{e,b}$  due to cable resonances and impedance mismatches in the setup leading to Fano interferences, we fit the temperature dependence of the total linewidth using

$$\kappa_b(T_s) = \kappa_{e,b} + \kappa_{i,b}(T_s) \quad (\text{S14})$$

with  $\kappa_{e,b}$  being a constant value we obtain for  $T_s = 2.5$  K. The theoretical variation of  $\kappa_{e,b}$  for large temperatures would only be  $\sim 140$  kHz and is therefore negligible compared to the total linewidth. The agreement between the experimental data and the fit line is very good, cf. Supplemental Fig. 3, and we obtain nearly identical curves and agreements for all three resonators discussed in this work.

### III. SUPPLEMENTAL NOTE III: THE CIRCUITS WITH CONSTRICTIONS

#### A. The lumped element circuit equivalent with the constrictions

We observe that cutting the constrictions into the circuit leads to a shift of the resonance frequency and to a broadening of the resonance linewidth. In agreement with the two-fluid model, we therefore model the circuit elements introduced by the junction as a constriction inductance  $L_c$  in parallel with a constriction resistance  $R_c$ . The inductance in turn we split into a series combination of a nonlinear Josephson part  $L_J$  and a linear contribution  $L_{\text{lin}}$ , cf. Fig. 1(b) of the main paper. This combination leads to a forward-skewed sinusoidal current-phase relation (CPR), where the skewedness is related to the ratio  $L_{J0}/L_{\text{lin}}$  with  $L_{J0} = \frac{\Phi_0}{2\pi I_0}$ ,  $\Phi_0 \approx 2.068 \cdot 10^{-15} \text{ Tm}^2$  and the critical constriction current  $I_0$ . Such a skewed CPR is typical for constriction-type Josephson junctions (cJJ) [33, 49]. We note that we omit any additional capacitance, as according to our simulations the impedance of a possible constriction capacitance is negligible compared to its inductance impedance.

Hence, the input impedance of a single constriction around the cavity resonance frequency  $\omega \approx \omega_0$  is given by

$$\frac{1}{Z_c} = \frac{1}{R_c} + \frac{1}{i\omega_0 L_c}, \quad (\text{S15})$$

which leads to the total SQUID input impedance

$$Z_S = \frac{1}{2} \frac{i\omega_0 L_c R_c}{R_c + i\omega_0 L_c} + i\omega_0 \frac{L_{\text{loop}}}{4}. \quad (\text{S16})$$

The originally purely inductive circuit branch then has the input impedance

$$Z_L = i\omega_0 L + \frac{1}{2} \frac{i\omega_0 L_c R_c}{R_c + i\omega_0 L_c}. \quad (\text{S17})$$

If we want to work with a low level of approximation, we transform this impedance into a series impedance of a single inductor  $L_+$  and a resistor  $R_+$  by

$$R_+ + i\omega_0 L_+ = \frac{1}{2} \frac{\omega_0^2 L_c^2 R_c}{R_c^2 + \omega_0^2 L_c^2} + i\omega_0 \left( L + \frac{1}{2} L_c \frac{R_c^2}{R_c^2 + \omega_0^2 L_c^2} \right). \quad (\text{S18})$$

As a next step and in order to easily integrate this impedance branch into the formalism used here, we now transform it into a parallel combination of an inductance  $L^*$  and a resistance  $R^*$

$$\frac{1}{R^*} + \frac{1}{i\omega_0 L^*} = \frac{1}{R_+ + i\omega_0 L_+} \quad (\text{S19})$$

from which we find

$$R^* = \frac{R_+^2 + \omega_0^2 L_+^2}{R_+}, \quad L^* = \frac{R_+^2 + \omega_0^2 L_+^2}{\omega_0^2 L_+}. \quad (\text{S20})$$

We approximate this using  $R_+^2 \ll \omega_0^2 L_+^2$  as

$$R^* \approx \frac{\omega_0^2 L_+^2}{R_+}, \quad L^* \approx L_+. \quad (\text{S21})$$

The total linewidth is now given as

$$\kappa_i = \frac{1}{C + C_c} \frac{1}{R} + \frac{1}{C + C_c} \frac{1}{R^*} \quad (\text{S22})$$

$$= \kappa_{i,b} + \kappa_c \quad (\text{S23})$$

$$\approx \kappa_c \quad (\text{S24})$$

and the resonance frequency as

$$\omega_0 = \frac{1}{\sqrt{(C + C_c) L^*}}. \quad (\text{S25})$$

From measuring  $\omega_0$  and  $\kappa_c$  we can then determine  $R_c$  and  $L_c$ .

For the work presented here, we can even work with a stronger approximation and still only have about 1%–2% error (obtained from comparing with exact results) in the extracted values, mainly for large flux biases  $\Phi_{\text{ext}}/\Phi_0 \sim \pm 0.5$ . Considering additionally  $R_c^2 \gg \omega_0^2 L_c^2$  we find the expressions

$$R^* \approx 2 \frac{(L + \frac{L_c}{2})^2}{L_c^2} R_c, \quad L^* = L + \frac{L_c}{2}. \quad (\text{S26})$$

With these, we can write for the internal linewidth and the resonance frequency

$$\kappa_i = \frac{\omega_0^2 L_c^2}{2L + L_c} \frac{1}{R_c}, \quad \omega_0 = \frac{1}{\sqrt{(C + C_c)(L + \frac{L_c}{2})}}. \quad (\text{S27})$$

#### IV. SUPPLEMENTAL NOTE IV: *S*-PARAMETER BACKGROUND CORRECTION AND FITTING

##### A. The real transmission function and fit-based background correction

Due to impedance imperfections in both, the input and output lines, the ideal transmission response is modified by cable resonances and interferences within the setup [41, 42]. Origin of these imperfections are connectors, attenuators, wirebonds, transitions to or from the PCB etc. in the signal lines. In addition, the cabling has a frequency-dependent attenuation. To take all these modifications into account, we assume that the final transmission parameter  $S_{21}^{\text{real}}$  can be described by

$$S_{21}^{\text{real}} = (a_0 + a_1\omega + a_2\omega^2) [1 - f(\omega)e^{i\theta}] e^{i(\phi_0 + \phi_1\omega)} \quad (\text{S28})$$

when the ideal response would be given by

$$S_{11}^{\text{ideal}} = 1 - f(\omega). \quad (\text{S29})$$

The real-valued numbers  $a_0, a_1, a_2, \phi_0, \phi_1$  describe a frequency dependent modification of the background transmission, and the phase factor  $\theta$  takes into account possible interferences such as parasitic signals bypassing the transmission along the device itself, for instance around the chip. The exact form of  $f(\omega)$  depends on the experiment performed (single-tone, two-tone etc).

Our standard fitting routine begins with removing the actual resonance signal from the transmission, leaving us with a gapped background transmission, which we fit using

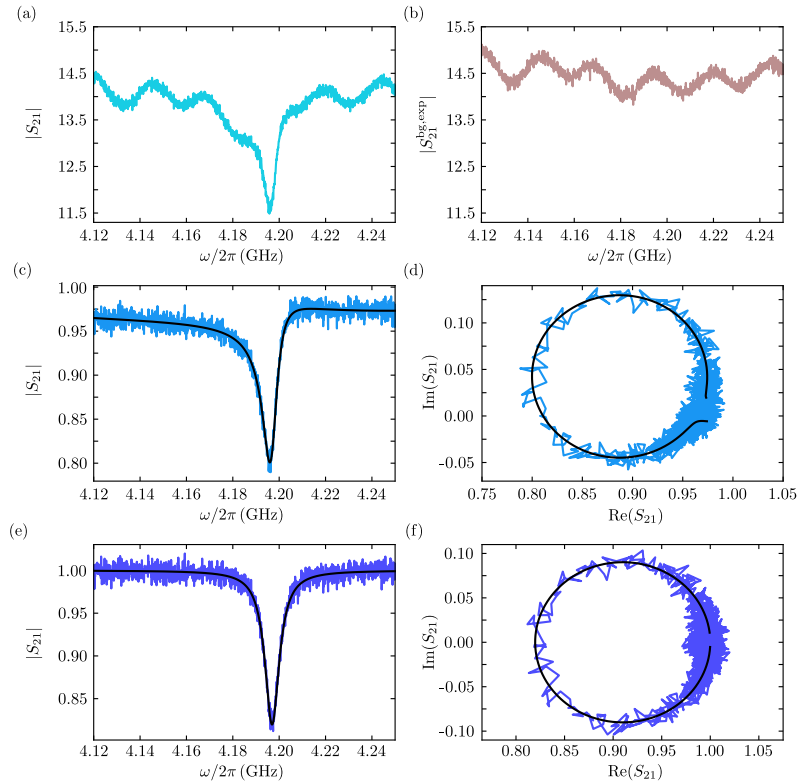
$$S_{21}^{\text{bg}} = (a_0 + a_1\omega + a_2\omega^2) e^{i(\phi_0 + \phi_1\omega)}. \quad (\text{S30})$$

Subsequently, we remove this background function from all measurement traces by complex division. The resonance circle rotation angle  $\theta$  is then rotated off additionally. The result of both corrections is what we present as background-corrected data or transmission/response data in all figures. For the power dependence measurements, we determine the background from the measurement in the linear regime and perform a background correction based on that single linear response line for all powers.

##### B. Data-based background correction

As the circuits in our experiments have a rather large linewidth between several MHz and tens of MHz and as the background transmission cannot be described over such a large frequency span with a simple second order polynomial as suggested by Eq. (S28), we perform a two-step background correction to obtain as clean *S*-parameters as possible. The procedure is exemplarily shown for one resonance of device 3D<sub>1</sub> in Supplemental Fig. 4.

In the first step, we record for each measurement (e.g. the one in panel (a)) also the resonance-less transmission function as shown in panel (b). The resonance-less  $S_{21}$  is obtained by increasing the sample temperature to about  $T_s = 3.7$  K, where the resonance frequency is out of the measurement window and  $\kappa_i$  is so large that the resonance is not impacting the data anymore. Then we perform a complex division of the full  $S_{21}$  signal by the bare background signal  $S_{21}^{\text{bg,exp}}$ , the result is a resonance with a nearly flat background as shown in (c), the complex-valued version can be seen in (d). Subsequently, we perform a fit using Eq. (S28) from which we obtain a second background function



Supplemental Figure 4. **Background correction and fitting routine.** (a) Transmission  $|S_{21}|$  vs probe frequency of the SQUID circuit 3D<sub>1</sub> for a flux bias value close to the flux sweetspot. The absorption resonance dip around 4.197 GHz is clearly visible, the measurement temperature is  $T_s^* = 2.5$  K. (b) Identical to (a), but at an elevated temperature  $T_s^* = 3.7$  K. What we detect here is the experimental background  $S_{21}^{\text{bg,exp}}$ , slightly modified by temperature-dependent transmission over the chip and the coldest parts of the microwave cables. We measure not only the amplitude, but also the phase of  $S_{21}$  and  $S_{21}^{\text{bg,exp}}$ . (c) Magnitude of  $S_{21}/S_{21}^{\text{bg,exp}}$  vs probe frequency, the background is nearly a flat line, but not yet at  $|S_{21}| = 1$  as expected for an ideal transmission. (d) Imaginary part of the background-divided transmission vs the real part. Noisy light blue lines in (c) and (d) are data, black smooth lines are a fit with Eq. (S28). (e) and (f) show the final background-corrected data, where also the remaining background from the fit is divided off and the resonance circle is corrected by the Fano rotation  $\theta$ . Noisy blue lines in (e) and (f) are data, black smooth lines are the fit curves.

as well as a Fano rotation angle  $\theta$ . We divide off the fit-background, again by complex division, and finally rotate the resonance circle by  $\theta$  around its anchor point. The final result including the corresponding fits can be seen in panels (e) and (f). For the circuits with constrictions, we perform this data processing with all  $S_{21}$  spectra used for the data analysis, and all shown resonances have been treated this way. For the data before constriction cutting, we do only the fit-based background correction.

## V. SUPPLEMENTAL NOTE V: FURTHER DATA AND ANALYSES

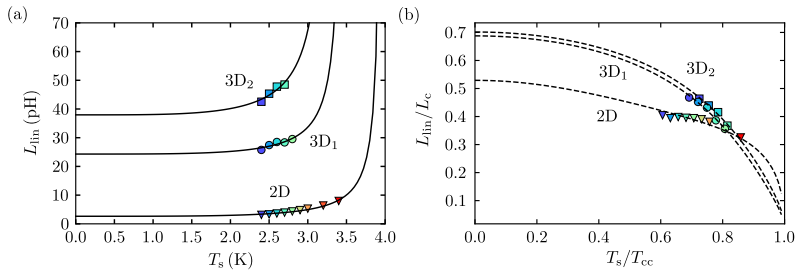
### A. The linear inductance contribution $L_{\text{lin}}$ for all three devices

The linear inductance contribution  $L_{\text{lin}}$  to the total constriction inductance  $L_c$ , which is necessary to model our results, is in agreement with many reports regarding the current-phase-relation (CPR) of niobium constriction junctions. Essentially all experiments to date found a forward-skewed sinusoidal CPR for this type of junctions, and such a CPR is very similar to the CPR of a series combination of a linear inductance and an ideal Josephson inductance [49]. In order to take this linear inductance and its temperature dependence into account for an extrapolation of the SQUID and circuit properties to lower temperatures, we analyze and model the data of  $L_{\text{lin}}$  we have from the limited range of  $T_s$ . In Supplemental Fig. 5 all extracted values for  $L_{\text{lin}}$  are shown. For all three devices  $L_{\text{lin}}$  increases with temperature and the absolute values span between a few pH in device 2D and several 10 pH in devices 3D<sub>1</sub> and 3D<sub>2</sub>, the values increase with increasing  $L_{J0}$ . Since the linear contribution is a kinetic inductance (the geometric inductance of a constriction is negligibly small), we model its temperature dependence as

$$L_{\text{lin}}(T_s) = L_{\text{off}} + \frac{L_{\text{lin},0}}{1 - \left(\frac{T_s}{T_{cc}}\right)^4}, \quad (\text{S31})$$

where  $L_{\text{lin},0}$  is the kinetic inductance at zero temperature,  $T_{cc}$  is the constriction critical temperature, and with  $L_{\text{off}}$  we allow for a possible temperature-independent offset. The result is shown in Supplemental Fig. 5 as solid lines. We note, that due to the small temperature range we could measure, the model and theory lines are somewhat speculative and need to be tested in the future by further experiments at lower temperatures. We believe, however, that it is still useful to extrapolate to lower temperatures by making reasonable assumptions about the temperature-dependence of  $I_0$ ,  $L_c$  and  $\beta_L$ , mainly based on theory and earlier results on similar systems. In panel (b), we show  $L_{\text{lin}}/L_c$  and see a clear trend for a decrease with increasing temperature, which also is in good agreement with previous reports on the CPR of constriction junctions, since a decreasing  $L_{\text{lin}}/L_c$  indicates a reduced skewedness as also found experimentally for higher temperatures. Theory lines in (b) are just directly calculated using the fit lines for  $I_0(T_s)$  of main paper Fig. 3(b) and that of Supplemental Fig. 5(a).

It is worth mentioning that it seems that for low temperatures  $T_s/T_{cc} \lesssim 0.9$  the relative linear contribution in the 3D devices is larger than in the 2D device. The reason behind this observation is currently unclear, but it might be related to a damage of the Nb in the 3D constrictions by the neon ion beam, which for instance leads to a smaller superconducting coherence length and therefore deteriorating the constriction quality.



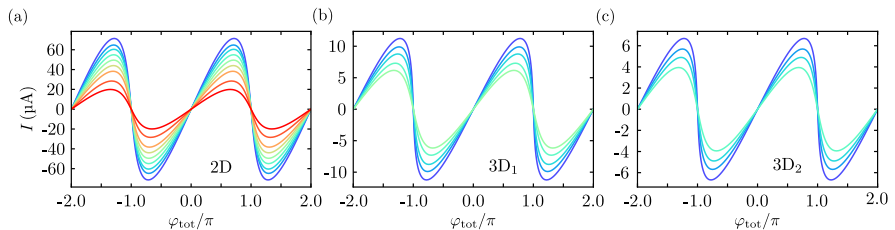
Supplemental Figure 5. **Linear contribution  $L_{\text{lin}}$  to the constriction inductance  $L_c$  for all three devices.** (a) Linear constriction inductance contribution  $L_{\text{lin}}$  as obtained from the flux-tuning curve fits vs sample temperature  $T_s$  for all three devices. Symbols are data, lines are fits. The linear inductance increases with decreasing constriction thickness, i.e., with increasing  $L_{J0}$ , and with temperature. (b) Participation ratio of the linear inductance  $L_{\text{lin}}$  to the total constriction inductance  $L_c$  vs reduced temperature  $T_s/T_{cc}$ , demonstrating that with increasing temperature the linear contribution gets less significant. Symbols are data, dashed lines are calculated from the individual fits of  $L_{\text{lin}}(T_s)$  and  $I_0(T_s)$ .

## B. The inferred current-phase-relation for all three constriction types

In order to visualize the current-phase-relation (CPR) of the three constriction types, which is consistent with our experimental findings and our data analyses, we infer a CPR from the model of an ideal Josephson inductance  $L_{J0}$  in series with a linear contribution  $L_{\text{lin}}$  for our three circuits and the temperatures we present in the other parts of the manuscript. To (piecewise) calculate and plot the CPRs, we use for the total phase  $\varphi_{\text{tot}}$  as function of the current  $I \leq I_0$

$$\begin{aligned}\varphi_{\text{tot}} &= \varphi_J + \varphi_{\text{lin}} \\ &= (-1)^n \arcsin\left(\frac{I}{I_0}\right) + \frac{2\pi}{\Phi_0} L_{\text{lin}} I + n\pi.\end{aligned}\quad (\text{S32})$$

The result is shown in Supplemental Fig. 6. All three constriction types show the expected forward-skewed CPRs and the skewedness decreases with increasing temperature, which can be seen from the maximum of the curves shifting to smaller phases, when  $T_s$  is increased.



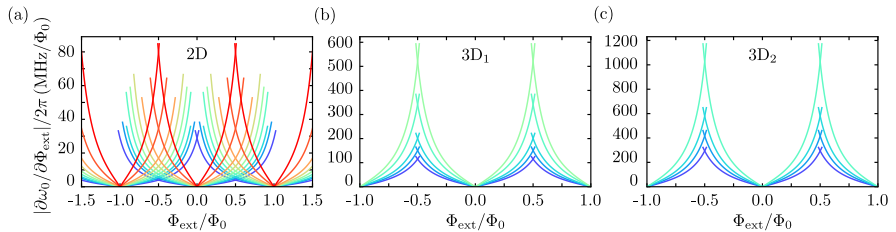
Supplemental Figure 6. **Inferred current-phase-relations (CPRs) of all constrictions and all presented temperatures.** CPRs for all three devices at all measurement temperatures  $T_s$ , calculated via  $L_{\text{lin}}$  and  $I_0$ , details cf. text. (a) circuit 2D at  $T_s = (2.4, 2.5, 2.6, 2.7, 2.8, 2.9, 3.0, 3.2, 3.4)$  K, (b) circuit 3D<sub>1</sub> at  $T_s = (2.4, 2.5, 2.6, 2.7, 2.8)$  K and (c) circuit 3D<sub>2</sub> at  $T_s = (2.4, 2.5, 2.6, 2.7)$  K. Increasing  $T_s$  corresponds to decreasing maximum supercurrent  $I_0$  in all panels. All constrictions show the expected forward-skewed CPRs and the skewedness decreases with increasing temperature, which can be seen from the maximum of the curves shifting to smaller phases, when  $T_s$  is increased.

## C. Flux responsivity $\partial\omega_0/\partial\Phi_{\text{ext}}$ for all devices vs temperature

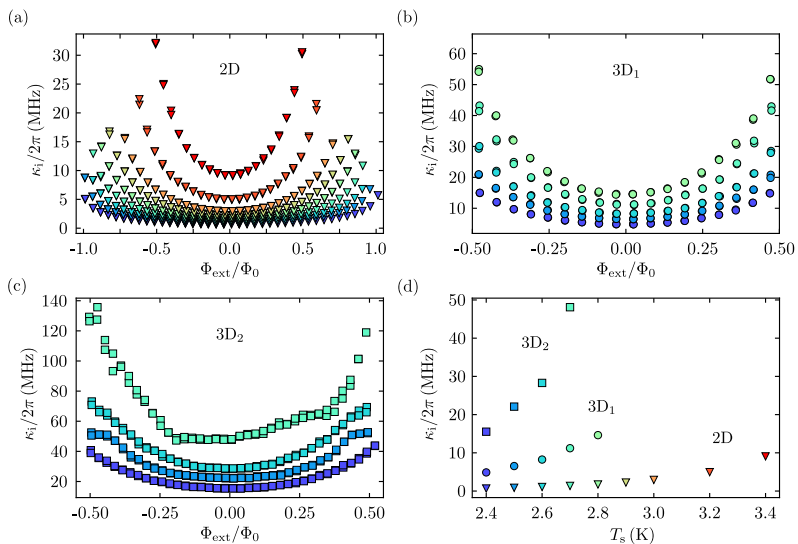
Next, we determine the flux responsivity of the three SQUID circuits. The flux responsivity is the derivative of the resonance frequency with respect to external flux  $\partial\omega_0/\partial\Phi_{\text{ext}}$ , usually given in  $\text{Hz}/\Phi_0$ . This responsivity is an extremely relevant parameter for instance for flux-mediated optomechanics and magnetomechanics [14–16, 57] or for photon-pressure circuits [10–12, 53], since it determines by how much the resonance frequency is fluctuating (in first order) for a given amount of flux fluctuations in the SQUID. In turn, this determines the single-photon coupling rates to the mechanical oscillator for example. In Supplemental Fig. 7 we plot the derivative of the flux-tuning fit curves (cf. main paper) for all three devices and at all recorded temperatures. Not surprisingly, and as expected already from main paper Figs. 3 and 8, we observe that the responsivities increase with increasing temperature and increase with decreasing constriction thickness. For the 2D device, we find maximum responsivities of about  $\gtrsim 80 \text{ MHz}/\Phi_0$  for the highest temperatures, while for the 3D<sub>2</sub> circuit we get up to  $\gtrsim 1 \text{ GHz}/\Phi_0$ . Even for the lower temperatures, we get still several hundred  $\text{MHz}/\Phi_0$  for the 3D circuits. The numbers are highly promising for many applications of these circuits, since many other devices based on aluminum and implemented in recent experiments have still smaller responsivities, but already led to very high radiation-pressure coupling rates to mechanical oscillators or radio-frequency circuits in the MHz domain [52, 53].

## D. Internal linewidth $\kappa_i$ for all devices vs temperature and flux

For several applications such as radiation-pressure experiments, parametric amplifiers or dispersive SQUID magnetometry, it is of interest to analyze how the external flux bias affects the losses in the circuit. Therefore, we extract



Supplemental Figure 7. **Flux responsivity of all three circuits for varying sample temperatures.** Magnitude of the flux responsivity  $\partial\omega_0/\partial\Phi_{\text{ext}}$  vs external flux bias  $\Phi_{\text{ext}}$  for (a) circuit 2D, (b) circuit 3D<sub>1</sub> and (c) circuit 3D<sub>2</sub>. The values are obtained by numerically calculating the derivative of the flux-tuning fit curves for all devices and all temperatures. The sample temperature  $T_s$  is color-coded into the lines, from dark blue  $T_s = 2.4$  K to red  $T_s = 3.2$  K. A list of the exact temperatures can be found in the caption of Supplemental Fig. 6.



Supplemental Figure 8. **Internal linewidth  $\kappa_i$  for all three circuits for varying sample temperatures.** Internal linewidth  $\kappa_i$  vs external flux bias  $\Phi_{\text{ext}}/\Phi_0$  for (a) circuit 2D, (b) circuit 3D<sub>1</sub> and (c) circuit 3D<sub>2</sub> at all measurement temperatures  $T_s$ . All circuits show an increase of  $\kappa_i$  with increasing flux  $|\Phi_{\text{ext}}/\Phi_0|$  and with increasing sample temperature  $T_s$ . Temperatures are equal to the ones in Supplemental Fig. 7. Panel (d) shows  $\kappa_i$  at the sweetspot ( $\Phi_{\text{ext}}/\Phi_0 = 0$ ) vs sample temperature  $T_s$ .

the internal linewidth  $\kappa_i$  for all three circuits for different flux bias points  $\Phi_{\text{ext}}/\Phi_0$  and temperatures  $T_s$ , cf. Supplemental Fig. 8(a)-(c). All three devices show a strong dependence of  $\kappa_i$  as function of  $\Phi_{\text{ext}}/\Phi_0$  and show an increase in their linewidth range  $\kappa_i^{\text{max}} - \kappa_i^{\text{min}}$  with increasing temperature. At the lowest temperature, circuit 2D has a tuning range of  $\sim 5$  MHz, which increases up to  $\sim 23$  MHz for highest sample temperature. For circuit 3D<sub>1</sub> it increases from  $\sim 10$  MHz to  $\sim 40$  MHz and for circuit 3D<sub>2</sub> from  $\sim 28$  MHz to  $\sim 88$  MHz. We believe the increase of internal loss rate with both flux and temperature is related to a locally reduced superconducting energy gap and therefore an increased quasiparticle density in the constriction, mainly due to a reduced critical temperature compared to the rest of the niobium film. This effect will be enhanced by the external flux bias, since the circulating current through

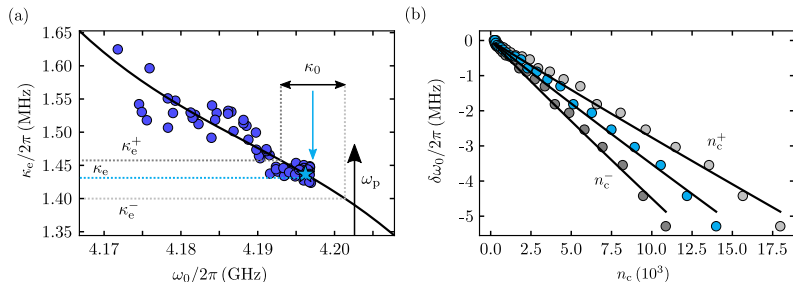
the constrictions is further reducing the gap and increasing the quasiparticle density. In Supplemental Fig. 8(d) we show the increase of  $\kappa_i$  at the sweetspot ( $\Phi_{\text{ext}}/\Phi_0 = 0$ ) as function of temperature related to the losses by thermal quasiparticles in the constriction. It is obvious that the linewidth trends towards smaller values for lower temperatures in all devices. It will be interesting to analyze the losses at much lower temperatures in future experiments, since currently we do not have a solid model to understand the temperature and flux dependence of  $\kappa_i$  and therefore also cannot make predictions for if and how the losses will saturate in the mK regime.

We show in Supplemental Note VI A, that the external linewidth is only weakly dependent on  $\Phi_{\text{ext}}/\Phi_0$  compared to  $\kappa_i$  and this effect is most likely due to a slightly different input impedance of the feedline for different resonance frequencies. The effect is small compared to the change of internal decay rate though.

## VI. SUPPLEMENTAL NOTE VI: ERROR BARS

### A. Error bars for the determination of the Kerr constant $\mathcal{K}$

The circuit Kerr nonlinearity  $\mathcal{K}$  is an important number for high-dynamic-range applications such as parametric amplifiers, radiation-pressure experiments or dispersive SQUID magnetometry. To reliably determine the value of  $\mathcal{K}$  from the pump-induced frequency shift, a good estimate of the intracircuit photon number  $n_c$  is essential. As discussed in the main paper appendix, we use Eq. (34) for calculating  $n_c$ , but two of the parameters going into that calculation might come with uncertainties and errors, the on-chip input power  $P_p$  and the external linewidth  $\kappa_e$ . Therefore we also perform an error estimation for  $\mathcal{K}$  based on estimated inaccuracies of these two parameters.



Supplemental Figure 9. **Error bar calculation using the uncertainties in  $\kappa_e$  and  $P_p$ .** (a) Experimentally determined external linewidth  $\kappa_e/2\pi$  of circuit 3D1 vs circuit resonance frequency  $\omega_0/2\pi$  at  $T_s = 2.5$  K. Circles are data, line is a polynomial fit. We describe our procedure for finding  $\kappa_e$  and its uncertainty here exemplarily for a flux bias point  $\Phi_{\text{ext}}/\Phi_0 = 0.14$ . This particular data point is displayed as a star. The pump tone is applied blue-detuned from the resonance frequency at  $\omega_p$  as indicated by the black vertical arrow here. In this case we do not have an experimental value for  $\kappa_e$  at the pump frequency and therefore use the closest available one indicated by the light blue arrow. If we have a value sitting exactly at the pump frequency we use that one. Since  $\kappa_e$  is a function of frequency but our fitting routine is assuming a frequency-independent  $\kappa_e$ , we estimate the uncertainty of  $\kappa_e$  to be given by the maximum and minimum of all  $\kappa_e$ -values in a window of width  $\kappa_0$  around  $\omega_p$  or around the point we chose for  $\kappa_e$ , respectively. The window for the particular point chosen here is indicated by the vertical black double-arrow and the corresponding vertical dotted lines. We call the resulting max/min values  $\kappa_e^+$  and  $\kappa_e^-$ , respectively. Additionally, we take into account a possible uncertainty in the on-chip pump power by  $\pm 1$  dB. As a result, we can find the standard  $n_c$ , the maximally possible  $n_c^+$  as well as the minimally possible  $n_c^-$ . For all three cases, we plot the frequency shift  $\delta\omega_0$  at the star-marked point vs intracavity photon number in panel (b). Circles are experimentally obtained data. We perform three individual fits, shown as lines here. The max/min values obtained for  $\mathcal{K}$  from these fits plus their fitting errors are plotted as error bars in main paper Fig. 4(d).

For the overall data analysis of the two-tone experiment and to obtain  $\mathcal{K}$ , we perform first raw data processing of the transmission response  $S_{21}$  for each pump power as described in Supplemental Note IV. Additionally, we cut out the visible strong pump tone with fixed frequency  $\omega_p$  from all measurements. As a next step, we extract  $\omega_0$ ,  $\kappa_e$  and  $\kappa_0$  for all flux bias values by our usual fitting routine, which also means that we have (a rough) knowledge of the frequency-dependence of  $\kappa_e$ . Then, we fit  $\kappa_e$  as a function of  $\omega_0$  for the whole flux-tuning-range with a fourth order polynomial, cf. Supplementary Fig. 9(a). Since we observe that  $\kappa_e$  is frequency dependent even over a frequency span of  $\kappa_0$ , we find the maximum and minimum possible value  $\kappa_e^+$  and  $\kappa_e^-$  for each pump power point as discussed in Supplemental Fig. 9(a) and process these two values as higher and lower errors for  $n_c$ .

We estimate the input power on the on-chip feedline by the generator output power and a total input attenuation as described in Supplemental Note I. Additionally a 10 dB directional coupler and a 1 dB microwave cable are added to the pump tone to perform the two-tone experiment. As uncertainty of the attenuation and as consequence also of the input power we assume  $\pm 1$  dB.

Using Eq. (34) (see main paper appendix) and the inaccuracies we get a highest and a lowest possible intracavity photon number  $n_c^+$  and  $n_c^-$ , respectively, for each pump frequency and pump power point, cf. Supplementary Fig. 9(b), where the measured frequency shift  $\delta\omega_0$  is plotted vs all three photon numbers (lowest, standard, highest). Finally, we perform a fit for all three cases using Eq. (28) to determine  $\mathcal{K}$ ,  $\mathcal{K}^+$  and  $\mathcal{K}^-$ . Note that  $|\mathcal{K}^-| > |\mathcal{K}| > |\mathcal{K}^+|$ . The error bars in  $\mathcal{K}$  resulting from the fit with  $n_c^+$ ,  $n_c^-$  and  $n_c$  are then given by  $|\mathcal{K}^-| - |\mathcal{K}|$  and  $|\mathcal{K}| - |\mathcal{K}^+|$  plus their direct errors obtained by the fit.

---

## VII. SUPPLEMENTAL REFERENCES

- [28] Uhl, K., Hackenbeck, D., Fuger, C., Kleiner, R., Koelle, D., and Bothner, D., **A flux-tunable YBa<sub>2</sub>Cu<sub>3</sub>O<sub>7</sub> quantum interference microwave circuit**. Applied Physics Letters **122**, 182603 (2023)
- [40] Khapaev, M. M., Kidiyarova-Shevchenko, A. Yu., Magnelind, P., and Kupriyanov, M. Yu., **3D-MLSI: software package for inductance calculation in multilayer superconducting integrated circuits**. IEEE Transactions on Applied Superconductivity **11**, 1090-1093 (2001)
- [61] Klein, N., Chaloupka, H., Muller, G., Orbach, S., and Piel, H., **The effective microwave surface impedance of high-*T<sub>c</sub>* thin films**. Journal of Applied Physics **67**, 6940 (1990)
- [62] Igreja, R. and Dias, C. J., **Analytical evaluation of the interdigital electrodes capacitance for a multi-layered structure**. Sensors and Actuators A **112**, 291-301 (2004)
- [49] Likharev, K. K., **Superconducting weak links**. Reviews of Modern Physics **51**, 101 (1979)
- [33] Hasselbach, K., Mailly, D., and Kirtley, J. R., **Micro-superconducting quantum interference device characteristics**. Journal of Applied Physics **91**, 4432 (2002)
- [41] Wenner, J., Neeley, M., Bialczak, Radoslav C., Lenander, M., Lucero, E., O’Connell, A. D., Sank, D., Wang, H., Weides, M., Cleland, A. N., and Martinis, J. M., **Wirebond crosstalk and cavity modes in large chip mounts for superconducting qubits**. Superconductor Science and Technology **24**, 065001 (2011)
- [42] Rieger, D., Gunzler, S., Spiecker, M., Nambisan, A., Wernsdorfer, W., and Pop, I. M., **Fano Interference in Microwave Resonator Measurements**. Physical Review Applied **20**, 014059 (2023)
- [14] Shevchuk, O., Steele, G. A., and Blanter, Ya. M., **Strong and tunable couplings in flux-mediated optomechanics**. Physical Review B **96**, 014508 (2017)
- [15] Rodrigues, I. C., Bothner, D., and Steele, G. A., **Coupling microwave photons to a mechanical resonator using quantum interference**. Nature Communications **10**, 5359 (2019)
- [16] Schmidt, P., Amawi, M. T., Pogorzalek, S., Deppe, F., Marx, A., Gross, R., and Huebl, H., **Sideband-resolved resonator electromechanics based on a nonlinear Josephson inductance probed on the single-photon level**. Communications Physics **3**, 233 (2020)
- [57] Zoepfl, D., Juan, M. L., Schneider, C. M. F., and Kirchmair, G., **Single-Photon Cooling in Microwave Magnetomechanics**. Physical Review Letters **125**, 023601 (2020)
- [10] Johansson, J. R., Johansson, G., and Nori, F., **Optomechanical-like coupling between superconducting resonators**. Physical Review A **90**, 053833 (2014)
- [11] Eichler, C., and Petta, J. R., **Realizing a Circuit Analog of an Optomechanical System with Longitudinally Coupled Superconducting Resonators**. Physical Review Letters **120**, 227702 (2018)
- [12] Bothner, D., Rodrigues, I. C., and Steele, G. A., **Photon-pressure strong coupling between two superconducting circuits**. Nature Physics **17**, 85-91 (2021)
- [53] Rodrigues, I. C., Bothner, D., and Steele, G. A., **Cooling photon-pressure circuits into the quantum regime**. Science Advances **7**, eabg6653 (2021)
- [52] Bothner, D., Rodrigues, I. C., and Steele, G. A., **Four-wave-cooling to the single phonon level in Kerr optomechanics**. Communications Physics **5**, 33 (2022)



# Publication 3

# A flux-tunable $\text{YBa}_2\text{Cu}_3\text{O}_7$ quantum interference microwave circuit

Cite as: Appl. Phys. Lett. **122**, 182603 (2023); doi: [10.1063/5.0146524](https://doi.org/10.1063/5.0146524)

Submitted: 14 February 2023 · Accepted: 27 March 2023 ·

Published Online: 1 May 2023



Kevin Uhl,<sup>a)</sup>  Daniel Hackenbeck, Christoph Füger, Reinhold Kleiner,  Dieter Koelle,  and Daniel Bothner<sup>a)</sup> 

## AFFILIATIONS

Physikalisches Institut, Center for Quantum Science (CQ) and LISA<sup>+</sup>, Universität Tübingen, 72076 Tübingen, Germany

<sup>a)</sup>Authors to whom correspondence should be addressed: [kevin.uhl@pit.uni-tuebingen.de](mailto:kevin.uhl@pit.uni-tuebingen.de) and [daniel.bothner@uni-tuebingen.de](mailto:daniel.bothner@uni-tuebingen.de)

## ABSTRACT

Josephson microwave circuits are essential for the currently flourishing research on superconducting technologies, such as quantum computation, quantum sensing, and microwave signal processing. To increase the possible parameter space for device operation with respect to the current standards, many materials for superconducting circuits are under active investigation. Here, we present the realization of a frequency-tunable, weakly nonlinear Josephson microwave circuit made of the high-temperature cuprate superconductor  $\text{YBa}_2\text{Cu}_3\text{O}_7$  (YBCO), a material with a high critical temperature and a very high critical magnetic field. An *in situ* frequency-tunability of  $\sim 300$  MHz is achieved by integrating a superconducting quantum interference device (SQUID) into the circuit based on Josephson junctions directly written with a helium ion microscope (HIM). Our results demonstrate that YBCO-HIM-SQUID microwave resonators are promising candidates for quantum sensing and microwave technology applications.

Published under an exclusive license by AIP Publishing. <https://doi.org/10.1063/5.0146524>

Superconducting microwave circuits with integrated Josephson junctions (JJs) and superconducting quantum interference devices (SQUIDs) are central components in many recent groundbreaking experimental developments.<sup>1–7</sup> This is because JJs allow for the circuit integration of a highly flexible Kerr nonlinearity, and a SQUID provides additional *in situ* frequency-tunability by magnetic flux, which also enables high-precision flux detection. Circuits with large Kerr nonlinearities constitute artificial atoms and qubits<sup>8,9</sup> used for microwave quantum optics, circuit quantum electrodynamics (QED),<sup>3</sup> and quantum computation.<sup>4</sup> Small nonlinearities are implemented for Josephson parametric amplifiers,<sup>5–8</sup> tunable microwave cavities for quantum hybrid systems,<sup>9</sup> for microwave SQUID magnetometry,<sup>10,11</sup> and for (generalized) radiation-pressure systems.<sup>12–16</sup> So far, the standard superconducting material of choice for most of these devices and technologies, in particular for the Josephson elements, has been aluminum<sup>17</sup> due to the high quality and controllability of Al JJs.

Recently, other materials are under intense investigation, for both the base circuit and the integrated JJs, which do not necessarily have to consist of one and the same material. One important objective of these studies is to implement superconducting Josephson circuits with a high tolerance to external magnetic fields, since this allows for instance for spin-qubit circuit QED,<sup>18,19</sup> advances in flux-mediated optomechanics,<sup>15,16</sup> dispersive quantum magnetometry<sup>10,11</sup> of individual magnetic nanoparticles, and potentially even topological quantum

computing.<sup>20,21</sup> Microwave resonators without JJs and based on niobium alloys,<sup>22–24</sup> on granular aluminum,<sup>25</sup> and on  $\text{YBa}_2\text{Cu}_3\text{O}_7$ <sup>26</sup> (YBCO) can provide magnetic-field tolerances up to the Tesla regime. Regarding the JJs, it has been demonstrated that constriction JJs in niobium<sup>27,28</sup> and NbN<sup>29</sup> and hybrid JJs based on graphene,<sup>30</sup> carbon nanotubes,<sup>31,32</sup> or semiconductors<sup>33,34</sup> have shown potential to be integrated into high-field Josephson microwave circuits. Most of these approaches, however, come with complications, such as non-sinusoidal current-phase relationships in constrictions<sup>35–37</sup> or impose complex fabrication challenges with limited junction reproducibility.

In this Letter, we report the realization of a superconducting quantum interference microwave circuit based solely on YBCO. In addition to having an extremely large critical magnetic field, YBCO circuits can also be operated at high temperatures, and they have a large superconducting gap and allow for the implementation of ideal Josephson tunnel junctions. Our starting point is an inductor-capacitor (LC) circuit that combines two parallel interdigitated capacitors (IDCs) with linear inductors, cf. Fig. 1. The total capacitance of the IDCs is  $C \approx 520$  fF, and the total inductance without the Josephson junctions is  $L \approx 586$  pH. The circuit is coupled to a coplanar waveguide feedline with a characteristic impedance of  $Z_0 \approx 54 \Omega$  by means of a coupling capacitance  $C_c \sim 18$  fF for driving and readout. The value for  $C$  was obtained through finite element simulations using Comsol Multiphysics, and the inductance  $L$  was calculated from

$C_{\text{tot}} = C + C_c$  and the measured circuit resonance frequency, cf. also [supplementary material](#), Note III. A square-shaped  $11.5 \times 11.5 \mu\text{m}^2$  large loop (inner hole dimensions) for the SQUID is integrated into the center of the circuit with a loop self-inductance  $L_{\text{loop}} = 71 \text{ pH}$  obtained from simulations,<sup>38</sup> cf. [supplementary material](#), Note III. Directly at the loop, the circuit is shorted to the ground plane to avoid charging during the later irradiation with  $\text{He}^+$  ions.

As material for our circuits, we chose a commercially purchased S-type YBCO film from Ceraco with a thickness of  $t_Y = 50 \text{ nm}$ , deposited via reactive coevaporation and without a buffer layer on a  $t_{\text{MgO}} = 500 \text{ nm}$  thick MgO substrate. For protection of the YBCO film, the wafer was additionally covered *in situ* with a  $t_{\text{Au}} = 40 \text{ nm}$  film of gold. According to the accompanying datasheet, the critical temperature of the film is  $T_c = 89 \text{ K}$ . For the device fabrication, we first remove the gold by wet-etching and then perform optical lithography with a laser writer to define the circuit and waveguide structures. Subsequently, we wet-etch the YBCO with phosphoric acid and finally remove the remaining photoresist with acetone/isopropanol, more details on the fabrication can be found in the [supplementary material](#), Note I.

The finished  $10 \times 10 \text{ mm}^2$  large chip is mounted into a radiation-tight copper housing and wire-bonded to a printed circuit board (PCB), which connects the on-chip coplanar waveguide to coaxial cables. For the application of an out-of-plane magnetic field, a

magnet coil is attached to the bottom of the copper housing on its outer wall and the whole configuration is attached to the tip of a microwave dipstick for measurements in a liquid helium dewar. The dipstick contains 30 dB of attenuation on the coaxial input line for equilibrating the thermal noise on the line to  $T_s = 4.2 \text{ K}$  and a cryogenic high-electron mobility transistor (HEMT) amplifier on the output line. The sample including the magnet, the amplifier, and the attenuators is covered with a cylindrical cryoperm magnetic shield when inserted into the liquid helium bath, where all the presented measurements were taken, cf. also [supplementary material](#), Note II.

After a first characterization in liquid helium, we de-mount the chip again and perform the helium ion microscope (HIM) irradiation as described in Refs. 39 and 40 and [supplementary material](#), Note I for the direct writing of two Josephson junctions into the circuit SQUID loop. The line dose was  $D_{\text{He}} = 900 \text{ ions/nm}$ , the ion energy  $E_{\text{He}} = 30 \text{ keV}$ , and the beam current  $I_{\text{He}} = 840 \text{ fA}$ . After the JJ writing, the chip is re-mounted into the PCB, the Cu housing and the dewar dipstick and the characterization is continued. As very first observation, we find that the resonance frequency of the circuit has shifted from  $\omega_b = 2\pi = 8.965 \text{ GHz}$  before the JJ writing to  $\omega_0 = 2\pi \times 8.64 \text{ GHz}$  after the JJ writing, cf. Fig. 1(c). From the frequency shift and the relation

$$\omega_0 = \frac{\omega_b}{\sqrt{1 + 2L}}, \quad (1)$$

we find the zero-flux inductance of a single junction to be  $L'_0 \approx 90 \text{ pH}$ , which would correspond to a critical current  $I'_0 = \Phi_0 \times (2\pi L'_0)^{-1} \approx 3.6 \mu\text{A}$ . From the flux-dependence discussed below in the context of Fig. 2, however, it turns out that we can best describe the data with  $I_0 = 4.0 \mu\text{A}$ , i.e.,  $L_0 = \Phi_0 \times (2\pi I_0)^{-1} = 82 \text{ pH}$ , and a small but finite additional linear inductance  $L_{\text{lin}} \sim 7.2 \text{ pH}$  per junction that was generated by the HIM irradiation. We believe that this indicates a slightly non-sinusoidal current-phase relationship,<sup>41</sup> a degradation of the YBCO properties next to the actual JJ barrier by the writing process, a small critical current asymmetry between the two junctions, or a combination of all three effects.

The total cavity decay rate has approximately doubled after HIM irradiation, and we have  $\kappa_0 \approx 2\kappa_b$ , where  $\kappa_b = 2\pi \times 21.2 \text{ MHz}$  is the linewidth before the HIM exposure and  $\kappa_0 = 2\pi \times 40 \text{ MHz}$  after the HIM exposure. The reason for the large linewidth both before and after the HIM-JJ introduction is currently unclear, but we suspect that it is a combination of incompletely etched gold/YBCO, damage of the YBCO next to the JJs by the helium beam, internal and external flux noise, and thermal noise in a nonlinear oscillator. Interestingly, the ratio of internal (i) to external (e) linewidths is nearly unmodified though  $(\kappa_i/\kappa_e)_b \approx (\kappa_i/\kappa_e)_0$ , indicating that we might additionally be dealing with cable resonances and the Fano effect, rendering the separation of internal and external losses somewhat unreliable.<sup>42</sup>

When we apply a magnetic field perpendicular to the circuit, we introduce an external magnetic flux  $\Phi_{\text{ext}}$  into the SQUID. Figure 2 summarizes our observations for what happens to the circuit resonance frequency  $\omega_0(\Phi_{\text{ext}})$  in this experiment. We find that  $\omega_0(\Phi_{\text{ext}})$  is shifting toward lower values for increasing flux, eventually modulating periodically with a periodicity of one flux quantum  $\Phi_0 \approx 2.068 \times 10^{-15} \text{ Tm}^2$ . The tuning range of  $\omega_0^{\text{max}} - \omega_0^{\text{min}} \sim 2\pi \times 300 \text{ MHz}$  that we observe here is a factor of two to three larger than in many similarly weakly

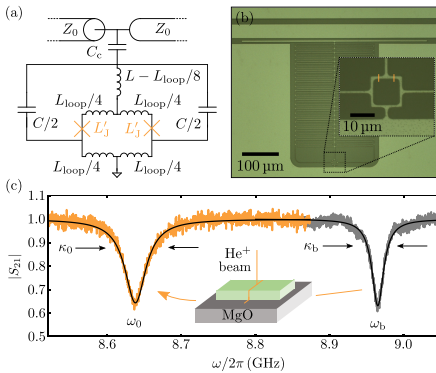


**FIG. 1.** A YBCO quantum interference microwave circuit with helium-ion-patterned Josephson junctions. (a) Circuit equivalent and (b) false-color optical micrograph of a typical device. The circuit main inductance is modeled by a linear inductor  $L$ , the two interdigitated capacitors (IDCs) by a total capacitance  $C$ . The center of the circuit is a loop structure for the SQUID, cf. zoom inset. The square-shaped  $11.5 \times 11.5 \mu\text{m}^2$  loop has a total loop inductance  $L_{\text{loop}}$ , and the Josephson junctions (JJs) have an inductance  $L'_j$  (only  $\neq 0$  after junction writing). The circuit is capacitively coupled to a coplanar waveguide feedline (center conductor width  $S \approx 37.5 \mu\text{m}$ , gap-to-ground  $W \approx 15 \mu\text{m}$ ) with a calculated characteristic impedance  $Z_0 \approx 54 \Omega$  by means of a coupling capacitance  $C_c$ . In (b), YBCO is bright, the MgO substrate is dark. (c) Transmission  $|S_{21}|$  of the circuit at  $T_s = 4.2 \text{ K}$  before and after the junction writing, black lines are fits to the data. Before introducing the JJs, the circuit has a resonance frequency  $\omega_b$  and a linewidth  $\kappa_b$ , after the cutting  $\omega_0$  and  $\kappa_0$ , respectively. Values can be found in the main text.

nonlinear Dayem-bridge SQUID-circuits reported for aluminum<sup>43,44</sup> or niobium.<sup>28</sup> Also, we do not observe a hysteretic flux response,<sup>26,45</sup> which in combination with the large tuning range indicates that the screening parameter  $\beta_L = \frac{2I_0(L_{\text{loop}}+2L_{\text{lin}})}{\Phi_0} = \frac{L_{\text{loop}}+2L_{\text{lin}}}{\pi L_0}$  is considerably smaller than 1.

The origin of the resonance frequency shift is a change in the JJ inductance with total flux  $\Phi$  in the SQUID,

$$L_J(\Phi) = \frac{L_{J0}}{\cos\left(\pi \frac{\Phi}{\Phi_0}\right)}, \quad (2)$$

where the relation between the external and the total flux is given by

$$\frac{\Phi}{\Phi_0} = \frac{\Phi_{\text{ext}}}{\Phi_0} - \frac{\beta_L}{2} \sin\left(\pi \frac{\Phi}{\Phi_0}\right). \quad (3)$$

In order to model the resonance frequency shift with external flux and to extract a numerical value for  $\beta_L$ , we fit a single-period flux tuning curve with

$$\omega_0(\Phi_{\text{ext}}) = \frac{\omega_b}{\sqrt{1 + \frac{L_J(\Phi) + L_{\text{lin}}}{2L}}}. \quad (4)$$

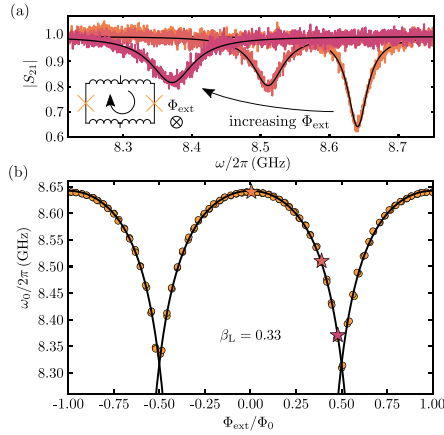


**FIG. 2.** Flux-tuning the resonance frequency of a YBCO quantum interference circuit. (a) Transmission response  $|S_{21}|$  of the YBCO-HIM-SQUID circuit for three different  $\Phi_{\text{ext}}/\Phi_0 = 0.0, 0.4, 0.5$ . With increasing flux in the SQUID, cf. inset schematic, the absorption resonance is shifting toward lower frequencies; colored noisy lines are data, and black smooth lines are fits. From the fits, we extract the resonance frequency  $\omega_0(\Phi_{\text{ext}})$ , which is shown as a function of flux in panel (b). The resonance frequency is modulated periodically with a periodicity of  $\Phi_0$ . Circles are data, lines are fits from which we determine the screening parameter  $\beta_L = 0.33$ . Star-shaped data points in (b) correspond to curves in (a).

As fit parameters, we get  $L_{\text{lin}}$  and  $I_0$  as mentioned above, and we obtain  $\beta_L \approx 0.33$ , which corresponds to  $L_{\text{loop}} + 2L_{\text{lin}} \approx 85$  pH. This  $\beta_L$  is much smaller than what has been reported for many aluminum and niobium quantum interference circuits with  $I_0 \sim 10$   $\mu$ A and similar or smaller SQUID loop sizes, mostly because many of these have used nano-constrictions for the JJs,<sup>28,43,44,46</sup> which are known to have a non-sinusoidal current-phase relationship that effectively adds much more linear inductance  $L_{\text{lin}}$  to the loop than what we observe here. We also note that in principle we can fit the dataset without  $L_{\text{lin}}$  if we leave  $\beta_L$  a completely free parameter and obtain the alternative parameters  $I_0^{\text{alt}} = 3.7$   $\mu$ A,  $\beta_L^{\text{alt}} = 0.35$ , and  $L_{\text{loop}} = 99$  pH, which would, however, mean that the loop inductance is considerably larger than expected from our simulations, cf. [supplementary material](#), Note III. Additional data on two more SQUID circuits with even lower critical currents, lower screening parameters, and a flux tuning range up to  $\geq 2$  GHz can be found in the [supplementary material](#), Note VIII.

As last important experiment, we determine the circuit Kerr non-linearity  $\mathcal{K}$ , since this is an extremely relevant number for high-dynamic-range applications,<sup>47</sup> such as parametric amplifiers, radiation-pressure experiments, or dispersive SQUID magnetometry.  $\mathcal{K}$  is also called anharmonicity, and it is equivalent to the resonance-frequency-shift per excitation (here, per microwave photon) in a non-linear oscillator. To do so, we perform a two-tone characterization of the transmission response, i.e., we continuously pump the circuit with a fixed-frequency high-power pump tone, that is slightly blue-detuned from the cavity resonance at  $\omega_p \approx \omega_0 + \kappa$  and then take a  $S_{21}$  trace of the pumped cavity with a low-power microwave probe signal, cf. [Fig. 3](#). We repeat this measurement for various pump powers and bias flux values. With the increase in intracircuit photon number from the pump tone  $n_c$ , the resonance frequency gets shifted toward lower frequencies, similar to the Stark effect in quantum optics. In the regime of our experiment, the frequency shift  $\delta\omega_0 = \omega'_0 - \omega_0$  is given by

$$\delta\omega_0 = \Delta_p - \sqrt{(\Delta_p - \mathcal{K}n_c)(\Delta_p - 3\mathcal{K}n_c - \frac{\kappa_1^2}{4})}, \quad (5)$$

where  $\Delta_p = \omega_p - \omega_0$  and, therefore, we obtain  $\mathcal{K}$  from a corresponding fit of the shift as a function of  $n_c$ , cf. [Fig. 3](#). The small correction factor  $\kappa_1^2/4$  with  $\kappa_1 = (\kappa_p - \kappa_0)/2$  ( $\kappa_0$  is the linewidth without pump,  $\kappa_p$  is the linewidth with pump) reflects a linear increase in the total linewidth with pump power, cf. [supplementary material](#), Notes IV and VI.

We perform this experiment for different bias flux values and, therefore, obtain  $\mathcal{K}(\Phi_{\text{ext}})/2\pi$  with values varying from  $-8$  kHz at the flux sweetspot (integer flux quanta) to  $-120$  kHz near the resonance frequency minima at  $\Phi_{\text{ext}}/\Phi_0 \approx 0.5$ . A comparison of the experimental data with the theoretical curve

$$\mathcal{K} = -\frac{e^2}{2\hbar C} \left( \frac{L_J}{2L + L_{\text{lin}} + L_J} \right)^3 \left[ 1 + 3\Lambda \tan^2\left(\pi \frac{\Phi}{\Phi_0}\right) \right], \quad (6)$$

where  $\Lambda = (L_{\text{lin}} + L_{\text{loop}}/4)/(L_{\text{lin}} + L_{\text{loop}}/4 + L_J)$  reveals good agreement, cf. [Fig. 3\(c\)](#). We believe that the deviations between experimental data and theory line originate from possible JJ asymmetries and from insufficient accuracy in the knowledge of the intracircuit pump photon numbers  $n_c$ . Details on the theoretical model, the data analysis, and how we determine intracircuit photon numbers can be found in the [supplementary material](#), Notes III–IX.

In conclusion, we have reported a superconducting quantum interference circuit based on  $\text{YBa}_2\text{Cu}_3\text{O}_7$  with integrated Josephson junctions directly written with a helium-ion-microscope. The single-junction critical current of  $I_0 \approx 4 \mu\text{A}$  allowed for a small screening parameter  $\beta_L \approx 0.33$  and  $I_0$  could be varied by several orders of magnitude in future devices just by adjusting the HIM ion dose to the desired value.<sup>39,40</sup> The Kerr nonlinearity in our devices was found to be  $\sim 8 \text{ kHz}$  to  $\sim 120 \text{ kHz}$ , i.e., sufficiently small to allow for high-power and high-dynamic-range applications.

One important future direction is to understand and to improve the large  $\kappa_i$  in our devices, even without the HIM-JJs, as other YBCO resonators with similar thickness (but different YBCO specifications) have shown much smaller decay rates.<sup>26,48</sup> It will also be interesting to investigate the properties of the resonators in large magnetic in-plane fields up to the Tesla regime, for which we unfortunately currently do not have a suitable experimental setup. As both YBCO resonators and YBCO-SQUIDS have been demonstrated to be resilient to magnetic fields up to the Tesla regime,<sup>26,49</sup> we have no reason to doubt that also the combination of the two will have excellent field-compatibility. Finally, it will be useful to investigate the temperature dependence and the noise properties of the presented devices in future experiments.

See the [supplementary material](#) for the details on the sample fabrication and the experimental setup, and a thorough discussion of the theoretical background and formal derivations required for this manuscript and its analyses. We furthermore present there supporting data and simulation results regarding the circuit before junction writing, and we discuss our raw data processing and error bar calculations.

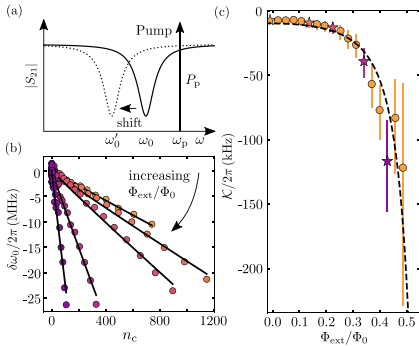


**FIG. 3.** Characterizing the circuit Kerr-nonlinearity. (a) Schematic of the two-tone experiment. A pump tone with power  $P_p$  is applied slightly blue-detuned to the circuit resonance with  $\omega_p \sim \omega_0 + \kappa$  and  $S_{21}$  of the pumped circuit is measured with a low-power probe tone. The frequency shift  $\delta\omega_0 = \omega'_0 - \omega_0$  we obtain from this is plotted vs intracavity pump photon number  $n_c$  for different bias flux values in panel (b); data shown are for  $\Phi_{\text{ext}}/\Phi_0 = 0, 0.14, 0.22, 0.34, \text{ and } 0.43$ ; arrow indicates direction of increasing flux. Circles are data, and lines are fits. In (c), the  $\mathcal{K}$  obtained from the fits are shown as function of  $\Phi_{\text{ext}}$ ; circles are data and dashed line is the theory curve based on Eq. (6). Stars in (c) correspond to data shown in (b). Error bars take into account uncertainties in the intracavity photon number, cf. [supplementary material](#), Note VII.

Finally, we include also data for two more YBCO HIM-JJ-SQUID cavities, which are not discussed in the main manuscript.

We gratefully acknowledge technical support by M. Turad and R. Löffler (both LISA<sup>+</sup>) and by C. Back. We would also like to thank L. Wolz, K. Fohmann, C. Schmid, and J. Rodriguez Lorenzo for experimental assistance and useful insights. The authors acknowledge funding by the Deutsche Forschungsgemeinschaft (DFG) via Grant Nos. BO 6068/1-1 and BO 6068/2-1.

## AUTHOR DECLARATIONS

### Conflict of Interest

The authors have no conflicts to disclose.

### Author Contributions

**Kevin Uhl:** Conceptualization (equal); Formal analysis (equal); Investigation (lead); Methodology (equal); Software (lead); Visualization (equal); Writing – original draft (equal); Writing – review & editing (equal). **Daniel Hackenbeck:** Investigation (supporting); Methodology (supporting); Software (supporting); Writing – review & editing (equal). **Christoph Fügner:** Investigation (supporting); Writing – review & editing (equal). **Reinhold Kleiner:** Funding acquisition (equal); Supervision (supporting); Writing – review & editing (equal). **Dieter Koelle:** Funding acquisition (equal); Supervision (supporting); Writing – review & editing (equal). **Daniel Bothner:** Conceptualization (equal); Formal analysis (equal); Funding acquisition (equal); Methodology (equal); Supervision (lead); Visualization (equal); Writing – original draft (equal); Writing – review & editing (equal).

### DATA AVAILABILITY

The data that support the findings of this study are available within the article and its [supplementary material](#). The data that support the findings of this study are openly available in Zenodo at <https://doi.org/10.5281/zenodo.7839911>, Ref. 50.

### REFERENCES

- J. Clarke and F. K. Wilhelm, “Superconducting quantum bits,” *Nature* **453**, 1031–1042 (2008).
- J. Q. You and F. Nori, “Atomic physics and quantum optics using superconducting circuits,” *Nature* **474**, 589–597 (2011).
- A. Blais, A. L. Grimsmo, S. M. Girvin, and A. Wallraff, “Circuit quantum electrodynamics,” *Rev. Mod. Phys.* **93**, 025005 (2021).
- F. Arute, K. Arya, R. Babbush, D. Bacon, J. C. Bardin, R.arends, R. Biswas, S. Boixo, F. G. S. L. Brandao, D. A. Buell, B. Burkett, Y. Chen, Z. Chen, B. Chiaro, R. Collins, W. Courtney, A. Dunsworth, E. Farhi, F. Brooks, A. Fowler, C. Gidney, M. Gustina, R. Graff, K. Guerin, S. Habegger, M. P. Harrigan, M. J. Hartmann, A. Ho, M. Hoffmann, T. Huang, T. S. Humble, S. V. Isakov, E. Jeffrey, Z. Jiang, D. Kafri, K. Kechedzhi, J. Kelly, P. V. Klimov, S. Knysh, A. Korotkov, F. Kostritsa, D. Landhuis, M. Lindmark, E. Lucero, D. Lyakh, S. Mandrà, J. R. McClean, M. McEwen, A. Megrant, X. Mi, K. Michielsen, M. Mohseni, J. Mutus, O. Naaman, M. Neeley, C. Neill, M. Y. Niu, E. Ostby, A. Pethukov, J. C. Platt, C. Quintana, E. G. Rieffel, P. Roushan, N. C. Rubin, D. Sank, K. J. Satzinger, V. Smelyanskiy, K. J. Sung, M. D. Trevithick, A. Vainsencher, B. Villalonga, T. White, Z. J. Yao, P. Yeh, A. Zalcman, H. Neven, and J. M. Martinis, “Quantum supremacy using a programmable superconducting processor,” *Nature* **574**, 505–510 (2019).
- M. A. Castellanos-Beltran, K. D. Irwin, G. C. Hilton, L. R. Vale, and K. W. Lehnert, “Amplification and squeezing of quantum noise with a tunable Josephson metamaterial,” *Nat. Phys.* **4**, 929–931 (2008).

- <sup>6</sup>N. Bergal, F. Schackert, M. Metcalfe, R. Vijay, V. E. Manucharyan, L. Frunzio, D. E. Prober, R. J. Schoelkopf, S. M. Girvin, and M. H. Devoret, "Phase-preserving amplification near the quantum limit with a Josephson ring modulator," *Nature* **465**, 64–68 (2010).
- <sup>7</sup>C. Macklin, K. O'Brien, D. Hover, M. E. Schwartz, V. Bolkhovsky, X. Zhang, W. D. Oliver, and I. Siddiqi, "A near-quantum-limited Josephson traveling-wave parametric amplifier," *Science* **350**, 307–310 (2015).
- <sup>8</sup>K. M. Sliwa, M. Hatridge, A. Narla, S. Shankar, L. Frunzio, R. J. Schoelkopf, and M. H. Devoret, "Reconfigurable Josephson circulator/directional amplifier," *Phys. Rev. X* **5**, 041020 (2015).
- <sup>9</sup>A. Palacios-Laloy, F. Nguyen, F. Mallet, P. Bertet, D. Vion, and D. Esteve, "Tunable resonators for quantum circuits," *J. Low Temp. Phys.* **151**, 1034–1042 (2008).
- <sup>10</sup>M. Hatridge, R. Vijay, D. H. Slichter, J. Clarke, and I. Siddiqi, "Dispersive magnetometry with a quantum limited SQUID parametric amplifier," *Phys. Rev. B* **83**, 134501 (2011).
- <sup>11</sup>E. M. Levenson-Falk, N. Antler, and I. Siddiqi, "Dispersive nanoSQUID magnetometry," *Supercond. Sci. Technol.* **29**, 113003 (2016).
- <sup>12</sup>J. R. Johansson, G. Johansson, and F. Nori, "Optomechanical-like coupling between superconducting resonators," *Phys. Rev. A* **90**, 053833 (2014).
- <sup>13</sup>C. Eichler and J. R. Petta, "Realizing a circuit analog of an optomechanical system with longitudinally coupled superconducting resonators," *Phys. Rev. Lett.* **120**, 227702 (2018).
- <sup>14</sup>D. Bothner, I. C. Rodrigues, and G. A. Steele, "Photon-pressure strong coupling between two superconducting circuits," *Nat. Phys.* **17**, 85–91 (2021).
- <sup>15</sup>O. Shevchuk, G. A. Steele, and Y. M. Blanter, "Strong and tunable couplings in flux-mediated optomechanics," *Phys. Rev. B* **96**, 014508 (2017).
- <sup>16</sup>I. C. Rodrigues, D. Bothner, and G. A. Steele, "Coupling microwave photons to a mechanical resonator using quantum interference," *Nat. Commun.* **10**, 5359 (2019).
- <sup>17</sup>Y. Nakamura, Y. A. Pashkin, and J. S. Tsai, "Coherent control of macroscopic quantum states in a single-Cooper-pair box," *Nature* **398**, 786–788 (1999).
- <sup>18</sup>N. Samkharadze, G. Zheng, N. Kalhor, D. Brousse, A. Sammak, U. C. Mendes, A. Blais, G. Scappucci, and L.-M. K. Vandersypen, "Strong spin-photon coupling in silicon," *Science* **359**, 1123–1127 (2018).
- <sup>19</sup>X. Mi, M. Benito, S. Putz, D. M. Zajac, J. M. Taylor, G. Burkard, and J. R. Petta, "A coherent spin-photon interface in silicon," *Nature* **555**, 599–603 (2018).
- <sup>20</sup>T. Hyart, B. van Heck, I. C. Fulga, M. Burrello, A. R. Akhmerov, and C. W. J. Beenakker, "Flux-controlled quantum computation with Majorana fermions," *Phys. Rev. B* **88**, 035121 (2013).
- <sup>21</sup>S. Plugg, A. Rasmussen, R. Egger, and K. Flensberg, "Majorana box qubits," *New J. Phys.* **19**, 012001 (2017).
- <sup>22</sup>N. Samkharadze, A. Bruno, P. Scarlino, G. Zheng, D. P. DiVincenzo, L. DiCarlo, and L. M. K. Vandersypen, "High-kinetic-inductance superconducting nanowire resonators for circuit QED in a magnetic field," *Phys. Rev. Appl.* **5**, 044004 (2016).
- <sup>23</sup>J. G. Kroll, F. Borsoi, K. L. van der Enden, W. Uilhoorn, D. de Jong, M. Quintero-Pérez, D. J. van Woerkom, A. Bruno, S. R. Plissard, D. Car, E. P. A. M. Bakkers, M. C. Cassidy, and L. P. Kouwenhoven, "Magnetic-field-resilient superconducting coplanar-waveguide resonators for hybrid circuit quantum electrodynamics experiments," *Phys. Rev. Appl.* **11**, 064053 (2019).
- <sup>24</sup>C. W. Zollitsch, J. O'Sullivan, O. Kennedy, G. Dold, and J. J. L. Morton, "Tuning high-Q superconducting resonators by magnetic field reorientation," *AIP Adv.* **9**, 125225 (2019).
- <sup>25</sup>K. Borisov, D. Rieger, P. Winkel, F. Henriques, F. Valenti, A. Ionita, M. Wessbecher, M. Specker, D. Gusenkova, I. M. Pop, and W. Wernsdorfer, "Superconducting granular aluminum resonators resilient to magnetic fields up to 1 Tesla," *Appl. Phys. Lett.* **117**, 120502 (2020).
- <sup>26</sup>A. Ghirri, C. Bonizzoni, D. Gerace, S. Sanna, A. Cassinese, and M. Affronte, "YBa<sub>2</sub>Cu<sub>3</sub>O<sub>7</sub> microwave resonators for strong collective coupling with spin ensembles," *Appl. Phys. Lett.* **106**, 184101 (2015).
- <sup>27</sup>E. J. Romans, S. Rozhko, L. Young, A. Blois, L. Hao, D. Cox, and J. C. Gallop, "Noise performance of niobium nano-SQUIDs in applied magnetic fields," *IEEE Trans. Appl. Supercond.* **21**, 404–407 (2011).
- <sup>28</sup>O. W. Kennedy, J. Burnett, J. C. Fenton, N. G. N. Constantino, P. A. Warburton, J. J. L. Morton, and E. Dupont-Ferrier, "Tunable Nb superconducting resonator based on a constriction nano-SQUID fabricated with a Ne focused ion beam," *Phys. Rev. Appl.* **11**, 014006 (2019).
- <sup>29</sup>M. Xu, R. Cheng, Y. Wu, G. Liu, and H. X. Tang, "Magnetic field-resilient quantum-limited parametric amplifier," *PRX Quantum* **4**, 010322 (2023).
- <sup>30</sup>J. G. Kroll, W. Uilhoorn, K. L. van der Enden, D. de Jong, K. Watanabe, T. Taniguchi, S. Goswami, M. C. Cassidy, and L. P. Kouwenhoven, "Magnetic field compatible circuit quantum electrodynamics with graphene Josephson junctions," *Nat. Commun.* **9**, 4615 (2018).
- <sup>31</sup>B. H. Schneider, S. Etaki, H. S. J. van der Zant, and G. A. Steele, "Coupling carbon nanotube mechanics to a superconducting circuit," *Sci. Rep.* **2**, 599 (2012).
- <sup>32</sup>M. Mergenthaler, A. Nersisyan, A. Patterson, M. Esposito, A. Baumgartner, C. Schönenberger, G. A. D. Briggs, E. A. Laird, and P. J. Leek, "Circuit quantum electrodynamics with carbon-nanotube-based superconducting quantum circuits," *Phys. Rev. Appl.* **15**, 064050 (2021).
- <sup>33</sup>F. Luthi, T. Stavenga, O. W. Enz, A. Bruno, C. Dickel, N. K. Langford, M. A. Rol, T. S. Jespersen, J. Nygård, P. Krogstrup, and L. DiCarlo, "Evolution of nanowire transmon qubits and their coherence in a magnetic field," *Phys. Rev. Lett.* **120**, 100502 (2018).
- <sup>34</sup>M. Pita-Vidal, A. Bargerbois, C.-K. Yang, D. J. van Woerkom, W. Pfaff, N. Haider, P. Krogstrup, L. P. Kouwenhoven, G. de Lange, and A. Kou, "Gate-tunable field-compatible fluxonium," *Phys. Rev. Appl.* **14**, 064038 (2020).
- <sup>35</sup>K. Hasselbach, D. Mailly, and J. R. Kirtley, "Micro-superconducting quantum interference device characteristics," *J. Appl. Phys.* **91**, 4432 (2002).
- <sup>36</sup>A. G. P. Troeman, S. H. W. van der Ploeg, E. Il'ichev, H.-G. Meyer, A. A. Golubov, M. Y. Kupriyanov, and H. Hilgenkamp, "Temperature dependence measurements of the supercurrent-phase relationship in niobium nanobridges," *Phys. Rev. B* **77**, 024509 (2008).
- <sup>37</sup>R. Vijay, E. M. Levenson-Falk, D. H. Slichter, and I. Siddiqi, "Approaching ideal weak link behavior with three dimensional aluminum nanobridges," *Appl. Phys. Lett.* **96**, 223112 (2010).
- <sup>38</sup>M. M. Khaepaev, A. Y. Kidiyarova-Shevchenko, P. Magnelind, and M. Y. Kupriyanov, "3D-MLSI: Software package for inductance calculation in multilayer superconducting integrated circuits," *IEEE Trans. Appl. Supercond.* **11**, 1090–1093 (2001).
- <sup>39</sup>S. A. Cybart, E. Y. Cho, T. J. Wong, B. H. Wehlin, M. K. Ma, C. Huynh, and R. C. Dynes, "Nano Josephson superconducting tunnel junctions in YBa<sub>2</sub>Cu<sub>3</sub>O<sub>7-x</sub> directly patterned with a focused helium ion beam," *Nat. Nanotechnol.* **10**, 598–602 (2015).
- <sup>40</sup>B. Müller, M. Karer, F. Limberger, M. Becker, B. Schröppel, C. J. Burkhardt, R. Kleiner, E. Goldobin, and D. Koelle, "Josephson junctions and SQUIDs created by focused helium-ion-beam irradiation of YBa<sub>2</sub>Cu<sub>3</sub>O<sub>7-x</sub>," *Phys. Rev. Appl.* **11**, 044082 (2019).
- <sup>41</sup>K. Likharev, "Superconducting weak links," *Rev. Mod. Phys.* **51**, 101 (1979).
- <sup>42</sup>D. Rieger, S. Günzler, M. Specker, A. Nambian, W. Wernsdorfer, and I. M. Pop, "Fano interference in microwave resonator measurements," *arXiv:2209.03036* (2022).
- <sup>43</sup>C. Rodrigues, D. Bothner, and G. A. Steele, "Cooling photon-pressure circuits into the quantum regime," *Sci. Adv.* **7**, eabg6653 (2021).
- <sup>44</sup>D. Bothner, I. C. Rodrigues, and G. A. Steele, "Four-wave-cooling to the single phonon level in Kerr optomechanics," *Commun. Phys.* **5**, 33 (2022).
- <sup>45</sup>S. Pogorzalek, K. G. Fedorov, L. Zhong, J. Goetz, F. Wulschner, M. Fischer, P. Eder, E. Xie, K. Inomata, T. Yamamoto, Y. Nakamura, A. Marx, F. Deppe, and R. Gross, "Hysteretic flux response and nondegenerate gain of flux-driven Josephson parametric amplifiers," *Phys. Rev. Appl.* **8**, 024012 (2017).
- <sup>46</sup>E. M. Levenson-Falk, R. Vijay, and I. Siddiqi, "Nonlinear microwave response of aluminum weak-link Josephson oscillators," *Appl. Phys. Lett.* **98**, 123115 (2011).
- <sup>47</sup>N. E. Frattini, V. V. Sivak, A. Lingenfelter, S. Shankar, and M. H. Devoret, "Optimizing the nonlinearity and dissipation of a SNAIL parametric amplifier for dynamic range," *Phys. Rev. Appl.* **10**, 054020 (2018).
- <sup>48</sup>A. Roitman, A. Shaulov, and Y. Yeshurun, "Characterization of YBa<sub>2</sub>Cu<sub>3</sub>O<sub>7-x</sub> coplanar resonator for microwave kinetic inductance detectors," *Supercond. Sci. Technol.* **36**, 015002 (2023).
- <sup>49</sup>T. Schwarz, J. Nagel, R. Wölbling, M. Kemmler, R. Kleiner, and D. Koelle, "Low-noise nano superconducting quantum interference device operating in Tesla magnetic fields," *ACS Nano* **7**, 844–850 (2013).
- <sup>50</sup>K. Uhl, D. Hackenbeck, C. Füger, R. Kleiner, D. Koelle, and D. Bothner, "A flux-tunable YBa<sub>2</sub>Cu<sub>3</sub>O<sub>7-x</sub> quantum interference microwave circuit: Data and figures," *Zenodo*. <https://doi.org/10.5281/zenodo.7839911>.

**Supplementary Material for:**  
**A flux-tunable  $\text{YBa}_2\text{Cu}_3\text{O}_7$  quantum interference microwave circuit**

K. Uhl *et al.*

**CONTENTS**

I. Supplementary Note I: Device fabrication	2
II. Supplementary Note II: Measurement setup	2
III. Supplementary Note III: The circuit model	4
A. The circuit equivalent without the JJs	4
B. Circuit parameters from simulation and measurements	4
C. The circuit equivalent with the JJs	5
IV. Supplementary Note IV: Nonlinear cavity model and the transmission $S_{21}$	6
A. Equation of motion and general $S_{21}$	6
B. The linear single-tone regime	6
C. The nonlinear single-tone regime	6
D. The linearized two-tone regime	7
E. The pumped Kerr-modes	8
F. The intracircuit pump photon number	9
G. The real transmission function	9
V. Supplementary Note V: Raw data processing and background removal	11
VI. Supplementary Note VI: Pump-dependent circuit linewidth	11
VII. Supplementary Note VII: Error bar calculation for main paper Fig. 3(c)	11
VIII. Supplementary Note VIII: Additional data on two further SQUID circuits	12
IX. Supplementary Note IX: Calculation of the Kerr nonlinearity	14
X. Supplementary References	16

## I. SUPPLEMENTARY NOTE I: DEVICE FABRICATION

- **Step 1: Gold patterning.**

From the company Ceraco we purchased a two inch MgO wafer (thickness 500  $\mu\text{m}$ ) covered with a layer of 50 nm S-type YBCO. The whole wafer additionally was covered by Ceraco in-situ with an evaporated 40 nm layer of gold for protection of the YBCO. On the complete wafer, we then perform a first optical lithography step to define gold marker structures for the later HIM writing of the Josephson junctions. The purpose of these markers is to focus the  $\text{He}^+$  ion beam as sharp as possible at the metal edges. The lithography is performed using a 600 nm thick layer of ma-P 1205 photoresist and a maskless laser writer (wavelength  $\lambda = 365$  nm, dose  $D = 180$  mJ/cm<sup>2</sup>). After development of the exposed sample in the developer maD331/s for 30 seconds, the wafer is inserted into a bath of 50:50 TechniEtch<sup>TM</sup> ACI2 and H<sub>2</sub>O for 30 seconds to remove the gold from the whole wafer surface except for the markers. The wet-etching is stopped by rinsing the sample in ultraclean water. We make sure that all remaining gold is sufficiently far away from the resonators patterned later (minimum distance  $\sim 100$   $\mu\text{m}$ ), such that its presence is not impacting the resonance frequency or the quality factor of the circuits. To finalize this step, the remaining resist is washed of by rinsing the wafer in several subsequent baths of acetone and isopropyl alcohol (IPA).

- **Step 2: Microwave cavity patterning.**

As second step, we perform another optical lithography with equal parameters as the one in step 1 to define the microwave cavity and waveguides structures of the YBCO film. Instead of TechniEtch solution, however, we use phosphoric acid with a concentration of 0.1% for 340 s for the YBCO wet-etching. The etching is stopped by rinsing with ultraclean water and finished by cleaning off the remaining photoresist using Acetone and IPA again.

- **Step 3: Dicing and mounting for pre-characterization.**

At the end of step 2, we spin-coat the wafer with photoresist for protection and dice it into individual  $10 \times 10$  mm<sup>2</sup> large chips for further processing. After cleaning with acetone and IPA, the chip is mounted into a printed circuit board (PCB), where it gets wire-bonded to microwave feedlines and ground and packaged into a radiation-tight copper housing. Then the package is mounted into the measurement setup, and the cryogenic pre-characterization of the resonators is performed.

- **Step 4: HIM-JJ fabrication.**

After the first characterization in liquid Helium, the chip is unmounted from the PCB again and mounted into a helium ion microscope (HIM). There, the Josephson junctions are written into the SQUID loops of three different microwave circuits with doses  $D_{\text{He},1} = 800$  ions/nm,  $D_{\text{He},2} = 900$  ions/nm and  $D_{\text{He},3} = 1000$  ions/nm. For the junction writing, the circular He-ion-beam with a spot-diameter of 0.5 nm, an ion energy  $E_{\text{He}}$  of 30 keV and a beam current of 840 fA irradiates pixel-by-pixel a single line along each JJ with a time-per-pixel of  $t_1 = 38$   $\mu\text{s}$ ,  $t_2 = 43$   $\mu\text{s}$ ,  $t_3 = 48$   $\mu\text{s}$  and a pixel-to-pixel distance of 0.25 nm.

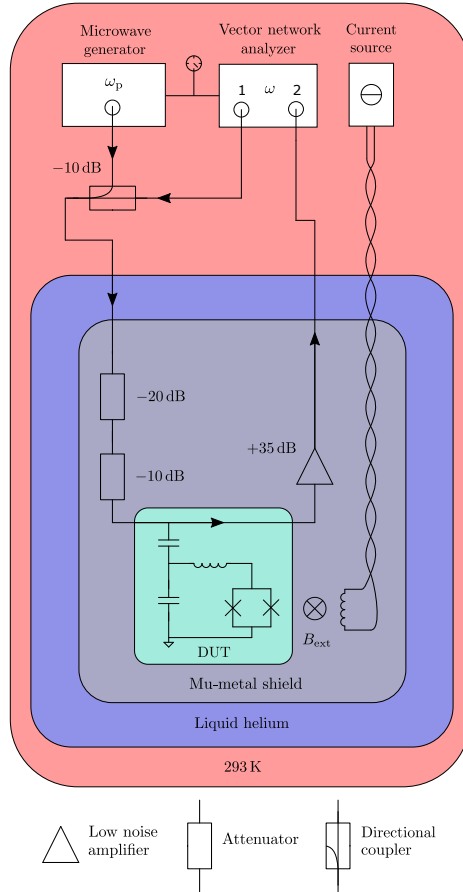
- **Step 5: Device mounting.**

After the HIM writing process the sample is mounted in the same way as in step 3.

## II. SUPPLEMENTARY NOTE II: MEASUREMENT SETUP

Both the junction-less circuits and the SQUID cavities, here generically named device under test (DUT), are characterized in a microwave dipstick, which is introduced into a liquid helium transport dewar. The sample space is covered by a long cryoperm magnetic shield cylinder, which is open at one side but filled with liquid He completely in the dewar during the measurements. A schematic illustration of the measurement setup is shown in Supplementary Fig. 1. The DUT inside the radiation-tight copper housing is attached to a copper mounting bracket and a magnet coil for the application of a magnetic field perpendicular to the chip surface  $B_{\text{ext}}$ . The magnet coil is connected to a low noise current source at room temperature with a twisted pair of copper wires. Additionally the DUT is connected to two coaxial lines for input and output of the microwave signals.

The SQUID cavities are designed in a side-coupled configuration, cf. also main paper Fig. 1. Therefore the input and output signals are sent and received through two separate coaxial lines in order to measure the transmission spectrum  $S_{21}$  of the DUT by means of a vector network analyzer (VNA). The input line is attenuated by  $-30$  dB in order to balance the thermal radiation from room temperature to the temperature of liquid helium. For amplification of the weak microwave signals used here, a cryogenic high electron mobility transistor (HEMT) amplifier is mounted to the output line. This cryogenic HEMT is placed close to the DUT in order to minimize signal losses between the sample and the amplifier.



Supplementary Figure 1. **Schematic of the measurement setup.** Detailed information is given in the text.

For the two-tone experiment an additional fixed-frequency microwave pump tone with frequency  $\omega_p$  and power  $P_p$  is sent to the DUT. This pump tone is generated by a microwave generator and combined via a 10 dB directional coupler with the VNA signal before both enter the cryogenic environment on a single coaxial line. In the experiment the VNA and microwave generator are both referenced to the 10 MHz clock of the generator.

### III. SUPPLEMENTARY NOTE III: THE CIRCUIT MODEL

#### A. The circuit equivalent without the JJs

The basic design of the circuit comprises two interdigitated capacitors with multiple linear inductors, that are combined into a single one in our model for the sake of simplicity. The interdigitated capacitors in the circuit have a finger length of  $100\ \mu\text{m}$ , a finger width of  $\sim 1.5\ \mu\text{m}$  and gap width of  $4.5\ \mu\text{m}$ , and a total finger number  $N_{\text{idc}}$  in each capacitor. For the circuit discussed in the main manuscript  $N_{\text{idc}} = 68$ .

We model the circuit (before the junction writing) by a parallel RLC circuit with the inductance  $L$ , the capacitance  $C$  and the resistance  $R$ . Note that the inductance has both a geometric contribution  $L_g$  and a kinetic contribution  $L_k$  with  $L = L_g + L_k$ , as it is common for superconducting thin film circuits. The parallel RLC circuit is coupled via a coupling capacitance  $C_c$  to the on-chip microwave feedline, which is a coplanar waveguide with characteristic impedance  $Z_0 \approx 50\ \Omega$ . The total inductance  $L$  contains also a contribution from the SQUID loop, which we denote as  $L_{\text{loop}}$  and so the circuit inductance without the loop would be given by  $L - L_{\text{loop}}/8$ , since half of the loop is not contributing to the microwave mode. For a schematic of the circuit and a corresponding optical micrograph see main paper Fig. 1. The circuit resonance frequency before writing the Josephson junctions (JJs) is given by

$$\omega_b = \frac{1}{\sqrt{L(C + C_c)}} \quad (\text{S1})$$

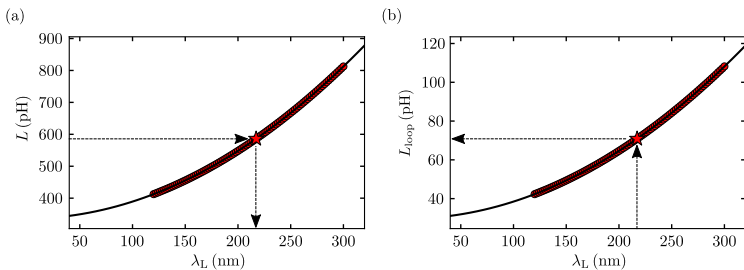
and the internal and external linewidths are

$$\kappa_{i,b} = \frac{1}{R(C + C_c)}, \quad \kappa_{e,b} = \frac{\omega_b^2 C_c^2 Z_0}{2(C + C_c)} \quad (\text{S2})$$

which are related to the corresponding quality factors via  $Q_{i,b} = \omega_b/\kappa_{i,b}$  and  $Q_{e,b} = \omega_b/\kappa_{e,b}$ .

#### B. Circuit parameters from simulation and measurements

We simulate the circuit capacitance with Comsol Multiphysics and obtain for the circuit presented in the main manuscript  $C = 520\ \text{fF}$ . The remaining parameters we obtain from the experiments and the data analysis. From a simultaneous consideration of  $\kappa_{e,b}$  and  $\omega_b$  we can find the coupling capacitance  $C_c \approx 18\ \text{fF}$  and the total linear inductance  $L = 586\ \text{pH}$ . The total inductance  $L = L_g + L_k$ , however, is the sum of a geometric contribution  $L_g$  and a kinetic contribution  $L_k$ , and an analogous consideration holds for the loop inductance  $L_{\text{loop},g} + L_{\text{loop},k}$ . Formally,



Supplementary Figure 2. **Determination of the penetration depth  $\lambda_L$  and the loop inductance  $L_{\text{loop}}$ .** In (a) we show the total inductance  $L(\lambda_L)$  of the cavity 2 vs the London penetration depth  $\lambda_L$ . The red circles are obtained from 3D-MLSI simulations using different  $\lambda_L$  and the line is a fit using Eq. (S5) with  $L_g = 332\ \text{pH}$  and  $g = 210$  as fit parameter. Comparing the experimentally obtained total inductance  $L = 586\ \text{pH}$  of the cavity, we get a corresponding London penetration depth  $\lambda_L = 217\ \text{nm}$  as is highlighted with arrows and a star. In panel (b), the total loop inductance  $L_{\text{loop}}$  is shown vs  $\lambda_L$ . The red circles are also data obtained from 3D-MLSI simulations using different  $\lambda_L$  and the line is a fit using Eq. (S6) with  $L_{\text{loop},g} = 29\ \text{pH}$  and  $g_{\text{loop}} = 35$  as fit parameter. Once we know  $\lambda_L$  for our cavity from (a), we can determine  $L_{\text{loop}} = 71\ \text{pH}$ , just as highlighted with the arrows and a star.

the kinetic inductance of the circuit can be written as [2]

$$L_k = \mu_0 g \lambda_{\text{eff}} \quad (\text{S3})$$

where  $\mu_0$  is the vacuum permeability,  $g$  is a dimensionless geometrical factor taking into account details of the superconducting structures and  $\lambda_{\text{eff}}$  is the effective penetration depth, related to the London penetration depth  $\lambda_L$  and the YBCO film thickness  $t_Y$  via

$$\lambda_{\text{eff}} = \lambda_L \coth \frac{t_Y}{\lambda_L}. \quad (\text{S4})$$

In order to find values for  $g$  and  $\lambda_L$ , and to afterwards estimate also the loop self-inductance  $L_{\text{loop}}$ , we calculate the total linear inductance  $L(\lambda_L) = L_g + L_k(\lambda_L)$  using the software package 3D-MLSI [1] for the range  $120 \text{ nm} \leq \lambda_L \leq 300 \text{ nm}$  as this is typically the regime of the penetration depth of our  $t_Y = 50 \text{ nm}$  thick YBCO film. The total inductance is then

$$L = L_g + \mu_0 g \lambda_L \coth \frac{t_Y}{\lambda_L} \quad (\text{S5})$$

which we use to fit the numerically obtained  $L(\lambda_L)$  with  $g$  and  $L_g$  as fit parameters, cf. Supplementary Fig. 2(a). By comparing the experimentally obtained inductance with the numerically obtained  $L(\lambda_L)$ , we find the corresponding London penetration depth  $\lambda_L = 217 \text{ nm}$  of our YBCO film, which is in good agreement with values reported in literature [3]. Once we know  $\lambda_L$ , we can also determine the loop inductance from the analogously obtained simulation dataset

$$L_{\text{loop}} = L_{\text{loop},g} + \mu_0 g_{\text{loop}} \lambda_L \coth \frac{t_Y}{\lambda_L}. \quad (\text{S6})$$

using 3D-MLSI the same way as for  $L(\lambda_L)$ . As final result for  $\lambda_L = 217 \text{ nm}$ , we obtain  $L_{\text{loop},g} = 29 \text{ pH}$ ,  $g_{\text{loop}} = 35$  and  $L_{\text{loop}} = 71 \text{ pH}$ , cf. Supplementary Fig. 2(b).

We perform a similar analysis for all three circuits that we have characterized and find that the exact parameters slightly vary between the devices, but overall are in good agreement with each other. Supplementary Tab. I summarizes all relevant parameters of the three different circuits, into which we have written HIM-JJs with the three different ion doses mentioned in Supplementary Note I. The cavity discussed in the main manuscript is circuit 2. Cavities 1 and 3 are briefly discussed in Supplementary Note VIII.

Supplementary Table I. **Simulated and experimental parameters of the three circuits before writing the Josephson junctions.** The finger number  $N_{\text{idc}}$  refers to the total number of fingers of each capacitance. The capacitance  $C$  is obtained via simulation with Comsol Multiphysics. From the measured  $\kappa_{e,b}$  and  $\omega_b$ , we get the coupling capacitance  $C_c$  and the total inductance  $L$  of each cavity. By cross-checking the experimentally obtained inductance with simulations of 3D-MLSI, cf. Supplementary Fig. 2, we get the London penetration depth  $\lambda_L$  and the loop inductance  $L_{\text{loop}}$ . For completeness we also give  $\kappa_{i,b}$  as obtained from the experiment.

Cavity no.	$N_{\text{idc}}$	$C$ (fF)	$C_c$ (fF)	$g$	$L_g$ (pH)	$L$ (pH)	$L_{\text{loop}}$ (pH)	$\lambda_L$ (nm)	$\frac{\omega_b}{2\pi}$ (GHz)	$\frac{\kappa_{e,b}}{2\pi}$ (MHz)	$\frac{\kappa_{i,b}}{2\pi}$ (MHz)
1	72	549	24	218	345	644	77	232	8.285	11.5	12.5
2	68	520	18	210	332	586	71	217	8.964	7.8	13.4
3	64	491	34	203	320	537	66	205	9.482	32.7	13.0

### C. The circuit equivalent with the JJs

Writing the junctions into the circuit leads to a shift of the resonance frequency due to the additional inductance of the Josephson junctions. We model the total additional inductance via two parallel Josephson inductances

$$L_J = \frac{\Phi_0}{2\pi I_0 \cos\left(\pi \frac{\Phi}{\Phi_0}\right)}, \quad (\text{S7})$$

each in series with an additional linear inductance  $L_{\text{lin}}$ , that was generated by the writing process. This linear contribution could either originate from a change of the YBCO properties in vicinity of the JJs due to stray radiation or from a slightly non-sinusoidal current-phase-relation of the JJs. We note that we omit any additional capacitance, as according to our simulations the impedance of the JJ capacitance is negligible compared to its inductance impedance.

Hence, the new resonance frequency after JJ writing and for zero bias-flux is given by

$$\begin{aligned}\omega_0 &= \frac{1}{\sqrt{(C + C_c) \left( L + \frac{L_{\text{lin}} + L_{J0}}{2} \right)}} \\ &= \frac{1}{\sqrt{(C + C_c) \left( L + \frac{L'_{J0}}{2} \right)}} \\ &= \frac{\omega_b}{\sqrt{1 + \frac{L'_{J0}}{2L}}}.\end{aligned}\tag{S8}$$

From measuring  $\omega_0$  we can then determine  $L'_{J0} = L_{\text{lin}} + L_{J0}$  with  $L_{J0} = \Phi_0/(2\pi I_0)$ . The relevant equations for the case of  $\Phi_{\text{ext}} \neq 0$  and how the external flux is related to the total flux in the SQUID  $\Phi$  are presented in the main manuscript, cf. also Supplementary Note IX.

#### IV. SUPPLEMENTARY NOTE IV: NONLINEAR CAVITY MODEL AND THE TRANSMISSION $S_{21}$

##### A. Equation of motion and general $S_{21}$

We model the classical intracavity field  $\alpha$  of the quantum interference circuits with Kerr nonlinearity using the equation of motion

$$\dot{\alpha} = \left[ i(\omega_c + \mathcal{K}|\alpha|^2) - \frac{\kappa + \kappa_{\text{nl}}|\alpha|^2}{2} \right] \alpha + i\sqrt{\frac{\kappa_e}{2}} S_{\text{in}}.\tag{S9}$$

Here,  $\omega_c$  is the cavity resonance frequency ( $= \omega_b$  before cutting and  $= \omega_0$  after),  $\mathcal{K}$  is the Kerr nonlinearity (frequency shift per photon),  $\kappa$  is the total linewidth ( $= \kappa_b$  before JJ writing and  $= \kappa_0$  after),  $\kappa_e$  is the external linewidth and  $S_{\text{in}}$  is the input field. We also include a possible nonlinear damping term  $\kappa_{\text{nl}}|\alpha|^2$ , that we need since we observe a power-dependent total linewidth in the two-tone experiment. The intracavity field is normalized such that  $|\alpha|^2 = n_c$  corresponds to the intracavity photon number  $n_c$  and  $|S_{\text{in}}|^2$  to the input photon flux (photons per second). The solution of this equation of motion depends significantly on the drive power and the number of tones sent to the cavity. The ideal transmission response function, however, will always be of the form

$$S_{21}^{\text{ideal}} = 1 + i\sqrt{\frac{\kappa_e}{2}} \frac{\alpha}{S_{\text{in}}}\tag{S10}$$

with the solution of interest  $\alpha$ .

##### B. The linear single-tone regime

In the linear single-tone regime, we set  $\mathcal{K} = 0$  and  $\kappa_{\text{nl}} = 0$ . Then, we can solve the remaining equation by Fourier transform and obtain

$$\alpha = \frac{i\sqrt{\frac{\kappa_e}{2}}}{\frac{\kappa}{2} + i(\omega - \omega_c)} S_{\text{in}}.\tag{S11}$$

The ideal transmission response of a capacitively side-coupled and linear LC circuit is then given by

$$S_{21}^{\text{ideal}} = 1 - \frac{\kappa_e}{\kappa + 2i(\omega - \omega_c)}.\tag{S12}$$

We use this equation to fit all the data with a linear cavity response, also the ones in the two-tone experiment.

##### C. The nonlinear single-tone regime

In the nonlinear single-tone regime (which we are not considering experimentally here), we have to solve the full equation and start by setting the input tone to  $S_{\text{in}} = S_0 e^{i\omega t}$  with real-valued  $S_0$ . For the intracavity field, we make

the Ansatz  $\alpha(t) = \alpha_0 e^{-i\phi_p} e^{i\omega t}$  with real-valued  $\alpha_0$  and the phase delay between probe and response of  $\phi_p$ . Then the equation of motion reads

$$i\omega\alpha_0 = \left[ i(\omega_c + \mathcal{K}\alpha_0^2) - \frac{\kappa + \kappa_{\text{nl}}\alpha_0^2}{2} \right] \alpha_0 + i\sqrt{\frac{\kappa_e}{2}} S_0 e^{i\phi_p} \quad (\text{S13})$$

which after multiplication with its complex conjugate yields the characteristic polynomial for the intracircuit photon number  $n_c = \alpha_0^2$

$$\left[ \mathcal{K}^2 + \frac{\kappa_{\text{nl}}^2}{4} \right] n_c^3 + \left[ \frac{\kappa\kappa_{\text{nl}}}{2} - 2\mathcal{K}\Delta \right] n_c^2 + \left[ \Delta^2 + \frac{\kappa^2}{4} \right] n_c - \frac{\kappa_e}{2} S_0^2 = 0. \quad (\text{S14})$$

Here  $\Delta = \omega - \omega_c$  is the detuning between the microwave input tone and the bare cavity resonance. The real-valued roots of this polynomial correspond to the physical solutions for the amplitude  $\alpha_0$  now, the highest and lowest amplitudes are the stable states in the case of three real-valued roots.

For the complete complex transmission, we also need the phase  $\phi_p$ , which we obtain via

$$\phi_p = \text{atan2} \left( -\frac{\kappa + \kappa_{\text{nl}}n_c}{2}, \Delta - \mathcal{K}n_c \right). \quad (\text{S15})$$

Having both parts of the complex field solution at hand, we can also calculate the transmission

$$\begin{aligned} S_{21,\text{nl}}^{\text{ideal}} &= 1 + i\sqrt{\frac{\kappa_e}{2}} \frac{\alpha}{S_{\text{in}}} \\ &= 1 + i\sqrt{\frac{\kappa_e}{2}} \frac{\alpha_0}{S_0} e^{-i\phi_p}. \end{aligned} \quad (\text{S16})$$

Although we do not use these equations anywhere in our analysis, we present them as the nonlinear single-tone treatment is very helpful to understand the two-tone formalism in the next subsection.

#### D. The linearized two-tone regime

In the two-tone experiment, we apply a strong pump tone with fixed frequency  $\omega_p$  and fixed power  $P_p$  and probe the cavity response with a weak additional scanning tone, the total input then is  $S_{\text{in}} = S_0 e^{i\phi_p} e^{i\omega_p t} + S_{\text{pr}} e^{i\omega_p t}$ . Here, we injected the phase shift between the intracircuit drive field and the drive tone already into the drive itself from the beginning to keep the intracavity field  $\alpha_0$  real-valued. The probe input amplitude  $S_{\text{pr}}$  is a complex-valued quantity too. As Ansatz for the intracavity field we choose  $\alpha(t) = \alpha_0 e^{i\omega_p t} + \alpha_{\text{pr}}(t) e^{i\omega_p t}$  with a complex and time-dependent  $\alpha_{\text{pr}}(t)$  and obtain the equation of motion

$$\begin{aligned} i\omega_p\alpha_0 + i\omega_p\alpha_{\text{pr}} + \dot{\alpha}_{\text{pr}} &= i \left[ \omega_c + \mathcal{K}(\alpha_0^2 + \alpha_0(\alpha_{\text{pr}} + \alpha_{\text{pr}}^*) + |\alpha_{\text{pr}}|^2) \right] \alpha_0 \\ &\quad + i \left[ \omega_c + \mathcal{K}(\alpha_0^2 + \alpha_0(\alpha_{\text{pr}} + \alpha_{\text{pr}}^*) + |\alpha_{\text{pr}}|^2) \right] \alpha_{\text{pr}} \\ &\quad - \left[ \frac{\kappa}{2} + \frac{\kappa_{\text{nl}}}{2} (\alpha_0^2 + \alpha_0(\alpha_{\text{pr}} + \alpha_{\text{pr}}^*) + |\alpha_{\text{pr}}|^2) \right] \alpha_0 \\ &\quad - \left[ \frac{\kappa}{2} + \frac{\kappa_{\text{nl}}}{2} (\alpha_0^2 + \alpha_0(\alpha_{\text{pr}} + \alpha_{\text{pr}}^*) + |\alpha_{\text{pr}}|^2) \right] \alpha_{\text{pr}} \\ &\quad + i\sqrt{\frac{\kappa_e}{2}} S_0 e^{i\phi_p} + i\sqrt{\frac{\kappa_e}{2}} S_{\text{pr}}. \end{aligned} \quad (\text{S17})$$

Now we perform the linearization, i.e., we drop all terms not linear in the small quantity  $\alpha_{\text{pr}}$  and get

$$\begin{aligned} i\omega_p\alpha_0 + i\omega_p\alpha_{\text{pr}} + \dot{\alpha}_{\text{pr}} &= \left[ i(\omega_c + \mathcal{K}n_c) - \frac{\kappa + \kappa_{\text{nl}}n_c}{2} \right] \alpha_0 \\ &\quad + \left[ i(\omega_c + 2\mathcal{K}n_c) - \frac{\kappa + 2\kappa_{\text{nl}}n_c}{2} \right] \alpha_{\text{pr}} \\ &\quad + \left[ i\mathcal{K} - \frac{\kappa_{\text{nl}}}{2} \right] n_c \alpha_{\text{pr}}^* + i\sqrt{\frac{\kappa_e}{2}} S_0 e^{i\phi_p} + i\sqrt{\frac{\kappa_e}{2}} S_{\text{pr}}. \end{aligned} \quad (\text{S18})$$

The time-independent terms are identical to the Eq. (S14) of the nonlinear single-tone formalism and allow to determine  $\alpha_0$  and  $n_c$  via the characteristic polynomial. The remaining equation can be Fourier transformed to give

$$\frac{\alpha_{\text{pr}}}{\chi_{\text{pr}}} = \left[ i\mathcal{K} - \frac{\kappa_{\text{nl}}}{2} \right] n_c \bar{\alpha}_{\text{pr}} + i \sqrt{\frac{\kappa_c}{2}} S_{\text{pr}} \quad (\text{S19})$$

where

$$\chi_{\text{pr}} = \frac{1}{\frac{\kappa + 2\kappa_{\text{nl}}n_c}{2} + i(\Delta_{\text{p}} - 2\mathcal{K}n_c + \Omega)} \quad (\text{S20})$$

with  $\Delta_{\text{p}} = \omega_{\text{p}} - \omega_c$ ,  $\Omega = \omega - \omega_{\text{p}}$  and  $\bar{\alpha}_{\text{pr}} = \alpha_{\text{pr}}^*(-\Omega)$ .

Using the equivalent equation for  $\bar{\alpha}_{\text{pr}}$  with  $\bar{S}_{\text{pr}} = 0$ , we get

$$\alpha_{\text{pr}} = i\chi_{\text{g}} \sqrt{\frac{\kappa_c}{2}} S_{\text{pr}} \quad (\text{S21})$$

with

$$\chi_{\text{g}} = \frac{\chi_{\text{pr}}}{1 - \left[ \mathcal{K}^2 + \frac{\kappa_{\text{nl}}^2}{4} \right] n_c^2 \chi_{\text{pr}} \bar{\chi}_{\text{pr}}} \quad (\text{S22})$$

and for the two-tone transmission parameter

$$S_{21,\text{tt}}^{\text{ideal}} = 1 - \frac{\kappa_c}{2} \chi_{\text{g}}. \quad (\text{S23})$$

As demonstrated elsewhere [4, 5], this is a response with two linearly appearing modes, which can also be approximated by two standard modes, of which we only consider one in what follows, the so-called signal-mode.

### E. The pumped Kerr-modes

To find the resonance frequency of the quasi-modes with susceptibility  $\chi_{\text{g}}$ , we solve the complex frequency for which  $\chi_{\text{g}}^{-1} = 0$ . The condition is

$$1 - \left[ \mathcal{K}^2 + \frac{\kappa_{\text{nl}}^2}{4} \right] n_c^2 \chi_{\text{pr}} \bar{\chi}_{\text{pr}} = 0 \quad (\text{S24})$$

which is solved by

$$\tilde{\omega}_{1,2} = \omega_{\text{p}} + i \frac{\kappa + 2\kappa_{\text{nl}}n_c}{2} \pm \sqrt{(\Delta_{\text{p}} - \mathcal{K}n_c)(\Delta_{\text{p}} - 3\mathcal{K}n_c) - \frac{\kappa_{\text{nl}}^2}{4}n_c^2}. \quad (\text{S25})$$

The real part corresponds to the resonance frequency  $\omega_{1,2} = \text{Re}(\tilde{\omega}_{1,2})$  and the imaginary part corresponds to half the mode linewidth  $\kappa_{1,2} = 2 \text{Im}(\tilde{\omega}_{1,2})$ . So, with respect to the pump frequency  $\omega_{\text{p}}$ , the system has two resonances

$$\omega_{1,2} = \omega_{\text{p}} \pm \sqrt{(\Delta_{\text{p}} - \mathcal{K}n_c)(\Delta_{\text{p}} - 3\mathcal{K}n_c) - \frac{\kappa_{\text{nl}}^2}{4}n_c^2}, \quad (\text{S26})$$

which are split symmetrically around  $\omega_{\text{p}}$ . Note that we only consider the lower frequency mode with  $\omega_2$  here and call it  $\omega'_0$ , i.e.,

$$\omega'_0 = \omega_{\text{p}} - \sqrt{(\Delta_{\text{p}} - \mathcal{K}n_c)(\Delta_{\text{p}} - 3\mathcal{K}n_c) - \frac{\kappa_{\text{nl}}^2}{4}n_c^2}, \quad (\text{S27})$$

or

$$\delta\omega_0 = \Delta_{\text{p}} - \sqrt{(\Delta_{\text{p}} - \mathcal{K}n_c)(\Delta_{\text{p}} - 3\mathcal{K}n_c) - \frac{\kappa_{\text{nl}}^2}{4}n_c^2}. \quad (\text{S28})$$

When we call the pumped and experimentally detected linewidth  $\kappa_p = \kappa_0 + 2\kappa_{n_1}n_c$  (we use explicitly  $\kappa_0$  again now as we only need this after writing the JJs), we can also find half of the experimentally observed change in linewidth by the pump

$$\kappa_1 = \frac{\kappa_p - \kappa_0}{2} = \kappa_{n_1}n_c \quad (\text{S29})$$

and then write

$$\delta\omega_0 = \Delta_p - \sqrt{(\Delta_p - \mathcal{K}n_c)(\Delta_p - 3\mathcal{K}n_c) - \frac{\kappa_1^2}{4}}. \quad (\text{S30})$$

### F. The intracircuit pump photon number

We calculate the intracircuit pump photon number  $n_c$  without the knowledge of the value of  $\mathcal{K}$  using

$$n_c = \frac{2P_p}{\hbar\omega_p} \frac{\kappa_e}{\kappa_{\text{eff}}^2 + 4\bar{\Delta}^2} \quad (\text{S31})$$

with

$$\bar{\Delta}^2 = \frac{2}{9} \left[ \Delta_p^2 + \Delta_p \sqrt{\Delta_p^2 + 3\delta_\kappa^2} + \frac{3}{2}\delta_\kappa^2 \right]. \quad (\text{S32})$$

Here

$$\delta_\kappa^2 = \delta^2 + \frac{\kappa_1^2}{4} \quad (\text{S33})$$

where  $\delta = \omega_p - \omega'_0$  is the driven frequency relative to the pump.

The relation Eq. (S31) for the intracircuit photon number can be obtained from combining Eq. (S14) and Eq. (S30) and solving for  $n_c$ . Explicitly, we start by setting  $x = \mathcal{K}n_c$  and solve the polynomial for  $x_{1/2}$ . We find (assuming  $n_c \neq 0$ )

$$x_{1/2} = \Delta_p \pm \sqrt{\frac{\kappa_e}{2} \frac{n_{\text{in}}}{n_c} - \frac{\kappa_{\text{eff}}^2}{4}} \quad (\text{S34})$$

where  $n_{\text{in}} = \frac{P_p}{\hbar\omega_p} = S_0^2$  is the incoming photon flux and  $\kappa_{\text{eff}} = \kappa_0 + \kappa_1$ . Injecting this into the frequency relative to the drive

$$\delta = \sqrt{(\Delta_p - x_2)(\Delta_p - 3x_2) - \frac{\kappa_1^2}{4}} \quad (\text{S35})$$

leads to

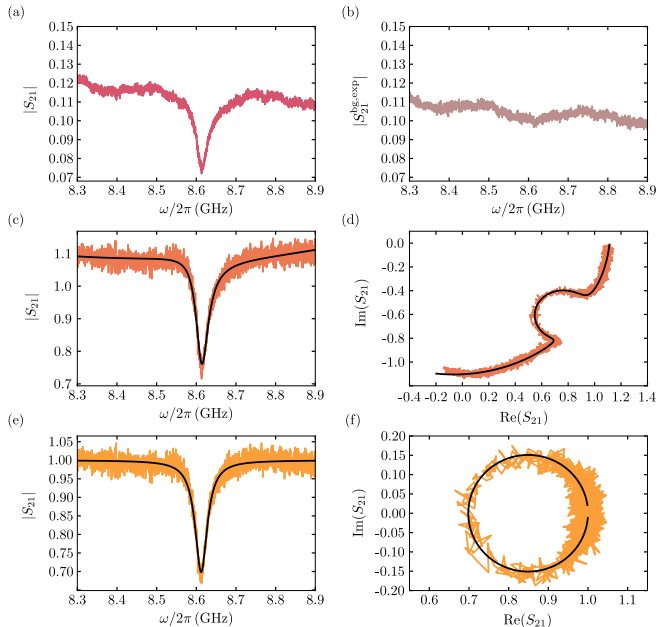
$$\delta^2 = \sqrt{\frac{\kappa_e}{2} \frac{n_{\text{in}}}{n_c} - \frac{\kappa_{\text{eff}}^2}{4}} \left( 3\sqrt{\frac{\kappa_e}{2} \frac{n_{\text{in}}}{n_c} - \frac{\kappa_{\text{eff}}^2}{4}} - 2\Delta_p \right), \quad (\text{S36})$$

which in turn we can solve for  $n_c$  to obtain Eq. (S31).

### G. The real transmission function

Due to impedance imperfections in both, the input and output lines, the ideal transmission response is modified by cable resonances and interferences within the setup [6, 7]. Origin of these imperfections are connectors, attenuators, wirebonds, transitions to or from the PCB etc. in the signal lines. In addition, the cabling has a frequency-dependent attenuation. To take all these modifications into account, we assume that the final transmission parameter  $S_{21}^{\text{real}}$  can be described by

$$S_{21}^{\text{real}} = (a_0 + a_1\omega + a_2\omega^2) [1 - f(\omega)e^{i\theta}] e^{i(\phi_0 + \phi_1\omega)} \quad (\text{S37})$$



Supplementary Figure 3. **Background correction and fitting routine.** (a) Transmission  $|S_{21}|$  vs probe frequency of the SQUID circuit discussed in the main paper for a flux bias value close to the flux sweetspot. The absorption resonance dip around 8.6 GHz is clearly visible. (b) Identical to (a), but with a strong pump tone applied (not visible), which has shifted the resonance dip to frequencies  $< 8.3$  GHz, i.e. out of the measurement window. What we detect here is the experimental background  $S_{21}^{\text{bg,exp}}$ . We of course measure not only the amplitude, but also the phase of  $S_{21}$  and  $S_{21}^{\text{bg,exp}}$ . (c) shows the magnitude of  $S_{21}/S_{21}^{\text{bg,exp}}$ , the background is nearly a flat line, but not yet at  $|S_{21}| = 1$  as expected for an ideal transmission. (d) shows the imaginary part of the background-divided transmission vs the real part. Noisy red lines in (c) and (d) are data, black smooth lines are a fit with Eq. (S37). (e) and (f) show the final background-corrected data, where also the remaining background from the fit is divided off and the resonance circle is corrected by the Fano rotation  $\theta$ . Noisy orange lines in (e) and (f) are data, black smooth lines are a fit.

when the ideal response would be given by

$$S_{11}^{\text{ideal}} = 1 - f(\omega). \quad (\text{S38})$$

The real-valued numbers  $a_0, a_1, a_2, \phi_0, \phi_1$  describe a frequency dependent modification of the background transmission, and the phase factor  $\theta$  takes into account possible interferences such as parasitic signals bypassing the transmission along the device itself, for instance around the chip [6]. The exact form of  $f(\omega)$  depends on the experiment performed as described above, but for all our data is of the form  $\frac{\kappa}{\kappa + 2i(\omega - \omega_c)}$ .

Our standard fitting routine begins with removing the actual resonance signal from the transmission, leaving us with a gapped background transmission, which we fit using

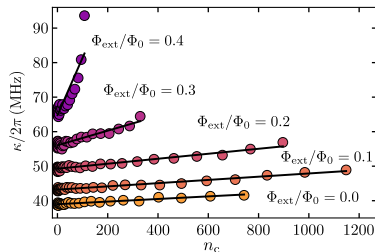
$$S_{21}^{\text{bg}} = (a_0 + a_1\omega + a_2\omega^2) e^{i(\phi_0 + \phi_1\omega)}. \quad (\text{S39})$$

Subsequently, we remove this background function from all measurement traces by complex division. The resonance circle rotation angle  $\theta$  is then rotated off additionally.

## V. SUPPLEMENTARY NOTE V: RAW DATA PROCESSING AND BACKGROUND REMOVAL

As the circuits in our experiments have a rather large linewidth of several 10 MHz and as the background transmission cannot be described over such a large frequency span with a simple polynomial as suggested by Eq. (S37), we perform a two-step background correction to obtain as clean  $S$ -parameters as possible. The procedure is exemplarily shown for one resonance in Supplementary Fig. 3. In the first step, we record for each measurement (e.g. the one in panel (a)) also the resonance-less transmission function as shown in panel (b). In this specific case it is measured with a very large pump power in the two-tone setting where the resonance is shifted to very low frequencies. Then we perform a complex division of the full  $S_{21}$  signal by the bare background signal  $S_{21}^{\text{bg,exp}}$ , the result is a resonance with a nearly flat background as shown in (c), the complex-valued version can be seen in (d). Subsequently, we perform a fit using Eq. (S37) from which we obtain a second background function as well as a Fano rotation angle  $\theta$ . We divide off the fit-background again by complex division and finally rotate the resonance circle by  $\theta$  around its anchor point. The final result including the corresponding fits can be seen in panels (e) and (f). Except for the resonances before junction writing in main paper Fig. 1 and Supplementary Fig. 5, we perform this data processing with all  $S_{21}$  spectra used for the data analysis and all shown resonances have been treated this way. The reason why the  $S_{21}$  measurements before JJ writing are not fully background-corrected is that their nonlinearity is not large enough to shift them away by a pump tone.

## VI. SUPPLEMENTARY NOTE VI: PUMP-DEPENDENT CIRCUIT LINEWIDTH



Supplementary Figure 4. **Pump-power dependent linewidth of circuit 2.** Total linewidth  $\kappa/2\pi$  vs intracavity photon number  $n_c$  for several different flux bias values  $\Phi_{\text{ext}}/\Phi_0$ . Circles are data, lines are linear fits. The values for  $\kappa$  have been extracted from fits to the resonance in the two-tone experiment, the intracavity photon numbers have been calculated using Eq. (S31).

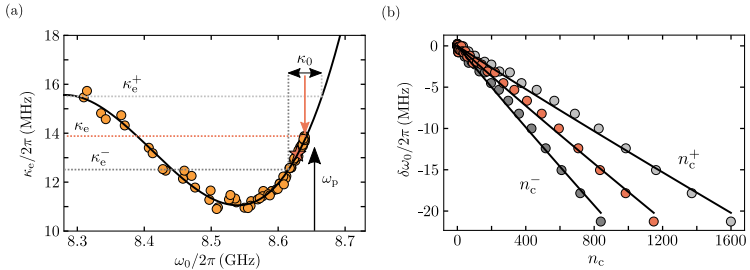
In our theoretical considerations in Supplementary Note IV and the calculation of the pump photon number, we have included a specific nonlinear damping term, i.e., a linewidth that grows linearly with intracavity pump photon number. To justify this approach, we show in Supplementary Fig. 5 the extracted total linewidth data that correspond to the experiment described in main paper Fig. 3. It can clearly be seen, that the total linewidth is in good approximation increasing linearly with the intracavity photon number, i.e., that it is described by

$$\kappa = \kappa_0 + 2\kappa_{\text{nl}}n_c \quad (\text{S40})$$

where both  $\kappa_0$  and  $\kappa_{\text{nl}}$  are a function of flux. Currently it is unclear to us what causes the flux dependence of  $\kappa_0$  and of  $\kappa_{\text{nl}}$  and what the origins and limitations of both are. We plan to investigate these questions in future experiments.

## VII. SUPPLEMENTARY NOTE VII: ERROR BAR CALCULATION FOR MAIN PAPER FIG. 3(C)

The circuit Kerr nonlinearity  $\mathcal{K}$  is an important number for high-dynamic-range applications such as radiation-pressure experiments, parametric amplifiers or dispersive SQUID magnetometry. To reliably determine the value of  $\mathcal{K}$  from the pump-induced frequency shift, a good estimate of the intracircuit photon number  $n_c$  is essential. As discussed above, we use Eq. (S31) for calculating  $n_c$ , but two of the parameters going into that calculation might come with uncertainties and errors, the external linewidth  $\kappa_e$  and the on-chip input power  $P_p$ . Therefore we also perform an error estimation for  $\mathcal{K}$  based on estimated inaccuracies of these two parameters.



Supplementary Figure 5. **Error bar calculation for  $\mathcal{K}$  from uncertainty in  $\kappa_e$  and  $P_p$ .** (a) Experimentally determined external linewidth  $\kappa_e/2\pi$  of circuit 2 vs circuit resonance frequency  $\omega_0/2\pi$ . Circles are data, line is a polynomial fit. We describe our procedure for finding  $\kappa_e$  and its uncertainty here exemplarily for a flux bias point  $\Phi_{\text{ext}}/\Phi_0 = 0.1$ . This particular data point is displayed as a star. The pump tone is applied blue-detuned from the resonance frequency at  $\omega_p$  as indicated by the black vertical arrow here. In this case we do not have an experimental value for  $\kappa_e$  at the pump frequency and therefore use the closest available one indicated by the orange arrow. If we have a value sitting exactly at the pump frequency we use that one. Since  $\kappa_e$  is a function of frequency but our fitting routine is assuming a frequency-independent  $\kappa_e$ , we estimate the uncertainty of  $\kappa_e$  to be given by the maximum and minimum of all  $\kappa_e$ -values in a window  $\kappa_0$  around  $\omega_p$ , or the point we chose for  $\kappa_e$ , respectively. The window for the particular point chosen here is indicated by the vertical black double-arrow and the corresponding vertical dotted lines. We call the resulting max/min values  $\kappa_e^+$  and  $\kappa_e^-$ , respectively. Additionally, we take into account a possible uncertainty in the on-chip pump power by  $\pm 1$  dB. As a result, we can find the standard  $n_c$ , the maximally possible  $n_c^+$  as well as the minimally possible  $n_c^-$ . For all three cases, we plot the frequency shift  $\delta\omega_0$  at the star-marked point vs intracavity photon number in panel (b). Circles are experimentally obtained data. We perform three individual fits as lines here. The max/min values obtained for  $\mathcal{K}$  from these fits plus their fitting errors are plotted as error bars in main paper Fig. 3(c).

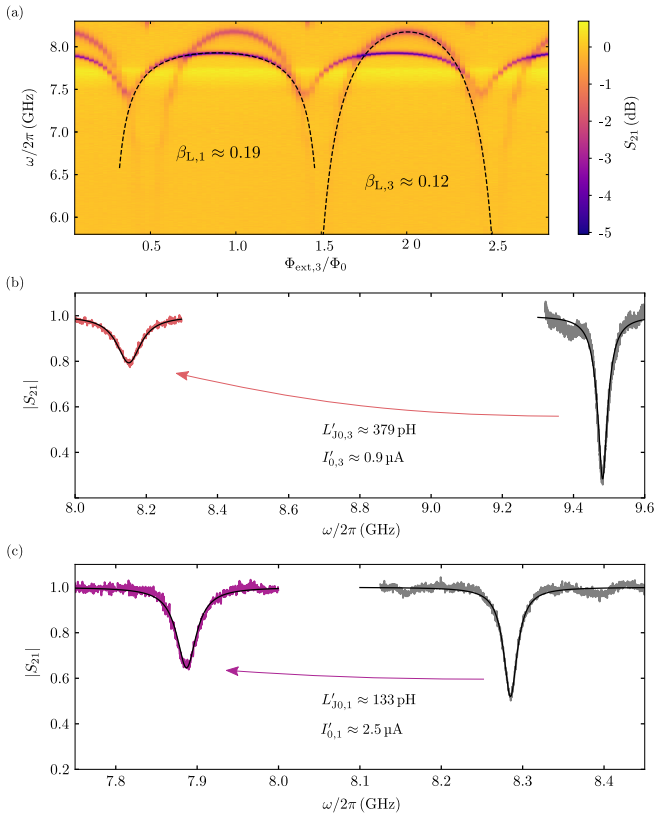
For the overall data analysis of the two-tone experiment and to obtain  $\mathcal{K}$ , we perform first raw data processing of the transmission response  $S_{21}$  for each pump power as described in Supplementary Note V. Additionally, we cut out the visible strong pump tone with fixed frequency  $\omega_p$  from all measurements. As next step, we extract  $\omega_0$ ,  $\kappa_e$  and  $\kappa_0$  for all flux bias values by our usual fitting routine, which also means that we have (a rough) knowledge of the frequency-dependence of  $\kappa_e$ . Then, we fit  $\kappa_e$  as a function of  $\omega_0$  for the whole flux-tuning-range with a fourth order polynomial, cf. Supplementary Fig. 5(a). Since we observe that  $\kappa_e$  is considerably frequency-dependent even over a frequency span of  $\kappa_0$ , we find the maximum and minimum possible value  $\kappa_e^+$  and  $\kappa_e^-$  for each pump power point as discussed in Supplementary Fig. 5(a) and process these two values as higher and lower errors for  $n_c$ .

To obtain a value for  $P_p$ , we estimate the input power on the on-chip feedline by the generator output power and a total input attenuation of  $-55$  dB (cables with attenuators and directional coupler 10), based on direct attenuation measurements at room temperature. As uncertainty of the attenuation and as consequence also of the input power we assume  $\pm 1$  dB.

Using Eq. (S31) and the inaccuracies we get a highest and lowest intracavity photon number  $n_c^+$  and  $n_c^-$ , respectively, for each pump frequency and pump power point, cf. Supplementary Fig. 5(b), where the measured frequency shift  $\delta\omega_0$  is plotted vs all three photon numbers (lowest, standard, highest). Finally, we perform a fit for all three cases using Eq. (S30) to determine  $\mathcal{K}$ ,  $\mathcal{K}^+$  and  $\mathcal{K}^-$ . Note that  $|\mathcal{K}^-| > |\mathcal{K}| > |\mathcal{K}^+|$ . The error bars in  $\mathcal{K}$  resulting out of the fit of  $n_c^+$ ,  $n_c^-$  and  $n_c$  are then given by  $|\mathcal{K}^-| - |\mathcal{K}|$  and  $|\mathcal{K}| - |\mathcal{K}^+|$  plus their direct errors obtained by the fit.

### VIII. SUPPLEMENTARY NOTE VIII: ADDITIONAL DATA ON TWO FURTHER SQUID CIRCUITS

In total, we have fabricated and characterized three different HIM-SQUID circuits, although in the main paper we only present the experimental results for one of them (SQUID 2). The main reason for choosing that one is that the flux tuning curves of the other two are overlapping and therefore the data analysis gets considerably more complicated (think for instance about the two-tone experiment with two cavities close to each other and the calculation of the corresponding intracircuit photon numbers). However, we still present the main junction-writing and flux-tuning results for the other two circuits (SQUID 1 and SQUID 3) in Supplementary Fig. 6. The Josephson junctions in the other two SQUID cavities have even lower critical currents and the SQUIDs lower screening parameters than SQUID circuit 2 and circuit 3 even has a maximum tuning range of more than 2 GHz, i.e.  $\gtrsim \omega_0/4$ , which once more shows



Supplementary Figure 6. **Basic characterization of two further YBCO-HIM-SQUID circuits.** (a) Normalized and color-coded transmission  $S_{21}$  in dB vs external bias flux in SQUID number three  $\Phi_{\text{ext},3}/\Phi_0$  and vs probe frequency  $\omega/2\pi$ . The resonance absorption dips are clearly visible as purple-shaded (dark) features, that oscillate periodically with flux. SQUID circuit 3 has a sweetspot resonance frequency  $\sim 8.2$  GHz and modulates in total by more than 2 GHz. SQUID circuit 1 has a sweetspot frequency of  $\sim 7.9$  GHz and modulates by about  $\sim 450$  MHz. Note that the flux axis for SQUID circuit 1 (not shown) is slightly different from circuit 3, most likely since the flux focussing factors differ due to different superconducting embeddings on the chip. At the very top of the figure ( $\sim 8.3$  GHz), there are also signatures of SQUID circuit 2 visible, which is the circuit discussed in the main paper; the lowest tuning point of that circuit appears here as small purple features. Dashed lines correspond to approximate flux tuning curves obtained by theory, the effective screening parameters are given as numbers below the theory lines. (b) Absorption resonance of SQUID circuit 3 before and after JJ writing with the HIM. Noisy gray and orange lines are data, smooth black lines are fits. From the shift, we determine an effective single-junction inductance of  $L'_{J0,3} \approx 379$  pH, which corresponds to a critical current of  $\sim 0.9$   $\mu$ A. (c) Absorption resonance of SQUID circuit 1 before and after JJ writing with the HIM. Noisy gray and purple lines are data, smooth black lines are fits. From the shift, we determine an effective single-junction inductance of  $L'_{J0,1} \approx 133$  pH, which corresponds to a critical current of  $\sim 2.5$   $\mu$ A. Note, that the theoretical flux tuning curves in panel (a) have been obtained by using all other parameters  $L, C, C_c, I_0$  from simulations/experiments and the only parameter adjusted was  $\beta_L$ .

the enormous potential of HIM-SQUID circuits based on YBCO.

### IX. SUPPLEMENTARY NOTE IX: CALCULATION OF THE KERR NONLINEARITY

For the calculation of the Kerr nonlinearity  $\mathcal{K}$  we follow the method described in Ref. [8] and start with the effective one-dimensional potential for the top half of the SQUID, i.e., the half that is connected to the remainder of the microwave circuit

$$U = \frac{1}{2}E_{\text{arm}}(\varphi_{\text{left}} - \varphi_1)^2 + \frac{1}{2}E_{\text{arm}}(\varphi_{\text{right}} - \varphi_2)^2 - E_J \cos \varphi_1 - E_J \cos \varphi_2. \quad (\text{S41})$$

Here  $\varphi_1, \varphi_2$  are the phase differences of the two Josephson junctions,  $\varphi_{\text{left}}$  and  $\varphi_{\text{right}}$  are the total phase differences of the upper left quarter and the upper right quarter of the SQUID loop including the JJs, and the energies are given by

$$E_J = \frac{\Phi_0 I_0}{2\pi}, \quad E_{\text{arm}} = \frac{\Phi_0^2}{4\pi^2 L_{\text{arm}}} \quad (\text{S42})$$

with  $L_{\text{arm}} = \frac{L_{\text{loop}}}{4} + L_{\text{lin}}$ . From fluxoid quantization in the SQUID it follows that

$$\varphi_{\text{right}} - \varphi_{\text{left}} = \varphi_{\text{ext}} - \varphi_{\text{bottom}} \quad (\text{S43})$$

where  $\varphi_{\text{bottom}}$  is the phase across the bottom half of the SQUID loop without junctions and shorted to ground, and  $\varphi_{\text{ext}} = 2\pi \frac{\Phi_{\text{ext}}}{\Phi_0}$  is the phase introduced by the external flux. For simplicity of our calculations we assume  $\varphi_{\text{bottom}} = \text{const.}$  and write  $\varphi_{\text{ext}} - \varphi_{\text{bottom}} = \varphi'_{\text{ext}}$ . Then, the potential can be written as function of a single phase-variable  $\varphi_s = \varphi_{\text{left}}$  as

$$U[\varphi_s] = \frac{1}{2}E_{\text{arm}}(\varphi_s - \varphi_1[\varphi_s])^2 + \frac{1}{2}E_{\text{arm}}(\varphi_s - \varphi_2[\varphi_s] + \varphi'_{\text{ext}})^2 - E_J \cos \varphi_1[\varphi_s] - E_J \cos \varphi_2[\varphi_s] \quad (\text{S44})$$

and as boundary conditions we have the current conservation relations [8]

$$\varphi_s = \varphi_1 + \zeta \sin \varphi_1 \quad (\text{S45})$$

$$\varphi_s = \varphi_2 + \zeta \sin \varphi_2 - \varphi'_{\text{ext}} \quad (\text{S46})$$

where  $\zeta = E_{\text{arm}}/E_J = L_{J0}/L_{\text{arm}}$ .

In order to find the Kerr nonlinearity, we have to Taylor-expand the potential up to fourth order

$$\frac{U(\varphi_s)}{E_J} = c_0 + c_1(\varphi_s - \varphi_{\text{min}}) + \frac{c_2}{2}(\varphi_s - \varphi_{\text{min}})^2 + \frac{c_3}{6}(\varphi_s - \varphi_{\text{min}})^3 + \frac{c_4}{24}(\varphi_s - \varphi_{\text{min}})^4 + \dots \quad (\text{S47})$$

where the coefficients are determined by the  $n$ -th derivative of the potential evaluated at the phase at the potential well minimum  $\varphi_{\text{min}}$

$$c_n = \frac{1}{E_J} \left. \frac{\partial^n U}{\partial \varphi_s^n} \right|_{\varphi_{\text{min}}} \quad (\text{S48})$$

To find the value for  $\varphi_{\text{min}}$ , we demand that in the minimum we have  $c_1 = 0$  and as result we get

$$\varphi_{\text{min}} = \frac{1}{2}(\varphi_{1,\text{min}} + \varphi_{2,\text{min}} - \varphi'_{\text{ext}}). \quad (\text{S49})$$

In the potential minimum, however, i.e., without any phase excitation, we also have

$$\sin \varphi_{1,\text{min}} = -\sin \varphi_{2,\text{min}} \quad \rightarrow \quad \varphi_{1,\text{min}} = -\varphi_{2,\text{min}} \quad (\text{S50})$$

since the same SQUID circulating current  $J = -I_0 \sin \varphi_1 = I_0 \sin \varphi_2$  is flowing through both JJs with opposite direction. Then, using Eq. (S49) we can follow

$$\varphi_{\text{min}} = -\frac{\varphi'_{\text{ext}}}{2} \quad (\text{S51})$$

and using Eq. (S45) we arrive at

$$\varphi_{1,\min} + \zeta \sin \varphi_{1,\min} + \frac{\varphi'_{\text{ext}}}{2} = 0 \quad (\text{S52})$$

which is completely equivalent to

$$\frac{\Phi}{\Phi_0} = \frac{\Phi_{\text{ext}}}{\Phi_0} - \frac{\beta_L}{2} \sin \left( \pi \frac{\Phi}{\Phi_0} \right) \quad (\text{S53})$$

with the screening parameter  $\beta_L$ , the total flux in the SQUID  $\Phi$  and when using the relation  $\varphi_{1,\min} = -\pi \frac{\Phi}{\Phi_0}$  as well as  $\varphi_{\text{bottom}} = 2\pi L_{\text{bottom}} J / \Phi_0$  with  $L_{\text{bottom}} = L_{\text{loop}}/2$ .

For the derivatives, we get

$$\frac{\partial U}{\partial \varphi_s} = E_{\text{arm}} (2\varphi_s - \varphi_1[\varphi_s] - \varphi_2[\varphi_s] + \varphi'_{\text{ext}}) \quad (\text{S54})$$

$$\frac{\partial^2 U}{\partial \varphi_s^2} = E_{\text{arm}} \left( 2 - \frac{\partial \varphi_1}{\partial \varphi_s} - \frac{\partial \varphi_2}{\partial \varphi_s} \right) \quad (\text{S55})$$

$$\frac{\partial^3 U}{\partial \varphi_s^3} = -E_{\text{arm}} \left( \frac{\partial^2 \varphi_1}{\partial \varphi_s^2} + \frac{\partial^2 \varphi_2}{\partial \varphi_s^2} \right) \quad (\text{S56})$$

$$\frac{\partial^4 U}{\partial \varphi_s^4} = -E_{\text{arm}} \left( \frac{\partial^3 \varphi_1}{\partial \varphi_s^3} + \frac{\partial^3 \varphi_2}{\partial \varphi_s^3} \right) \quad (\text{S57})$$

and the phase derivatives we can obtain from Eqs. (S45, S46) as

$$\frac{\partial \varphi_s}{\partial \varphi_1} = 1 + \zeta \cos \varphi_1 \quad (\text{S58})$$

$$\frac{\partial \varphi_s}{\partial \varphi_2} = 1 + \zeta \cos \varphi_2 \quad (\text{S59})$$

which can be inverted as

$$\frac{\partial \varphi_1}{\partial \varphi_s} = \frac{1}{1 + \zeta \cos \varphi_1} \quad (\text{S60})$$

$$\frac{\partial \varphi_2}{\partial \varphi_s} = \frac{1}{1 + \zeta \cos \varphi_2}. \quad (\text{S61})$$

The consecutive derivatives are for  $j = 1, 2$

$$\frac{\partial^2 \varphi_j}{\partial \varphi_s^2} = \frac{\zeta \sin \varphi_j}{(1 + \zeta \cos \varphi_j)^3} \quad (\text{S62})$$

$$\frac{\partial^3 \varphi_j}{\partial \varphi_s^3} = \frac{\zeta \cos \varphi_j (1 + \zeta \cos \varphi_j) + 3\zeta^2 \sin^2 \varphi_j}{(1 + \zeta \cos \varphi_j)^5} \quad (\text{S63})$$

which we can finally use to express our Taylor coefficients with  $\varphi_0 = -\varphi_{1,\min} = \pi \frac{\Phi}{\Phi_0}$  as

$$c_2 = \frac{2 \cos \varphi_0}{1 + \zeta \cos \varphi_0} \quad (\text{S64})$$

$$c_3 = 0 \quad (\text{S65})$$

$$c_4 = -2 \frac{\cos \varphi_0 (1 + \zeta \cos \varphi_0) + 3\zeta \sin^2 \varphi_0}{(1 + \zeta \cos \varphi_0)^5} \quad (\text{S66})$$

The SQUID inductance and Kerr nonlinearity of the SQUID, when shunted with  $C_{\text{tot}}$  are now given by [8]

$$\begin{aligned} L_s &= \frac{L_{J0}}{c_2} \\ &= \frac{1}{2} (L_J + L_{\text{arm}}) \end{aligned} \quad (\text{S67})$$

and

$$\begin{aligned}\mathcal{K}_s &= \frac{e^2}{2\hbar C_{\text{tot}}} \frac{c_4}{c_2} \\ &= -\frac{e^2}{2\hbar C_{\text{tot}}} \left( \frac{L_J}{L_{\text{arm}} + L_J} \right)^3 \left[ 1 + 3 \frac{L_{\text{arm}}}{L_{\text{arm}} + L_J} \tan^2 \varphi_0 \right]\end{aligned}\quad (\text{S68})$$

where  $L_J = L_{J0}/\cos \varphi_0$ ,  $e$  is the elementary charge and  $\hbar$  the reduced Planck number. When we add a linear inductance  $L - L_{\text{loop}}/8$  in series, we get the modified parameters [8]

$$\tilde{c}_2 = p c_2 \quad (\text{S69})$$

$$L_{\text{tot}} = \frac{L_s}{p} \quad (\text{S70})$$

$$\tilde{c}_4 = p^4 c_4 \quad (\text{S71})$$

$$\mathcal{K} = p^3 \mathcal{K} \quad (\text{S72})$$

where  $p$  is the inductance participation ratio

$$p = \frac{L_s}{L - L_{\text{loop}}/8 + L_s}. \quad (\text{S73})$$

Then, we have finally the explicit expression for the circuit Kerr nonlinearity

$$\mathcal{K} = -\frac{e^2}{2\hbar C_{\text{tot}}} \left( \frac{L_J}{2L + L_{\text{in}} + L_J} \right)^3 \left[ 1 + 3 \frac{L_{\text{arm}}}{L_{\text{arm}} + L_J} \tan^2 \varphi_0 \right] \quad (\text{S74})$$

which we use in main paper Fig. 3.

---

## X. SUPPLEMENTARY REFERENCES

- [1] Khapaev, M. M., Kidiyarova-Shevchenko, A. Yu., Magnelind, P., and Kupriyanov, M. Yu.. 3D-MLSI: software package for inductance calculation in multilayer superconducting integrated circuits, *IEEE Transactions on Applied Superconductivity* **11**, 1090-1093 (2001).
- [2] Klein, N., Chaloupka, H., Müller, G., Orbach, S., Piel, H., Roas, B., Schultz, L., Klein, U., and Peiniger, M.. The effective microwave surface impedance of high- $T_c$  thin films, *Journal of Applied Physics* **67**, 6940 (1990).
- [3] Zaitsev, A. G., Schneider, R., Linker, G., Ratzel, F., Smithey, R., Schweiss, P., and Geerk, J.. Microwave measurements of the absolute London penetration depth in double-sided YBa<sub>2</sub>Cu<sub>3</sub>O<sub>7-x</sub> thin films on sapphire, *Review of Scientific Instruments* **73**, 335 (2002).
- [4] Fani Sani, F., Rodrigues, I. C., Bothner, D., and Steele, G. A.. Level attraction and idler resonance in a strongly driven Josephson cavity, *Physical Review Research* **3**, 043111 (2021).
- [5] Rodrigues, I. C., Steele, G. A., and Bothner, D.. Parametrically enhanced interactions and nonreciprocal bath dynamics in a photon-pressure Kerr amplifier, *Science Advances* **8**, eabq1690 (2022).
- [6] Wenner, J., Neeley, M., Bialczak, Radoslav C., Lenander, M., Lucero, E., O'Connell, A. D., Sank, D., Wang, H., Weides, M., Cleland, A. N., and Martinis, J. M.. Wirebond crosstalk and cavity modes in large chip mounts for superconducting qubits, *Superconductor Science and Technology* **24**, 065001 (2011).
- [7] Rieger, D., Günzler, S., Spiecker, M., Nambisan, A., Wernsdorfer, W., and Pop, I. M.. Fano Interference in Microwave Resonator Measurements, arXiv:2209.03036 (2022).
- [8] Frattini, N. E., Sivak, V. V., Lingenfelter, A., Shankar, S., and Devoret, M. H.. Optimizing the Nonlinearity and Dissipation of a SNAIL Parametric Amplifier for Dynamic Range, *Physical Review Applied* **10**, 054020 (2018).

# Publication 4

## High-Q Magnetic Levitation and Control of Superconducting Microspheres at Millikelvin Temperatures

J. Hofer<sup>1,2,\*</sup>, R. Gross<sup>3,4,5</sup>, G. Higgins<sup>6,2,6</sup>, H. Huebl<sup>3,4,5</sup>, O. F. Kieler<sup>7</sup>, R. Kleiner<sup>8</sup>, D. Koelle<sup>8</sup>, P. Schmidt<sup>2</sup>, J. A. Slater<sup>1,7</sup>, M. Trupke<sup>1</sup>, K. Uhl<sup>8</sup>, T. Weimann<sup>7</sup>, W. Wiczczonek<sup>1,6</sup>, and M. Aspelmeyer<sup>1,2</sup>

<sup>1</sup>Faculty of Physics, Vienna Center for Quantum Science and Technology (VCQ), University of Vienna, A-1090 Vienna, Austria

<sup>2</sup>Institute for Quantum Optics and Quantum Information (IQOQI), Austrian Academy of Sciences, A-1090 Vienna, Austria

<sup>3</sup>Walther-Meißner-Institut, Bayerische Akademie der Wissenschaften, D-85748 Garching, Germany

<sup>4</sup>Physik-Department, Technische Universität München, D-85748 Garching, Germany

<sup>5</sup>Munich Center for Quantum Science and Technology (MCQST), D-80799 München, Germany

<sup>6</sup>Department of Microtechnology and Nanoscience (MC2), Chalmers University of Technology, SE-412 96 Gothenburg, Sweden

<sup>7</sup>Physikalisch-Technische Bundesanstalt (PTB), D-38116 Braunschweig, Germany

<sup>8</sup>Physikalisches Institut, Center for Quantum Science (CQ) and LISA<sup>†</sup>, University of Tuebingen, D-72076 Tuebingen, Germany

 (Received 6 December 2022; accepted 27 June 2023; published 25 July 2023)

We report the levitation of a superconducting lead-tin sphere with 100  $\mu\text{m}$  diameter (corresponding to a mass of 5.6  $\mu\text{g}$ ) in a static magnetic trap formed by two coils in an anti-Helmholtz configuration, with adjustable resonance frequencies up to 240 Hz. The center-of-mass motion of the sphere is monitored magnetically using a dc superconducting quantum interference device as well as optically and exhibits quality factors of up to  $2.6 \times 10^7$ . We also demonstrate 3D magnetic feedback control of the motion of the sphere. The setup is housed in a dilution refrigerator operating at 15 mK. By implementing a cryogenic vibration isolation system, we can attenuate environmental vibrations at 200 Hz by approximately 7 orders of magnitude. The combination of low temperature, large mass, and high quality factor provides a promising platform for testing quantum physics in previously unexplored regimes with high mass and long coherence times.

DOI: 10.1103/PhysRevLett.131.043603

Diamagnets and superconductors partially expel magnetic fields, allowing stable levitation in field minima [1]. A prominent application of magnetically levitated systems is the use as ultraprecise acceleration sensors, most notably in the superconducting gravimeter [2], which relies on the levitation of centimeter-sized hollow superconducting spheres in a stable magnetic field generated by superconducting coils in persistent current mode. More recently, several proposals [3,4] have highlighted the potential of magnetic levitation for tests of quantum physics with macroscopic, micrometer-sized objects.

Successfully preparing a magnetically levitated particle in a quantum state requires a magnetic trap with low damping, low heating rates, and the ability to control the mechanical motion. Some of these features are already present in recent demonstrations of magnetically levitated systems, such as the levitation of permanent magnets above a superconducting surface [5,6] and the levitation of

diamagnets in the field of permanent magnets at cryogenic temperatures [7] or room temperature [8]. However, as of yet, no system has combined these features. Furthermore, as typical levitation frequencies for these systems range from subhertz to kilohertz, the heating rate is dominated by environmental vibrations.

One of the most promising avenues toward the quantum regime is the levitation of a type-I (or zero-field-cooled type-II) superconductor in a magnetic field produced by persistent currents, as this avoids dissipation due to hysteresis and eddy currents, which is inherent to levitation schemes involving ferromagnets or flux-pinned type-II superconductors [9,10]. Using persistent currents should result in an extremely stable trap, as both the drift and noise can be kept extremely low [2,11,12]. Working at millikelvin temperatures also naturally enables coupling to nonlinear quantum systems such as superconducting qubits [3], and miniaturizing the trap architecture [13–15] might lead to fully on-chip coupled quantum systems [16]. In comparison with optical levitation, which has already been established as a means for studying massive objects in the quantum regime [17–19], magnetostatic levitation has the potential to access a new parameter regime of even larger mass [20,21] and longer coherence times [3,16]: While the size of optically levitated particles is, in practice, limited by

Published by the American Physical Society under the terms of the Creative Commons Attribution 4.0 International license. Further distribution of this work must maintain attribution to the author(s) and the published article's title, journal citation, and DOI.

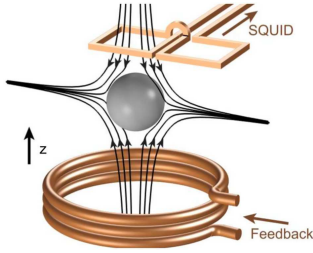


FIG. 1. Conceptual representation of the experiment showing the levitated sphere, the pickup coil, and the feedback coil. The trap field is depicted by its field lines.

the available laser power to the micrometer scale [22], magnetic levitation can support train-scale objects [23], and due to the static nature of the fields, there is no heating from photon absorption.

A first step toward a fully superconducting platform was presented in [24], where a lead particle was levitated in the magnetic field of a superconducting coil. This approach, however, was limited in performance by the presence of cryogenic exchange gas at 4 K and environmental vibrations. Here, we report an experiment that provides orders of magnitude improvements in both damping and vibration isolation. We demonstrate the levitation of a superconducting sphere in the magnetic field generated by a superconducting coil. We detect the center of mass (c.m.) motion of the particle magnetically by inductive coupling to a superconducting quantum interference device (SQUID) via a pickup coil (cf. Fig. 1) and demonstrate feedback control of all three c.m. translational degrees of freedom by real-time processing of the SQUID signal. We find that the motion of the particle has a low damping rate, corresponding to quality factors of up to  $2.6 \times 10^7$ . We also implement a custom vibration isolation system to reduce heating from environmental vibrations. Finally, we discuss the limitations of our current setup and the improvements that are necessary for ground state cooling.

**Trapping.**—The energy of an object of volume  $V$  with permeability  $\mu$  in an applied magnetic field  $B_0$  in free space can be approximated by  $-1/2V(\mu - \mu_0)B_0^2$  [1], where  $\mu_0$  is the permeability of free space. Because  $\nabla^2 B_0^2 \geq 0$ , stable levitation is possible in a field minimum for  $\mu < \mu_0$ , i.e., for diamagnets. A superconducting sphere can act as a perfect diamagnet ( $\mu = 0$ ), because it reacts to a change in the applied magnetic field by forming screening currents on its surface, counteracting the applied field and keeping the interior of the sphere field free.

For a sphere trapped in the field of an anti-Helmholtz coil, the resulting potential close to the field minimum is harmonic and two of the c.m. modes are degenerate [3,20]; to lift the degeneracy we use elliptical coils [25]. The  $z$

direction is along the coil axis, which coincides with the vertical direction, while  $x$  and  $y$  are perpendicular to  $z$ , with  $x$  along the major axis of the coils. We use numerical simulations [25] to model the magnetic field created by such an arrangement and confirm that the magnetic field near the center between the coils is well described by  $(b_x x, b_y y, b_z z)$ , where the field gradients  $b_i$  are proportional to the trap current with  $|b_x| < |b_y| < |b_z|$  and  $b_z = -(b_x + b_y)$ . This field shape constitutes a three-dimensional harmonic trap for a levitated superconducting sphere with the c.m. frequencies [25]

$$f_i = \sqrt{\frac{3}{8\pi^2 \mu_0 \rho}} |b_i|, \quad (1)$$

where  $\rho$  is the density of the sphere.

Our setup is housed in a dilution refrigerator (Bluefors BF-LD400) with a loaded base temperature of approximately 15 mK. The microspheres are commercial (EasySpheres) solder balls with diameter 100(6)  $\mu\text{m}$ , made of a 90-10 lead-tin alloy with density  $\rho = 10.9 \times 10^3 \text{ kg/m}^3$ . Lead-tin is a type-II superconductor with a critical temperature of approximately 7 K [37]. A single sphere is initially placed in a 3D-printed polylactide bowl glued to the lower trap coil, such that it rests around 1 mm below the trap center. The bowl helps to prevent accidental loss of the sphere during assembly and between measurement runs. After cooling down the system to millikelvin temperatures, lift-off is achieved by increasing the coil current until the upward magnetic force on the sphere is stronger than the downward gravitational and adhesive forces. The trap coils are surrounded by an aluminum shield with small openings for optical access and wires, which screens the sphere from magnetic field fluctuations when the aluminum is superconducting. To suppress field fluctuations from the trapping coils and feedback coil, we use a low pass filter and attenuation stages, respectively [25].

**Readout.**—A planar Niobium thin film gradiometric pickup coil consisting of two square loops positioned approximately 400  $\mu\text{m}$  above the trap center is used to magnetically probe the particle motion. Each loop is 145  $\mu\text{m} \times 145 \mu\text{m}$  and the separation between the loops is 3  $\mu\text{m}$ . As the particle moves, it induces a current in the pickup loop [25], which is connected with Nb wires to the input coil of a SQUID current sensor [38]. The SQUID has an intrinsic flux noise level of  $S_\Phi^{1/2} = 0.8 \mu\Phi_0/\sqrt{\text{Hz}}$ , where  $\Phi_0 \approx 2.1 \times 10^{-15} \text{ Wb}$  is the flux quantum. When the SQUID is incorporated into the setup, and the pickup loop is connected, the noise rises to  $S_\Phi^{1/2} \approx 10 \mu\Phi_0/\sqrt{\text{Hz}}$ . We believe this is due to external field fluctuations inductively coupling into the wires connecting the pickup loop and the SQUID. With a commercial SQUID (Supracon CSBlue), that was used for some of the measurements, the noise floor in the setup further increased by an order of magnitude.

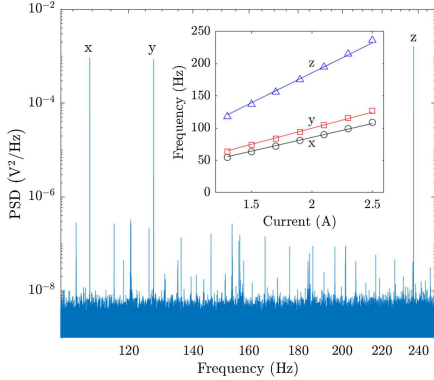


FIG. 2. The PSD of the SQUID signal displays three peaks which correspond to the c.m. modes of the particle. The motion of the particle is excited to approximately one micrometer rms displacement in this figure—measurement noise prevents us from resolving the equilibrium motion of the particle. The inset shows the linear dependence of the c.m. frequencies on the trap current. The solid lines are zero-intercept linear fits.

To calibrate the SQUID signal, we optically record the motion of the sphere by illuminating it and imaging its shadow on a camera, while simultaneously recording the motion with the SQUID [25]. The coupling strengths (flux induced in the SQUID per sphere displacement) for the different motional modes depend on the position of the pickup loop in relation to the sphere as well as the trap gradients, i.e., mechanical frequencies. The highest measured coupling strength was approximately  $13 \times 10^3 \Phi_0/m$  for the  $z$  mode and  $3 \times 10^3 \Phi_0/m$  for the  $x$  and  $y$  modes. Together with a flux noise floor of  $10 \mu\Phi_0/\sqrt{Hz}$  these coupling strengths correspond to a displacement sensitivity of approximately  $1 \text{ nm}/\sqrt{Hz}$  for the  $z$  mode. During these measurements the separation between pickup loop and sphere was approximately  $400 \mu\text{m}$ . We estimate that, with a smaller separation and an optimized pickup loop geometry, an improvement of 4 orders of magnitude is possible [25].

**Mechanical frequencies.**—The c.m. frequencies of the particle are visible in the power spectral density (PSD) of the SQUID signal, as shown in Fig. 2. The c.m. frequencies depend linearly on the magnetic field gradient of the trap [see Eq. (1)] and, thus, the current in the trap coils, as shown in the inset. The highest frequency reached in the present setup is 240 Hz (corresponding to  $b_z \approx 150 \text{ T/m}$ ), limited by the maximum current output of the low-noise current source. We can trap at lower frequencies, down to  $f_z \approx 20 \text{ Hz}$ , where the lower limit stems from the gravity-induced shift of the trapping position and our trap geometry. However, at low trapping frequencies, the sphere is strongly excited by environmental vibrations.

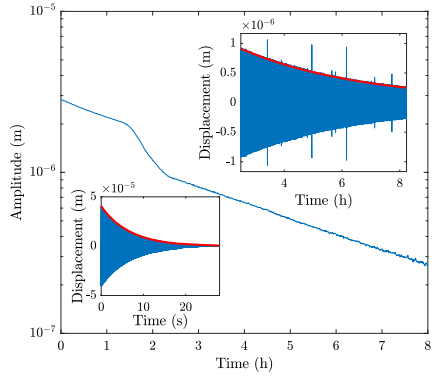


FIG. 3. Ringdown measurement of the  $z$  mode. The upper right inset shows a linear plot for the latter part of the data, starting at  $t = 2.5 \text{ h}$ . The red line is a fit to an exponential decay. The spikes correspond to a brief loss of the SQUID lock, they were removed for the amplitude plot. The lower left inset shows a ringdown while direct feedback is applied (note that the  $x$  axis scale is in seconds).

We can apply a magnetic feedback force on the levitated sphere by processing the SQUID signal on an FPGA (STEMlab 125-14) and applying a feedback current to a small coil with approximately 20 windings positioned approximately  $1 \text{ mm}$  below the trap center [25]. As measurement noise prevents us from resolving the equilibrium c.m. motion of the particle, we use feedback here only as a means to quickly adjust the amplitudes and prepare other measurements (cf. Fig. 3, inset).

**Quality factor.**—We measure the quality factor by performing ringdown measurements, where the initial starting amplitude is set by applying an appropriate feedback signal before the start of the measurement. We do see occasional jumps in the damping rate (cf. Fig. 3), which we attribute to the detaching and attaching of flux lines to a pinning center. Unpinned flux lines can move within the superconductor (flux creep), a mechanism that is known to cause damping in the levitation of flux-pinned superconductors or magnets [10,39]. Although we do not apply a magnetic field during the cooldown, there is a nonzero background field, and hence, we expect some frozen-in flux to be present in the levitated sphere. As a consequence, the measured quality factors vary with time and between measurement runs, but they are generally between  $1 \times 10^7$  and  $2.5 \times 10^7$  for the  $z$  mode and about half as high for the  $x$  and  $y$  modes. The highest quality factor we have measured is  $2.6 \times 10^7$  at 212 Hz, corresponding to a dissipation rate of  $5 \times 10^{-5} \text{ s}^{-1}$ , and likely still limited by flux creep inside the particle. We also consider other possible contributions to the damping [25], but find that the

expected contributions cannot explain the measured values. In future experiments, we plan to use a particle made of a type-I superconductor such as monocrystalline lead, which will expel all magnetic flux via the Meissner effect and prevent flux creep.

**Sensing.**—A massive system acting as a harmonic oscillator can be used for force and acceleration sensing, with the sensitivities depending on the mass  $m$  and the dissipation rate  $\gamma$  of the oscillator. In equilibrium with a thermal bath at temperature  $T_0$ , the thermal force noise is given by  $\sqrt{S_{FF}^{\text{th}}} = \sqrt{4k_B T_0 m \gamma}$  [40], where  $k_B$  is Boltzmann's constant. The dissipation rate  $\gamma$  is related to the quality factor  $Q$  and the angular mechanical resonance frequency  $\omega_0$  by  $\gamma = \omega_0/Q$ . The corresponding acceleration sensitivity is  $\sqrt{S_{FF}^{\text{th}}}/m$ . For a particle of mass  $m \approx 5.6 \mu\text{g}$ , assuming it is in thermal equilibrium with its surroundings in the dilution refrigerator at 15 mK, this sets the limits for force and acceleration sensing at  $5 \times 10^{-19} \text{ N}/\sqrt{\text{Hz}}$  and  $9 \times 10^{-12} \text{ g}/\sqrt{\text{Hz}}$ , using our highest measured quality factor  $Q = 2.6 \times 10^7$  at 212 Hz. Our current experimental sensitivities are approximately 1 order of magnitude above the thermal noise, limited by drifts in the trap current and measurement noise [25].

**Cryogenic vibration isolation.**—Vibrations of the cryostat accelerate the trapping coils and, thus, the trap center, effecting a motion onto the levitated sphere. Denoting the vibrational PSD by  $S_{cc}$ , the displacement PSD of our sphere becomes  $|\chi(\omega)|^2 m^2 \omega_0^2 S_{cc}(\omega)$ , where  $\chi$  denotes the mechanical susceptibility. From independent accelerometer measurements on the cryostat, we estimate  $\sqrt{S_{cc}} \approx 1 \times 10^{-10} \text{ m}/\sqrt{\text{Hz}}$  at 200 Hz, which would result in a peak height of  $2.6 \times 10^{-3} \text{ m}/\sqrt{\text{Hz}}$  and a root-mean-square displacement of  $9 \mu\text{m}$ , corresponding to an effective temperature of  $6 \times 10^{10} \text{ K}$ . To mitigate the effects of vibrations, we implement a passive cryogenic vibration isolation system: the aluminum shield containing the trap is hung from the 4 K stage of the dilution refrigerator via  $38 \mu\text{m}$ -thick stainless steel wires and two intermediate stages. The system acts like a triple pendulum, offering isolation from horizontal ( $x$  and  $y$ ) vibrations, while the elasticity of the wires provides isolation from vertical ( $z$ ) vibrations. To prevent coupling of external vibrations into the experimental setup via electrical wires and the copper braids used for thermalization, we connect these wires and braids to an additional vibration isolation platform, as represented in Fig. 4. Vibrations of the experimental system could also be induced by fluctuating magnetic fields acting on the aluminum shield. To prevent this, we surround the setup by a second aluminum shield which is rigidly mounted to the cryostat. We typically operate at vertical ( $z$ ) trap frequencies above 200 Hz and initially found that the vibration isolation system attenuates vibrations at these frequencies by approximately 5 orders of magnitude. We have further improved the system by optimizing the mass

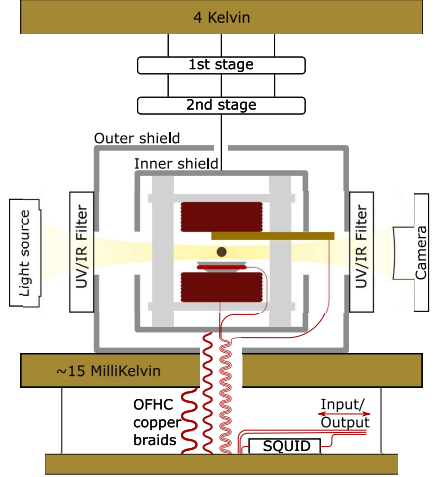


FIG. 4. Sketch of the setup including the vibration isolation system (not to scale). The light source is turned on only for calibration measurements. The UV-IR cutoff filters on the millikelvin stage prevent ambient radiation from heating the levitated sphere. Thermal connections are made with oxygen free high conductivity (OFHC) copper braids.

and wire length for each stage, leading to an attenuation of almost 7 orders of magnitude at 200 Hz. Theoretically, vibrations along the horizontal axis as well as librational fluctuations around the axes are suppressed even more, but in practice, we expect vibrations from the vertical axis to couple into all degrees of freedom [41]. More details on the vibration isolation platform are provided in [25].

**Prospects for ground state cooling.**—Now, we discuss the potential of this system to reach the ground state, which would be a first step toward accessing the quantum regime. SQUID noise can be separated into flux noise  $S_{\phi\phi}$  and noise in the circulating current  $S_{JJ}$ , which may be partially correlated [42] and fulfill  $\sqrt{S_{\phi\phi} S_{JJ}} - S_{\phi J}^2 \geq \hbar$  [43,44]. The flux noise results in the measurement noise  $(S_{\phi\phi}/\eta^2)$ , while the current noise corresponds to a back action  $\eta^2 S_{JJ}$ , where  $\eta$  is the coupling strength. Applying direct feedback with optimum gain and assuming vanishing correlations between flux and current noise, one can estimate the final phonon occupation [25] as

$$\bar{n} = \frac{1}{\hbar\eta^2} (k_B T_0 m \gamma \tilde{L}_S) + \frac{1}{2} \left( \frac{\sqrt{S_{\phi\phi} S_{JJ}}}{\hbar} - 1 \right),$$

where  $\tilde{L}_S = \sqrt{(S_{\phi\phi}/S_{JJ})}$  depends on the working point of the SQUID and is typically on the order of the SQUID

inductance  $L_S$ . The first term describes heating from coupling to an effective thermal reservoir with temperature  $T_0$ , while the second term is the backaction limit under continuous feedback. We can reach a coupling strength of  $\eta \approx 5.5 \times 10^7 \Phi_0/\text{m}$  [25], so assuming  $T_0 \approx 15$  mK and a typical SQUID inductance of  $L_S \approx 15$  pH, we need  $\gamma \approx 1 \times 10^{-6} \text{ s}^{-1}$  to keep the former negligible. Ground state cooling then requires  $\sqrt{S_{\phi\phi} S_{JJ}} < 3\hbar$ . In addition to feedback cooling with a SQUID, we will investigate other potential avenues for ground state cooling such as coupling the levitated sphere to a flux qubit or a microwave cavity [3,45–47].

*Discussion and outlook.*—We built a platform based on the diamagnetic levitation of a superconductor in a magnetostatic trap in a dilution refrigerator at 15 mK and demonstrate quality factors exceeding  $1 \times 10^7$  for the three c.m. modes of a 5.6  $\mu\text{g}$  oscillator. The high quality factors result in excellent sensing capabilities, with achievable force (acceleration) sensitivities that are, otherwise, only reached with much smaller (larger) masses [2,48]. We also demonstrated simultaneous feedback cooling of all c.m. modes using either direct or parametric feedback. While we have focused, here, on a 100  $\mu\text{m}$ -sized sphere, the setup allows for particles from submicron size to millimeter size to be levitated [20]. We have identified improvements to mitigate technical issues: First, we plan to use a type-I superconducting sphere to avoid trapped flux and dissipation caused by flux creep, which we expect is limiting our quality factor. Second, we can improve the magnetomechanical coupling by 4 orders of magnitude by better positioning of the pickup coil and by using a pickup coil with multiple windings matched to the input coil of the SQUID. Together with an optimized SQUID shielded from environmental noise (such that our readout is limited by the intrinsic SQUID noise), this would result in an improvement of the measurement noise floor by 6 orders of magnitude [25]. Third, we plan to implement a persistent current switch to improve the trap current stability. With these improvements, our system offers a promising approach for bringing microgram objects to the quantum regime, which opens a potential avenue for quantum-limited acceleration sensing or even probing quantum effects of gravity [49–52].

The data of this study are available at the Zenodo repository [53].

We thank G. Kirchmair, O. Romero-Isart, and A. Sanchez for discussions. We thank Matthias Rudolph for assisting with the initial setup of a SQUID measurement system. We thank F. Wulschner for setting up a helium flow cryostat and assisting with measurements during the initial phase of the project. This work was supported by the European Union’s Horizon 2020 research and innovation programme under Grant Agreement No. 863132 (iQLev), the European Union’s Horizon Europe 2021–2027 Framework Programme under Grant Agreement No. 101080143

(SuperMeQ), the European Research Council (ERC CoG QLev4G and ERC Synergy QXtreme), and the Austrian Science Fund (FWF) under Project No. F40 (SFB FOQUS). We gratefully acknowledge financial support from the Deutsche Forschungsgemeinschaft (DFG, German Research Foundation) under Germany’s Excellence Strategy Grant No. EXC-2111–390814868. G. H. acknowledges support from the Swedish Research Council (Grant No. 2020-00381). P. S. is supported by the Alexander von Humboldt Foundation through a Feodor Lynen Fellowship.

\*joachim.hofer@univie.ac.at

Present address: QuTech, Delft University of Technology, Delft, The Netherlands.

- [1] E. H. Brandt, Levitation in physics, *Science* **243**, 349 (1989).
- [2] J. M. Goodkind, The superconducting gravimeter, *Rev. Sci. Instrum.* **70**, 4131 (1999).
- [3] O. Romero-Isart, L. Clemente, C. Navau, A. Sanchez, and J. I. Cirac, Quantum Magnetomechanics with Levitating Superconducting Microspheres, *Phys. Rev. Lett.* **109**, 147205 (2012).
- [4] M. Cirio, G. K. Brennen, and J. Twamley, Quantum Magnetomechanics: Ultrahigh- $Q$ -Levitated Mechanical Oscillators, *Phys. Rev. Lett.* **109**, 147206 (2012).
- [5] A. Vinante, P. Falferi, G. Gasbarri, A. Setter, C. Timberlake, and H. Ulbricht, Ultralow Mechanical Damping with Meissner-Levitated Ferromagnetic Microparticles, *Phys. Rev. Appl.* **13**, 064027 (2020).
- [6] J. Gieseler, A. Kabenell, E. Rosenfeld, J. D. Schaefer, A. Safira, M. J. A. Schuetz, C. Gonzalez-Ballester, C. C. Rusconi, O. Romero-Isart, and M. D. Lukin, Single-Spin Magnetomechanics with Levitated Micromagnets, *Phys. Rev. Lett.* **124**, 163604 (2020).
- [7] Y. Leng, R. Li, X. Kong, H. Xie, D. Zheng, P. Yin, F. Xiong, T. Wu, C.-K. Duan, Y. Du, Z.-q. Yin, P. Huang, and J. Du, Mechanical Dissipation Below 1  $\mu\text{Hz}$  with a Cryogenic Diamagnetic Levitated Micro-Oscillator, *Phys. Rev. Appl.* **15**, 024061 (2021).
- [8] C. W. Lewandowski, T. D. Knowles, Z. B. Etienne, and B. D’Urso, High-Sensitivity Accelerometry with a Feedback-Cooled Magnetically Levitated Microsphere, *Phys. Rev. Appl.* **15**, 014050 (2021).
- [9] T. Wang, S. Lourette, S. R. O’Kelley, M. Kayci, Y. B. Band, Derek F. Jackson Kimball, A. O. Sushkov, and D. Budker, Dynamics of a Ferromagnetic Particle Levitated Over a Superconductor, *Phys. Rev. Appl.* **11**, 044041 (2019).
- [10] E. H. Brandt, Friction in levitated superconductors, *Appl. Phys. Lett.* **53**, 1554 (1988).
- [11] R. S. Van Dyck, D. L. Farnham, S. L. Zafonte, and P. B. Schwinberg, Ultrastable superconducting magnet system for a penning trap mass spectrometer, *Rev. Sci. Instrum.* **70**, 1665 (1999).
- [12] J. W. Britton, J. G. Bohnet, B. C. Sawyer, H. Uys, M. J. Biercuk, and J. J. Bollinger, Vibration-induced field fluctuations in a superconducting magnet, *Phys. Rev. A* **93**, 062511 (2016).

- [13] M. G. Latorre, J. Hofer, M. Rudolph, and W. Wieczorek, Chip-based superconducting traps for levitation of micrometer-sized particles in the Meissner state, *Supercond. Sci. Technol.* **33**, 105002 (2020).
- [14] M. G. Latorre, A. Paradkar, D. Hambraeus, G. Higgins, and W. Wieczorek, A chip-based superconducting magnetic trap for levitating superconducting microparticles, *IEEE Trans. Appl. Supercond.* **32**, 1 (2022).
- [15] M. Gutierrez Latorre, G. Higgins, A. Paradkar, T. Bauch, and W. Wieczorek, Superconducting Microsphere Magnetically Levitated in an Anharmonic Potential with Integrated Magnetic Readout, *Phys. Rev. Appl.* **19**, 054047 (2023).
- [16] H. Pino, J. Prat-Camps, K. Sinha, B. P. Venkatesh, and O. Romero-Isart, On-chip quantum interference of a superconducting microsphere, *Quantum Sci. Technol.* **3**, 025001 (2018).
- [17] U. Delic, M. Reisenbauer, K. Dare, D. Grass, Vuletic Vladan, N. Kiesel, and M. Aspelmeyer, Cooling of a levitated nanoparticle to the motional quantum ground state, *Science* **367**, 892 (2020).
- [18] L. Magrini, P. Rosenzweig, C. Bach, A. Deutschmann-Olek, S. G. Hofer, S. Hong, N. Kiesel, A. Kugi, and M. Aspelmeyer, Real-time optimal quantum control of mechanical motion at room temperature, *Nature (London)* **595**, 373 (2021).
- [19] F. Tebbenjohanns, M. L. Mattana, M. Rossi, M. Frimmer, and L. Novotny, Quantum control of a nanoparticle optically levitated in cryogenic free space, *Nature (London)* **595**, 378 (2021).
- [20] J. Hofer and M. Aspelmeyer, Analytic solutions to the Maxwell–London equations and levitation force for a superconducting sphere in a quadrupole field, *Phys. Scr.* **94**, 125508 (2019).
- [21] C. Navau, S. Minniberger, M. Trupke, and A. Sanchez, Levitation of superconducting microrings for quantum magnetomechanics, *Phys. Rev. B* **103**, 174436 (2021).
- [22] F. Monteiro, S. Ghosh, A. G. Fine, and D. C. Moore, Optical levitation of 10-ng spheres with nano- $g$  acceleration sensitivity, *Phys. Rev. A* **96**, 063841 (2017).
- [23] Francis C. Moon and P.-Z. Chang, *Superconducting Levitation: Applications to Bearings and Magnetic Transportation* (Wiley-VCH, New York, 1995).
- [24] B. van Waarde, The lead zeppelin: A force sensor without a handle, Ph.D. thesis, Leiden University, 2016.
- [25] See Supplemental Material at <http://link.aps.org/supplemental/10.1103/PhysRevLett.131.043603> for more information on the derivation of trap parameters, the effects of trap current fluctuations, the vibration isolation system, estimations of different contributions to the damping, the calibration of the SQUID signal, as well as more details on ground state cooling, which includes Refs. [26–36].
- [26] L. Neuhaus, R. Metzendorf, S. Chua, T. Jacqmin, T. Briant, A. Heidmann, P.-F. Cohadon, and S. Deléglise, PyRPL (Python Red Pitaya Lockbox)—An open-source software package for FPGA-controlled quantum optics experiments, in *Proceedings of the 2017 Conference on Lasers and Electro-Optics Europe European Quantum Electronics Conference (CLEO/Europe-EQEC)* (IEEE, New York, 2017), p. 1.
- [27] L. D. Hinkle and B. R. F. Kendall, Pressure-dependent damping of a particle levitated in vacuum, *J. Vac. Sci. Technol. A* **8**, 2802 (1990).
- [28] J. M. Martinis and J. Clarke, Signal and noise theory for a dc SQUID amplifier, *J. Low Temp. Phys.* **61**, 227 (1985).
- [29] J. C. Crocker and D. G. Grier, Methods of digital video microscopy for colloidal studies, *J. Colloid Interface Sci.* **179**, 298 (1996).
- [30] D. D. Awschalom, J. R. Rozen, M. B. Ketchen, W. J. Gallagher, A. W. Kleinsasser, R. L. Sandstrom, and B. Bumble, Low-noise modular microsusceptometer using nearly quantum limited dc SQUIDS, *Appl. Phys. Lett.* **53**, 2108 (1988).
- [31] P. Carelli, M. G. Castellano, G. Torrioli, and R. Leoni, Low noise multiwasher superconducting interferometer, *Appl. Phys. Lett.* **72**, 115 (1998).
- [32] H. Wheeler, Simple inductance formulas for radio coils, *Proc. Inst. Radio Eng.* **16**, 1398 (1928).
- [33] T. W. Penny, A. Pontin, and P. F. Barker, Performance and limits of feedback cooling methods for levitated oscillators: A direct comparison, *Phys. Rev. A* **104**, 023502 (2021).
- [34] J. Martinis and J. Clarke, Measurements of current noise in dc SQUIDS, *IEEE Trans. Magn.* **19**, 446 (1983).
- [35] P. Falferi, M. Bonaldi, M. Cerdonio, R. Mezzena, G. A. Prodi, A. Vinante, and S. Vitale,  $10\hbar$  superconducting quantum interference device amplifier for acoustic gravitational wave detectors, *Appl. Phys. Lett.* **93**, 172506 (2008).
- [36] M. E. Gehm, K. M. O'Hara, T. A. Savard, and J. E. Thomas, Dynamics of noise-induced heating in atom traps, *Phys. Rev. A* **58**, 3914 (1998).
- [37] J. D. Livingston, Magnetic properties of superconducting lead-base alloys, *Phys. Rev.* **129**, 1943 (1963).
- [38] J.-H. Storm, O. Klier, and R. Körber, Towards ultra-sensitive SQUIDS based on submicrometer-sized Josephson junctions, *IEEE Trans. Appl. Supercond.* **30**, 1 (2020).
- [39] V. V. Nemoshkalenko, E. H. Brandt, A. A. Kordyuk, and B. G. Nikitin, Dynamics of a permanent magnet levitating above a high- $T_c$  superconductor, *Physica (Amsterdam)* **170C**, 481 (1990).
- [40] R. Kubo, The fluctuation-dissipation theorem, *Rep. Prog. Phys.* **29**, 255 (1966).
- [41] T. L. Aldcroft, P. F. Michelson, R. C. Taber, and F. A. McLoughlin, Six-degree-of-freedom vibration isolation systems with application to resonant-mass gravitational radiation detectors, *Rev. Sci. Instrum.* **63**, 3815 (1992).
- [42] C. D. Tesche and J. Clarke, dc SQUID: Current noise, *J. Low Temp. Phys.* **37**, 397 (1979).
- [43] R. H. Koch, D. J. Van Harlingen, and J. Clarke, Quantum noise theory for the dc SQUID, *Appl. Phys. Lett.* **38**, 380 (1981).
- [44] V. Danilov, K. Likharev, and A. Zorin, Quantum noise in squids, *IEEE Trans. Magn.* **19**, 572 (1983).
- [45] P. Schmidt, M. T. Amawi, S. Pogorzalek, F. Deppe, A. Marx, R. Gross, and H. Huebl, Sideband-resolved resonator electromechanics based on a nonlinear Josephson inductance probed on the single-photon level, *Commun. Phys.* **3**, 233 (2020).
- [46] O. Shevchuk, G. A. Steele, and Y. M. Blanter, Strong and tunable couplings in flux-mediated optomechanics, *Phys. Rev. B* **96**, 014508 (2017).

- [47] D. Zoepfl, M. L. Juan, C. M. F. Schneider, and G. Kirchmair, Single-Photon Cooling in Microwave Magneto-mechanics, *Phys. Rev. Lett.* **125**, 023601 (2020).
- [48] D. Hempston, J. Vovrosh, M. Toroš, G. Winstone, M. Rashid, and H. Ulbricht, Force sensing with an optically levitated charged nanoparticle, *Appl. Phys. Lett.* **111**, 133111 (2017).
- [49] S. P. Kumar and M. B. Plenio, On quantum gravity tests with composite particles, *Nat. Commun.* **11**, 3900 (2020).
- [50] C. Marletto and V. Vedral, Gravitationally Induced Entanglement Between Two Massive Particles is Sufficient Evidence of Quantum Effects in Gravity, *Phys. Rev. Lett.* **119**, 240402 (2017).
- [51] S. Bose, A. Mazumdar, G. W. Morley, H. Ulbricht, M. Toroš, M. Paternostro, A. A. Geraci, P. F. Barker, M. S. Kim, and G. Milburn, Spin Entanglement Witness for Quantum Gravity, *Phys. Rev. Lett.* **119**, 240401 (2017).
- [52] M. Aspelmeyer, How to avoid the appearance of a classical world in gravity experiments, [arXiv:2203.05587](https://arxiv.org/abs/2203.05587).
- [53] J. Hofer *et al.*, Data Used in the Article “High-Q Magnetic Levitation and Control of Superconducting Microspheres at Millikelvin Temperatures,” Zenodo, 10.5281/zenodo.7837944 (2023).

# Supplemental material: High-Q magnetic levitation and control of superconducting microspheres at millikelvin temperatures

J. Hofer,<sup>1,2,\*</sup> R. Gross,<sup>3,4,5</sup> G. Higgins,<sup>2,6</sup> H. Huebl,<sup>3,4,5</sup> O. F. Kieler,<sup>7</sup> R. Kleiner,<sup>8</sup> D. Koelle,<sup>8</sup> P. Schmidt,<sup>2</sup> J. A. Slater,<sup>1,†</sup> M. Trupke,<sup>1</sup> K. Uhl,<sup>8</sup> T. Weimann,<sup>7</sup> W. Wieczorek,<sup>1,6</sup> and M. Aspelmeyer<sup>1,2</sup>

<sup>1</sup>University of Vienna, Faculty of Physics, Vienna Center for Quantum Science and Technology (VCQ), A-1090 Vienna, Austria

<sup>2</sup>Institute for Quantum Optics and Quantum Information (IQOQI),

Austrian Academy of Sciences, A-1090 Vienna, Austria

<sup>3</sup>Walther-Meißner-Institut, Bayerische Akademie der Wissenschaften, D-85748 Garching, Germany

<sup>4</sup>Physik-Department, Technische Universität München, D-85748 Garching, Germany

<sup>5</sup>Munich Center for Quantum Science and Technology (MCQST), D-80799 München, Germany

<sup>6</sup>Department of Microtechnology and Nanoscience (MC2),

Chalmers University of Technology, S-412 96 Gothenburg, Sweden

<sup>7</sup>Physikalisch-Technische Bundesanstalt (PTB), D-38116 Braunschweig, Germany

<sup>8</sup>Physikalisches Institut, Center for Quantum Science (CQ) and LISA<sup>+</sup>,

University of Tuebingen, D-72076 Tuebingen, Germany

(Dated: June 26, 2023)

We provide more information on: (i) The field distribution of the magnetic trap, the resulting trap frequencies and the derivation of the coupling strength. (ii) Effects of current fluctuations and drifts on the measured spectral density. (iii) Limits to the force sensitivity due to measurement noise and current drifts. (iv) Feedback control of the levitated particle. (v) The vibration isolation system. (vi) Possible contributions to the damping. (vii) Calibration of the SQUID signal. (viii) Optimizations and requirements for ground state cooling.

## DERIVATION OF THE MAGNETIC TRAP'S PROPERTIES

### Trapping field

We performed numerical simulations in COMSOL MULTIPHYSICS to predict the field configuration generated by the arrangement of our trapping coils. The design of the coils and the simulated magnetic field density are shown in Fig. 1a,b. The field gradients for a trap current of 2.5 A are obtained as  $(b_x, b_y, b_z) = (57, 90, 147)$  T/m, which would correspond to frequencies of (92, 144, 236) Hz. Comparing this to the measured values of (109, 127, 236) Hz we can see that the agreement between the numerical and measured z-mode frequency is excellent, but that the simulations predict a much stronger split for the x- and y-mode than what we see in the experiment. This is likely due to the fact that the spooling process resulted in coils that were more circular than the design (cf. Fig. 1c). For a perfectly circular coil the x- and y-mode frequencies are degenerate [1], so a smaller frequency split is to be expected. Close to the center the field is very well approximated by a quadrupole field: Within a cubic volume of  $200 \mu\text{m} \times 200 \mu\text{m} \times 200 \mu\text{m}$  the maximum relative root-mean-square deviation, defined as  $|\mathbf{B}_{\text{sim}} - (b_x x, b_y y, b_z z)|/|\mathbf{B}_{\text{sim}}|$ , is less than 0.1 %.

### Mechanical frequencies

In this section we build on the calculations in [1] to analytically calculate the magnetic field distribution for a su-

perconducting sphere in an axially-asymmetric magnetic quadrupole field. We consider a superconducting sphere at the origin of the coordinate system and displaced from the center the quadrupole field by  $\mathbf{x}_0 = (x_0, y_0, z_0)$ . The applied field then reads

$$\mathbf{B}_0 = (b_x(x + x_0), b_y(y + y_0), b_z(z + z_0)).$$

As our sphere's radius  $R$  is much larger than the expected penetration depth  $\lambda$  [2], we can use the approximation  $\lambda/R \rightarrow 0$ , i.e. we assume  $\mathbf{B} = 0$  inside the sphere and  $B_r = 0$  on the sphere's surface [1], where  $B_r$  denotes the radial component of the field. As there are no currents outside the sphere, there exists a scalar potential  $\Phi$  s.t.  $\mathbf{B} = \mathbf{B}_0 - \nabla\Phi$  and

$$\Phi = \sum_{n=0}^{\infty} r^{-(n+1)} \sum_{m=-n}^n a_{n,m} Y_n^m,$$

where  $r = \sqrt{x^2 + y^2 + z^2}$  and the  $Y_n^m$  are spherical harmonics. The coefficients  $a_{n,m}$  are determined by the boundary condition  $B_{0,r} = (\nabla\Phi)_r$  on the sphere's surface as

$$\begin{aligned} a_{1,0} &= -b_z \sqrt{\pi/3} R^3 z_0, \\ a_{1,-1} &= -\sqrt{\pi/6} R^3 (b_x x_0 + i b_y y_0), \\ a_{1,1} &= \sqrt{\pi/6} R^3 (b_x x_0 - i b_y y_0), \\ a_{2,0} &= -b_z \sqrt{4\pi/45} R^5, \\ a_{2,-2} &= (b_y - b_x) \sqrt{2\pi/135} R^5, \\ a_{2,2} &= a_{2,-2}, \end{aligned}$$

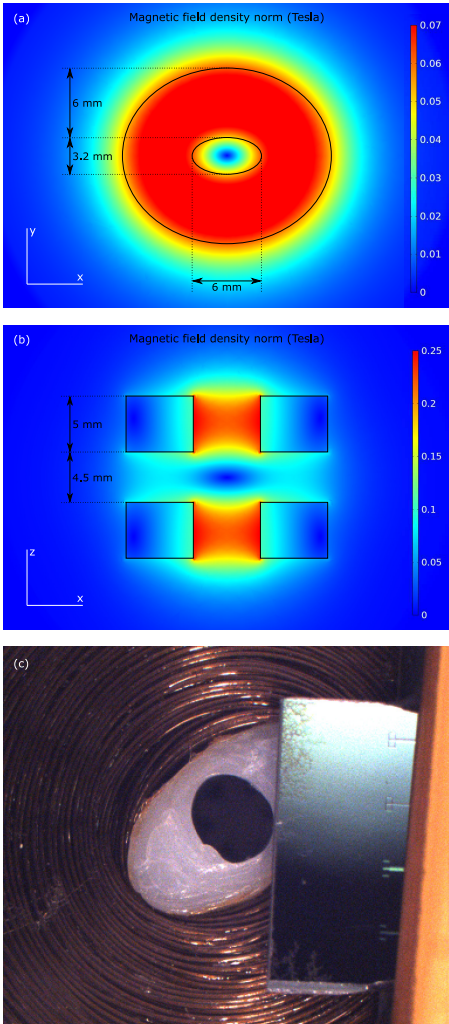


FIG. 1. (a,b) Numerical simulations of the magnetic field density created by coaxial elliptical coils with counter-propagating currents. (c) Photograph of the top surface of a single trap coil. On the right side the wafer with the pickup loops is visible (not in its final position).

all other coefficients are zero. From this field distribution we obtain the force on the sphere as

$$\mathbf{F} = -\frac{3V}{2\mu_0} (b_x^2 x_0, b_y^2 y_0, b_z^2 z_0),$$

where  $V$  is the volume of the sphere. The magnetic field thus creates a harmonic trapping potential for a superconducting sphere, with trapping frequencies described by

$$f_i = \sqrt{\frac{3}{8\pi^2\mu_0\rho}} |b_i|.$$

### Coupling strength

The linear coupling strength with respect to a pickup loop that is described by a closed path  $\gamma$  is defined as  $\nu_i = \partial_i \Phi_\gamma$ , where  $\Phi_\gamma$  is the flux through the area enclosed by the pickup loop and  $i \in \{x_0, y_0, z_0\}$ . We can express this as

$$\nu_i = \int_\gamma d\gamma \partial_i \mathbf{A}, \quad (1)$$

where  $\mathbf{A}$  denotes the magnetic vector potential, defined by  $\nabla \times \mathbf{A} = \mathbf{B}$  and  $\nabla \cdot \mathbf{A} = 0$ . While the resulting expressions are generally bulky, they can be easily evaluated using a computer algebra system, we use WOLFRAM MATHEMATICA. We measure the current that is induced in the pickup loop using a SQUID current sensor, i.e. the pickup loop is connected to an input coil on the same wafer as the SQUID and inductively coupled to the SQUID. The coupling strength with respect to the SQUID is thus obtained as  $\eta_i = \nu_i M/L$ , where  $L$  is the inductance of the circuit formed by pickup loop, input coil of the current sensor, and the connecting wires, while  $M$  is the mutual inductance between input coil and SQUID. In our case  $M/L \approx 0.02$ . In Fig. 2 we plot the dependence of the coupling strength on the vertical separation between trap center and pickup loop, when the  $x$ - and  $y$ -position of the pickup loop relative to the trap center (as shown in the inset) is approximately the same as what we estimate for our setup (from pictures taken at room temperature, cf. Fig. 1c). The horizontal dotted lines correspond to the measured coupling strengths, while the vertical dotted line corresponds to the vertical separation extracted from camera images (approx.  $400 \mu\text{m}$ ) of the levitated sphere.

### Trap displacement due to gravity

The rest position of the sphere is slightly displaced from the field minimum due to gravity. In our case the

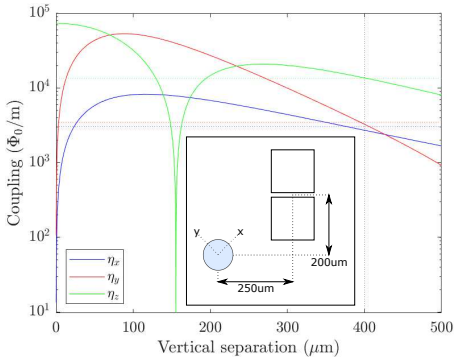


FIG. 2. Dependence of the coupling strength on the vertical separation between trap center and pickup loop, when the separation along  $x$  and  $y$  is as shown in the inset - these are the values we estimate for our setup. The vertical separation in our setup is approximately  $400\ \mu\text{m}$ . The dotted horizontal lines correspond to the measured coupling strengths.

setup is aligned such that the direction of gravity coincides with the  $z$ -axis. The expected displacement is thus

$$z_g = -g/(2\pi f_z)^2,$$

where  $g \approx 9.81\ \text{m/s}^2$ . In general this displacement needs to be taken into account when calculating the coupling strength, but for larger trapping frequencies it becomes negligible. We usually operate at  $f_z > 200\ \text{Hz}$ , for which  $z_g < 6\ \mu\text{m}$ .

## CURRENT FLUCTUATIONS

Since the sphere's motional frequencies depend linearly on the trap current, current fluctuations result in frequency fluctuations, and thus can cause heating as well as broadening of the mechanical spectral peaks. We stabilize the trap current both passively and actively, as described in the following. We implement a first-order low-pass RL-filter by adding a short copper wire (resistance  $R_C$ ) in parallel to the trap coils (inductance  $L_C$ ). We characterize the filter's cut-off frequency by measuring its step response in an empty trap (Fig. 3). The cutoff frequency is  $R_C/L_C \approx 0.036\ \text{s}^{-1}$ , which results in an attenuation of approximately  $-180\ \text{dB}$  at  $200\ \text{Hz}$ , while the added thermal current noise from the copper wire is only on the order of  $1 \times 10^{-11}\ \text{A}/\sqrt{\text{Hz}}$ .

We actively stabilize the filtered trap current by monitoring the mean current source output using a digital ammeter and updating the current source output based on an estimation of the trap current. This lessens current

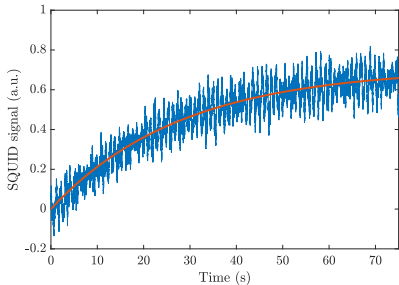


FIG. 3. Step response of the filter measured using the SQUID. The solid line is a fit of the filter's step response  $1 - \exp(-R_C/L_C t)$ .

drifts and the associated resonance broadening, as seen by comparing Fig. 4(a) with (b). Even with active current stabilization we observe drifts of the particle's resonance frequency shown in Fig. 4(d), which we attribute to low-frequency noise in the ammeter reading.

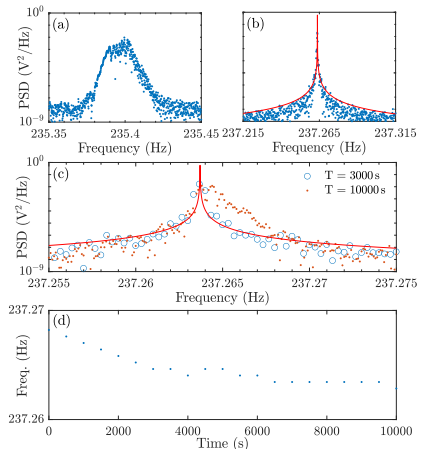


FIG. 4. (a) Typical motional resonance without active current stabilization. (b) Typical motional resonance with active current stabilization. (c) Comparison of PSDs for different measurement lengths  $T$  with trap current feedback on. For short  $T$  the linewidth is determined by the spectral resolution  $1/T$  and spectral leakage, while for longer  $T$  there is still linewidth broadening due to drifts in frequency. The solid line in (b) and (c) is a Lorentzian with the linewidth set by a ringdown measurement. (d) The resonance frequency drifts by around  $5\ \text{mHz}$  over three hours.

## SENSING

Taking into account measurement noise, we can calculate the force sensitivity as

$$\sqrt{S_{FF}} = \sqrt{4k_B T_0 m \gamma + |\chi|^{-2} S_{nn}},$$

where  $\sqrt{S_{nn}} \approx 1 \times 10^{-9} \text{ m}/\sqrt{\text{Hz}}$  is the measurement noise and  $\chi(\omega) = 1/[m(\omega_0^2 - \omega^2 - i\gamma\omega)]$  denotes the mechanical susceptibility. In our case, using  $Q = 2.6 \times 10^7$  at 212 Hz and assuming  $T_0 = 15 \text{ mK}$ , this would result in a force sensitivity of  $\sqrt{S_{FF}} = 6.3 \times 10^{-19} \text{ N}/\sqrt{\text{Hz}}$  on resonance, close to the thermal limit of  $4.9 \times 10^{-19} \text{ N}/\sqrt{\text{Hz}}$ , and a noise equivalent temperature of  $T_n = T_0 + |\chi(\omega_0)|^{-2} S_{nn}/(4k_B m \gamma) = 24 \text{ mK}$  (cf. Fig. 5). However,

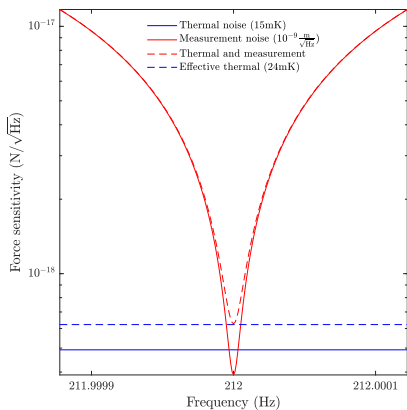


FIG. 5. (a) Force sensitivity limits due to thermal noise and measurement noise. The parameters used for the plot are  $Q = 2.6 \times 10^7$  and  $f_0 = 212 \text{ Hz}$ .

due to the stochastic frequency fluctuations described in the last section the susceptibility is stochastic as well. We briefly sketch how this reduces our sensitivity: Note that a measurement with frequency drifts can be approximated as a series of shorter measurements at different, but constant, resonance frequencies. For a finite measurement duration  $T$  the measured force power spectral density at resonance is approximately

$$4k_B T_0 m \gamma + S_{nn} \frac{\Delta f}{\int_{\Delta f} df |\chi(f)|^2},$$

where the integration runs over the bin width  $\Delta f = \frac{1}{T}$  of the bin containing the resonance. Our force sensitivity thus becomes  $\sqrt{S_{FF}} = \sqrt{4k_B T_0 m \gamma + |\chi|_{avg}^{-2} S_{nn}}$

with  $|\chi|_{avg}^2 = \frac{1}{\Delta f} \int_{\Delta f} df |\chi(f)|^2$ . For  $\Delta f > \frac{\gamma}{2\pi}$ , we get  $\frac{|\chi(f_0)|^2}{|\chi|_{avg}^2} \propto \frac{\Delta f}{\gamma}$ . In our case this boosts the measurement noise above the thermal noise and, for a typical measurement, our force sensitivity worsens by at least an order of magnitude, corresponding to an noise equivalent temperature of at least 2.5 K. Both improving the coupling, which corresponds to an effective decrease of the measurement noise, and improving the stability of the resonance frequency will allow us to perform measurements limited by thermal noise. We show below that we can increase the coupling by almost four orders of magnitude. Regarding the latter, we note that persistent current coils have reached a relative current stability better than  $2 \times 10^{-11}/\text{h}$  [3].

## FEEDBACK

We can apply a magnetic feedback force on the levitated sphere by processing the SQUID signal and applying a feedback current to a small coil with approximately 20 windings positioned approximately 1 mm below the trap center. The feedback current generates an additional magnetic field, thereby shifting the field minimum of the trapping field and enabling us to apply direct feedback. The gradient of the trapping field is changed as well, such that we also have the possibility to apply parametric feedback at twice the particle's resonance frequencies. Since the COM modes are separated in frequency, we can apply feedback to all modes simultaneously. When we apply direct feedback, we pass the SQUID signal to a FPGA (STEMlab 125-14), which, for each of the mechanical frequencies, applies a bandpass filter, gain and phase shift [4]. The resulting signals are then recombined on the FPGA and fed back to the feedback coil. When we apply parametric feedback at twice the mechanical frequencies we additionally use a phase-locked loop and a clock divider on a second FPGA. As described in the last section, our current noise floor corresponds to a noise equivalent temperature that is higher than the base temperature of our dilution refrigerator. This noise equivalent temperature also sets the limit for feedback cooling. Due to the large ambient noise reduction provided by our vibration isolation, magnetic shielding and trap current filter, the equilibrium temperature of the particle is below the noise equivalent temperature, meaning that even without applied feedback the particle's motion undergoes exponential decay until it is not detectable anymore. We thus cannot cool the particle's modes below their equilibrium temperature and use feedback currently only as a way to quickly adjust the amplitudes and prepare other measurements.

## CHARACTERIZATION OF THE VIBRATION ISOLATION SYSTEM

Our vibration isolation system consists of several cylindrical plates connected by straight wires, with the top plate mounted to the 4K-platform of the dilution refrigerator and the bottom plate mounted to the aluminum can containing the magnetic trap. Electrical and thermal connections going to the setup are loosely coiled up and guided to the setup via a separate vibration isolation stage hung from the Mixing Chamber platform (cf. Fig. 6). We first characterized a single stage at room temperature, by exciting it mechanically and recording its motion with a camera. We find that the horizontal and vertical resonance frequencies are  $f_h = 1.1$  Hz and  $f_v = 18.7$  Hz, respectively, while the librational resonance frequencies are  $f_{l,1} = 0.6$  Hz (around vertical axis),  $f_{l,2} = 8.7$  Hz and  $f_{l,3} = 9.0$  Hz (around horizontal axes). We are thus limited by vertical vibrations, which in general couple to the other degrees of freedom as well [5]. We then assembled the setup as shown in Fig. 6, with the bottom plate mounted to an accelerometer (instead of the setup) used to measure acceleration along the vertical axis. The mass of the bottom plate (including the accelerometer) was 0.29 kg in this assembly. The intermediate stages are each supported by three wires of equal length, while the bottom stage is supported by a single wire. The wires are made from type 304 stainless steel with a diameter of  $D = 38\mu\text{m}$  and a yield load of 0.37 kg, as specified by the manufacturer (Fort Wayne Metals). The wires are connected to the stages with clamping connections. The vertical spring constant for the  $i$ -th stage is given by  $k_{v,i} = (N_i Y D^2 \pi) / (4 L_i)$ , s.t.  $f_{v,i} = 1/(2\pi) \sqrt{k_{v,i}/m_i}$  is the resonance frequency of a single stage. Here  $Y$  is the Young's modulus,  $N_i$  the number of supporting wires,  $L_i$  the wire length and  $m_i$  the mass of the stage. The normal mode frequencies  $f_{n,i}$  of the assembled system are obtained by solving the characteristic equation of the system [5], resulting in the transfer function

$$\prod_{i=1}^3 \frac{f_{v,i}^2}{|f_{n,i}^2 - f^2|}. \quad (2)$$

In Fig. 7 we compare the vibrations measured without vibration isolation (with the accelerometer mounted to the Mixing Chamber stage of the dilution fridge) and with vibration isolation. The highest normal mode frequency is approximately 30 Hz, above which the measured accelerations quickly drop below the sensitivity of the accelerometer, when it is mounted to the vibration isolation system. At lower frequencies the measured transfer function corresponds very well to the analytical values and we use the analytic expression to extrapolate the attenuation at higher frequencies, resulting in an attenuation of  $1 \times 10^{-5}$  at 100 Hz and  $1.5 \times 10^{-7}$  at 200 Hz. The peaks

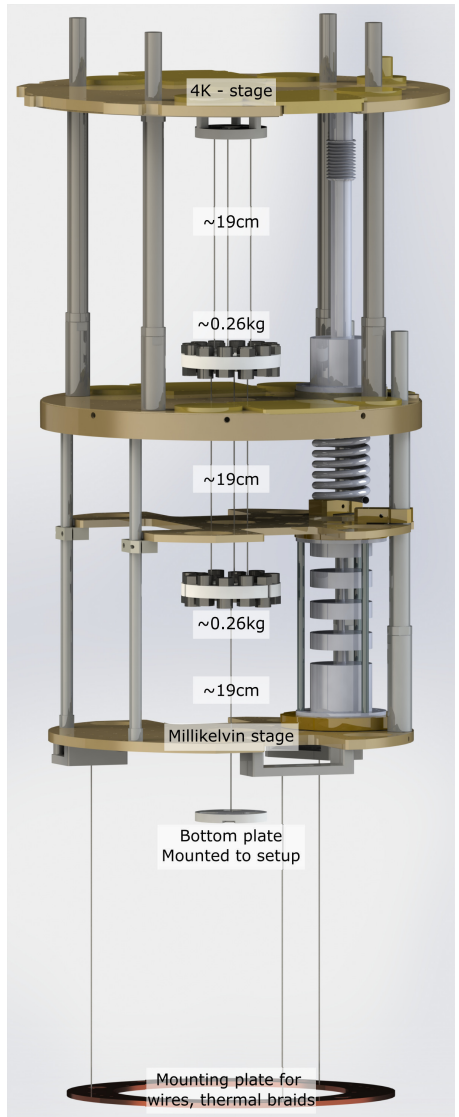


FIG. 6. Model of the vibration isolation system.

at higher frequencies correspond to the electromagnetic

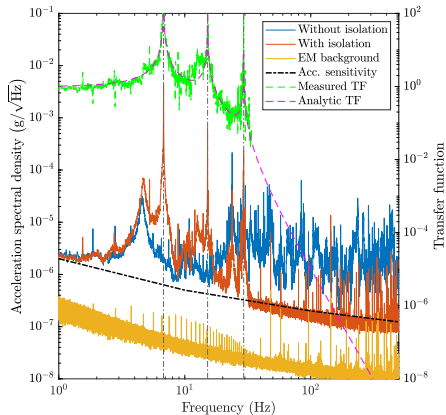


FIG. 7. Characterization of the vibration isolation. The dashed-dotted black line is the sensitivity of the accelerometer, as specified by the manufacturer. The solid orange and blue lines correspond to the measured acceleration with and without the vibration isolation, respectively, while the solid yellow line is data recorded with a  $1\text{ M}\Omega$  resistor connected to the SMA port inside the fridge. The dashed pink line is the analytic transfer function (Eq. 2), while the dashed green line is the measured transfer function, i.e. the ratio of the measured accelerations. The horizontal lines correspond to the normal mode resonance frequencies.

background in the lab, which is verified by an independent measurement in which the accelerometer is replaced by an  $1\text{ M}\Omega$  resistor inside the fridge. This measurement reproduces the peaks at precisely the same frequencies as in the accelerometer measurement, although with a lower magnitude - this we attribute to the additional (unshielded) wiring going from the SMA port to the accelerometer, which can act as an antenna. In an initial approach we used different masses and wire lengths, such that the attenuation was approximately 5 orders of magnitude at  $200\text{ Hz}$ .

### QUALITY FACTOR

In this section we estimate contributions to the dissipation due to gas damping and eddy currents. We also consider dissipation in the SQUID and flux creep in the pickup loop, which we rule out experimentally.

Collisions with background gas result in an additional damping of [6]

$$\gamma_P = \beta \frac{P}{\rho R v_{th}},$$

where  $\beta \approx 1.8$  and  $v_{th}$  is the mean thermal velocity of the molecules. We do not have a direct measure of the pressure at the trap location, but we can use the measured pressure at the room temperature side of the vacuum can,  $P \approx 1 \times 10^{-6}\text{ mbar}$ , to set an upper limit for the expected damping. Assuming the background gas consists mostly of Helium, we get  $\gamma_P \approx 3 \times 10^{-7}\text{ s}^{-1}$ , two orders of magnitude below the measured damping rates.

We avoid eddy current damping by not placing any normal conductors within the inner shield. Eddy currents can still be induced in conductors outside the shield, either via openings in the shield or via the pickup circuit, part of which is placed outside the shield. In the first case, we can estimate possible eddy current losses by imagining a conductive loop with resistance  $R_o$  and inductance  $L_o$  placed around the openings in the shield. The dissipation in mode  $i \in \{x_0, y_0, z_0\}$  then takes a maximum value for  $R_o = 2\pi f_i L_o$ , corresponding to a damping

$$\gamma_i = \frac{(\partial_i \phi)^2}{2\pi m f_i L_o}.$$

Here  $\phi$  denotes the flux in the loop induced by the oscillation of the sphere, which can be calculated from Eq. 1. Using the dimensions of our windows and estimating  $L_o > 10\text{ nH}$  for a similarly sized conductive loop, we get  $\gamma_i < 1 \times 10^{-9}\text{ s}^{-1}$  for all modes.

We now consider eddy current damping mediated by the pickup circuit or damping due to flux creep in the pickup circuit, as well as dissipation in the SQUID due to a real part in the SQUID input impedance [7]. This implies  $\gamma_i \propto \nu_i^2$ , while in the experiment the damping is approximately equal for all three COM modes. In addition, during initial measurements the pickup loop was positioned farther from the trap center and coupling strengths were approximately one order of magnitude lower than the ones reported here, but we did not see any change in the quality factor.

### CALIBRATION

Our optical readout scheme is shown schematically in Fig. 8. The light source (Leica CLS150) produces a beam

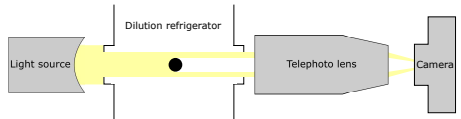


FIG. 8. Sketch of the optical setup.

of light, which is further collimated by small windows

in the cryostat and the magnetic shields. After passing through the cryostat, the light is focused by a teleobjective into the camera (DFK 33UX287). Any object in the light path thus appears as a shadow on a bright background, corresponding to the projection of the object onto the image sensor. We use a frame rate of 596fps and 0.5ms exposure time to record the videos and then process them as follows. Each frame is first converted to grayscale, smoothed with Gaussian blurring, thresholded and then analyzed using the particle tracking software TRACKPY [8]. This results in datasets for the horizontal and vertical (as defined by the camera's orientation) position of the sphere. The camera is aligned such that the vertical axis is along the trap coil axis and the direction of the particle's z-motion, while the particle's motion along x and y is projected onto the camera's horizontal axis. The trap coils are aligned such that the elliptic axes are at around 45° to the optical axis, so both the x and y motion can be imaged. To get separate trajectories for each mode we implement a digital bandpass filter around the respective resonance frequency. Calibration of the sphere's displacement relies on knowledge of the optical system's magnification, which we determine using knowledge of the sphere's size (100(6)  $\mu\text{m}$ , as specified by the manufacturer). Including the uncertainty from the alignment of the trap coils with respect to the optical axis in addition to the  $\pm 6\%$  uncertainty from the size of the sphere, we estimate a total uncertainty of  $\pm 13\%$  for the calibrated COM displacement.

The light source is turned on only for calibration measurements, as the illumination heats the particle and limits the levitation time to approximately one hour. Further, optical band-pass filters (approximately 400 nm – 650 nm) on the millikelvin stage reduce ambient light reaching the particle and heating it. Without the filters (and the light source turned off) levitation times are limited to around four hours, while we have not yet found a limit (>30 h) using the filters.

## OPTIMIZATIONS AND GROUND STATE COOLING

In this section we provide more detail on how to implement the improvements that are necessary to perform feedback cooling to the ground state. We will consider only cooling of the z-mode, cooling of the other modes and 3D-cooling can be characterized and optimized in an analogous manner. We first show that the coupling strength can be increased by almost four orders of magnitude, s.t. the measurement noise (in units of  $\text{m}/\sqrt{\text{Hz}}$ ) with a state-of-the-art SQUID decreases to  $1 \times 10^{-15} \text{ m}/\sqrt{\text{Hz}}$ . We then take into account the back action from the SQUID due to the circulating current and determine the standard quantum limit (SQL) of our system. We proceed to evaluate the requirements for

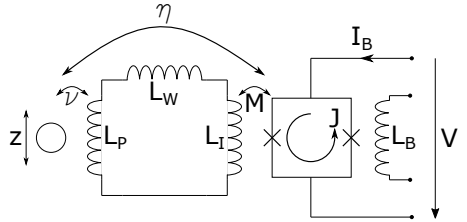


FIG. 9. Schematic of the readout circuit. The working point of the SQUID is set by the bias current  $I_B$  and the bias flux coupled into the SQUID via  $L_B$ . For appropriate bias values and small changes in flux (in FLL mode this is assured by applying feedback over  $L_B$ ), the voltage drop  $V$  is proportional to the flux in this SQUID loop.

ground state cooling as well as contributions to heating from vibrations and frequency fluctuations.

### Coupling strength

We can increase the coupling strength by better positioning of the pickup loop relative to the superconducting sphere and by increasing the number of turns of the pickup loop, thus matching its inductance to that of the input coil. For the calculation, we will assume a planar pickup loop with circular windings, positioned coaxial with the z-axis. Then Eq. 1 leads to

$$\nu_1 = \pi b_z R_P^2 \left( \frac{R^2}{R_P^2 + Z_P^2} \right)^{\text{net}} \times \left( 1 - \frac{R^2}{R_P^2 + Z_P^2} \left( 1 - \frac{5Z_P^2}{R_P^2 + Z_P^2} \right) \right) \quad (3)$$

for the coupling strength w.r.t. a single turn of the pickup loop with radius  $R_P$  and z-position  $Z_P$ . The coupling strength to a multi-turn pickup loop can be written as a sum of terms of this form,  $\nu = \sum_i \nu_1(R_{P,i}, Z_{P,i})$ , and the coupling strength to the SQUID (cf. Fig. 9) is obtained as

$$\eta = \nu \frac{k\sqrt{L_I L_S}}{L_P + L_I + L_W}.$$

Here  $L_P$ ,  $L_I$  and  $L_S$  are the inductances of pickup coil, SQUID input coil and SQUID, respectively. We have used that the mutual inductance  $M$  between input coil and SQUID can be written as  $M = k\sqrt{L_I L_S}$  with  $|k| < 1$ .  $L_W$  denotes the stray inductance of the pickup circuit and is in our case dominated by the wires connecting the pickup coil to the SQUID,  $L_W \approx 100nH$ .

A relevant figure of merit for the measurement noise of the SQUID is the so-called energy resolution  $S_{EE} = \frac{S_{\phi\phi}}{2L_S}$ , with state-of-the-art SQUIDs reaching values on the

order of  $\hbar$  [9, 10]. In terms of position resolution this can be written as

$$S_{nn} = \frac{S_{\phi\phi}}{\eta^2} = \frac{2S_{EE}(L_P + L_I + L_W)^2}{k^2 \nu^2 L_I}. \quad (4)$$

In order to get a realistic estimate for this we will use the SQUID parameters presented in [10], i.e.  $L_S = 15$  pH,  $L_I = 0.53$   $\mu$ H,  $M = 2.3$  nH and  $\frac{S_{\phi\phi}}{2k^2 L_S} = 5.5\hbar$ . For the pickup coil we assume a wire width of  $0.3$   $\mu$ m and a distance between the wires of  $0.45$   $\mu$ m, which is also the resolution of the input coil of our existing SQUID. We use the modified Wheeler formula [11] to determine  $L_P$ , s.t. we get a fully analytical expression for  $S_{nn}$ . We also restrict us to  $Z_P \geq R$ . Given these parameters, as well as  $b_z = 147$  T/m, we minimize  $S_{nn}$  with respect to  $R_P$ ,  $Z_P$  and  $N$ , where  $R_P$  now denotes the inner radius of the pickup coil and  $N$  is the number of turns. This results in  $\eta \approx 5.5 \times 10^7$   $\phi_0$ /m and  $S_{nn} \approx 1 \times 10^{-15}$  m for  $Z_P = R$ ,  $R_P \ll R$  and  $N \approx 87$ . We note that the scaling of the coupling (Eq. 3) means that the measurement noise can be further decreased by working with higher gradients or using larger particles (a scale-independent expression for the coupling is easily obtained by measuring distance in units of  $R$ , magnetic fields in units of  $b_z R$  and thus the coupling in units of  $b_z R^2$ ).

### The standard quantum limit

Equation 4 for the readout signal measured with the SQUID is valid only when the back-action stemming from the circulating SQUID current onto the levitating particle is negligible. This is a reasonable assumption given the weak coupling in our current setup, but for increased coupling strength the back-action should be considered. All relevant parameters are stated for the SQUID coupled to the input circuit and can be different than the parameters of the uncoupled SQUID, depending on the capacitive coupling at the Josephson frequency [7]. The readout noise is set by the flux noise, while the back-action noise is determined by fluctuations of the circulating current  $J$ . For a shunted SQUID the origin of both flux and current fluctuations is current noise in the shunt resistors and the quantum limit that arises from zero-point-fluctuations is  $\sqrt{S_{\phi\phi} S_{JJ}} - S_{\phi J}^2 \geq \hbar$  [12, 13]. We will assume in the following that correlations between flux and current noise are negligible,  $S_{\phi J} \approx 0$  [13, 14].

A current  $J$  around the SQUID loop will effect a force  $-\eta J$  on the levitated sphere and thus the measured displacement PSD of the sphere becomes

$$S_{zz}^m = \frac{S_{\phi\phi}}{\eta^2} + |\chi|^2 (S_{FF}^{th} + \eta^2 S_{JJ}).$$

The product of measurement noise and back-action force noise thus fulfills the Heisenberg-like inequality

$$\frac{S_{\phi\phi}}{\eta^2} \eta^2 S_{JJ} \geq \hbar^2 \text{ and } S_{zz}^m \text{ is minimized for } \eta^2 = \frac{1}{|\chi|} \sqrt{\frac{S_{\phi\phi}}{S_{JJ}}},$$

such that

$$S_{zz}^m = 2|\chi| \sqrt{S_{\phi\phi} S_{JJ}} + |\chi|^2 S_{FF}^{th}.$$

For  $\sqrt{S_{\phi\phi} S_{JJ}} = \hbar$  this corresponds to the standard quantum limit.

### Feedback cooling

We now assume we provide direct feedback s.t. the effective damping of the oscillator becomes  $\gamma + \Gamma$ , where  $\Gamma$  is the cold damping added by the feedback [15] and  $\tilde{\chi}(\omega) = 1/[m(\omega_0^2 - \omega^2 - i(\gamma + \Gamma)\omega)]$  is the effective susceptibility. The measurement noise will also enter the feedback system, resulting in an additional force, and the displacement power spectral density becomes

$$S_{zz} = |\tilde{\chi}|^2 \left( S_{FF}^{th} + \eta^2 S_{JJ} + (m\omega\Gamma)^2 \frac{S_{\phi\phi}}{\eta^2} \right).$$

For  $\Gamma = \frac{\eta^2}{m\omega_0 L_S} \gg \gamma$  this corresponds a mean phonon number

$$\bar{n} = \frac{1}{\hbar\eta^2} \left( k_B T_0 m \gamma \tilde{L}_S \right) + \frac{1}{2} \left( \frac{\sqrt{S_{\phi\phi} S_{JJ}}}{\hbar} - 1 \right),$$

where we have introduced the shorthand  $\tilde{L}_S = \sqrt{\frac{S_{\phi\phi}}{S_{JJ}}}$ .

Close to the optimum working point  $\tilde{L}_S \approx L_S$  [14]. Using  $\eta = 5.5 \times 10^7$   $\Phi_0$ /m as well as assuming  $T_0 = 15$  mK,  $m = 5.6$   $\mu$ g and  $L_S = 15$  pH, we need  $\gamma \approx 1 \times 10^{-6}$  s $^{-1}$  to keep the left term negligible. Ground state cooling then requires  $\sqrt{S_{\phi\phi} S_{JJ}} < 3\hbar$ . While current noise in SQUIDS is challenging to measure [16], a DC-SQUID with  $\sqrt{S_{\phi\phi} S_{JJ}} \approx 10\hbar$  has been reported [17]. Further, for  $\tilde{L}_S \approx L_S$  we would expect  $\sqrt{S_{\phi\phi} S_{JJ}} \approx 2S_{EE}$ . The lowest energy resolution reported up to date is  $S_{EE} \approx 1.7\hbar$  [9], so ground state cooling by continuous feedback will require a state-of-the-art SQUID.

### Heating

We now consider fluctuations of the trap center with spectral density  $S_{\epsilon\epsilon}$  as well as fractional fluctuations of the spring constant with spectral density  $S_{\delta\delta}$ . We note that the heating rate  $\Gamma_\delta E$  due to frequency fluctuations is proportional to the energy  $E$  of the oscillator. The average energy of the oscillator is then described by

$$\langle \dot{E} \rangle = (\Gamma_\delta - \gamma) \langle E \rangle + k_B T_0 \gamma + \dot{Q}_\epsilon,$$

where  $\dot{Q}_\epsilon$  is the heating rate due to fluctuations of the trap center. For  $\Gamma_\delta < \gamma$  this results in an effective temperature of

$$T_{eff} = \frac{k_B T_0 \gamma + \dot{Q}_\epsilon}{k_B (\gamma - \Gamma_\delta)}.$$

The heating rates are given by [18]

$$\dot{Q}_\epsilon = \frac{1}{4} m \omega_0^4 S_{\epsilon\epsilon}(\omega_0),$$

and

$$\Gamma_\delta = \frac{1}{4} \omega_0^2 S_{\delta\delta}(2\omega_0).$$

Using the values from the preceding paragraph, ground state cooling requires approximately  $\sqrt{S_{\delta\delta}(2\omega_0)} < 1 \times 10^{-7}/\sqrt{\text{Hz}}$  and  $\sqrt{S_{\epsilon\epsilon}(\omega_0)} < 1 \times 10^{-19} \text{ m}/\sqrt{\text{Hz}}$  (corresponding to  $T_{eff} < 20 \text{ mK}$ ). Regarding the former we note that relative fluctuations on the order of one part per billion can be reached in superconducting coils [19], while the latter requires further improvements to our vibration isolation system. Suspending the system from the top plate of the cryostat would allow us to add two more stages and achieve the required vibration suppression.

---

\* joachim.hofer@univie.ac.at

† Currently at: QuTech, Delft University of Technology, Delft, The Netherlands

- [1] J. Hofer and M. Aspelmeyer, Analytic solutions to the Maxwell–London equations and levitation force for a superconducting sphere in a quadrupole field, *Physica Scripta* **94**, 125508 (2019).
- [2] J. D. Livingston, Magnetic properties of superconducting lead-base alloys, *Phys. Rev.* **129**, 1943 (1963).
- [3] R. S. Van Dyck, D. L. Farnham, S. L. Zafonte, and P. B. Schwinberg, Ultrastable superconducting magnet system for a penning trap mass spectrometer, *Review of Scientific Instruments* **70**, 1665 (1999).
- [4] L. Neuhaus, R. Metzdorff, S. Chua, T. Jacqmin, T. Briant, A. Heidmann, P.-F. Cohadon, and S. Deléglise, PyRPL (Python Red Pitaya Lockbox) — An open-source software package for FPGA-controlled quantum optics experiments, in *2017 Conference on Lasers and Electro-Optics Europe European Quantum Electronics Conference (CLEO/Europe-EQEC)* (2017) pp. 1–1.
- [5] T. L. Aldcroft, P. F. Michelson, R. C. Taber, and F. A. McLoughlin, Six-degree-of-freedom vibration isolation systems with application to resonant-mass gravitational radiation detectors, *Review of Scientific Instruments* **63**, 3815 (1992).
- [6] L. D. Hinkle and B. R. F. Kendall, Pressure-dependent damping of a particle levitated in vacuum, *Journal of Vacuum Science & Technology A* **8**, 2802 (1990).
- [7] J. M. Martinis and J. Clarke, Signal and noise theory for a dc SQUID amplifier, *Journal of Low Temperature Physics* **61**, 227 (1985).
- [8] J. C. Crocker and D. G. Grier, Methods of digital video microscopy for colloidal studies, *Journal of Colloid and Interface Science* **179**, 298 (1996).
- [9] D. D. Awschalom, J. R. Rozen, M. B. Ketchen, W. J. Gallagher, A. W. Kleinsasser, R. L. Sandstrom, and B. Bumble, Low-noise modular microsusceptometer using nearly quantum limited dc SQUIDS, *Applied Physics Letters* **53**, 2108 (1988).
- [10] P. Carelli, M. G. Castellano, G. Torrioli, and R. Leoni, Low noise multiwasher superconducting interferometer, *Applied Physics Letters* **72**, 115 (1998).
- [11] H. Wheeler, Simple inductance formulas for radio coils, *Proceedings of the Institute of Radio Engineers* **16**, 1398 (1928).
- [12] R. H. Koch, D. J. Van Harlingen, and J. Clarke, Quantum noise theory for the dc SQUID, *Applied Physics Letters* **38**, 380 (1981).
- [13] V. Danilov, K. Likharev, and A. Zorin, Quantum noise in squids, *IEEE Transactions on Magnetics* **19**, 572 (1983).
- [14] C. D. Tesche and J. Clarke, dc SQUID: Current noise, *Journal of Low Temperature Physics* **37**, 397 (1979).
- [15] T. W. Penny, A. Pontin, and P. F. Barker, Performance and limits of feedback cooling methods for levitated oscillators: A direct comparison, *Phys. Rev. A* **104**, 023502 (2021).
- [16] J. Martinis and J. Clarke, Measurements of current noise in dc SQUIDS, *IEEE Transactions on Magnetics* **19**, 446 (1983).
- [17] P. Falferi, M. Bonaldi, M. Cerdonio, R. Mezzena, G. A. Prodi, A. Vinante, and S. Vitale,  $10\hbar$  superconducting quantum interference device amplifier for acoustic gravitational wave detectors, *Applied Physics Letters* **93**, 172506 (2008).
- [18] M. E. Gehm, K. M. O’Hara, T. A. Savard, and J. E. Thomas, Dynamics of noise-induced heating in atom traps, *Phys. Rev. A* **58**, 3914 (1998).
- [19] J. W. Britton, J. G. Bohnet, B. C. Sawyer, H. Uys, M. J. Biercuk, and J. J. Bollinger, Vibration-induced field fluctuations in a superconducting magnet, *Phys. Rev. A* **93**, 062511 (2016).